Tesis Doctoral

Object-oriented modeling for the transient performance simulation of solar thermal power plants using parabolic trough collectors - A review and proposal of modeling approaches for thermal energy storage

Author:
Fritz Zaversky

Director:
David Astrain Ulibarrena, Dr. D.
Departamento de Ingeniería Mecánica,
Energética y de Materiales,
Universidad Pública de Navarra (UPNA)

Codirector:
Marcelino Sánchez González, Dr. D.
Director, Departamento de Energía Solar Térmica,
Centro Nacional de Energías Renovables (CENER)

Pamplona, 2014

"We are like tenant farmers chopping down the fence around our house for fuel when we should be using Nature's inexhaustible sources of energy — sun, wind and tide. ...I'd put my money on the sun and solar energy. What a source of power! I hope we don't have to wait until oil and coal run out before we tackle that."

Thomas Edison, 1931

Resumen

La energía solar termoeléctrica (solar thermal electricity: STE), también llamada como energía solar térmica concentrada (concentrated solar power: CSP) es una energía renovable con un gran potencial, ya que emplea directamente la abundante cantidad de energía solar que incide en el planeta Tierra. Una estimación aproximada proporciona un total de 85 petawatts ($85 \cdot 10^{15}$ W) de potencia solar disponible para los captadores solares terrestres. Es importante resaltar que esta potencia es más de 5000 veces la demanda mundial actual, que es de unos 15 terawatts ($15 \cdot 10^{12}$ W). Además, a diferencia de otras energías renovables (como la energía eólica o la fotovoltaica), las centrales solares termoeléctricas pueden suministrar energía de manera gestionable, mediante el almacenamiento térmico y/o la hibridación. Las centrales CSP captan la radiación solar normal directa (direct normal irradiation: DNI), la concentran en una superficie receptora, transforman el calor absorbido en trabajo mecánico y subsecuentemente en energía eléctrica, utilizando para ello ciclos termodinámicos de última generación.

Debido a que el comportamiento de las centrales solares térmicas está fuertemente relacionado con las condiciones de contorno ambientales que cambian significativamente en el tiempo (no solo a lo largo del día, sino también a lo largo del año), un nuevo campo de modelización ha surgido en este contexto ya que la consideración de simulaciones transitorias de la central en su conjunto (en particular, de periodos de tiempo mayores) se ha convertido en indispensable. Crear un modelo robusto de central solar que funcione de manera estable, y que tenga en cuenta la variación de las condiciones meteorológicas de entrada o las restricciones de las estrategias de operación introducidas por el usuario, no es una tarea trivial.

La intención de este trabajo es extender las técnicas actuales de modelización del almacenamiento térmico activo directo y activo indirecto, con dos tanques y sales fundidas como medio de almacenamiento. Con el objetivo de conseguir aumentar el conocimiento sobre su comportamiento térmico y los aspectos operacionales, los modelos desarrollados deben permitir la evaluación del sistema de almacenamiento térmico en condiciones transitorias.

Así, la parte principal de este trabajo (la Parte II) se centra en la modelización y evaluación del comportamiento de los intercambiadores de calor para la tecnología de almacenamiento térmico activo indirecto, que emplea sales fundidas (60 % en peso de nitrato sódico, $NaNO_3$, y 40 % en peso de nitrato potásico, KNO_3) como medio de almacenamiento y aceite térmico (una mezcla de difenilo, $C_{12}H_{10}$, y oxido de difenilo, $C_{12}H_{10}O$) como fluido caloportador. Asumiendo un diseño de intercambiador de calor del tipo carcasa y tubos, el comportamiento del proceso de intercambio de calor entre el medio de almacenamiento y el fluido caloportador se analiza en detalle, considerando condiciones de operación estacionarias y transitorias bajo cargas nominales y parciales. El modelo estacionario proporciona información útil sobre el coeficiente global de transmisión de calor y los rangos de variación de pérdidas de carga para dos configuraciones de intercambiadores de calor específicas. Se demuestra que la configuración de dos intercambiadores en paralelo supera a la configuración convencional de un único intercambiador en funcionamiento. Por otro lado, la evaluación del modelo transitorio suministra parámetros típicos del proceso como la ganancia, el tiempo muerto y la constante del tiempo para el modo de carga y descarga, en condiciones nominales y parciales.

Además, se ha obtenido un modelo transitorio del tanque de almacenamiento a alta temperatura razonablemente simple, el cual es muy adecuado para simulaciones del comportamiento de centrales CSP en su conjunto. En el estudio se ha demostrado que las pérdidas térmicas por convección natural en la atmosfera de gas encima de la superficie libre de las sales fundidas se pueden omitir en el modelo, causando errores despreciables. También, se pueden asumir coeficientes de convección constantes entre la superficie de las paredes del tanque y las sales fundidas. Sin embargo, la transmisión de calor por radiación entre la superficie libre de las sales fundidas y las paredes interiores del tanque, que no están en contacto con las sales, deben de ser consideradas, dada su importante influencia en las pérdidas totales. Además, debido al modelado de la trasmisión de calor por las paredes del tanque en modo transitorio y al cálculo preciso de la temperatura de la superficie exterior, la influencia que las condiciones de contorno ambientales tienen sobre las pérdidas de calor, pueden ser caracterizadas de manera mucho más adecuada que mediante métodos cuasi-estacionarios, que solo tienen en cuenta la temperatura ambiente.

Finalmente, la Parte III trata de la aplicación de los modelos desarrollados para los componentes del almacenamiento térmico, a un modelo exhaustivo y completo de una central de captadores cilindro-parabólicos a nivel global. De este modo se simula, no solo el comportamiento del sistema de almacenamiento térmico activo indirecto, sino también las respuestas de la central

solar térmica al completo, debido a los cambios en las condiciones de contorno ambientales. Se observa que la inercia térmica del sistema de almacenamiento activo indirecto es muy considerable, influyendo de manera notable en los rápidos cambios de carga necesarios para capturar la mayor cantidad posible de la energía solar disponible, y para alimentar el bloque de potencia con una potencia térmica constante, independientemente de la actual radiación solar.

Por último pero no menos importante, los modelos presentados han sido desarrollados de manera flexible, bien estructurada y con una programación orientada a objetos, particularmente dando importancia a una implementación independiente de la plataforma de simulación, hecho que ha sido llevado a cabo utilizando el lenguaje de modelación Modelica. Este es un lenguaje de modelizado de sistemas físicos multiobjetivo, que ha sido desarrollado en un esfuerzo internacional para unificar las técnicas de simulación ya existentes y para permitir el intercambio fácil de los modelos y librerías de modelos que se desarrollen. El concepto de Modelica se basa en modelos no causales que utilizan ecuaciones diferenciales ordinarias y algebraicas.

Kurzfassung

Solarthermische Elektrizität, international meist unter der Bezeichnung “concentrated solar power”(CSP) bekannt, ist ein vielversprechender erneuerbarer Energiesektor mit großem Potential. Grundsätzlich deswegen, weil solarthermische Kraftwerke die im Überfluß vorhandene Solarstrahlung direkt nutzen und in elektrischen Strom umwandeln. Durch einen überschlägigen Rechengang kommt man auf rund 85 Petawatt ($85 \cdot 10^{15}$ W) einfallender solarer Strahlungsleistung, die für Solarkollektoren auf dem Planeten Erde nutzbar sind. Dabei muss betont werden, dass diese Summe das 5000-fache des derzeitigen mittleren Weltenergiebedarfs pro Sekunde (mittlere Gesamtleistung) von 15 Terawatt ($15 \cdot 10^{12}$ W) übersteigt. Darüber hinaus, ermöglichen solarthermische Kraftwerke, im Gegensatz zu anderen erneuerbaren Technologien wie Windturbinen oder Photovoltaikanlagen, eine abrufbare Stromerzeugung. Dies wird entweder durch Speicherung von thermischer Energie ermöglicht, oder durch Kombination mit herkömmlicher fossiler Feuerung realisiert. Solarthermische Kraftwerke bündeln die verfügbare Direktnormalstrahlung der Sonne auf einen Solarabsorber, und wandeln die absorbierte Wärme danach mit Hilfe von modernen Wärmekraftanlagen in elektrischen Strom um.

Im Anbetracht der Tatsache, dass die Leistungsabgabe von solarthermischen Kraftwerken stark von den vorherrschenden Solarstrahlungs- und Wetterbedingungen abhängt, die signifikant im Laufe des Tages und darüber hinaus, im Laufe des Jahres variieren, hat sich in letzter Zeit ein neuer Bereich von Simulationsmethoden entwickelt, da instationäre Kraftwerkssimulationen auf Anlagenniveau, speziell über längere Zeiträume, unverzichtbar geworden sind. Der Entwurf eines robusten Kraftwerkmodells, welches unabhängig der vom Anwender zur Verfügung gestellten Wetterdaten oder Betriebsrichtlinien stabil läuft, ist auf keinen Fall ein einfaches Unterfangen.

Es ist das Ziel dieser Arbeit den derzeitigen Stand der Technik im Bereich der Modellierung des aktiven direkten und des aktiven indirekten Zwei-Tank-Wärmespeicherkonzeptes, basierend auf Salzschmelzen als Speichermedium und Thermalöl als Wärmetransportmedium (im Falle des aktiven indirekten

Konzeptes), zu erweitern. Es soll der derzeitige Wissensstand im Bereich ihres thermischen Verhaltens und bezüglich betriebstechnischer Aspekte erweitert werden. Im Speziellen sollen die entwickelten Modelle die Evaluierung des instationären Verhaltens des Wärmespeichersystems ermöglichen.

Daher geht der Hauptteil dieser Arbeit (Teil II) einerseits auf die Modellierung von Rohrbündelwärmeüberträgern für den Austausch von Wärme zwischen Thermalöl und Salzschmelze ein (für das aktive indirekte Wärmespeicherkonzept). Als Salzschmelze wird das sogenannte solare Salz betrachtet. Dies ist eine Mischung aus 60 Gewichtsprozent Natriumnitrat ($NaNO_3$) und 40 Gewichtsprozent Kaliumnitrat (KNO_3). Als Thermalöl wird eine Mischung aus Diphenyl ($C_{12}H_{10}$) und Diphenyloxid ($C_{12}H_{10}O$) betrachtet. Das Verhalten des Rohrbündelwärmeüberträgers wird mit Hilfe eines stationären, als auch anhand eines instationären Modells im Detail untersucht, sowohl im nominalen Betriebspunkt als auch in der Teillast. Das stationäre Modell liefert überaus brauchbare Information über die Bandbreiten des globalen Wärmeübergangskoeffizienten und des Druckverlustes für zwei unterschiedliche Wärmetauscherkonfigurationen. Es wird gezeigt, dass zwei separate parallele Wärmetauschereinheiten die konventionelle Konfiguration mit nur einer Wärmetauschereinheit bezüglich Betriebseigenschaften übertreffen. Andererseits liefert das instationäre Wärmetauschermodell wichtige Information über typische Prozessparameter wie Verstärkungsfaktoren, Totzeiten und Zeitkonstanten für repräsentative Lastpunkte, sowohl für den Ladevorgang als auch für den Entladevorgang des Wärmespeichersystems.

Darüber hinaus wird ein angemessen einfaches Modell eines Salzschmelzentanks diskutiert, welches einen guten Kompromiss zwischen numerischem Aufwand und Genauigkeit darstellt, wodurch es sich optimal für Kraftwerkssimulationen auf Anlagenniveau eignet. Zum Beispiel wurde herausgefunden, dass der konvektive Wärmetransport in der Gasatmosphäre über dem Flüssigkeitsspiegel der Salzschmelze im Modell vernachlässigt werden kann, da Simulationsergebnisse praktisch nicht unterscheidbar sind. Auch die konvektiven Wärmeübergangskoeffizienten zwischen der Salzschmelze und den benetzten inneren Wandflächen des Tanks können als konstant angenommen werden. Allerdings ist die Berücksichtigung des Wärmeübergangs durch Strahlung zwischen dem Flüssigkeitsspiegel der Salzschmelze und den unbenetzten inneren Wandflächen des Tanks unerlässlich, und ist in dieser Arbeit unter der Annahme einer idealen zylindrischen Geometrie implementiert. Dadurch dass die Hülle des Tanks im Modell instationär betrachtet wird, und die Temperatur der äußeren Hülle relativ genau approximiert wird, können Schwankungen der Umweltrandbedingungen (wie Einstrahlung oder Lufttemperatur) genauer erfasst werden als im Falle von quasi-stationären Methoden, die nur die vorherrschende Lufttemperatur berücksichtigen.

Teil III dieser Arbeit befasst sich mit der Anwendung der im vorhergehenden Teil entwickelten Modellkomponenten für thermische Energiespeicherung. Genauer gesagt, wird die Einbindung der neu entwickelten Modellkomponenten in ein umfassendes Kraftwerksmodell auf Anlagenniveau beschrieben. Mit der anschließenden numerischen Simulation wird nicht nur das instationäre Verhalten eines typischen aktiven indirekten Zwei-Tank-Wärmespeichersystems gezeigt, sondern auch die Reaktion des gesamten Kraftwerks auf wechselhafte Umweltbedingungen. Es wird demonstriert, dass die thermische Trägheit des aktiven indirekten Wärmespeicherkonzeptes nicht zu vernachlässigen ist und ein großes Hindernis für schnelle Lastwechsel darstellt, welche allerdings enorm wichtig sind um ein Maximum an Sonnenenergie einzuspeichern, und um den gekoppelten Wärmekraftprozess, unabhängig von der aktuellen Sonneneinstrahlung, mit einem konstanten Wärmestrom zu versorgen.

Abschließend muss erwähnt werden, dass die präsentierten Modelle in einer flexiblen, gut strukturierten und objektorientierten Art und Weise entwickelt wurden. Im Speziellen wurde auf eine von der Simulationsumgebung unabhängige Implementierung Wert gelegt, was mit Hilfe der Modellierungssprache Modelica erzielt wurde. Modelica ist eine fachbereichsübergreifende Beschreibungssprache für physikalische Systeme, die in einem internationalen Bemühen entwickelt wurde um bereits existierende und ähnliche Konzepte zu vereinheitlichen. Der große Vorteil von Modelica ist, dass entwickelte Modelle und Modellbibliotheken einfach austauschbar sind und von verschiedenen Simulationsumgebungen numerisch behandelt werden können. Modelica basiert auf nicht-kausalen Modellformulierungen unter der Verwendung von differential-algebraischen Gleichungen.

Abstract

Solar thermal power, also known as concentrated (or concentrating) solar power (CSP) or solar thermal electricity (STE), is a renewable energy sector with great potential, as it directly harnesses the abundant amount of solar energy incident on planet earth. A rough estimate gives a total of 85 petawatts ($85 \cdot 10^{15}$ W) of solar power available for terrestrial solar collectors. It has to be emphasized that this is more than 5000 times the current world's power demand of about 15 terawatts ($15 \cdot 10^{12}$ W). Furthermore, unlike other renewable energy sectors (like wind or photovoltaic power), solar thermal power plants can provide dispatchable power by means of thermal energy storage (TES) and/or hybridization. CSP plants capture the sun's direct normal irradiation (DNI), concentrate it onto a receiving surface and transform the absorbed heat into mechanical work and subsequently electric energy, by using state-of-the-art thermodynamic power cycles.

Given that the performance of solar thermal power plants is strongly related to the environmental boundary conditions that significantly change over time (not only over one day, but also throughout the year), a new field of modeling has emerged in this context since the consideration of transient power plant simulations on system level (in particular, over longer periods of time) has become indispensable. Creating a robust performance model of a solar power plant that runs stable, no matter what weather input data or operational strategy constraints are provided by the user, is not a trivial task.

This work's intention is to extend the current state-of-the-art regarding the modeling of the active direct and the active indirect two-tank molten-salt-based thermal energy storage (TES) concept. The aim is to widen the knowledge about their thermal behavior and operational aspects. In particular, the developed models shall enable the evaluation of the storage system's transient behavior.

Thus, the main part of this work (Part II) focuses on the modeling and the performance evaluation of oil-to-molten salt heat exchangers for the active indirect thermal energy storage technology, applying molten salt (60%,

by weight, sodium nitrate, $NaNO_3$, and 40%, by weight, potassium nitrate, KNO_3) as storage medium and thermal oil (a mixture of diphenyl, $C_{12}H_{10}$, and diphenyl oxide, $C_{12}H_{10}O$) as heat transfer fluid. Assuming a shell-and-tube heat exchanger design, the performance of the heat exchange process between the storage medium and the heat transfer fluid is discussed in detail, considering steady-state as well as transient operating conditions under nominal as well as partial loads. On the one hand, the steady-state model gives useful information about overall heat transfer coefficient and pressure drop ranges for two specific heat exchanger setups. In particular, it is shown that two separate heat exchanger trains in parallel exceed the conventional single train setup in performance. On the other hand, the evaluation of the transient performance model yields typical process parameters as process gain, dead time and time constant for charging as well as for discharging mode at representative heat exchanger loads.

In addition to this, a reasonable simple transient high-temperature storage tank model is derived, which is well suited for CSP performance simulations on system level due to reasonable model simplifications. For example, it is found in this work that the convective heat losses via the tank's gas atmosphere (usually nitrogen at ambient pressure) above the molten salt surface can be neglected by only introducing negligible calculation errors. Also, the convective heat transfer coefficients between the molten salt and the wetted parts of the tank's inner steel jacket may be set to constant values. However, the important radiative heat transfer between the surface of the molten salt and the non-wetted parts of the tank's inner steel jacket must be considered, which is done assuming an ideal cylindrical geometry. Furthermore, due to the transient modeling of the storage tank walls and a detailed estimation of the exterior surface temperature, the influence of altering environmental boundary conditions can be captured more accurately than by quasi-steady-state methods that only account for the current ambient air temperature.

Finally, Part III treats the application of the developed TES model components in a comprehensive model of a parabolic trough collector plant on system level, showing not only the behavior of a typical active indirect two-tank TES system under transient operating conditions, but also the responses of the entire solar thermal power plant to changing environmental boundary conditions. It is shown that the thermal inertia of the active indirect TES concept is considerable and forms a major obstacle for rapid load changes that are crucial for capturing as much solar energy as possible, and to supply the power block with constant thermal power, independently of the current solar irradiance.

Last but not least, the presented models have been developed in a flexible, well-structured and object-oriented way, particularly giving importance

to a simulation-platform-independent implementation, which has been accomplished applying Modelica, a multi-purpose physical system modeling language, developed in an international effort in order to unify already existing similar modeling approaches, and to enable developed models and model libraries to be easily exchanged. Modelica's concept is based on non-causal models featuring true ordinary differential and algebraic equations.

Preface

The course for achieving the present work was set in the summer of 2010 on a beautiful Greek island, in particular, at the southernmost point of the Dodecanesian island Rhodes, called Prasonisi, where I decided to spend 3 months windsurfing, after successfully finishing my Master's degree (Dipl.-Ing.) in mechanical engineering at Graz University of Technology (Austria) in April that year.

There, living in my father's minivan[1] or, as I used to say, my "thousand-star hotel" (as the sky was clear almost every night), I had enough time to reflect what I wanted to do in my life after university. Since the beginning, it was clear to me that I wanted to work in the field of renewable energies, because out there, in direct contact with nature, it makes you easily forget about prerequisites of the civilized world, such as electric power supply or Internet connections, making huge coal-fired or even nuclear-based power plants become completely useless. Clearly, the only power plant that I would had tolerated at that point in my immediate vicinity would had been a wind turbine, a photovoltaic or solar thermal plant [2]. Obviously, this immediately leads to the key point: Industrial processes or power plants, in whose immediate vicinity people would, purely instinctively, never ever dare to build their homes, are clearly not supportable and must be considered as obsolete.

Anyway, that summer I decided to send my records to companies and research institutions working in the field of solar thermal energy. With a reasonable amount of stubbornness, partly caused by the expectation of doing my PhD close to Europe's best surf breaks, I finally got a scholarship at the National Renewable Energy Center (CENER) in Spain. Thus, in February 2011, I packed my stuff (including my surfboards) into my car and drove to Pamplona in order to start my new life as a PhD student.

[1] I really appreciate the fact that my father was always willing to lend me his car for holiday activities. However, due to numerous surfing trips, it more and more resembled a sandbox on wheels, one of the reasons, why he finally handed it over to me.

[2] In fact, all of these technologies would had worked perfectly right there at the beach, since the Meltemi blew consistently almost every day above force 4, and the sun truly scorched your skin without using protection.

Acknowledgments

I have to thank so many people that helped me and supported me during the last 3 years.

First of all, I have to thank Marcelino who was my first contact person here at CENER. I am grateful that he initiated the necessary organizational tasks in order to welcome me as a scholarship PhD student. In this context, I am also grateful to Oihana who finally helped me accomplishing the paper work, since my Spanish level was literally speaking at level zero at that time.

Next, special thanks go to my supervisor David who accepted me as one of his PhD students and organized many things for me at the Public University of Navarre. I am deeply grateful for his assistance during the last 3 years.

Furthermore, I am grateful to the staff of the Solar Thermal Energy Department for cordially welcoming me in their office. It has been a pleasure to work together with Javier, Michael, Amaia and Rodrigo on our "Modelica mission", whose aim has been the development of a comprehensive model library for the simulation of solar thermal power plants. Despite the fact that we were all newbies to object-oriented modeling 3 years ago, I think we have done a great job. Especially, Javier has had good ideas regarding library and model structure, which are partly reflected in the present work. Many thanks go also to Edurne, who always and most efficiently has accomplished the administrative tasks :-). I have to thank Iñigo for providing me weather and solar irradiation data for some of my simulations, furthermore, for translating the abstract into Spanish, and additionally, for numerous surfing adventures at the coastline of Basque Country. Thank you Fabienne, for organizing "international pincho" nights in your home. Definitely, they have been culinary highlights.

Of course, I am deeply grateful for receiving so much support from my family during my time at university and down to the present day. Especially, I would like to thank my parents, since without their help, my academic career would not have been possible in this form. Thank you Estibaliz, for being patient, especially during our weekends, when I was busy with writing my articles and thinking about my thesis. I am also grateful to you for

proofreading some parts of this work.

Additionally, I appreciate the effort made by the reviewers of my published articles. Thank you for your comments and recommendations, which, of course, are also reflected in the present work.

Last but not least, special thanks go of course to LaTeX, since without its help, I would have gone crazy at some point during my PhD adventure.

Contents

Nomenclature

$\alpha_{surface}$	solar absorptivity of the tank's outer surface (-)
β	volumetric thermal expansion coefficient ($\frac{1}{K}$)
χ	storage tank fill factor (-)
Δh_{HTF}	increase in specific enthalpy of the heat transfer fluid when flowing through the solar field ($\frac{J}{kg}$)
Δp	heat exchanger duct pressure drop (Pa)
ΔT	temperature drop of molten salt inventory (K)
Δt	time difference (s)
ΔT_1	temperature difference between fluids at the left heat exchanger end (K)
ΔT_2	temperature difference between fluids at the right heat exchanger end (K)
ΔT_{lm}	logarithmic mean temperature difference of heat exchanger (K)
ΔT_{melt}	assumed temperature difference for melting (K)
ΔT_m	true mean temperature difference of heat exchanger (K)
ϵ	ratio of liquid phase volume to total volume (solid + liquid) (-), page 70
ϵ	solar receiver or absorber emissivity (-), page 8
$\epsilon_{surface}$	tank outer surface emissivity (-)
η	dynamic viscosity ($Pa\ s$)

η_{Carnot}	Carnot efficiency of a heat engine (-)
η_c	critical pressure ratio for flow across a valve (-)
$\eta_{opt\ peak}$	peak optical efficiency for zero incidence angle of a PTC (-), page 205
η_{opt}	PTC optical efficiency, including the cosine of the incidence angle (-), page 29
η_{opt}	optical efficiency of a solar receiver-concentrator unit (-), page 8
$\eta_{pump\ nom}$	nominal pump efficiency (-)
η_{pump}	pump efficiency (-)
$\eta_{receiver}$	solar receiver efficiency (-)
$\eta_{solar\ power\ plant}$	theoretical solar-to-mechanical conversion efficiency of a solar thermal power plant (-)
η_s	isentropic efficiency of a turbine stage (-)
κ	isentropic exponent or heat capacity ratio (-)
ν	kinematic viscosity ($\frac{m^2}{s}$)
ω	excitation frequency ($\frac{rad}{s}$)
Ψ	outflow function (-)
ρ	density ($\frac{kg}{m^3}$)
ρ_0	upstream density ($\frac{kg}{m^3}$)
ρ_f	fluid density ($\frac{kg}{m^3}$)
ρ_i	density of fluid within control volume i ($\frac{kg}{m^3}$)
ρ_{salt}	density of molten salt ($\frac{kg}{m^3}$)
ρ_s	density of solid storage material ($\frac{kg}{m^3}$)
σ	Stefan-Boltzmann constant ($\frac{W}{m^2K^4}$)
τ	process time constant (s)

τ_d	controller derivative time (s)
τ_i	controller integral time (s)
Θ	incidence angle of the direct normal irradiance (deg), page 205
Θ	process dead time (s)
Θ_{sun}	half of the apex angle of the sun when viewed from planet earth (deg), page 12
Θ_{zenith}	zenith angle of the sun (rad), page 119
φ	smooth transition variable that varies between 1 and zero (-), page 256
ζ	pressure drop factor (-)
ζ_{IAM}	incidence angle modifier (IAM) including the cosine of the incidence angle (-)
$\zeta_{shading}$	shading attenuation factor (-)
A	area of heat transfer of a heat exchanger (m^2), page 91
A	cross sectional area (m^2), page 150
A	reference surface area of heat transfer (m^2), page 62
$A_{aperture}$	solar plant or collector aperture area (m^2)
$A_{coll\ i}$	solar collector aperture area at segment i (m^2)
A_c	cross sectional area of the storage tank (m^2)
$A_{receiver}$	area of a solar receiver or absorber (m^2)
A_{roof}	roof surface area of storage tank (m^2)
A_s	solid storage medium surface area for heat transfer between solid and liquid phase (m^2)
$A_{tube\ inner\ i}$	inner area of heat transfer of tube segment i (m^2)
$A_{tube\ outer\ i}$	outer area of heat transfer of tube segment i (m^2)
A_{valve}	valve cross sectional area (m^2)

A_{wall}	circumferential surface area of the infinitesimal storage tank slice (m^2)
BSRN	Baseline Surface Radiation Network
C	area concentration ratio (-)
c_{fluid}	specific heat capacity of the HTF ($\frac{J}{kgK}$)
C_f	specific heat capacity of fluid ($\frac{J}{kgK}$), page 70
$C_{glass\,i}$	heat capacity of discrete glass envelope section i ($\frac{J}{K}$)
C_{max}	theoretical maximum concentration ratio (-)
$C_{p\,melt}$	assumed specific heat capacity for melting ($\frac{J}{kgK}$)
c_p	specific heat capacity ($\frac{J}{kgK}$)
C_s	specific heat capacity of solid storage material ($\frac{J}{kgK}$), page 70
$C_{tube\,i}$	heat capacity of discrete tube section i ($\frac{J}{K}$)
c_{tube}	specific heat capacity of the absorber tube material ($\frac{J}{kgK}$
CFD	computational fluid dynamics
CSP	concentrating solar power - concentrated solar power
CV	control volume
D	storage tank diameter (m)
d_f	fin outer diameter (m)
D_{inner}	absorber tube inner diameter (m)
D_{outer}	absorber tube outer diameter (m)
D_{ref}	storage tank reference diameter (m)
d_r	fin root diameter (m)
ds	infinitesimal length of the flow filament s (m)
DNI	direct normal irradiance ($\frac{W}{m^2}$), or direct normal irradiation ($\frac{J}{m^2}$)

DSG	direct steam generation
$e(t)$	continuous controller error input (unit depends on the application)
f	fractional porosity of the solid, i.e. free space per unit volume (-), page 69
f	friction factor (-)
F_f	friction force acting on the fluid within control volume i (N)
F_g	gravitational force acting on the fluid within control volume i (N)
F_p	pressure force acting on the fluid within control volume i (N)
$\vec{F}$	force vector (N)
G	solar flux incident on planet earth $(\frac{W}{m^2})$
g	acceleration due to gravity $(\frac{m}{s^2})$
Gr	Grashof number (-)
h	convective heat transfer coefficient $(\frac{W}{m^2K})$
h	heat transfer coefficient between solid and liquid phase $(\frac{W}{m^2K})$, page 70
h_1	specific enthalpy at the turbine stage inlet $(\frac{J}{kg})$
h_{2s}	specific enthalpy after an isentropic state transformation from turbine stage inlet state to the pressure level of the outlet state $(\frac{J}{kg})$
h_2	specific enthalpy at the turbine stage outlet $(\frac{J}{kg})$
$h_{a,i}$	upstream specific enthalpy at the left boundary of control volume i $(\frac{J}{kg})$
h_a	specific enthalpy stream variable at port a of T-junction - if mass flow at port positive then inflow enthalpy - if mass flow at port negative then outflow, i.e. ideally mixing enthalpy $(\frac{J}{kg})$, page 250

$h_{b,i}$	upstream specific enthalpy at the right boundary of control volume i ($\frac{J}{kg}$)
h_b	specific enthalpy stream variable at port b of T-junction - if mass flow at port positive then inflow enthalpy - if mass flow at port negative then outflow, i.e. ideally mixing enthalpy ($\frac{J}{kg}$), page 250
h_c	specific enthalpy stream variable at port c of T-junction - if mass flow at port positive then inflow enthalpy - if mass flow at port negative then outflow, i.e. ideally mixing enthalpy ($\frac{J}{kg}$), page 250
$h_{extraction}$	specific enthalpy of extracted steam ($\frac{J}{kg}$)
$h_{feed\,water\,entering}$	specific enthalpy of feed water entering the deaerator ($\frac{J}{kg}$)
$h_{feed\,water\,leaving}$	specific enthalpy of the feed water leaving the deaerator (bubble enthalpy at current deaerator pressure) ($\frac{J}{kg}$)
$h_{fluid\,i}$	forced convective heat transfer coefficient between tube-side fluid and the tube wall ($\frac{W}{m^2K}$)
h_{fluid}	heat transfer coefficient between HTF and the absorber tube's inner surface ($\frac{W}{m^2K}$)
h_g	heat capacity per unit volume of the liquid ($\frac{J}{m^3K}$), page 69
h_{in}	specific enthalpy entering the control volume ($\frac{J}{kg}$)
h_i	convective heat transfer coefficient between tube inner wall and tube-side fluid ($\frac{W}{m^2K}$), page 91
h_i	specific enthalpy of control volume i ($\frac{J}{kg}$)
h_{la}	laminar flow convective heat transfer coefficient ($\frac{W}{m^2K}$)
$h_{loss\,wall}$	overall heat transfer coefficient to the ambient ($\frac{W}{m^2K}$), page 72
h_{melt}	specific heat of fusion of the PCM ($\frac{J}{kg}$)
h_{out}	specific enthalpy leaving the control volume ($\frac{J}{kg}$)
h_o	convective heat transfer coefficient between tube outer wall and shell-side fluid ($\frac{W}{m^2K}$), page 91

h_s	heat capacity per unit volume of the solid ($\frac{J}{m^3 K}$), page 69
h_{tu}	turbulent flow convective heat transfer coefficient ($\frac{W}{m^2 K}$)
HCE	heat collector element of a parabolic trough collector
i	control volume numerator (integer from 1 to n)
$I_{diffuse\,horizontal}$	diffuse horizontal solar irradiance ($\frac{W}{m^2}$)
$I_{global\,horizontal}$	global horizontal solar irradiance ($\frac{W}{m^2}$)
$\vec{I}$	momentum vector ($\frac{kg\,m}{s}$)
IAPWS	International Association for the Properties of Water and Steam
j	conduction model radial section numerator (integer from 1 to 2)
k	constant of heat transfer ($\frac{W}{m^3 K}$), page 69
k	thermal conductivity ($\frac{W}{mK}$)
k_{air}	thermal conductivity air ($\frac{W}{mK}$)
k_{eff}	effective thermal conductivity of the solid/liquid mass mixture ($\frac{W}{mK}$), page 72
$k_{pressure\,drop}$	constant component overall pressure drop factor ($\frac{1}{kg\,m}$)
K_p	controller proportional gain (unit depends on the application)
K_s	process gain (-) or ($\frac{K\,s}{kg}$)
k_{tube}	thermal conductivity of tube material ($\frac{W}{mK}$)
L	characteristic length (m)
L_i	length of discrete longitudinal segment i (m)
L_{loop}	total length of one representative loop (m)
$\dot{m}$	pump mass flow ($\frac{kg}{s}$), page 243
$\dot{m}$	steam mass flow across turbine ($\frac{kg}{s}$), page 239

$\dot{m}_0$	steam mass flow across turbine at reference conditions ($\frac{kg}{s}$), page 239
$\dot{m}_{a,i}$	mass flow at the left boundary of control volume i, if entering positive else negative ($\frac{kg}{s}$)
$\dot{m}_{b,i}$	mass flow at right boundary of control volume i, if leaving positive else negative ($\frac{kg}{s}$)
$\dot{m}_{extraction}$	turbine extraction mass flow rate entering the deaerator ($\frac{kg}{s}$)
$\dot{m}_{feed\ water\ entering}$	feed water mass flow rate entering the deaerator ($\frac{kg}{s}$)
$\dot{m}_{feed\ water\ leaving}$	feed water mass flow rate leaving the deaerator ($\frac{kg}{s}$)
$\dot{m}_f$	fluid mass flow rate ($\frac{kg}{s}$)
$\dot{m}_{HTF}$	heat transfer fluid mass flow rate ($\frac{kg}{s}$)
$\dot{m}_{in}$	entering mass flow ($\frac{kg}{s}$)
$\dot{m}_{nom}$	nominal pump mass flow ($\frac{kg}{s}$), page 243
$\dot{m}_{out}$	leaving mass flow ($\frac{kg}{s}$)
$\dot{m}_{port\ a}$	mass flow rate at port a of T-junction - entering positive, leaving negative ($\frac{kg}{s}$), page 250
$\dot{m}_{port\ b}$	mass flow rate at port b of T-junction - entering positive, leaving negative ($\frac{kg}{s}$), page 250
$\dot{m}_{port\ c}$	mass flow rate at port c of T-junction - entering positive, leaving negative ($\frac{kg}{s}$), page 250
$\dot{m}_{valve}$	mass flow rate across valve ($\frac{kg}{s}$)
m	control volume fluid mass (kg), page 113
m	storage tank molten salt mass (kg), page 63
m	total fluid mass of T-junction control volume (kg), page 250
M_{fluid}	mass of HTF per unit length of tube ($\frac{kg}{m}$)
m_i	fluid mass within control volume i (kg)

m_{max}	storage tank molten salt mass at maximum filling level (kg)
m_{min}	storage tank molten salt mass at minimum filling level (kg)
M_{sun}	radiant flux at the sun's surface ($\frac{W}{m^2}$), page 12
M_{tube}	mass of absorber tube per unit length of tube ($\frac{kg}{m}$)
MSL	Modelica Standard Library
n	number of finite control volumes along the flow direction (integer)
n_{loops}	number of identical parallel collector loops per solar field (integer)
$n_{t\,lumped}$	number of tubes that are lumped together to a single representative tube-like object (integer)
n_t	number of parallel tubes in a tube bundle (integer)
$Nu_{\,la}$	laminar flow Nusselt number (-)
$Nu_{\,tu}$	turbulent flow Nusselt number (-)
NTU	number of transfer units (-)
p_0	upstream pressure (Pa), page 232
p_1	pressure at valve cross section (Pa), page 232
p_2	downstream pressure (Pa), page 232
p_c	critical pressure (Pa), page 232
P_f	fin pitch (distance between fins) (m)
p_{i0}	turbine stage inlet pressure at reference conditions (Pa), page 239
p_i	pressure within control volume i (Pa)
p_i	turbine stage inlet pressure (Pa), page 239
p_{o0}	turbine stage outlet pressure at reference conditions (Pa), page 239

p_o	turbine stage outlet pressure (Pa), page 239
PCM	phase change material
PTC	parabolic trough collector
$\dot{Q}$	heat exchanger heat duty or thermal power transferred (W), page 91
$\dot{Q}_{absorbed}$	thermal power absorbed by a solar receiver (W), page 8
$\dot{Q}_{absorbed}$	total absorbed solar power for one representative collector loop (W), page 258
$\dot{Q}_j$	heat flow in radial direction (W), page 155
$\dot{Q}_{loss,\,empty}$	heat loss of the empty storage tank (W), page 63
$\dot{Q}_{loss,\,full}$	heat loss of the full storage tank (W), page 63
$\dot{Q}_{loss}$	heat loss of a solar receiver (W), page 8
$\dot{Q}_{loss}$	storage tank heat loss (W), page 62
$\dot{Q}_{loss}$	total heat loss of one representative solar collector loop (W), page 258
$\dot{q}_{loss}$	specific heat loss of the storage tank ($\frac{kW}{m^2}$)
$\dot{Q}_{net,i}$	net heat flow over the boundary of control volume i (W)
$\dot{Q}_{net}$	net heat flow (W)
$\dot{Q}_{radiation\,roof}$	radiative heat loss to the environment at the horizontal tank roof (W)
$\dot{Q}_{radiation\,wall}$	radiative heat loss to the environment at the vertical tank wall (W)
$\dot{Q}_{solar\,input\,glass}$	solar heat input at discrete glass envelope section i (W)
$\dot{Q}_{solar\,input\,i}$	solar heat input at discrete absorber section i (W)
$\dot{Q}_{solar\,roof}$	solar heat input at storage tank roof (W)
$\dot{Q}_{useful}$	thermal power collected by the solar power plant's heat transfer fluid (W), page 256

$\dot{Q}_{useful}$	useful thermal power harnessed by a solar receiver (W), page 8
R	radius of successive concentric spheres relative to the sun's center (m)
r_{center}	cylindrical conduction model center radius (m)
r_{inner}	cylindrical conduction model inner radius, at heat connector a (m)
r_i	heat exchanger tube inner radius (m)
R_j	thermal resistance of cylindrical conduction model radial section j $(\frac{K}{W})$
r_{outer}	cylindrical conduction model outer radius, at heat connector b (m)
r_o	heat exchanger tube outer radius (m)
$R_{sun\,earth}$	radius of the concentric sphere (with respect to the sun) that touches the earth's surface (m)
R_{sun}	radius of the sun (m)
RMSE	root-mean-square error (°C)
s	length of discrete flow filament (m)
SCA	solar collector assembly
t	time (s)
T_∞	fluid bulk temperature (K)
T_{air}	ambient air temperature (K)
$T_{ambient}$	ambient temperature (K)
T_a	ambient temperature (K)
T_{fluid}	HTF bulk temperature (K)
T_f	temperature of fluid (K)
t_f	fin thickness (m)

$T_{glass\,i}$	glass envelope node temperature of discrete segment i (K)
T_g	temperature of the liquid flowing through the prism (K), page 69
$T_{HTF\,mean}$	HTF mean temperature in the loop; arithmetic mean between current inlet and desired outlet temperature (K)
T_{i0}	turbine stage inlet temperature at reference conditions (K), page 239
T_i	bulk fluid temperature within control volume i (K)
T_i	turbine stage inlet temperature (K), page 239
T_m	temperature of media inside the storage tank (K)
$T_{receiver}$	solar receiver temperature (K)
T_{salt}	temperature of molten salt (K)
T_{sky}	sky temperature (K)
$T_{surface}$	surface temperature (K)
T_s	temperature of the porous solid media within the prism (K), page 69
$T_{tube\,inner\,i}$	tube inner surface temperature of discrete segment i (K)
$T_{tube\,i}$	tube node temperature of discrete segment i (K)
$T_{tube\,outer\,i}$	tube outer surface temperature of discrete segment i (K)
T_{tube}	absorber tube temperature (K)
TEMA	Tubular Exchanger Manufacturers Association
TES	thermal energy storage
U	overall heat transfer coefficient of a heat exchanger $(\frac{W}{m^2K})$, page 91
U	total internal energy within the control volume (J)
u	specific internal energy within the control volume $(\frac{J}{kg})$

$u(t)$	continuous controller signal (unit depends on the application)
U_i	total internal energy of control volume i (J)
u_i	specific internal energy of control volume i $(\frac{J}{kg})$
U_{loss}	overall heat loss coefficient from the absorber tube's outer surface to the ambient $(\frac{W}{m^2K})$
U_{nom}	overall heat transfer coefficient at nominal conditions $(\frac{W}{m^2K})$
$U_{overall}$	overall heat transfer coefficient $(\frac{W}{m^2K})$
V	total volume of a control volume (m^3)
V	volume of T-junction control volume (m^3), page 250
v	average linear velocity of the fluid in direction x $(\frac{m}{s})$, page 69
v	flow velocity $(\frac{m}{s})$
V_i	total volume of the control volume i (m^3)
v_i	flow velocity within control volume i $(\frac{m}{s})$
$\dot{W}_{net,i}$	net work flow over the boundary of control volume i (W)
$\dot{W}_{net}$	net work flow (W)
$\dot{W}_{pump}$	pump power (W)
$\dot{W}_{turbine}$	turbine stage power (W)
w_{coll}	parabolic trough collector width (m)
x	coordinate along absorber tube (m)
x	distance from prism entrance (m), page 69
$x_{default\ model\ A}$	the default initialization value of variable x of model A
$x_{input\ model\ A}$	any input variable x of model A
$y_{output\ model\ B}$	any output variable of model B
z	number of simulated and measured values taken for the RMSE calculation (integer)

Part I

Research work motivation, the state-of-the-art and objectives

Part one of this work presents the general topic and the motivation for further research; it discusses the current state-of-the-art and states the intended objectives.

Chapter 1

An introduction to concentrated solar power

This chapter presents the general topic of this work, namely concentrated solar power (CSP), also known as concentrating solar power, solar thermal power or solar thermal electricity (STE). Basically, solar thermal power plants collect the sun's thermal energy and convert it into electric energy. This is done via conventional thermodynamic power cycles that are adapted to the specific needs of solar power generation. Instead of providing thermal energy via burning fossil fuels (which causes vast CO_2 emissions and air pollution) or via nuclear reactions (which creates *not* sustainably manageable radioactive waste; not to mention ever and anon occurring horrible accidents), the *freely available* solar irradiation is used to increase the working fluid's enthalpy, which finally expands in a turbine in order to generate electricity. For the most part, water/steam is used as working fluid (Rankine steam cycles). Some concepts that are still under research use air or CO_2 as working fluid, which expands in a gas turbine (Brayton gas turbine cycle). In this case, it is even possible to run an attached bottoming steam cycle, using heat recovery boilers, resulting in a so-called solar thermal combined cycle plant. Also Stirling engines are used to convert solar thermal energy into mechanical work.

1.1 Motivation

The progress in engineering during the 20^{th} century and up to now, has enabled a standard of living, including individual mobility, people would never had imagined centuries ago. However, this high standard of living is only available for a limited number of people so far and the number of people im-

proving theirs is on the rise. As a consequence, since the demand of energy continually increases, conventional energy resources become more and more expensive and the environmental pollution as well as the emission of CO_2 increases. Considering the bad effects on the world's climate and especially on our immediate environment, we have to improve the conventional power generation and the efficiency of mobility. Additionally, we have to develop new ways of using renewable energy in large scale. The use of solar thermal power plants is one of several ways to mitigate the ongoing climate change, the environmental pollution as well as environmental changes that force people in many places in the world to leave their beloved homes, in some cases forever.

Solar thermal power plants capture the sun's direct normal irradiation (DNI), concentrate it onto a receiving surface and transform the absorbed heat into mechanical work and subsequently electric energy, by using state-of-the-art thermodynamic power cycles. Hence, solar thermal power plants directly harness the abundant amount of solar energy incident on planet earth. A rough estimate gives a total of 85 PW of solar power available for terrestrial solar collectors [1]. It has to be emphasized that this is more than 5000 times the current world's power demand of about 15 TW [1]. Therefore, the large-scale capture and conversion of solar energy is to be regarded as *the* sustainable and *ultimate* long-term solution to cover the world's ever-growing energy demand.

However, although these facts look pretty well at the first sight and seem to be an easy way of resolving the world's energy issue, many aggravating circumstances have to be taken into account:

- First of all, as commonly known, the solar irradiation is limited to a certain number of hours per day.
- Furthermore, the solar irradiation's angle of incidence, which influences the efficiency of any receiving device, varies throughout the day and throughout the year. Depending on the collector's location and orientation as well as the applied concept, it is usually small during summer but rather big during winter.
- In addition to this, the solar irradiation, which enters the earth's atmosphere, is attenuated by several more factors, like humidity, clouds and small particles. Unlike solar thermal applications for domestic and low temperature process heat generation, the collecting devices for solar thermal power generation need the sun's direct normal irradiation (DNI). In order to obtain higher temperatures and consequently high quality heat for running a heat engine in an efficient way, the sunlight

has to be focused onto a special receiver surface (CSP – Concentrated Solar Power) (see Section 1.2.1). Thus, the generation of solar thermal power is also limited to certain locations on earth where the sky is clear during most days of the year. Suitable are arid to semi-arid regions, located in the "solar belt" within 40° latitude north and south [2].

- Unlike conventional electric power generation, where the working fluid of the thermodynamic cycle is heated by burning fossil fuels that can be easily controlled, the exact solar power input for solar thermal power plants is not known in advance. Even if there has been solar irradiation data collected over years and additionally state-of-the-art weather forecast methods are applied, nobody can predict the exact distribution of solar radiation throughout one day or one hour. Hence, solar thermal power plants need a rather sophisticated control and operation strategy in order to utilize the solar energy as best as possible.

In order to extend the operating time of solar thermal power plants, several concepts of heat storage systems have been developed and further research is still going on in order to find the most effective solutions [3]. Basically, these storage systems consist of huge well insulated tanks that contain fluids at high temperatures in order to store the solar thermal energy in sensible form. As fluids are typically used molten salts. In order to provide the required excess heat for the charging of these storage tanks, the number of installed solar collectors is increased. Hence, the solar field (collector field) delivers more thermal power than the thermodynamic power cycle requires at rated conditions.

Recent storage concepts which are currently under research use the latent heat, which is delivered or gathered during the phase change of appropriate materials at constant temperature (PCM – Phase Change Materials). These concepts promise advantages in terms of costs [4]. Also sensible heat solid media storage is considered to be an alternative cost effective option, using concrete or castable ceramics [3].

A well developed heat storage system is able to even variations of solar irradiation during the day and extends the possible operating time, enabling the electric power generation during hours without, or too weak solar irradiation, which can be seen as the key advantage over other renewable technologies, such as wind or photovoltaic power that inherently depend on storage options for electric energy.

In addition to this, also auxiliary fossil fuel burners (hybridization) are used in order to help during the plant's start-up procedure or to even variations in solar irradiation during the day. However, the use of fossil fuels in

solar thermal power plants may be limited due to legal regulations (depending on the country), which requires a well optimized application strategy, and it is usually (depending on the concept) not the most efficient way as conventional power plants are better designed for that task of burning fossil fuels (e.g. modern combined cycle plants).

At many possible CSP plant locations on planet earth, especially in Europe, partially or slightly overcast periods occur on a certain number of days, which can not be neglected. Therefore, well developed control and operation strategies are needed to increase the electric output, making solar thermal plants more cost-efficient and competitive. Besides the optimization of control strategies, which aims to compensate for disturbances caused by fluctuating DNI levels, recently, also short-term DNI forecasting methods are applied. These short-term forecasting methods are also known as "DNI nowcasting" methods and include for example DNI forecasting via satellite images or photos of the sky taken by special fish-eye cameras. Knowing the plant's disturbance in advance (DNI nowcast), makes it much easier to achieve the current control target.

In summary, the efficient and reliable operation of solar thermal power plants is a challenging task due to the fluctuating and inconstant nature of solar energy. Nevertheless, solar thermal power plants represent a highly promising sustainable technology, strongly driving the motivation of research. A key solution to cope with the variable nature of the incident solar irradiation is the possibility of thermal energy storage, which has, however, not been treated in sufficient detail so far, especially when thinking of modeling approaches that are crucial for the evaluation of the power plant's performance. Thus, it is the aim of this work to summarize already proposed modeling approaches, and to extend the current state-of-the-art where needed.

Studies show, that concentrated solar power could be a feasible and affordable replacement for coal, reaching price parity approximately between 2025 and 2030 [5]. Hence, further research in this area will definitely improve the usage of solar energy, and may contribute to a trend-setting sustainable energy supply.

1.2 Solar thermal power plant concepts

Solar thermal power plant concepts can be divided into two basic categories, namely line focusing and point focusing technology.

Line focusing systems concentrate the incident solar direct irradiation onto a focal line, in particular onto solar receiver tubes that are placed concentrically to the focal lines of the solar collectors.

Point focusing systems concentrate the incoming solar irradiation onto a single focal point or better, onto a focal area that is very small compared to the total size of the reflecting mirror surface. One single solar receiver is therefore placed at this focal point or area.

Generally speaking, the concentration of the incoming solar irradiation is the fundamental principle in order to reach high temperatures and thus provide high quality thermal power that enables the operation of conventional thermodynamic power cycles (see Section 1.2.1).

Concentration is either reached by parabolic structures or by many slightly curved mirror elements that concentrate the radiation onto a certain receiver area. The working fluid temperatures that are reached range from 400 °C up to over 1000 °C.

Today's most used concept is the parabolic trough collector technology (line focusing). There, the power cycle's working fluid is heated indirectly, using a heat transfer fluid that is heated within the focal lines of the parabolic troughs. Temperatures reached range between 400 and 550 °C, depending on the used heat transfer fluid (thermal oil or molten salts).

Another concept that has been tested and operated successfully is the solar power tower or central receiver concept (point focusing). There, the solar radiation is concentrated onto a central receiver area which is placed at the top of a tower, using many slightly curved mirror elements. At the receiver, the concentrated solar energy is transferred to the working fluid or heat transfer fluid. Depending on the concept, temperature levels can exceed 1000 °C. Power towers promise high efficiencies if used with Brayton cycles, as they can be extended to solar combined cycle plants.

Additional concepts are the linear Fresnel collector concept (line focusing) and the parabolic dish collector concept (point focusing).

The linear Fresnel concept is similar to the parabolic trough systems, also line focusing. There, many longish mirror elements concentrate solar radiation onto a horizontal receiver tube.

Parabolic dish collectors concentrate the sunlight onto the focal point, where Stirling engines transform the thermal energy into electric energy. They provide good efficiencies in small power classes, ideal for remote off-grid applications.

1.2.1 Why concentration?

The fundamental element of any solar thermal power plant is its solar absorber or receiver, a physical component that should harness the incident solar energy in the form of heat. Since this solar absorber or receiver can not be considered as adiabatic, there will always be heat losses to the relatively

cold environment. Thus, considering the solar receiver's steady-state performance, the finally useful thermal power $\dot{Q}_{useful}$ is the difference between the solar thermal power absorbed $\dot{Q}_{absorbed}$ and the heat loss to the environment $\dot{Q}_{loss}$:

$$\dot{Q}_{useful} = \dot{Q}_{absorbed} - \dot{Q}_{loss} \tag{1.1}$$

By defining the absorbed thermal power as product of the solar plant's total aperture area[1] $A_{aperture}$, the direct normal irradiance and the optical efficiency η_{opt}:

$$\dot{Q}_{absorbed} = DNI \cdot A_{aperture} \cdot \eta_{opt} \tag{1.2}$$

and furthermore, defining the receiver's heat loss, assuming the ambient as black body and neglecting any convective heat loss:

$$\dot{Q}_{loss} = A_{receiver} \cdot \sigma \cdot \epsilon \cdot \left(T^4_{receiver} - T^4_{ambient}\right) \tag{1.3}$$

gives the useful thermal power as follows:

$$\dot{Q}_{useful} = DNI \cdot A_{aperture} \cdot \eta_{opt} - A_{receiver} \cdot \sigma \cdot \epsilon \cdot \left(T^4_{receiver} - T^4_{ambient}\right). \tag{1.4}$$

Thus, the solar receiver's efficiency, defined as the ratio between the useful thermal power absorbed $\dot{Q}_{useful}$ and the total incident solar power based on the plant's total aperture area, can be stated as follows:

$$\eta_{receiver} = \frac{DNI \cdot A_{aperture} \cdot \eta_{opt} - A_{receiver} \cdot \sigma \cdot \epsilon \cdot (T^4_{receiver} - T^4_{ambient})}{DNI \cdot A_{aperture}} \tag{1.5}$$

Of course, the direct normal irradiance and the plant's total aperture area cancel out in the useful power's first term, simplifying Equation 1.5 as follows:

[1]The definition of the total aperture area of a solar thermal power plant depends on the concept. In principle, for the understanding of this chapter, it can be associated with the total reflecting mirror surface area of the plant. However, for a single parabolic trough collector, the aperture area would be the product of the collector's width times the collector's length.

$$\eta_{receiver} = \eta_{opt} - \frac{A_{receiver} \cdot \sigma \cdot \epsilon \cdot (T^4_{receiver} - T^4_{ambient})}{A_{aperture} \cdot DNI} \tag{1.6}$$

Introducing as a next step the area concentration ratio C as the ratio between the plant's total aperture area $A_{aperture}$ and the solar receiver's area $A_{receiver}$:

$$C = \frac{A_{aperture}}{A_{receiver}} \tag{1.7}$$

and substituting this relationship in Equation 1.6, gives the efficiency of the solar receiver as a function of the receiver's optical efficiency, the receiver's emissivity, the temperature difference between the receiver and the ambient, the direct normal irradiance, and finally, the area concentration ratio, which can be written as follows [6]:

$$\eta_{receiver} = \eta_{opt} - \frac{\sigma \cdot \epsilon \cdot (T^4_{receiver} - T^4_{ambient})}{C \cdot DNI} \tag{1.8}$$

Considering Equation 1.8, leads to the following fundamental conclusions [6]:

- The maximum theoretical efficiency of the solar receiver is its optical efficiency. Since the optical efficiency is, generally speaking[2], the product of the receiver's solar absorptivity, the reflecting mirrors' reflectivity and the intercept factor[3], the solar absorptivity should be as high as possible, the reflecting mirrors as clean as possible, and the geometric and tracking accuracy as high as possible.
- The lower the long wave emissivity of the solar absorber is, the lower are the heat losses, and the better is the receiver's efficiency.
- The higher the temperature of the solar receiver is, the higher are its thermal losses per area.

[2]The exact definition of the optical efficiency depends on the solar collector or concentrator concept.

[3]The intercept factor defines the fraction of the reflected solar irradiation that is actually correctly reflected towards the solar absorber. Due to microscopic imperfections of the reflecting surfaces, macroscopic shape errors of the mirrors, tracking errors, or the fact that the sun light is not perfectly parallel, some of the reflected rays do not reach the solar absorber.

- The higher the area concentration ratio C is, the higher is the efficiency of the solar receiver. This is due to the fact that the heat loss depends on the area of heat transfer and on the surface temperature. Thus, smaller absorbers will have lower heat losses compared to larger absorbers at the same temperature [7].

- Last but not least, the higher the incident direct normal radiation is, the higher is the solar receiver's efficiency.

In order to determine the plant's total theoretical efficiency (for the conversion of solar energy into mechanical work), the Carnot efficiency has to be taken into account additionally, since a solar thermal power plant is, according to its principle, a combination of a solar receiver and a heat engine. In particular, the plant's solar-to-mechanical efficiency is obtained via multiplying the receiver's theoretical efficiency by the Carnot efficiency, assuming that the heat engine's temperature at heat input equals the receiver's surface temperature, and the heat engine's temperature at heat rejection equals the ambient temperature (see Equations 1.9 and 1.10).

$$\eta_{Carnot} = 1 - \frac{T_{heat\ rejection}}{T_{heat\ input}} = 1 - \frac{T_{ambient}}{T_{receiver}} \tag{1.9}$$

$$\eta_{solar\ power\ plant} = \eta_{receiver} \cdot \eta_{Carnot} \tag{1.10}$$

Figure 1.1 displays the theoretical efficiency of a solar receiver for different area concentration ratios. The black lines represent the range of typical concentration ratios of line focusing systems. The blue and the orange lines indicate typical ranges of area concentration ratios of point focusing systems. Specifically, the blue lines represent values for power towers, and the orange lines represent values for parabolic dish concentrators.

Figure 1.2 shows the theoretical conversion efficiencies from solar energy to mechanical work, representing the ideal limits for solar thermal power plants having the specific area concentration ratios as indicated, and furthermore a receiver emittance ϵ of 0.5, an optical efficiency η_{opt} of 0.8, and the environmental boundary conditions of $T_{ambient} = 20$ °C and $DNI = 900$ W/m^2.

As can be seen in Figure 1.2, the solar-to-mechanical conversion efficiency for non-concentrating ($C = 1$) solar systems is tiny since achievable equilibrium receiver temperatures are around 100 °C. Thus, non-concentrating solar collectors are typically suitable for domestic hot water supply or low temperature process heat.

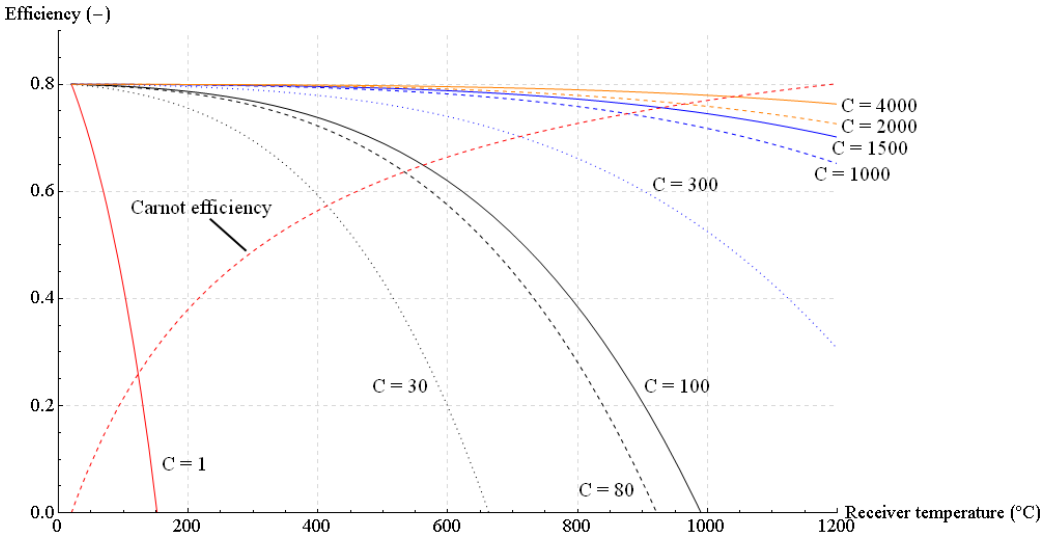

Figure 1.1: Theoretical efficiency of a solar receiver for different area concentration ratios ($\epsilon = 0.5$, $\eta_{opt} = 0.8$, $T_{ambient} = 20$ °C, $DNI = 900\ W/m^2$)

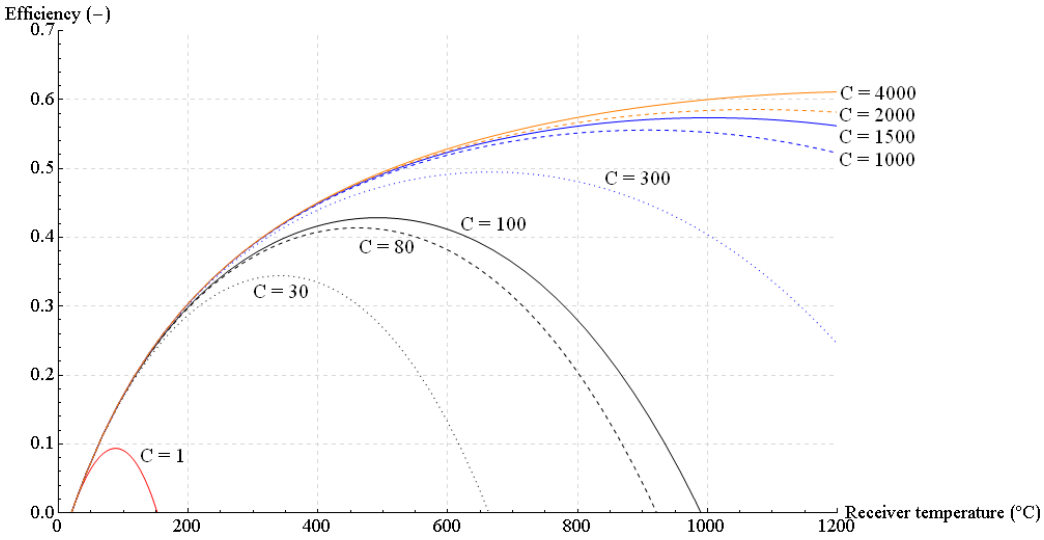

Figure 1.2: Theoretical solar-to-mechanical conversion efficiency of a solar thermal power plant for different area concentration ratios ($\epsilon = 0.5$, $\eta_{opt} = 0.8$, $T_{ambient} = 20$ °C, $DNI = 900\ W/m^2$)

In order to obtain higher temperatures and consequently high quality heat for running a heat engine in an efficient way, the area concentration ratio must be increased. Hence, *the fundamental conclusion* that can be drawn from this section *is, that concentration is absolutely necessary for converting solar energy into mechanical work* [8, 6]. Furthermore, for a specific solar thermal power plant having a certain area concentration ratio C, there exists a theoretical optimum surface temperature of the solar receiver. In particular, this point is reached where the derivative of the solar-to-mechanical conversion efficiency, with respect to the receiver surface temperature, approaches the value zero (see Figure 1.2) [6].

1.2.1.1 The theoretical maximum concentration ratio C_{max}

In this context, the question arises whether there is any upper limit of the value of C. The answer to this question can be found in the work of Winston et al. [8].

The derivation of this theoretical maximum value C_{max} is based on the premise that no terrestrial device can boost the incident solar flux (in W/m^2) above the radiant flux at the sun's surface M_{sun}. Thus, via formulating the conservation of power through successive concentric spheres of area $4\pi R^2$, leads to the following relationship [8]:

$$M_{sun} \cdot 4 \cdot \pi \cdot R_{sun}^2 = G \cdot 4 \cdot \pi \cdot R_{sun\,earth}^2 \tag{1.11}$$

where R_{sun} is the sun's radius and $R_{sun\,earth}$ is the radius of the concentric sphere (with respect to the sun) that touches the earth's surface, i.e. $R_{sun\,earth}$ is the distance between the sun's center and the earth's surface, and G is the solar flux incident on planet earth.

By solving Equation 1.11 for the solar flux G incident on planet earth gives:

$$G = M_{sun} \cdot \left(\frac{R_{sun}}{R_{sun\,earth}} \right)^2 \tag{1.12}$$

It is obvious, that the theoretical possible concentration ratio is the inverse of the term $\left(\frac{R_{sun}}{R_{sun\,earth}} \right)^2$. By simple geometry this is equal to $\left(\frac{1}{\sin \Theta_{sun}} \right)^2$, being Θ_{sun} half of the apex angle of the sun when viewed from planet earth ($\Theta_{sun} \approx 0.27°$), which gives a theoretical maximum concentration ratio of about 45032 (for point focusing systems).

Winston et al. [8] called this the sine law of concentration, which can be correspondingly derived for line focusing systems, yielding $\frac{1}{\sin \Theta_{sun}}$, which gives roughly 212.

1.2.2 The parabolic trough collector concept

Parabolic trough collectors concentrate the solar irradiation onto a tube which is placed concentric to the focal line of the parabolic mirrors (see Figure 1.3). In order to achieve high efficiencies of the collectors, the absorbed solar irradiation has to be maximized and the thermal losses of the receiver tube have to be minimized. In order to accomplish this, two crucial methodologies are applied. Firstly, the absorber tube's outer surface features a selective coating that provides high absorptance in the solar spectrum, but low emittance in the infrared range. Secondly, the absorber tube is surrounded by an evacuated glass envelope, in order to also keep the convective losses low. The corresponding assembly of the absorber tube and the coaxially placed glass envelope is usually referred to as heat collector element (HCE) (see Figure 1.4).

Furthermore, parabolic trough collectors track the sun via one axis that is parallel to the focal line. Commonly, they are placed in north-south direction. Although an east-west orientation provides solar energy at much smaller seasonal variations, the north-south orientation provides more energy on a yearly basis, particularly more during summer months [6]. Hence, due to a higher electricity demand and thus higher electricity rates in summer, the north-south orientation is the preferred orientation for solar power generation.

Many of these parabolic trough collectors are connected in series (solar collector loops) and in parallel (solar fields, see Figure 1.5) in order to increase the heat transfer fluid's temperature by a certain value and achieve a certain mass flow rate (thus thermal power) that is necessary for the following Rankine steam cycle.

Basically, there are two possible setups. Parabolic trough power plants can either directly evaporate water or use heat transfer fluids (high temperature oil or molten salt) that evaporate the water for the Rankine steam cycle later on indirectly via a heat exchanger.

The direct steam generation (DSG) promises higher conversion efficiencies due to higher live steam temperatures and less pumping losses within the field, but is not yet commercially available in large scale, as controllability and design are still under research.

Figure 1.3: View of a parabolic trough collector [9]

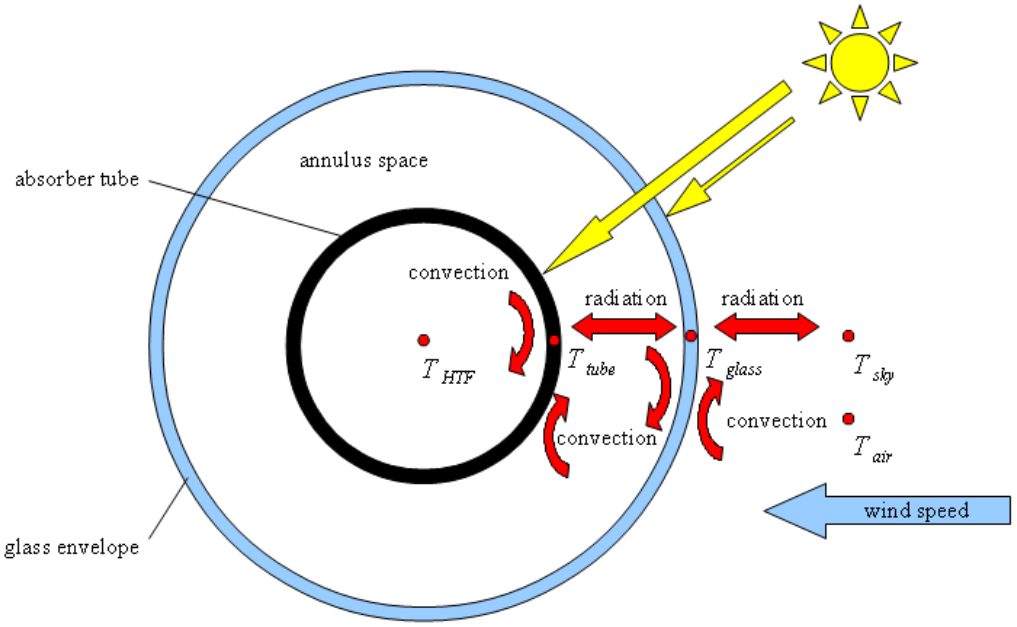

Figure 1.4: Cross-sectional view of a parabolic trough collector's heat collector element - Note: The magnitude of the convective heat transfer inside the annulus depends on the pressure and the contained gas

Figure 1.5: A broad view of parabolic trough solar collectors at Kramer Junction, California, USA [10]

1.2.2.1 Parabolic trough plants using heat transfer fluids

Basically, a solar thermal power plant using parabolic troughs and heat transfer fluid, consists of the solar field, a large assembly of solar collector loops connected in parallel, and the thermodynamic power cycle. In particular, the heat transfer fluid collects the sun's thermal power in the solar field and delivers it to the thermodynamic power cycle via a heat exchanger (the steam generator). Already commercially operated parabolic trough collector plants use thermal oil as heat transfer fluid. It is a mixture of diphenyl ($C_{12}H_{10}$) and diphenyl oxide ($C_{12}H_{10}O$) and is chemically stable up to about 400 °C [11, 12]. Thus, taking safety margins into account, live steam temperatures are typically around 371 °C, which is relatively low compared to today's conventional Rankine steam cycle power plants. Since the conversion of thermal energy into mechanical work is ideally limited by Carnot efficiency $\eta_{Carnot} = 1 - \frac{T_{heat\ rejection}}{T_{heat\ input}}$, the power block's live steam temperature has to be increased in order to improve the solar-to-electric efficiency. Therefore, if an increased efficiency is wanted, the thermal oil has to be replaced by other heat transfer fluids that allow for higher operating temperatures. Possible alternatives are molten salts [13] or gaseous fluids such as CO_2 [14].

The steam generator is the interface between the solar system (heat transfer fluid circuit) and the power conversion system. There, the heat transfer fluid's energy is used to produce superheated steam that is required by the

turbine. As usual, the steam generator consists of a preheating section (where water is preheated to a temperature close to saturation), an evaporating section (where the preheated water is evaporated and converted into saturated steam) and a super-heating section (where the saturated steam is heated up to the temperature required by the turbine). The steam turbine is usually composed of several stages, and steam is extracted between them for the regenerative feed water preheating. Steam leaving the high pressure turbine section is usually reheated before entering the low pressure turbine. After that, the steam is condensed. The selection of the best cooling system depends on the available water resources. The cooling of the condenser can either be achieved through evaporative (wet) cooling, where water is available, or through dry cooling (with air) - both conventional technologies [15]. The condensate is then pumped through the feed water preheaters and the deaerator. In the deaerator, oxygen and other gases dissolved in the water are removed in order to avoid corrosion [16]. From the deaerator, the water is pumped back to the steam generator, reaching the required pressure level and starting the Rankine thermodynamic cycle again.

1.2.2.2 The direct steam generation (DSG)

Direct steam generation is a concept to generate steam in the solar field itself (see Figure 1.6 for a typical plant layout). Thus, there is no need for the heat transfer fluid and the centralized steam generator in the form of a heat exchanger. For this reason significant cost savings can be achieved [17]. In addition to this, there is a reduced environmental risk and fire hazard in case of leaks, without the use of oil. Furthermore, performance gains due to the following mechanisms are possible: First, by eliminating the heat transfer fluid, the solar field's operating temperature can be lowered without affecting the temperature of the steam entering the turbine. This will slightly reduce thermal losses, by omitting the oil-water/steam heat exchanger. Nevertheless, if direct steam generation is used, one's ambitions are more towards higher turbine entry temperatures, resulting in a higher steam cycle efficiency, as there is no temperature limit given by the oil. Another important reason is that there is by far less pumping power required because the system will only operate boiler feed water pumps. The pumping power is mainly reduced due to the higher specific heat capacity of water and the high enthalpy of vaporization, so that a lower mass flow is required when transporting the same amount of heat. However, a sophisticated control has to facilitate the two-phase flow of water and steam [18]. In direct steam generation plants, live steam temperatures of 500 °C at pressure levels of about 100 bar are possible [19].

Unfortunately, the direct steam generation technology involves certain technical risks. Tube overheating in the boiling region and flow instabilities in parallel arrays may occur. The major problem facing that technology is stratification of the flow in the absorber tube that causes temperature gradients and tube failure [20].

Direct steam generation in parabolic troughs is a technology that is still under research. Large-scale commercial PTC power plants using direct steam generation are not yet available.

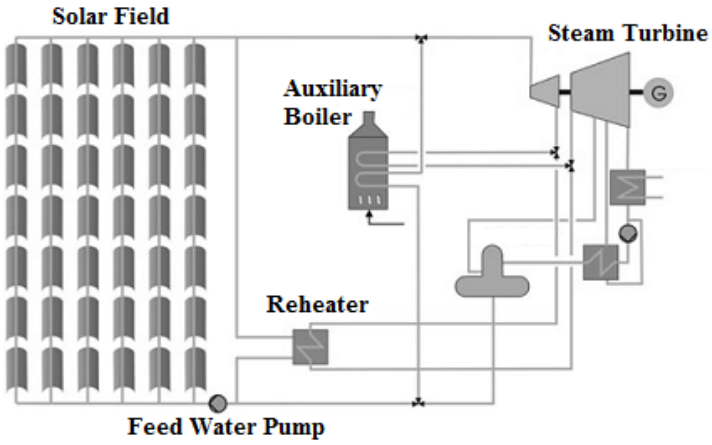

Figure 1.6: Scheme of a typical DSG plant layout [21]

1.2.3 The linear Fresnel concept

The linear Fresnel concept is another line focusing method, which is similar to the parabolic trough technology that has been described in the previous section. The basic idea of this concept is to replace large continuous reflectors that are for the most part quite complex and therefore expensive to manufacture by small elements distributed over a certain area. *Flat or elastically curved glass reflectors mounted close to the ground are used to minimize structural costs [22].* It even offers the potential of greater concentration ratios than those achievable with parabolic trough collectors, as the size of single-piece reflectors is limited [23]. A classic linear Fresnel collector consists of one linear absorber that is placed several meters above a bank of parallel mirror rows (see Figure 1.7). Each mirror row (primary mirror) has to be aligned in a certain angle to reflect the incident solar radiation onto the absorber's surface. However, it is difficult to avoid shading of the incident solar radiation and blocking of reflected solar radiation by adjacent mirror

rows. This problem can either be solved by using higher absorber towers or by increasing the spacing between mirror rows. Both possibilities will lead to higher costs and are therefore not suitable improvements. A much more promising remedy is provided by the compact linear Fresnel reflector (CLFR) concept. As the classic linear Fresnel collector has only one linear absorber, each mirror's alignment is determined. Adjacent mirrors are tilted towards the same direction, but at different angles. *However, if one assumes that the size of the field will be large, as it must be in technology supplying electricity in the multi-MW class, it is reasonable to assume that there will be many linear absorbers in the system. If they are close enough, then individual reflectors will have the option of directing reflected solar radiation to at least two absorbers [22].* Thus, it is possible to pack the mirror arrays much more densely when alternating the inclination, as shading and blocking can be avoided then. This concept is called compact linear Fresnel reflector (CLFR) concept and allows higher reflector densities and lower absorber tower heights to be used [22].

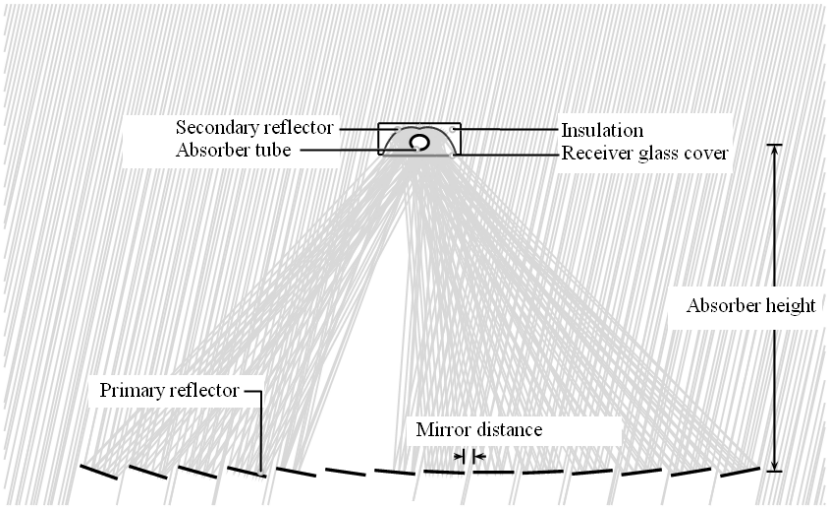

Figure 1.7: Scheme of a linear Fresnel solar collector [24]

Unlike the parabolic trough collector concept, the heat transfer loop is separated from the reflector field and fixed in space. High costs of flexible high pressure lines or especially high pressure rotating joints can be avoided [22]. Furthermore, wind loads are substantially reduced due to the reflector array's planarity and its low height. Thus, the reflector area for one absorber can easily be three times the area of comparable parabolic troughs. These advantages can lead to a substantial cost reduction for the solar field compared to parabolic trough technologies. Besides lower investment costs, there is

potential for reasonable savings offered by lower operation and maintenance costs [25].

Linear Fresnel collectors can be used for direct steam generation as well as for power generation with heat transfer fluids.

However, the linear Fresnel technology is still at a first development level when compared to the parabolic trough technology.

1.2.4 The power tower or central receiver concept

Unlike solar thermal power plant concepts where the solar energy is collected by numerous absorber devices equally distributed over the solar field, central receiver configurations have one single tower with the solar field's only absorber at the top of it. This tower is surrounded by a field of sun-tracking mirrors (heliostats) that reflect the solar radiation towards the absorber. There, the solar energy is transferred to a heat transfer fluid (molten salt), which is then used to produce steam for a following conventional steam cycle. It is also possible to directly generate steam within the receiver tubes, without using an additional heat transfer fluid. Another possibility is to directly expand the heated fluid (air or CO_2) in a gas turbine (Brayton cycle). Even combined cycle configurations are possible that promise high efficiencies. Solar power towers can operate at temperatures ranging from 500 up to 1500 °C [26]. The heliostat field can either be placed just north of the tower (northern hemisphere), or surround it. In the first case, the receiver faces northward. The second case requires a cylindrical receiver surface (see Figure 1.8), facing in all directions [18].

Although power towers are a recent technology at commercial level, they benefit from over 30 years of experimental projects.

1.2.5 The parabolic dish collector concept

As the name already implies, this kind of collectors consist of a mirror surface in the shape of a parabolic dish (see Figures 1.9 and 1.10). At the focal point, the receiver surface of the heat engine is placed. As heat engines are commonly used Stirling engines. They are usually small units, having an electric output of about 5 kW with a dish diameter of about 5 – 6 m. They can be connected to the grid, or can be used as remote off-grid applications. The solar-to-electric efficiencies are quite high and can reach 30% and more [6]. However, this type of collector concept is still in its early development phase. Already installed projects have a rather small size, compared to today's parabolic trough collector pants, due to the relatively high technological risk.

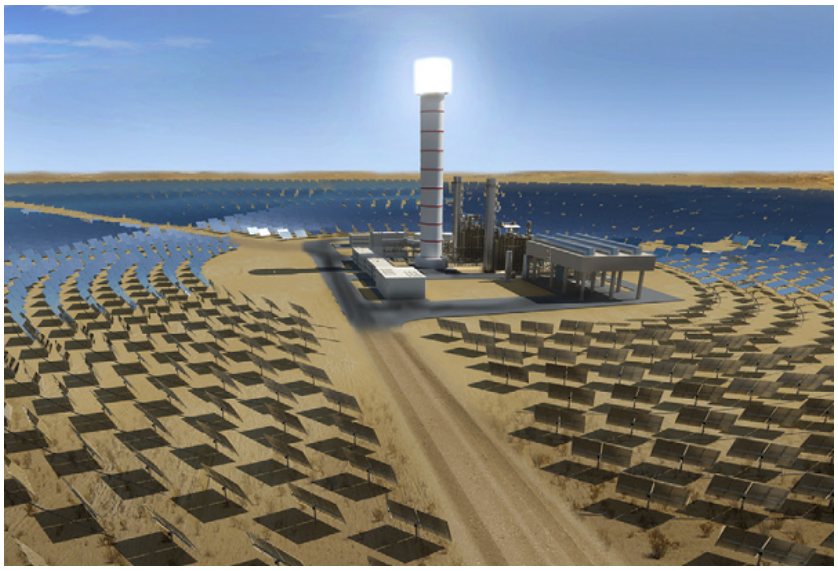

Figure 1.8: View of a power tower plant (cylindrical external receiver) [9]

Figure 1.9: View of a parabolic dish solar system [27]

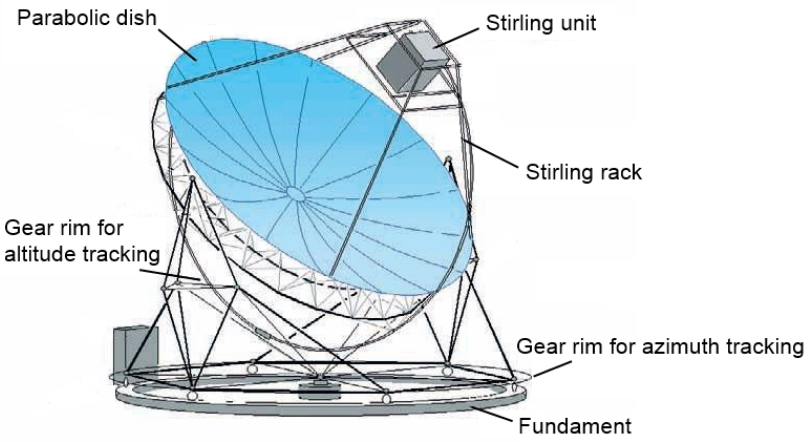

Figure 1.10: Schematic view of a parabolic dish solar system [28]

Chapter 2

Performance simulation of solar thermal power plants

In order to design and establish solar thermal power plant projects, it is necessary to simulate the operating behavior, calculate energy conversion efficiencies as well as annual performance values, like net electricity production, in advance. This is done via running a performance model of the entire plant over certain periods of time, ranging from typical days, weeks or months up to whole years. However, depending on the required modeling detail, this performance evaluation over longer periods of time can be a rather demanding task, especially, when thinking of detailed physical models of solar thermal power plants on system level. Due to the fact that the performance evaluation of solar thermal power plants is strongly related to the environmental boundary conditions that significantly change over time, the consideration of transients during operation is crucial and classic steady-state models of power plants, which are typical for the evaluation of conventional fossil-fired systems, are usually not sufficient. Therefore, a new field of modeling has emerged in the past few years, specifically tailored to the needs of concentrated solar power. Specific modeling and simulation tools have been developed, which differ in detail, concept and availability.

The modeling detail can be defined by the number of considered system components and the number of considered physical effects. Here, the trade-off between accuracy and computing time has to be taken into account. However, one should keep in mind that a higher level of detail will not automatically lead to a better result, since all the additionally required parameters may not be available in the required form. An example for this would be whether the individual performance parameters of solar collectors within a distributed collector field should be considered in the model or not. Here the question arises as to whether it is appropriate to model just one representative collector

loop and to assign mean values of typically observed parameters, as the mirrors' reflectivity or the solar absorptivity of the receiver tubes, instead of modeling each loop and assigning performance parameters according to probability functions. The answer will clearly depend on the results to be achieved. For instance, for determining the annual electricity yield of a plant, the former concept is typically sufficient. However, for the evaluation of the influence of performance parameter scattering within the solar field, the latter approach would be necessary.

Regarding the modeling concept, there can be distinguished between steady-state models and transient models. Although a pure quasi-steady-state consideration of solar thermal power plants provides a rather rough performance approximation, it may be sufficient accurate for specific tasks, such as preliminary feasibility studies.

Steady state models estimate the solar thermal power plant's design point performance as well as its off-design (part load) performance, i.e. its performance at certain steady-state operating points. Using typical meteorological data sets and plant operating data (including the electric production objective, the operation strategy of the thermal energy storage system and the possible fossil fuel backup use) as simulation input, the annual electricity production, the annual solar-to-electric efficiency or the auxiliary fuel consumption can be estimated (all important factors for project financing or feasibility studies), assuming quasi-steady behavior of the plant. Thus, the power plant model is evaluated at certain discrete points in time, yielding the current power output as a function of the current solar irradiance data (DNI, sun position) and the operating strategy. The final annual energy production is obtained via integration of the discrete simulation results. Of course, the required simulation time as well as the obtained accuracy strongly depends on the chosen time step and the model's detail.

In order to minimize the required calculation time, the results of a full annual performance simulation of a plant can also be approximated by only simulating a certain number of representative time intervals. For instance, this means that the plant's model is only evaluated during one representative day per month, which considerable reduces the required computational effort. However, the determination of the representative environmental boundary conditions, as solar irradiation or ambient temperature, is by far more complex and time intensive than just providing yearly measurement data of a certain plant location as model input.

Since the source of energy, the sun, provides its energy on a time varying basis, which cannot be controlled by mankind, the consideration of transient effects, mainly concerning the solar field and solar receivers, plays an important role for more detailed performance oriented simulations as well as for

power plant design studies.

Transient models take for example the thermal inertia of important components into account. Thus, elementary transient operating modes like start-up or shut-down procedures can be considered, which is important for detailed long-term performance simulations since e.g. daily start-up procedures require a considerable amount of time. On the other hand, transient models only intended for short-term simulations can offer a much greater modeling detail. For example, their application would typically be the simulation of the dynamic behavior of the solar field under varying boundary conditions (partial shading due to clouds, etc.). Detailed transient short-term simulations are crucial in order to define certain dynamic operating strategies during strong changes in direct normal irradiance, or to determine the exact temperature and pressure distributions and loads in power plant components.

Detailed transient simulations require reliable direct normal irradiance measurement data in a temporal high resolution. For example, good meteorological data sets provide solar irradiance and other ambient conditions data as air temperature, relative humidity and wind speed in a temporal resolution of about 1 to 5 minutes. A reliable and freely accessible meteorological data base is, e.g., provided by the Baseline Surface Radiation Network (BSRN).

Regarding the availability of simulation tools, it can be differentiated between free open-source software and rather expensive commercial programs. However, specific software for the performance simulation of solar thermal power plants on system level is not yet widely available and mainly based on individually developed in-house codes.

Furthermore, modeling and simulation tools for solar thermal power plants can be separated into two groups. On the one hand, there exist tools that are able to calculate the total system's performance (i.e. the performance of the whole solar thermal plant on system level), and on the other hand, there are tools that are only suitable for specific parts or components of the system (e.g. that are only suitable for the power cycle or the solar field).

Tools that are suitable for total systems (whole-system[1] simulation software) usually lack in modeling detail of specific parts. For instance, they can only provide simplified models for the power cycle. Hence, the behavior of single components (e.g. turbines, pumps, boilers) is not modeled individually. The detailed consideration of thermodynamic power cycles of solar thermal plants is typically done via well established state-of-the-art process simulation software (e.g. [29]). Another example for the use of software specifically applied to certain plant components would be CFD studies of

[1]Simulation tools that consider the solar thermal power plant as a whole, are referred to as "whole-system" models in this work.

solar receivers. Especially, at linear Fresnel [30, 31] or power tower cavity receivers, CFD studies are important in order to obtain heat loss correlations that can be used in zero or one-dimensional performance-oriented models. Also the application of ray-tracing software for the characterization of optical solar concentrating systems (e.g. for the determination of incidence angle modifiers of collectors or heliostat field efficiencies) would be a typical example for tools specifically applied to single components of a solar thermal power pant.

In whole-system models of parabolic trough collector power plants, the solar field is usually reproduced via modeling one representative solar collector loop connected to header pipe models. Corresponding mass flow gains are added in order to obtain the equivalent thermal power that would be produced by a certain number of identical parallel loops. The model of the power block (Rankine steam cycle) is either a detailed zero-dimensional physical model, i.e. each component (turbine stages, heat exchangers, pumps etc.) is modeled according to a steady-state energy balance, or it is based on a performance map, where the electric output is, e.g., simply calculated as a function of the current heat transfer fluid mass flow rate, the heat transfer fluid inlet temperature and the ambient air temperature (which determines the condenser pressure). The latter concept offers very short calculation times which are typically in the range of about 20 minutes for an annual yield calculation. When using more sophisticated models, this annual calculation time goes easily up to about 4 to 6 hours. Thus, very detailed transient models are only suitable for short-term simulations in order to estimate the power plant's behavior during start-up or shut-down. On the other hand, simple steady-state models are ideal for multiple simulation runs that are, e.g., required for parameter optimization studies or probabilistic modeling approaches [32]. The quasi-steady consideration of the power block's behavior is usually a good trade-off between model accuracy and calculation effort. Transient performance models usually only consider the heat transfer fluid circuit and the solar receiver system as transient sub-models as these subsystems are directly exposed to the plants disturbance, i.e. the fluctuating solar irradiance. Due to the use of thermal energy storage, the power block is anyways kept at a rather constant thermal power and short transients are thus negligible. However, the thermal inertia of the steam generator has to be considered during power block start-up and shut-down in the morning or in the evening.

For power tower plants, the general modeling approach is very similar. Also here the power block model is either based on a performance map, or a detailed physical zero-dimensional energy balance model is applied (considering turbine stages, heat exchangers and pumps etc.). The solar receiver

model is however different. Unlike distributed solar collector fields, here the solar receiver is centrally placed at the top of the tower, which of course also leads to a model that is much more limited in space than for example a model of a parabolic trough collector loop of 800 meters length. Nevertheless, depending on the type of solar receiver, the complexity of, e.g., the heat loss model shall not be underestimated. Furthermore, the determination of the heliostat field's optical efficiency can be a demanding task. A common approach for estimating the heliostat field's performance is to use a ray-tracing program in a separate modeling step beforehand. In particular, with the help of a ray-tracing software [33], an efficiency map of the heliostat field can be generated via calling the ray tracer in a loop, providing representative solar vector values (solar azimuth and altitude angle combinations) as input. Then, the obtained efficiency map or matrix is used in the whole-system simulation model of the central receiver plant, providing a certain current solar field efficiency value via interpolation. Thus, the total heliostat area multiplied with the current direct normal irradiance and the current optical efficiency of the solar field, gives the solar power incident on the receiver's surface. The current useful thermal power is then determined by the solar absorptivity of the receiver coating and the thermal efficiency of the receiver, i.e. the heat losses to the ambient.

2.1 The modeling of parabolic trough collectors - A short review

Today's most mature commercial CSP plants are based on the parabolic trough collector technology. Therefore, given its importance, the modeling of parabolic trough collectors (PTCs) and whole PTC power plants has already been subject of numerous publications. Thus, a thorough literature review has been performed and is summarized in the following. Note that this review text is entirely based on a previously published work [34] of the author.

Parabolic trough collector models that can be found in open literature can be subdivided into three main groups, namely (i) zero or one-dimensional steady-state models, suitable for quasi-steady solar plant yield and performance simulations, (ii) transient zero-dimensional lumped or one-dimensional distributed parameter models, suitable for solar plant control design and dynamic response simulations, and/or dynamic performance simulations, and finally, (iii) detailed two or three-dimensional models of high spatial resolution, suitable for thorough heat transfer analyses for component design and optimization.

The first category of PTC models has been subject of many works, as those published by Edenburn [35], Clark [36], Lippke [37], Fraidenraich et al. [38], Odeh et al. [39], Jones et al. [40], Forristall [41], Patnode [42], Rheinländer et al. [43], Rolim et al. [44], Larraín et al. [45] and Manzolini et al. [46, 47]. In the following, a summary of these contributions is given.

Back in 1976, Edenburn [35] published a PTC performance model that applied detailed one-dimensional steady-state heat transfer equations to discrete sections of the heat collector element by neglecting the thermal resistance of the absorber tube, as well as that of the envelope. Clark [36] discussed several design factors that influence the technical performance of PTCs for process heat applications. He used a zero-dimensional steady-state model to estimate the annual energy yield, based on a typical meteorological year (TMY) as model input data, and performed an economic analysis in order to find out whether solar process heat would become competitive with fossil fuel based technology. Also Lippke [37] used a zero-dimensional steady-state PTC solar field model, which was based on empirical collector efficiency equations, in this case, developed by Dudley et al. [48]. Lippke [37] presented a part-load model of a typical 30 MW SEGS (Solar Energy Generating Systems) plant, located at Kramer Junction, California, USA. A similar PTC solar field model was presented by Jones et al. [40]. Odeh et al. [39] developed a PTC single-equation heat loss correlation, based on the absorber wall temperature, rather than based on the HTF bulk temperature. This correlation was derived from one-dimensional steady-state conductive, convective and radiative heat transfer equations. Patnode [42] presented a comprehensive quasi-steady-state model of the SEGS VI plant, including a zero-dimensional PTC solar field model that applied a linear regression heat loss model, based on the detailed work of Forristall [41]. Forristall [41] performed a detailed one-dimensional steady-state heat transfer study of a PTC's heat collector element, considering several convective, conductive and radiative heat transfer phenomena. Furthermore, since the real temperature distribution along the receiver tube is non-linear, he discretized the heat collector element in longitudinal direction, assuming a constant temperature profile for each discrete element, i.e. being able to apply one-dimensional heat transfer equations for each of them. Rolim et al. [44] presented an analytical steady-state PTC power plant model, based on an analytical closed form solution for the non-linear temperature profile along a line focusing collector, which was originally presented by Fraidenraich et al. [38]. Rheinländer et al. [43] presented a comprehensive technical and economic PTC power plant performance model. All plant components were modeled in steady state. The solar field model consisted of one representative collector loop divided into 4 discrete sections, applying empirical efficiency correlations for each of

them. Larraín et al. [45] described a steady-state PTC performance model that discretized the absorber tube in longitudinal sections, as done by Forristall [41], but applied the absorber heat loss correlation presented by Odeh et al. [39]. Manzolini et al. [46, 47] also presented a detailed steady-state PTC plant performance model, applying Forristall's [41] modeling approach for the heat collector element.

Works related to the second category can be furthermore subdivided into PTC models for transient performance and energy yield simulations (e.g. García et al. [49], Bergmann et al. [50], Rossi et al. [51], Spelling et al. [52]), and PTC models primarily intended for control design (Camacho et al. [53, 54, 55], Meaburn & Hughes [56], Zunft [57], Stuetzle et al. [58], Valenzuela et al. [59], Hirsch et al. [60], Eck & Hirsch [17], Gálvez-Carrillo et al. [61], Yebra et al. [62, 63], Powell & Edgar [64]), some of them also suitable for accurate dynamic energy yield simulations.

Regarding PTC models intended for transient energy yield studies, García et al. [49] presented a PTC plant performance model discretizing one representative collector loop into 4 sections in longitudinal direction. Heat losses were estimated by evaluating an empirical correlation. The governing differential equations were simplified by assuming a linear and discrete approximation, which required time steps smaller than 10 seconds. Bergmann et al. [50] described a transient PTC plant performance model applying a so called "time-series" method, using a constant time step size. The PTC loop, consisting of 6 solar collectors of 150 m length in series, was discretized in 6 sections, i.e. each modeled section corresponded to 1 real collector assembly. They applied an empirical efficiency correlation for each section. Spelling et al. [52] wrote on a more detailed transient performance model. They also included the HCE's glass envelope in their PTC model and solved the governing system of coupled partial differential equations numerically by applying an implicit formulation of the finite difference technique to guarantee stability for time steps larger than 5 minutes. One representative collector loop was discretized in 40 nodes in longitudinal direction.

Concerning PTC models mainly intended for control design, many important works have been published by Camacho et al. [53]. They presented detailed control design analyses for distributed PTC fields, which were also confirmed through tests at the ACUREX solar field at the Plataforma Solar de Almería. A detailed review of modeling, as well as control approaches, can be found in [54] and [55].

The general simplifying assumptions of transient performance, as well as control-oriented models, are a uniform circumferential temperature distribution of the absorber tube, a uniform circumferential distribution of the HTF flow, a uniform circumferential as well as longitudinal distribution of

the incident solar irradiance, and a negligible heat transfer via conduction in longitudinal direction.

Furthermore, assuming a uniform radial temperature distribution of the absorber tube, neglecting radiative heat losses and any thermal inertia influences of the surrounding glass envelope, the governing partial differential equations of the solar collector modeling problem can be written as follows [53] (see also Figure 1.4):

$$M_{fluid} \cdot c_{fluid} \cdot \frac{\partial T_{fluid}}{\partial t} + M_{fluid} \cdot c_{fluid} \cdot v \cdot \frac{\partial T_{fluid}}{\partial x} = h_{fluid} \cdot \pi \cdot D_{inner} \cdot (T_{tube} - T_{fluid}) \tag{2.1}$$

$$\begin{aligned} M_{tube} \cdot c_{tube} \cdot \frac{\partial T_{tube}}{\partial t} =& w_{coll} \cdot \eta_{opt} \cdot DNI - U_{loss} \cdot \pi \cdot D_{outer} \cdot (T_{tube} - T_{ambient}) \\ & - h_{fluid} \cdot \pi \cdot D_{inner} \cdot (T_{tube} - T_{fluid}) \end{aligned} \tag{2.2}$$

By neglecting partial shading, modeling one characteristic loop, hence solving the partial differential equations given above numerically, and additionally considering the supply and return header pipe, will be representative for the whole solar field dynamics.

For the sake of completeness, the third category of PTC models, i.e. detailed two or three-dimensional models of high spatial resolution, is e.g. represented by the works of Cheng et al. [65], He et al. [66], and Wirz et al. [67]. Padilla et al. [68] wrote on a detailed one-dimensional heat transfer model. Basically, these models are devoted to component design and optimization and lie beyond the scope of the present work.

In summary, the modeling and the performance evaluation of solar thermal power plants using parabolic trough collectors has already been treated by numerous authors and a common practice of modeling procedures has already been established in many areas.

In the following, a review of thermal energy storage concepts and their modeling approaches will be given.

Chapter 3

Thermal energy storage concepts for concentrated solar power

This chapter gives an overview of thermal energy storage concepts for solar thermal power plants. It summarizes the classification and states important characteristics.

3.1 Introduction

The electric output of a basic solar thermal power plant, which consists of the solar field, the heat transfer fluid transport system and the power block, directly depends on the current availability of solar irradiation. Hence, there will typically be a certain mismatch between electric energy supply and demand. In operated solar thermal power plants, this mismatch is evened by either using auxiliary fossil fuel burners or heat storage systems.

Heat storage systems collect thermal energy during periods where solar irradiation is available in excess and deliver it later on to the power block's steam generator, in the case of too weak solar irradiation. This can smoothen the power plant's output during cloudy weather conditions, and can even extend the power plant's operating time beyond sunset, without the need for burning fossil fuels. Times of mismatch between possible energy supply and demand can be reduced, making solar thermal power plants more competitive.

Heat storage systems represent a key element for increasing the market penetration of solar thermal power plants. A heat storage system extends the power block's utilization time, improves efficiency and furthermore extends

the life expectancy of components due to a reduction in thermal transients. Also, electricity generation can be adapted according to the actual tariff structure, which increases the financial profit [69].

The use of thermal energy storage in parabolic trough plants reduces the required power block size for providing the same annual electricity production. Partial loads of the power block are greatly reduced [70].

The need for thermal energy storage systems strongly depends on the daily and yearly variation of solar irradiation and the corresponding electricity demand profile. The theoretical main objectives of thermal energy storage are buffering, delivery period displacement, delivery period extension and yearly averaging [71].

Buffering is the usage of stored thermal energy in order to even short transients caused by passing clouds. Hence, short partial load and transient operating modes of the turbine can be avoided, increasing the efficiency of electricity generation. Buffer thermal energy storage systems require a rather small storage capacity of up to about 1 hour of full load thermal supply [71].

Delivery period displacement is a shift between solar energy collection and electricity generation, which does not necessarily increase either the solar fraction[1] or the required size of the solar field. The electric energy supply is simply shifted to periods with higher electricity demand or tariffs. Typical storage capacities range from about 3 to 6 hours of full load operation [71].

As the name already implies, a delivery period extension, increases the hours of solar powered electricity generation, which raises the solar fraction and requires a larger solar field [71]. Concerning the optimum storage capacity in relation to minimized costs of components and minimized costs of electric energy generation, 6 to 9 hours of full load operation are proposed [72].

Yearly averaging of electricity production would require a very large and therefore very expensive solar field in order to reach equal power plant performance throughout the year. During summer months, parts of the solar field would have to be defocused, as the solar field delivery exceeded the capacity of the power block and that of the thermal energy storage system. Due to very high costs, this is a rather theoretical option and has not been given serious consideration [71].

The definitive selection of a suitable storage capacity is site- and system-dependent. Feasibility studies have to perform detailed statistical analysis of the electrical demand, as well as the site specific weather patterns. Also

[1]The term “solar fraction”, or “solar share” is defined as the ratio of the amount of pure solar energy to the total amount of energy supplied to a process or system. It is usually given in percent.

comprehensive economic trade-off analysis are required in order to get the optimum storage capacity and the optimum type of system [71].

Basically, heat storage systems can be classified into active and passive systems.

In active systems the heat storage medium is a moving, circulating liquid, which stores and delivers sensible heat. Active heat storage systems can furthermore be subdivided into direct and indirect systems.

In active direct systems, a certain fraction of the heat transfer fluid, which leaves the collector field or solar receiver, is directly pumped into highly insulated storage tanks, where it remains, until some additional thermal power is required by the thermodynamic power cycle. Thus, the heat transfer fluid itself, also acts as storage medium.

In active indirect systems, the heat storage medium and the heat transfer fluid are two separate media. Here, the heat transfer fluid's thermal energy is transferred to the storage medium via a heat exchanger. The storage medium is again stored in highly insulated tanks, until additional thermal power is required by the power block. Then, the heat storage medium is pumped through a heat exchanger, where it delivers the stored energy to the heat transfer fluid stream. Due to this additional heat exchange between the heat transfer fluid and the storage medium, there is a certain penalty in efficiency.

Passive heat storage systems can either store sensible or latent heat. As the name already implies, here the heat storage medium is in a passive state and does not circulate.

Passive sensible heat storage systems use solid storage media (e.g. concrete or ceramics), where the heat transfer fluid is pumped through, in order to transfer thermal energy to the storage medium or vice versa.

Passive latent heat storage systems use the latent heat which is gathered or delivered at almost constant temperature during the phase change of an appropriate storage material. Here, the solid to liquid phase change, or vice versa, is used. The system setup is similar to passive sensible heat storage systems. Phase change materials proposed are for instance sodium nitrate or potassium nitrate. They have to be chosen according to their phase-transition temperature, which should match the temperature level at that heat is required or delivered.

Another heat storage concept that has been proposed and already successfully tested is the thermochemical energy storage. This concept is based on endothermic and exothermic chemical reactions that are reversible. During charging, the endothermic reaction collects thermal energy, and during discharging, the exothermic reaction delivers the before chemically stored thermal energy. A thermochemical energy storage system provides a high energy density as well as a long and stable storage period [73]. However,

this type of thermal energy storage is at the moment at a very early level of development and subject of research.

3.2 Active heat storage systems

Active heat storage systems use insulated tanks for storing liquids at certain temperature levels. Either two-tank or single-tank active storage systems are used.

Two-tank systems have one cold and one hot tank. During charging mode, the cold storage medium is taken from the cold tank, is heated up by the thermal power of the solar field, and is pumped to the hot storage tank, where it remains until some additional thermal power is required by the thermodynamic power cycle, thus initiating the discharging process. During the discharging mode, the hot storage medium leaves the hot storage tank, delivers its thermal energy to the thermodynamic power cycle, either directly or indirectly[2], before it is pumped to the cold storage tank.

Single-tank systems store the hot and the cold storage medium in one single tank. This can be done by stratification. Due to the density difference between the hot and the cold storage medium, it stratifies naturally, from coolest layers at the bottom to warmest layers at the top. This provides lower system costs but requires a more sophisticated charging and discharging strategy, in order to avoid mixing. The single-tank storage system is also called thermocline storage system [71]. In addition to the storage fluid itself, a low-cost filler material is used in order to increase the thermal capacity by keeping the required amount of the more expensive storage fluid as low as possible. This approach is called packed bed concept. In this way, the tank of the single-tank storage system is marginally larger than one of a comparable two-tank thermal energy storage approach, which offers a significant cost advantage [74]. The filler material prevents convective mixing within the storage tank and reduces the amount of storage fluid required [75]. While charging, the hot storage medium enters the storage tank at the top, and the cold storage medium leaves the tank at the bottom, respectively. While discharging, the hot storage medium is taken from the top of the tank and returned to the bottom after heat extraction [74].

Concerning the ideal filler material for the packed bed, the following properties would be favorable: cheap, a high specific heat capacity, a low void fraction, compatible with the heat storage fluid used, and finally nonhazardous. For solar salt[3] as heat storage fluid, tests have shown that quartzite

[2]The term "indirectly" means that an additional heat exchange process is required.

[3]Solar salt is a mixture of 60% $NaNO_3$ and 40% KNO_3 (weight percent). This ni-

and silica sand are the best choice as a filler material [78].

Despite the existence of a temperature gradient within the storage tank, the packed bed single-tank thermocline storage concept is able to provide thermal power at nearly constant temperature over most of its discharge cycle. While discharging, the temperature of the molten salt leaving the top of the tank has a slight downward trend, which becomes more pronounced when the temperature gradient reaches the top of the tank. Hence, the major part of the temperature gradient within the storage tank is more or less narrowed to a certain relatively small storage tank height interval [78].

Another single-tank active heat storage possibility is the accumulation of saturated water within a pressurized tank. It is discharged by extracting saturated steam via flashing. But due to the high costs for the high pressure storage vessel and the limited storage capacity, this option is not very favorable.

3.2.1 Active direct thermal energy storage

An active direct heat storage system uses the heat transfer fluid that comes from the collector field or the solar receiver also as storage medium. At the moment, there are either used high temperature oils or molten salts as heat transfer fluids. In the case of direct steam generation (DSG) within the solar receivers, saturated water can be stored in special high pressure tanks.

An active direct heat storage system was used at the SEGS I (Solar Energy Generating Systems) solar power plant in California, which was unfortunately destroyed by a fire in 1999, and has not been replaced since then. High temperature mineral oil was used as heat transfer fluid, which also served as storage medium [4]. The oil was stored in two different tanks, one for the cold oil at 240 °C, and the other one for the hot oil at 307 °C (see Figure 3.1) [79].

Due to the higher vapor pressure and higher costs of the synthetic oil, used in subsequently built plants, this active direct heat storage concept has not been used again. The new oil enabled higher plant operating temperatures, but would had required pressurized storage vessels in case of an active direct

trate salt mixture has its solidus temperature at 223 °C and its liquidus temperature at 238 °C [76]. According to a review performed by Bradshaw & Carling [77], the upper design temperature limit is 600 °C because of the salts' chemical decomposition and the rapidly increasing corrosion rates of piping materials at higher temperatures. Although a composition of 46% $NaNO_3$ and 54% KNO_3 (weight percent) featured the minimum melting point of 222 °C [76], in solar thermal applications, a mixture slightly enriched in $NaNO_3$ is the preferred option since it means a significant cost reduction that outweighs the disadvantage of a slightly increased melting point [77].

storage system layout. Besides that fact, the higher costs of the synthetic oil were actually the main reason why oil has not been used as storage fluid in later SEGS plants [4, 79, 80].

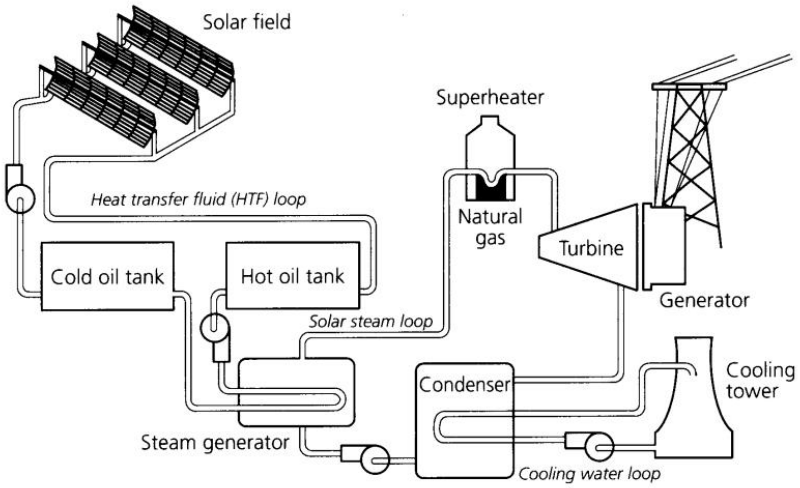

Figure 3.1: Active direct two-tank storage system at the SEGS I plant [71]

The disadvantage of the oil's high vapor pressure and the oil's high costs can be avoided by using molten salts as heat transfer fluid and storage medium at the same time. This approach is especially suitable for central receiver plants, which was demonstrated by the Solar Two project between 1995 and 1999. For the Solar Two project, a mixture of 60% (weight) sodium nitrate ($NaNO_3$) and 40% (weight) potassium nitrate (KNO_3), also known as solar salt, was used as heat transfer fluid and storage medium. This nitrate salt mixture has its solidus temperature at 223 °C and its liquidus temperature at 238 °C [76]. According to a review performed by Bradshaw & Carling [77], the upper design temperature limit is 600 °C because of the salts' chemical decomposition and the rapidly increasing corrosion rates of piping materials at higher temperatures. Although a composition of 46% $NaNO_3$ and 54% KNO_3 (weight percent) featured the minimum melting point of 222 °C [76], in solar thermal applications, a mixture slightly enriched in $NaNO_3$ is the preferred option since it means a significant cost reduction that outweighs the disadvantage of a slightly increased melting point [77]. At the Solar Two project, the two-tank storage system concept was used. The cold tank had a temperature level of 290 °C, and the hot tank was kept at 565 °C. The total storage capacity was 107 MWht and enabled a rated power output for three hours. The working molten salt mass in the system was estimated to be 1380 tonnes [81]. In order to avoid freezing of the salt, immersion

heaters were installed within the cold and the hot storage tank. The cold storage tank contained two active (plus one spare) 25 kWe immersion heaters that kept the salt temperature above 290 °C. The hot tank contained three active (plus one spare) 25 kWe immersion heaters that kept the tank at 565 °C. Although the immersion heaters had been designed to keep the molten salt at its nominal operating temperature, the main purpose of the heaters was to prevent the salt from freezing during outages. Hence, the immersion heaters were not activated during normal operation [81].

The Solar Tres central receiver power plant is the first commercial facility that uses molten salt as heat transfer fluid and as storage medium, based on the Solar Two technology. It is located near Seville in Spain and was built in 2008. It has a rated power output of 15 MW and the two-tank molten salt storage system has a capacity of 600 MWht, allowing for 15 hours of operation during hours of no sunshine [79]. A scheme of the plant is shown in Figure 3.2.

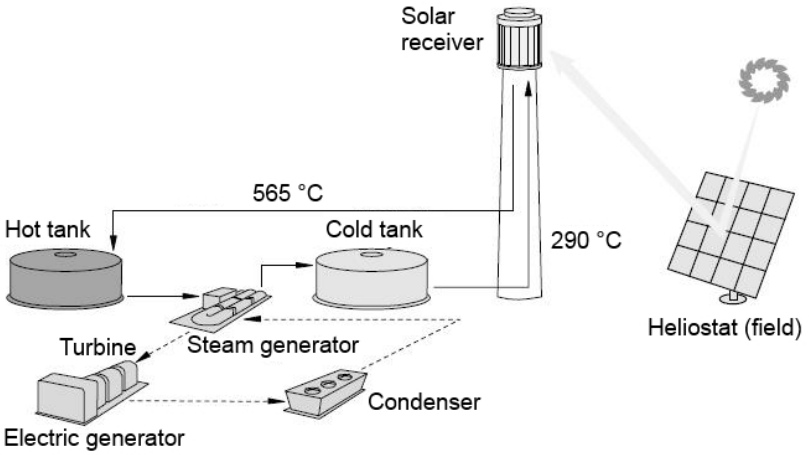

Figure 3.2: Solar Tres concept - Active direct two-tank heat storage system [6]

Concerning the above mentioned possibility of combining the direct steam generation with an active direct storage system, the two similar central receiver solar power plants PS10 and PS20 should be stated. The 11 MW central receiver solar power plant PS10 is located near Seville. The water for the thermodynamic power cycle is directly evaporated in the solar receiver, which produces saturated steam at 40 bar. During full-load hours a certain fraction of the saturated steam leaving the receiver is used for charging the thermal energy storage system, which stores saturated water at 20 bar. Steam recovered from the saturated water storage tanks is able to drive the

turbine at 50% load for about 50 minutes. A scheme of the PS10 concept is shown in Figure 3.3. The 20 MW central receiver solar thermal power plant PS20 is based on the same concept.

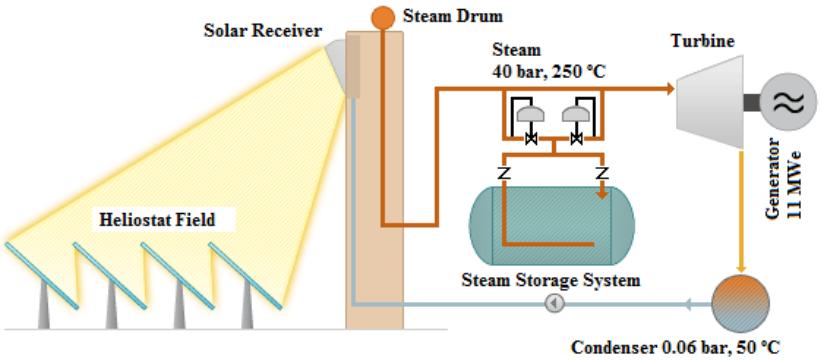

Figure 3.3: PS10 - Active direct heat storage system [82]

3.2.2 Active indirect thermal energy storage

Active indirect heat storage systems use a heat storage medium that is different from the heat transfer fluid. Hence, an additional heat exchanger is required between the heat transfer fluid cycle and the heat storage system. This concept has been applied by parabolic trough collector plants, where high temperature oil is used as heat transfer fluid and the oil's high vapor pressure, as well as the oil's high costs, restrict its usage as heat storage medium. Molten salts have shown to be the best option as heat storage medium, which is usually stored in 2 separated well insulated tanks (hot and cold tank) at atmospheric pressure [80].

Also, first central receiver research projects used the active indirect storage concept.

At the CESA-I project in Spain, an active indirect molten salt heat storage system was used in combination with a direct steam generating central receiver. Hence, water/steam was used as heat transfer fluid. The CESA-I project started its operation in 1984 and had two separate molten salt tanks for thermal energy storage. Superheated steam left the receiver at 525 °C and either expanded in the turbine or charged the molten salt storage system. In charging mode, the molten salt left the cold tank at 220 °C, was heated to 340 °C in a water-steam-to-molten-salt heat exchanger, and was finally pumped to the hot salt tank. In discharging mode, this happened vice versa, but in a second heat exchanger that served as steam generator, producing steam at 330 °C (see Figure 3.4). Although the salt mixture used would have

been suitable for operating temperatures up to 565 °C, the system was only designed to operate up to 340 °C, which considerably reduced the efficiency in discharging mode [83].

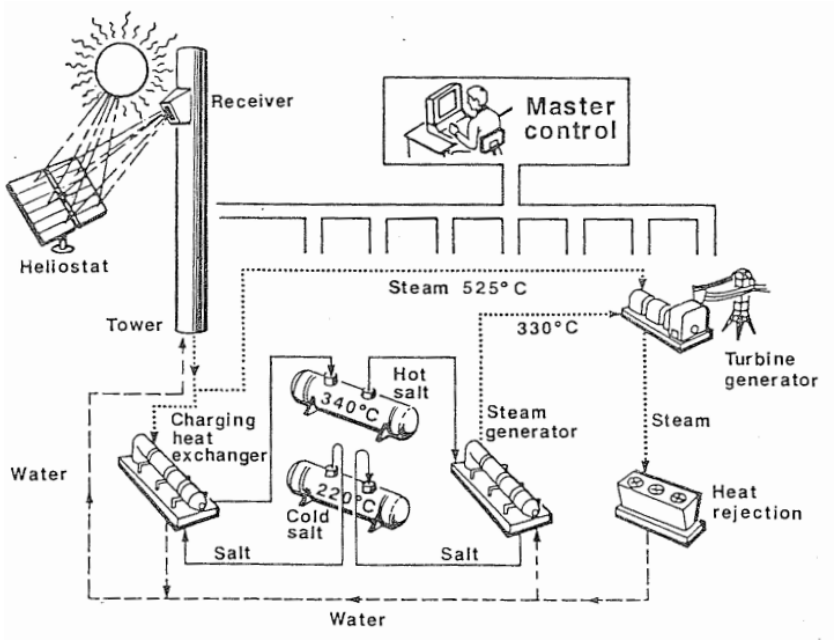

Figure 3.4: CESA-I plant schematic [83]

An active indirect heat storage system was also applied at the 10 MW central receiver project Solar One. It was located at Daggett, California, USA, and operated between 1982 and 1988. There, the storage fluid was oil instead of salt. Water/steam was used as heat transfer fluid. The steam was directly generated within the receiver. Unlike the CESA-I project, which used a two-tank approach, here an active indirect thermocline oil/rock single-tank storage system was used. Rocks and sand were used to increase the thermal capacity of the storage unit. The superheated steam left the receiver at 516 °C and either expanded in the turbine or was sent to the storage unit's heat exchanger, where oil was heated from 218 °C to 304 °C while charging. During discharging, the hot oil left the storage at about 302 °C, was sent to the steam generator, and returned to the bottom of the storage tank at 218 °C (see Figure 3.5). A major drawback of this system was the low steam temperature of 277 °C during discharging mode [83].

Concerning the active indirect storage concept for parabolic trough collector power plants, where an oil-to-salt heat exchanger is used, the following facts apply:

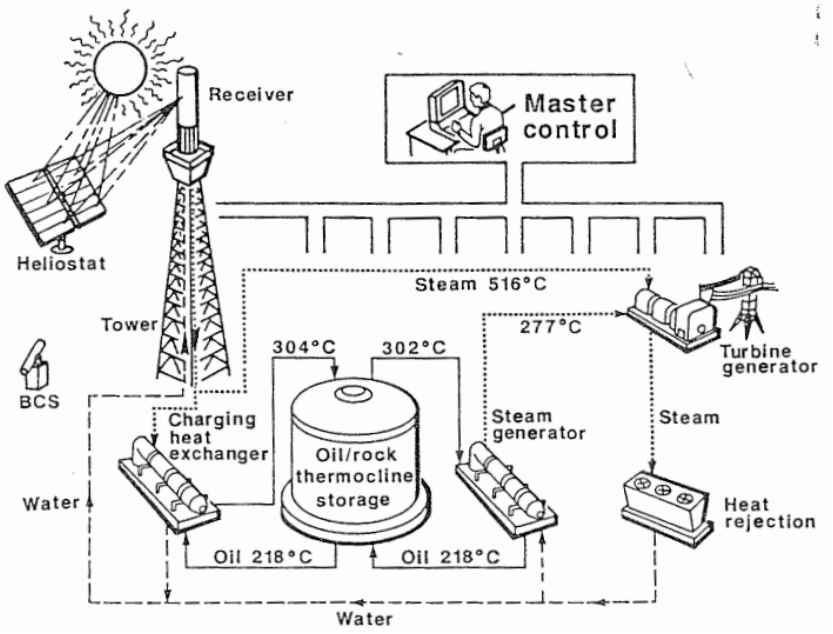

Figure 3.5: Solar One plant schematic [83]

While charging the storage system, the heat transfer fluid (oil) transfers the gained thermal energy to the molten salt circuit via an oil-to-salt heat exchanger, and vice versa during discharging mode. The oil-to-salt heat exchanger's approach temperatures have to be kept small, and pressure differences of up to about 15 bar between the salt and the oil have to be considered. In order to keep the Rankine cycle's performance penalty as low as possible, the approach temperatures in the oil-to-salt heat exchangers have to be kept in the range of 3 to 10 °C [80].

The oil's vapor pressure is approximately 10 bar at the prevailing operating temperatures of up to 393 °C. Hence, taking the pressure drop of the collector field and the heat exchangers into account, the heat exchanger's entry pressure has a nominal value of about 20 bar. As the molten salt is stored at atmospheric pressure level, the molten salt pressure level in the heat exchanger is only that which is required for pumping and constitutes about 5 bar. Thus, the oil-to-salt heat exchanger has to cope with a pressure difference of about 15 bar, which leads to a conventional shell-and-tube design, where the oil is pumped through the tubes [80].

This active indirect heat storage concept is currently used at the parabolic trough solar thermal power plant Andasol 1 (see Figure 3.6), which is located in Guadix, Granada, Spain. Molten salt, a mixture of 60% $NaNO_3$ and 40% KNO_3 (weight percent), is used as heat storage medium. The storage fluid's

working temperatures are about 292 °C in the cold tank, and about 386 °C in the hot tank. The storage system has a capacity of about 1010 MWht, which allows for full-load electricity generation up to 7.5 hours [79].

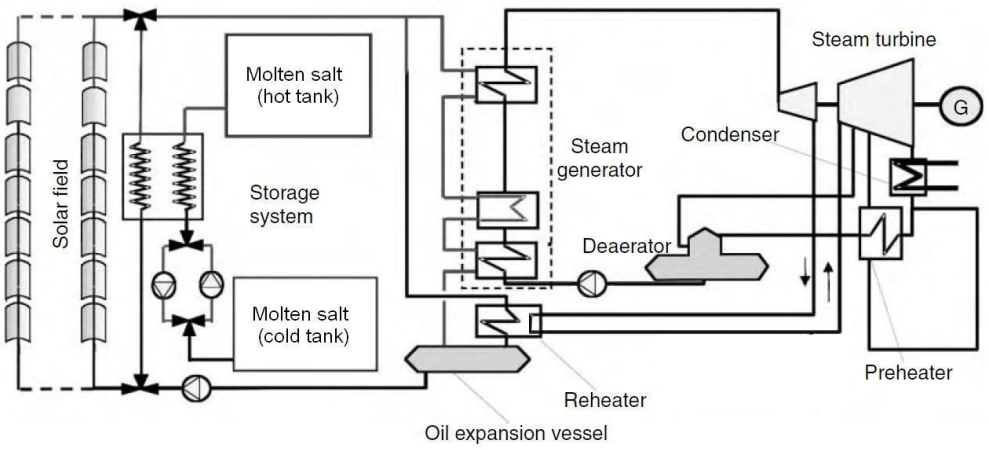

Figure 3.6: Parabolic trough solar thermal power plant scheme - Active indirect two-tank heat storage system [6]

In Figure 3.7 an active indirect thermocline storage concept for a parabolic trough collector plant is shown. In order to save system costs, an active indirect two-tank thermal energy storage system, which is at the moment the state-of-the-art solution, could be replaced by an active indirect thermocline system. Instead of two, only one slightly larger storage tank could be used. However, thermal ratcheting of the storage tank's walls remains a significant design concern [84] that still has to be solved.

3.3 Passive heat storage systems

In passive heat storage systems, the heat storage medium does not circulate and is rather fixed in its place. Heat can either be stored in a sensible or latent way, using the heat of fusion during phase change of appropriate materials (PCM – Phase Change Materials).

This latent heat storage approach is especially suitable for direct steam generation, as the evaporating section of the steam generator ideally requires heat input at constant temperature. A combination of both systems, that is, passive sensible heat storage for the preheating as well as the superheating

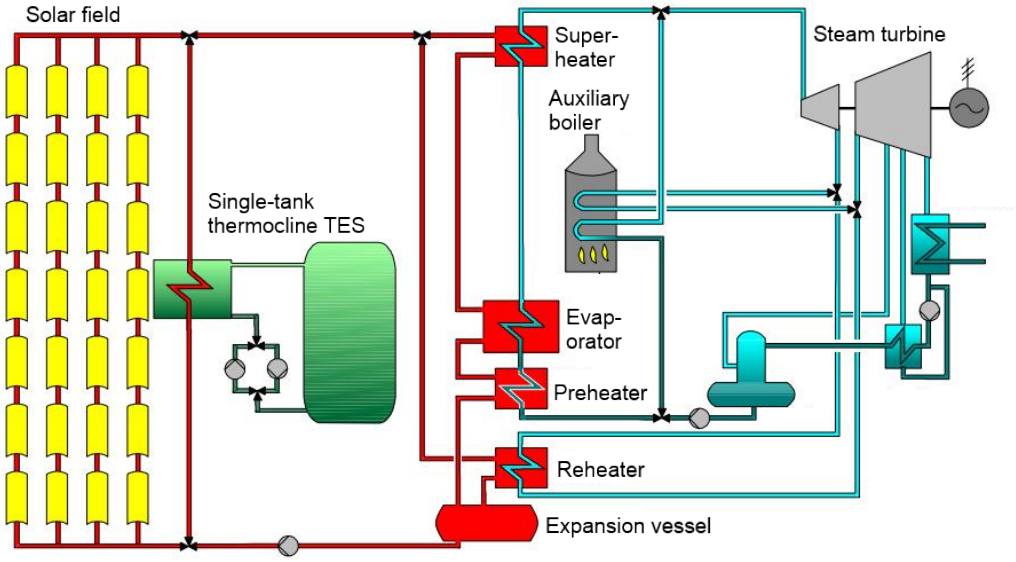

Figure 3.7: Parabolic trough collector plant scheme - Single-tank thermocline heat storage [85]

section, and latent heat storage for the evaporating section, would be an ideal solution [86].

3.3.1 Passive sensible thermal energy storage

Passive sensible heat storage systems use solid storage media (high temperature concrete or ceramics), where the heat transfer fluid is pumped through in order to charge or discharge the system. Solid media thermal energy storage systems provide low investment as well as low maintenance costs [69], and are basically suitable for solar thermal power plants using heat transfer fluids or direct steam generation.

Passive sensible heat storage can be applied at central receiver solar thermal power plants in combination with volumetric air receivers. There, air/ceramic or air/rock storage modules are proposed and already used at first research projects. For instance, the solar power tower Jülich in Germany is based on the open volumetric receiver technology, where an air/ceramic storage system is connected in parallel to the steam generator (see Figure 3.8). While charging, the hot air coming from the receiver passes through the storage unit and transfers the heat to the ceramic material, generating a temperature profile between the hot and the cold end of the storage [87].

Air/rock or air/ceramic thermal energy storage units in combination with

volumetric central receiver power plants have certain advantages over other power plant concepts that use molten salts or oil as heat transfer fluid or storage medium. There are neither maximum temperature limitations due to chemical instability, nor minimum temperature limitations due to solidification. Furthermore, the thermal energy storage unit can be directly installed after the receiver, without any need for an additional heat exchanger. Additionally, lower building costs are expected, due to more conventional construction materials. However, a drawback of an air/rock storage unit is a rather high pressure drop, due to the air's low volumetric heat capacity and low density. Depending on the rock particle size, the pumping work required is in the range of about 1% of the stored energy [88].

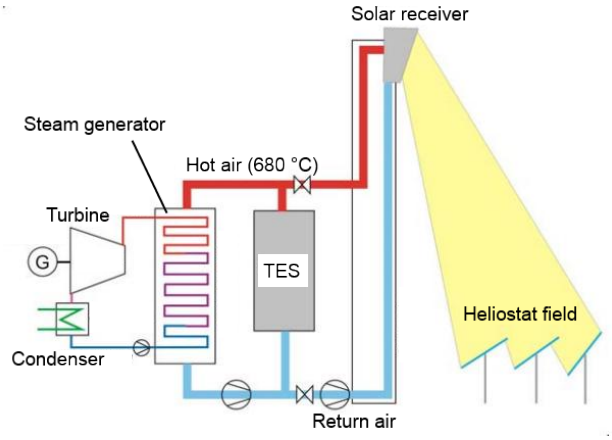

Figure 3.8: Open volumetric receiver solar power tower concept scheme [87]

Possible storage vessel core geometries are packed beds, consisting of spheres or broken particles, stacks of plates, perforated bricks or extruded shapes [89]. In packed beds, the efficiency of thermal energy storage depends on the heat transfer between the air and the filler material, as well as on the reached stratification or thermocline. Good heat transfer and limited heat transport within the solid storage media that enhances thermal stratification is reached by porous structures [88]. The resulting temperature profile within a storage vessel that uses a packed bed depicts three zones. A zone of rather constant high temperature, starting at the top of the vessel, is followed by a thermocline zone that provides the transition to the following rather constant low temperature zone, reaching to the bottom of the vessel. While charging, the thermocline zone moves downwards, leaving an increasing high temperature zone behind. The low temperature zone decreases accordingly. This happens vice versa during discharging. The heat transfer between the passing air and the storage material takes place within the thermocline zone. The

smaller the thermocline zone is, the better is the utilization of the storage material [89]. A steeper temperature gradient, hence a narrower thermocline zone, can be reached by reducing the average particle diameter of the packed bed. Additionally, due to an improved convective heat transfer, the temperature difference between the fluid and the solid decreases. Although the pumping power significantly increases with smaller particle size, the overall efficiency remains higher [88].

Concerning the design of passive sensible heat storage systems for parabolic trough solar thermal power plants, parallel tube assemblies are proposed, where the space between these tubes is filled with the solid heat storage medium (see Figure 3.9). As heat storage medium, either castable ceramics, or high temperature concrete, are possible. However, high temperature concrete seems to be the better option, due to lower costs, higher material strength and easier handling [69]. Concrete has shown to be a suitable storage material, and provides thermal stability up to about 500 °C [86]. Furthermore, due to a good contact between the concrete and the piping, quite high heat transfer rates into and out of the solid medium are reached [3]. A disadvantage of such systems is, that during discharging mode, the heat transfer fluid's outlet temperature does not stay constant and decreases as the temperature level of the storage medium decreases. And accordingly, while charging the system, the outlet temperature of the heat transfer fluid steadily rises, which has to be taken into account in the collector field's control, as the maximum temperature allowed may be exceeded. This issue is especially critical when used with a parabolic trough collector field and high temperature oil as heat transfer fluid. Passive sensible heat storage systems for solar thermal power plants are still under research and are not yet commercially applied.

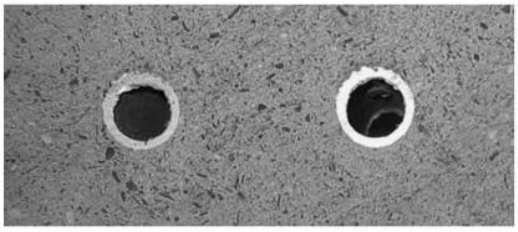

Figure 3.9: Cut through a high temperature concrete storage module [69]

First design concepts have been proposed for a 50 MW parabolic trough collector power plant using high temperature oil as heat transfer fluid ("Andasol-type"). Laing & Bahl [91] proposed a modular concrete thermal energy storage system with a capacity of about 1100 MWht. Each of the 252 concrete

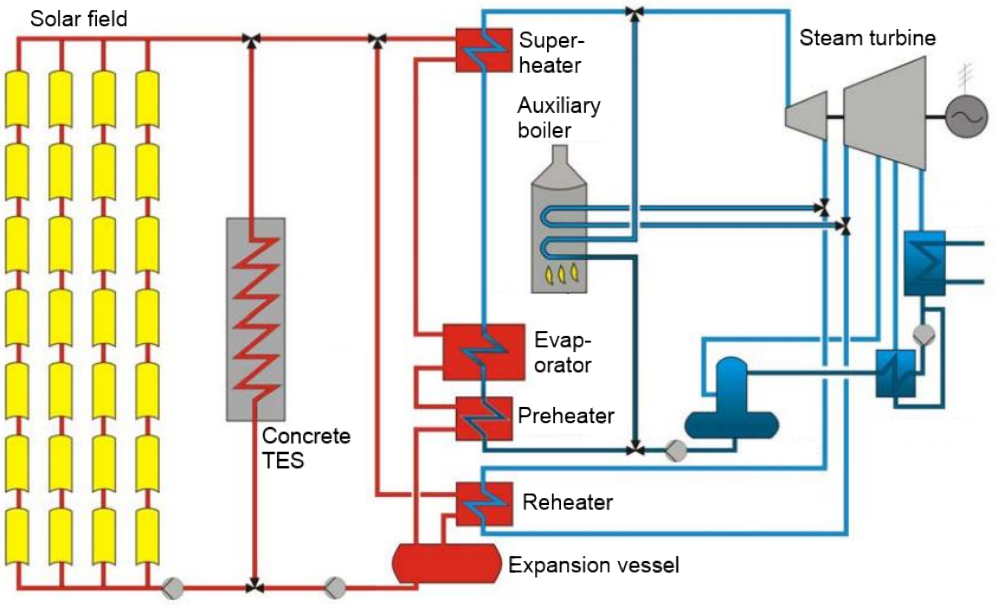

Figure 3.10: Parabolic trough power plant scheme using heat transfer fluid and concrete thermal energy storage [90]

storage modules is planned to have a mass of about 400 tonnes. The concrete storage modules would be packed together, connecting them in series and parallel. This would require a space of about 300 times 100 meters. A theoretical life cycle assessment study showed that a hypothetical concrete storage has an advantage over the original two-tank molten salt storage in terms of environmental impacts [90].

The major drawback of a basic single module (Figure 3.10) concrete storage concept for a conventional parabolic trough collector power plant, using oil as heat transfer fluid, is the limitation of the temperature differences between charging and discharging mode. During charging mode, the oil, coming from the collector field, enters the concrete storage system at a temperature level of about 390 °C. As the oil temperature at the end of the collector loop must not exceed 400 °C, the concrete storage's exit temperature is limited to about 315 °C. On the other hand, the discharging process is stopped, when the concrete storage exit temperature reaches 350 °C, which is at least required by the steam generator. Hence, the temperature difference between charging and discharging is limited to about 40 °C [90]. The use of one single concrete storage element limits the maximum average storage temperature that can be reached, and thus the amount of energy that can be stored. A possible approach could be the division of the solar field into two separate

parts. A smaller temperature difference in the solar collectors can lead to a higher concrete storage exit temperature, increasing the storage mean temperature and thus the storage capacity [90]. Also the discharging process has room for improvements. Compared to the single concrete storage module concept, a division of the concrete storage block into 3 parts, one for the preheating section, one for the evaporating section and one for the superheating section, could further improve the efficiency dramatically (see Figure 3.11) [90].

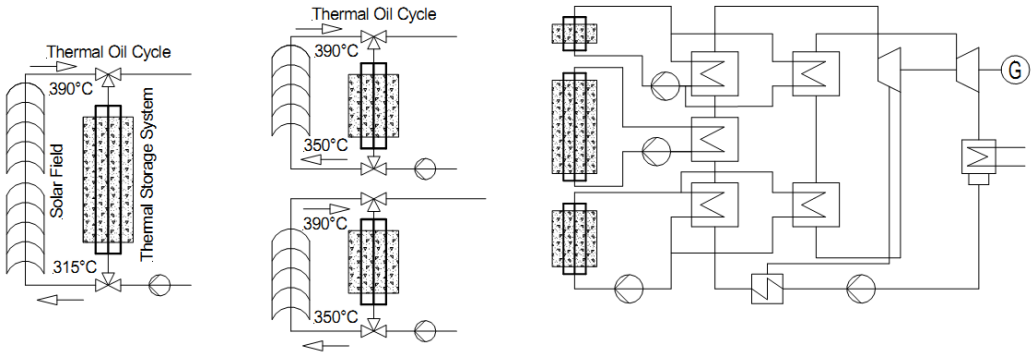

Figure 3.11: Passive concrete storage system schemes - charging (left) - discharging (right) [90]

3.3.2 Passive latent thermal energy storage

Passive latent heat storage systems use the latent heat, which is gathered or delivered during the phase change of appropriate materials at almost constant temperature. In already performed studies and research projects, salts have shown to be appropriate phase change materials (PCMs). The solid-to-liquid phase change, and vice versa, has been used in order to store or deliver thermal energy.

The overall system layout is similar to passive sensible heat (concrete or ceramics) storage systems. At passive latent heat storage systems, the melting temperature of the heat storage material (salt mixture) is within the range of the charging and discharging temperatures of the heat transfer fluid [3]. Proposed phase change materials are eutectic salt mixtures of potassium nitrate and sodium nitrate ($KNO_3/NaNO_3$), potassium nitrate and potassium chloride (KNO_3/KCl), a mixture of magnesium chloride, potassium chloride and sodium chloride ($MgCl_2/KCl/NaCl$), sodium nitrate ($NaNO_3$) alone, potassium hydroxide (KOH), as well as potassium nitrate (KNO_3) alone (see Table 3.1) [4, 92].

Table 3.1: Phase change material data [4]

Composition (% weight)	$NaNO_3$	KNO_3/KCl (95.5/4.5)	KNO_3	KOH	$MgCl_2/KCl/NaCl$ (60/20.4/19.6)
Melting point ($°C$)	306	320	335	360	380
Enthalpy of fusion (kJ/kg)	172	74	95	134	400
Density (solid) (kg/m^3)	2261	2100	2109	2040	1800
Specific heat capacity (solid) ($kJ/(kgK)$)	1.1	1.21	0.953	1.34	0.96
Thermal conductivity (solid) ($W/(mK)$)	0.5	0.5	0.5	0.5	n/a

For applications at higher temperatures (solar Brayton cycles) Hoshi et al. [93] proposed potassium carbonate (K_2CO_3), as well as sodium carbonate (Na_2CO_3), with melting temperatures of 891 and 851 °C, respectively. Especially, sodium carbonate promises to be a good option, since its thermal conductivity constitutes about 1.8 $\frac{W}{mK}$, which is a rather high value when compared to 0.5 $\frac{W}{mK}$ of the previously mentioned salts.

Phase change heat storage systems are able to provide the same storage capacity in smaller and cheaper units than conventional or prior proposed sensible heat storage concepts, as the heat of fusion is by far larger than the corresponding specific heat capacity [4]. However, a major drawback of the latent heat storage concept is the low thermal conductivity of possible phase change materials (see Figure 3.12). This is actually the main reason why latent heat storage has not been used in large scale and is still at an early development level [92]. In order to make latent heat storage concepts competitive, the thermal conductivity should be increased to about 2 $\frac{W}{mK}$ [4].

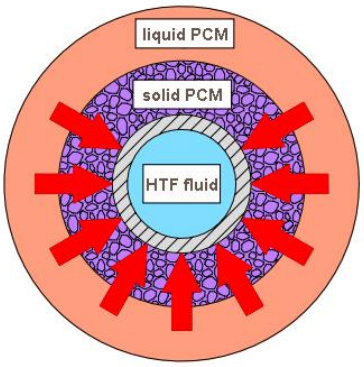

Figure 3.12: The low thermal conductivity of the PCM dominates the heat transfer [94]

Hence, several approaches are being proposed and developed in order to increase the thermal conductivity within basic latent heat storage modules.

The basic proposed layout of these modules is an assembly of parallel tubes that are surrounded by the phase change material. Thus, while discharging and charging, the heat transfer fluid is pumped through the tubes, transferring or gathering the thermal energy. In order to enhance the thermal conductivity within the phase change material an addition of material with high thermal conductivity is proposed. This can either happen through aluminum and graphite fins, arranged in "sandwich" configuration normal to the heat transfer fluid tubes (Figure 3.13), or through added graphite flakes. Also metal foams (copper and copper-steel alloy foams with different porosities) have been investigated, which promise to significantly enhance heat transfer within phase change storage modules [92].

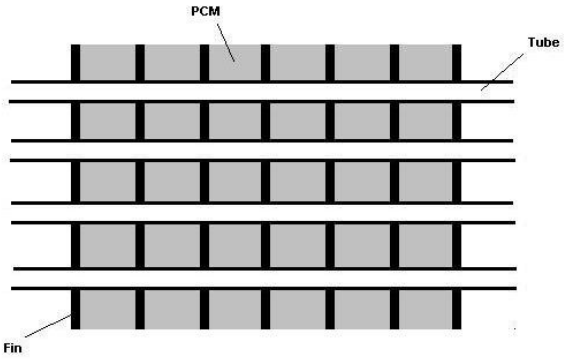

Figure 3.13: PCM heat storage module scheme - Fins enhance heat transfer

A latent heat storage unit provides thermal energy at a certain almost constant temperature level. In order to make the heat transfer to the heat transfer fluid as efficient as possible, a combination of several latent heat storage modules with different melting temperatures is proposed. In this way, the mean temperature difference between the heat transfer fluid and the storage medium can be kept small in order to limit the occurring exergy losses. Thus, the melting temperature should be cascaded upwards, from the lowest to the highest operating temperature, which is about 390 °C for the conventional parabolic trough collector concept, using oil as heat transfer fluid, and about 500 °C for the innovative direct steam generation concept. Considering the latter concept, a cascaded latent heat storage module layout would be only required for the preheating and the superheating section, as the delivery of thermal energy at almost constant temperature is ideal for the evaporating section [4]. Studies show, that compared to an active indirect two-tank molten salt storage system, which is at the moment state-of-the-art and commercially applied, a comparable cascaded latent heat storage system would require less storage material, and furthermore, would not require any

temperature tracing in order to keep the salt liquid, hence being cheaper concerning these aspects. However, a relative high number of heat exchanger pipes would be required, and in addition to this, while discharging, the heat transfer fluid outlet temperature would not be as uniform [4].

A combination of latent and sensible heat storage seems to be best for the application in direct steam generation power plants. Hence, sensible heat concrete storage modules could be used for the preheating and superheating section, and a latent heat storage module for the evaporating section (see Figure 3.14). At the proposed steam pressure level of 100 bar, almost 70% of the energy is transferred during condensation, while charging, and vice versa, during evaporation, while discharging. Therefore, the major amount of energy can be stored and delivered by a PCM storage unit [86].

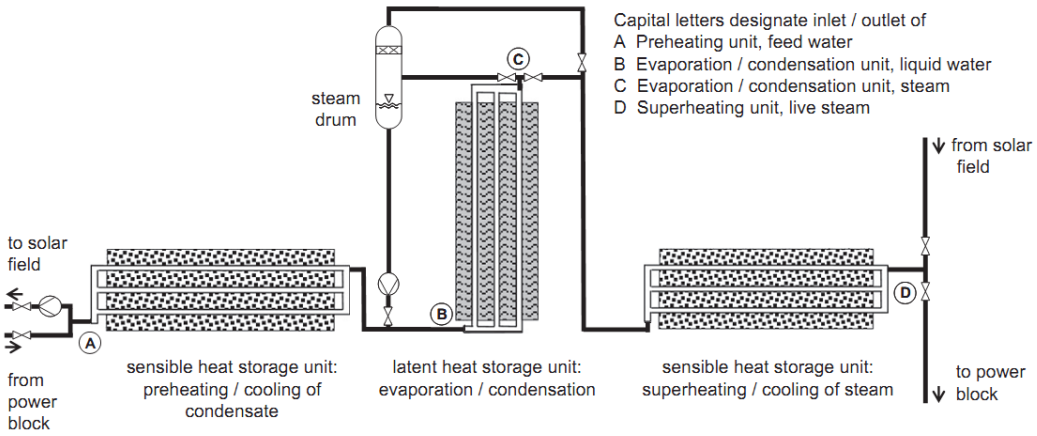

Figure 3.14: Latent and sensible heat storage unit for the direct steam generation [86]

An important fact, that has to be noted is that the PCM storage unit would be placed vertically in contrast to the horizontally placed sensible concrete modules. That is due to the phase change material's (sodium nitrate) change in volume while melting. The volume increases approximately 10% during melting. For this reason, an excess volume is provided at the top of the PCM storage module [86]. This provides a uniform PCM distribution around the tubes at all times and is crucial in order to enable the expansion and shrinkage of the PCM during the phase change. The steam (while charging) has to enter at the top and the preheated water (while discharging) has to enter at the bottom. In this way the PCM is able to expand or shrink without creating voids or destroying the casing. Furthermore, with the vertical setup, a circumferentially uniform heat transfer coefficient between water/steam and tube wall is assured. Hence, circumferential tube

wall temperature gradients that occur in horizontal steam generator tubes are no issue.

3.4 Thermochemical energy storage

According to N'Tsoukpoe et al. [95], the term "thermochemical energy storage" describes a rather wide field of thermal energy storage concepts and applications, including the areas of thermochemical storage without sorption and thermochemical storage with sorption. Since the term "sorption" includes both, adsorption as well as absorption, the latter term of the previous sentence can be divided into chemical adsorption storage and chemical absorption storage. In relation with storage applications, the term absorption refers to the absorption of a gas by a liquid, where the gas "enters" the liquid. Whereas the term adsorption refers to an attachment of gas or liquid phase to the surface of another substance.

In general, thermochemical storage systems use reversible physico-chemical phenomena to store thermal energy [95]:

$$AB + Heat \leftrightarrow A + B \tag{3.1}$$

The pair of substances A and B is called working pair or sorption couple. Under supply of a certain amount of heat the compound AB is dissociated into two separate components A and B that can be stored, in order to store thermal energy in form of chemical potential. When A and B are put together in the presence of a catalyst or even without, component AB is formed while releasing heat [95].

Now, focusing on these thermochemical storage concepts that are suitable for high temperature storage, as required for concentrated solar thermal power applications, only thermochemical storage concepts without sorption, using chemical catalytic reversible reactions, are adequate [96]. Other methods using sorption processes are suitable for low temperature storage for domestic applications, as well as for heat pump technologies and refrigeration [95].

High temperature thermochemical energy storage uses reversible endothermic/exothermic chemical reactions. While charging, the solar receiver provides heat for the endothermic reaction, and while discharging the corresponding exothermic reaction delivers heat for the thermodynamic power cycle. This storage concept provides high energy density, as well as good long-term storage behavior near ambient temperature [3].

However, this very promising heat storage concept is at the moment still at an early level of development and subject of research. The most rele-

vant chemical processes are reactions with ammonia (NH_3), the reforming of methane (CH_4) using carbon dioxide (CO_2), and reactions with metals and metal oxides (e.g. ZnO/Zn) [3, 96, 97].

3.4.1 Ammonia-based thermochemical energy storage

The ammonia-based thermochemical energy storage concept uses the following reversible reaction [98]:

$$NH_3 \pm \Delta H_{(Enthalpy\ of\ Reaction)} \leftrightarrow 0.5 \cdot N_2 + 1.5 \cdot H_2 \tag{3.2}$$

Figure 3.15 shows a basic solar thermal power plant layout using a closed loop ammonia-based thermochemical energy storage system. The solar receiver supplies the endothermic reactor with thermal power. Within the endothermic reactor, the liquid ammonia is dissociated into nitrogen (N_2) and hydrogen (H_2). Then, the reaction products are cooled in an ammonia/N_2-H_2 heat exchanger and are returned to the ammonia/N_2-H_2 storage vessel. This storage vessel is the heart of the system, and stores both, the undissociated ammonia and the 3:1 hydrogen/nitrogen gas mixture at ambient temperature and high pressure. The ammonia fraction is for the most part present in liquid state and thus enables an automatic phase separation of ammonia and the N_2-H_2 gas mixture [99]. Independently of the storage process (the dissociation of ammonia and the accumulation of the N_2-H_2 gas mixture in the storage vessel), the thermal energy is recovered by the synthesis of ammonia within the exothermic reactor, which delivers the thermal power to the connected steam cycle. Therefore, the N_2-H_2 gas mixture is taken from the top of the tank, compressed and fed into a following buffer vessel. Then, the fraction of ammonia vapor is condensed within a cooled separator and fed back to the storage vessel. The pure N_2-H_2 gas mixture then passes to the exothermic reactor, where ammonia is synthesized using an appropriate catalyst. Finally, the synthesized ammonia passes through an ammonia/N_2-H_2 heat exchanger and is fed back to the storage vessel [100].

First demonstration projects showed that ammonia-based thermochemical storage is ideally suited for operation through solar transients and provides the recovered heat at temperature levels well suited for high quality superheated steam production (steam at 430 – 450 °C at 100 bar [98]). Furthermore, the required high pressure system that should be suitable for pressures up to 30 MPa, can be designed using standard components as well as manufacturing techniques, although the required system pressure constrains the material choice for reactor and storage vessel design [100, 102].

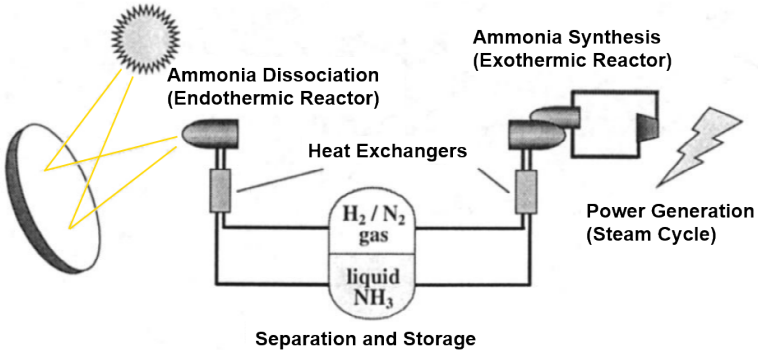

Figure 3.15: Thermochemical energy storage scheme with ammonia [101]

The fact that there are no possible side reactions, makes these solar reactors easy to control. Furthermore, the temperature levels of the endothermic reaction are well suited for solar receivers. In a first laboratory-scale system, the reactor design operating temperature was set to 650 °C [100].

Concerning the endothermic reactor two possible design setups are proposed [98]:

The first type is a directly irradiated multi tube reactor that is placed inside a solar cavity receiver suitable for parabolic dish collectors. These parabolic dish collectors are connected by a high pressure storage and transport network containing the ammonia/N_2-H_2 mixture [99]. With this method a parabolic dish collector array with the appropriate total power can be used with ammonia-based thermochemical storage.

The second type is a conventional megawatt-scale tube-bundle reactor for ammonia dissociation that is supplied with thermal power by hot air (780 – 860 °C) coming from a volumetric solar central receiver.

3.4.2 Reforming of methane (CH_4) using carbon dioxide (CO_2)

The reforming of methane (CH_4) using carbon dioxide (CO_2) is based on the following reaction [103]:

$$CH_4 + CO_2 = 2 \cdot H_2 + 2 \cdot CO \quad \Delta H = 250\, kJ/mol \tag{3.3}$$

This reaction above is always accompanied by the reverse water gas shift reaction [103]:

$$CO_2 + H_2 = CO + H_2O \tag{3.4}$$

However, if the initial reactor feed consists of a carbon dioxide/methane mixture with a CO_2:CH_4 ratio only slightly above one, the water formed is only in the range of a few percent and remains in the gaseous phase [103].

Unlike the ammonia-based method, here, also other unwanted side reactions may occur. These side reactions lead to carbon formation and may block the reactor, if not kept under control. The possible carbon forming side reactions are as follows [103]:

$$CO + H_2 = C + H_2O \tag{3.5}$$

$$2 \cdot CO = C + CO_2 \tag{3.6}$$

$$CH_4 = C + 2 \cdot H_2 \tag{3.7}$$

The main endothermic reaction products hydrogen (H_2) and carbon monoxide (CO) can be stored and later on used for the reverse reaction, in order to release the chemically stored thermal energy [104].

Like the ammonia-based method, the methane reforming method is technically feasible in combination with parabolic dish collectors or central tower receivers [104].

According to Muir et al. [105], the solar reforming of methane with carbon dioxide was successfully demonstrated by the commercial-scale parabolic dish collector/receiver unit CAESAR (CAtalytically Enhanced Solar Absorption Receiver). This parabolic dish collector unit had a special type of a volumetric receiver/reactor combination that converted the absorbed solar radiation into a stored chemical potential using the methane reforming method. The volumetric chemical reactor operated successfully during both, steady-state and solar transient conditions. However, the CAESAR project was only a first step regarding the development of a mature technology ready for commercialization.

When comparing the ammonia-based storage method to the methane reforming method, the former method avoids the unwanted and blocking carbon formation that requires careful attention to reactor operating conditions. Additionally, the ammonia-based storage method provides an automatic phase separation of the reaction products which simplifies storage. However, the ammonia-based storage method has a relatively low enthalpy of reaction, which only constitutes 66.5 kJ/mol [102].

3.4.3 Thermochemical energy storage using reactions with metals and metal oxides

The first step of thermochemical energy storage using reactions with metals and metal oxides is the dissociation of the metal oxide into the corresponding metal and the oxygen. This reaction is endothermic and can be written in a general form as follows [97]:

$$M_xO_y \rightarrow x \cdot M + \frac{y}{2} \cdot O_2 \tag{3.8}$$

By providing the required thermal energy by highly concentrated solar irradiation, the created metal enables easy storage and transport of solar energy. The stored energy can be released by providing process heat through combustion or electricity through fuel cells or batteries. Furthermore, it can be used for hydrogen production in an exothermic water splitting reaction [97]:

$$x \cdot M + y \cdot H_2O \rightarrow M_xO_y + y \cdot H_2 \tag{3.9}$$

However, most of the suitable metal oxides require very high dissociation temperatures, which cannot be reached with present technology. For instance, the direct dissociation (endothermic reaction) of SnO_2 and SnO into SnO/Sn and O_2 is only possible at temperatures above 2330 K. Furthermore, it may not be possible even up to 3000 K [106]. Fe_2O_3 and MgO require 3700 K, Al_2O_3, TiO_2, SiO_2 and CaO even require more than 4000 K. Only zinc oxide (ZnO) already dissociates at a temperature of 2335 K, and furthermore promises to be the best option regarding the hydrogen production [97].

Although the use of metals as energy storage seems to be impossible with today's technology due to the high temperatures required, there exists a way of dissociating metal oxides at lower temperatures. By adding a reducing agent, such as carbon or methane, to the dissociation reaction, the temperature required is significantly lowered (to about 920 K for Fe_2O_3, to about 1200 K for ZnO, and to still around 2000 K for the other metal oxides mentioned before). These reactions with carbon or methane would be as follows [97]:

$$M_xO_y + y \cdot C \rightarrow x \cdot M + y \cdot CO \tag{3.10}$$

$$M_xO_y + y \cdot CH_4 \rightarrow x \cdot M + y \cdot (2 \cdot H_2 + CO) \tag{3.11}$$

As can be seen in the reaction equations above, also carbon monoxide and hydrogen would be directly produced. In this way, the solar energy would be

also stored in the carbon monoxide and the hydrogen, respectively. Today's possibilities of hydrogen storage have to be taken into account though. This method can be seen as a temporary solution, until the direct metal oxide dissociation is technically feasible [97].

Keunecke [97] investigated the possibilities of dissociating ZnO in a direct way, without the use of any additional fossil fuels. In his work, he proposed ways for the design of a solar reactor for the direct dissociation of zinc oxide. He emphasized the importance of inhibiting the back reaction, in order to provide sufficient zinc production rates.

Chapter 4

Modeling approaches for thermal energy storage concepts for concentrated solar power

This chapter gives an overview of already proposed modeling approaches for thermal energy storage concepts for solar thermal power plants. Basically, this chapter summarizes the governing equations and states important characteristics.

4.1 Introduction

In order to develop models for the simulation of concentrated solar power thermal energy storage units, a profound literature research is required to gather as much information about already existing knowledge as possible. In the following, a summary of the governing equations, the model simplifications and the numerical methods, is given. However, for more detailed information, mainly concerning correlations for heat transfer coefficients or pressure drop, the interested reader is referred to the original sources.

4.2 Active indirect two-tank thermal energy storage modeling

An active indirect two-tank thermal energy storage system, for thermal oil as heat transfer fluid and molten salt (solar salt) as storage medium, can be seen

in Figure 4.1. It consists of one cold molten salt tank, one hot molten salt tank, the corresponding salt pumps, and the oil-to-salt heat exchanger. The molten salt is stored at two temperature levels defining a certain temperature difference that is used in order to charge or discharge sensible heat. While charging, the molten salt is drained from the cold tank and fed into the hot tank while passing through the oil-to-molten-salt heat exchanger, where the molten salt reaches the hot tank's temperature level. The discharging process happens vice versa by pumping the molten salt from the hot tank through the heat exchanger to the cold tank, while transferring the required heat to the thermal oil.

Usually, the oil-to-salt heat exchanger module is separated into several units, as the maximum possible heat exchanger length is limited due to design and fabrication aspects. In already commercially operated systems, the number of heat exchanger units used ranges between 6 and 3 [107, 108]. The oil-to-salt heat exchanger consists of several shell-and-tube subunits, which are connected in series. The oil, which is under higher pressure (about 20 bar), is flowing inside the tubes, and the molten salt is flowing on the shell side. A two-pass tube and two-pass shell layout with a longitudinal baffle is a possible design option [109]. They are operated in counter-flow mode, and additionally are designed for bidirectional flow (charging and discharging). According to already commercially operated systems of this type, the hot tank is kept at a temperature of about 386 °C, and the cold tank is kept at a temperature of about 292 °C. The maximum oil temperature allowed is limited to about 400 °C [11].

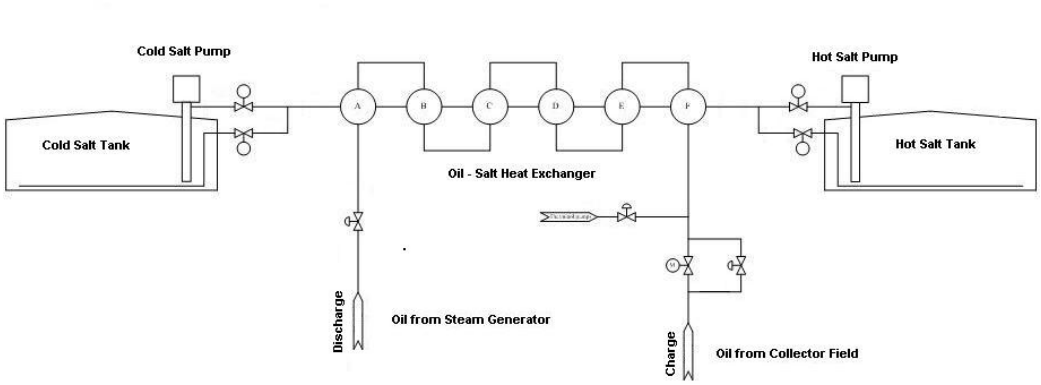

Figure 4.1: Active indirect two-tank heat storage scheme – tanks and heat exchangers [109]

An important part of the active indirect heat storage model is the sub-

model of the heat exchanger that is responsible for the heat transfer between the thermal oil and the molten salt. Of course, depending on the intended level of simulation detail, different modeling approaches shall be chosen.

In order to obtain an appropriate heat exchanger simulation model that is useful for power plant long-term simulations as well as for transient short-term simulations, two different concepts can be implemented. One that is suitable for the transient points of operation, and another one that is suitable for quasi-steady long-term simulations, offering an acceptable level of calculation effort in each case.

4.2.1 The modeling of the oil-to-salt heat exchanger for long-term simulations

For long-term simulations, where short heat exchanger dynamics can be neglected, a steady-state model can be applied, using well established correlations for steady-state heat exchanger behavior, such as the epsilon-NTU method or the log-mean temperature method, as published by Shah & Sekulic [110].

A crucial feature of this steady-state heat exchanger model is the consideration of partial loads, i.e. the overall heat transfer coefficient as well as the pressure drop have to be implemented as functions of mass flows. Depending on the actual charge or discharge rate, low mass flow rates may limit the heat transfer in the heat exchanger that may result in a higher mean temperature difference for a given heat duty, reducing the storage system's performance.

4.2.2 The modeling of the oil-to-salt heat exchanger for short-term simulations

Considering the dynamic modeling of this active indirect storage system, a reasonable amount of modeling work has to be assigned to the oil-to-salt heat exchanger, hence taking into account the dominant transient phenomena.

As stated above, a proposed heat exchanger design is a shell-and-tube layout. Given the importance of shell-and-tube heat exchangers in process engineering, their performance modeling has already been subject of numerous publications[1].

In summary, already proposed heat exchanger models can be subdivided into two groups, namely (i) three-dimensional numerical models with high spatial resolution, also referred to as computational fluid dynamics (CFD),

[1]It has to be noted that the following paragraphs are entirely based on a previously published work [111] of the author.

and (ii) numerical as well as analytical models of much lower spatial resolution, e.g. approaches using one-dimensional fluid flow models for each of the heat exchanger ducts.

CFD shell-and-tube heat exchanger models give detailed information about flow fields, heat transfer coefficients and pressure drop, which is important for improving and optimizing heat exchanger design, such as baffle sizing, alignment and spacing, without the need of expensive and time-consuming experiments. For example, such detailed shell-and-tube heat exchanger simulations were accomplished by Prithiviraj & Andrews [112], Zhang et al. [113], Ozden & Tari [114] and You et al. [115]. However, due to the relatively high computational effort, models of much lower spatial resolution are applied for transient response simulations that are required for the evaluation of heat exchanger operation and control strategies, i.e. the subject-matter of this work.

Also in this area, many important works have already been published. Proposed models range from analytical methods, which apply the Laplace transform to cope with the resulting set of differential equations, to more flexible, object-oriented Modelica-based numerical models.

The consideration of multi-pass shell-and-tube heat exchanger modeling approximately dates back to the 1950's and 1960's. Earlier works on the transient behavior of heat exchangers were mainly confined to the evaluation of double-pipe heat exchanger configurations [116]. For example in 1959, Masubuchi [117] applied the frequency response analysis to evaluate the transient behavior of shell-and-tube heat exchangers with multiple tube passes and one single shell pass. He defined the transfer function as a dynamic ratio of the outlet temperature of one fluid to the inlet temperature of the other fluid. Considering sinusoidal solution, sinusoidal temperature variation was superposed on the steady-state temperature. He assumed that fluid velocities and heat transfer coefficients are all constant and do not change with temperature. The thermal conductivity of the tubes was assumed to be infinite in direction normal to flow and zero in direction of flow. Furthermore, the heat capacity of any solid parts of the exchanger as well as the heat exchange with the surroundings was neglected. The resulting problem was solved numerically using a graphical method. Experimental results were found to be in good agreement with the theoretical results. Morris [116], for example, based his modeling on introducing a correction factor that relates the dynamic behavior of single-pass exchangers to that of corresponding multi-pass configurations. This was based on the fact that the steady-state temperature behavior of multi-pass exchangers can be represented by a single-pass approximation applying the LMTD correction factor F. He applied the Laplace transform to cope with the governing set of partial

differential equations. Good agreement between the model and experimental data was observed too. In 1975, Gaddis & Schlünder [118] presented an effective method to evaluate the behavior of multi-pass shell-and-tube heat exchangers. As the heat exchanger's performance strongly depends on the specific flow arrangement that is determined by the number of baffles, the number of tube-side and shell-side passes, and furthermore, by the locations of the fluid feeds and drains, they divided the heat exchanger into a certain number of cells, solving an ideally mixed energy balance for each of them. The specific flow arrangement was modeled via "connecting" the fluid cells accordingly. Their proposed method is therefore commonly known as the cell-method and has been applied and extended by various authors. It is actually a specific application of the nowadays well established finite volume method. Roppo & Ganic [119] built upon the modeling approach proposed by Gaddis & Schlünder [118, 120] and extended it for time-dependent fluid inlet conditions and heat transfer, obtaining a powerful tool for the dynamic modeling of processes involving multi-pass shell-and-tube heat exchangers. They assumed constant physical properties, a constant overall heat transfer coefficient and additionally neglected the thermal capacitance of any solid part of the exchanger. They reassured the correctness of the steady-state results obtained by Gaddis & Schlünder [118, 120], since their model converged to the same stationary solutions. 6 years later, Correa & Marchetti [121] presented a transient shell-and-tube heat exchanger model using the cell-method as well. But unlike Roppo & Ganic [119], they incorporated the thermal capacitance of the metallic parts in their model. They solved the governing system of equations numerically approximating the derivative terms by first-order finite differences. In order to check their simulation results for consistency, they compared them with the data obtained by Gaddis & Schlünder [118, 120] and Roppo & Ganic [119], observing almost complete agreement. Roetzel & Xuan [122] also developed a method for predicting the transient responses of multi-pass shell-and-tube heat exchangers exposed to inlet temperature changes. They assumed constant heat transfer coefficients for each tube-side pass, constant thermal flow rates ($\frac{W}{K}$), and an ideally mixed shell-side fluid flow at any cross section, neglecting any bypass streams. Additionally, they set the thermal properties to constant values, and considered the longitudinal heat conduction as well as the radial thermal resistance to be negligible. Furthermore, they neglected the shell's thermal inertia and did not consider the heat exchange with the environment. They applied the Laplace transform to solve the resulting system of equations, but had to use a numerical inverse Laplace transform in order to obtain the solution in the time domain. Botsch et al. [123] described the behavior of an industrial scale shell-and-tube condenser by subdividing the heat exchanger into discrete con-

trol volumes determined by the free spaces in between the vertical baffles, a method that can be considered similar to that originally proposed by Gaddis & Schlünder [118] in steady-state. They applied mass and energy balances for each of these baffle spaces by using heat and mass transfer correlations from literature and assuming ideally mixed control volumes. Fluid properties were calculated as a function of temperature, pressure and composition for each control volume. They solved the resulting system of algebraic and time-dependent differential equations (DAE-system) numerically applying a solver tool developed at the Department of Chemical Engineering at the University of Stuttgart. Also Manenti & Ravaghi-Ardebili [124] considered the transient modeling of a shell-and-tube heat exchanger in their work, which presented a transient model of a molten-salt-based solar thermal power plant on system level. Amongst other things, they described the dynamic sub-model of the plant's economizer, a shell-and-tube unit having the water on the shell side and the molten salt on the tube side. Also their model's formulation was accomplished according to the well established cell-method. Recently, Milián et al. [125] presented a dynamic model of a shell-and-tube condenser, in order to study the influence of the applied mean void fraction correlation. Instead of the commonly applied finite volume distributed parameter approach, they implemented a moving boundary lumped parameter model, which significantly reduced the computational effort while maintaining the accuracy within a reasonable limit. In order to reduce the complexity of the model, they assumed that an equivalent axial double-pipe heat exchanger model setup in counter-flow arrangement was an acceptable simplification of the actual component. By comparing the model's predictions with experimental data, they showed the great influence of the used mean void fraction correlation on the simulated results.

Mattsson [126] was presumably the first to propose an object-oriented transient heat exchanger model, implemented in the back then recently developed physical system modeling language Modelica [127]. He modeled a heat exchanger as two parallel fluid ducts, separated by a wall and discretizing the so obtained assembly into sections along flow direction. This was done by implementing sub-model classes for a fluid duct section and a wall section, and consequently declaring a Modelica array with a certain user-defined number of sections in flow directions. By finally writing the corresponding connecting equations, the final heat exchanger model was obtained. Once again, heat conduction in longitudinal direction was neglected and mass and energy balances were formulated assuming ideally mixed control volumes. Unfortunately, back then, existing Modelica translators were not able to handle array definitions of components. Therefore, the model had also been implemented and simulated using the object-oriented language Omola [128]. Years

later, meanwhile powerful Modelica simulation environments head been developed, Casella & Schiavo [129] presented a detailed Modelica-based heat exchanger model, featuring a rigorous implementation of the one-dimensional fluid flow in each fluid duct, also considering a dynamic momentum balance, being able to simulate fast pressure dynamics, as well. They solved the governing partial differential equations (PDEs) by applying the finite element method (FEM), obtaining a set of ordinary differential equations (ODEs) suitable for the model formulation in Modelica. The final heat exchanger model consisted of two instances of the one-dimensional fluid flow model, and a correspondingly connected dynamic model of the separating tube wall. Also Skoglund et al. [130] proposed a Modelica-based object-oriented dynamic heat exchanger model, but designed for the thermal evaluation of the effects of changes in fluid composition, which is e.g. necessary for simulations of liquid food production lines. They also used the already aforementioned basic concept of two parallel ducts separated by a wall, but applied the finite volume method (FVM) for discretizing the two fluid ducts in longitudinal direction. Assaf et al. [131] developed a detailed distributed parameter model of a shell-and-tube dry-expansion evaporator, having one shell pass and two tube passes in U-tube design. This model takes the rather complicated shell-side flow between the vertical segmental baffles into account by discretizing the shell-side flow into corresponding control volumes located in between the baffles, also corresponding to the cell-method originally proposed by Gaddis & Schlünder [118]. Although the Modelica modeling language was used too, this shell-and-tube heat exchanger model was formulated in steady state only, resulting in a non-linear system of time-independent equations.

Summarizing the above, it can be said that the transient response modeling of shell-and-tube heat exchangers is a common engineering problem in process industry and a huge number of models has already been developed. Furthermore, the physical system modeling language Modelica has become a well recognized and frequently applied approach for the transient modeling of heat exchangers and related thermodynamic systems. It is obvious that these already proposed modeling approaches can be applied to the performance modeling of thermal energy storage systems for concentrated solar power as well.

4.2.3 The modeling of the storage tanks

Storage tank heat loss data and models can already be found in open literature[2]. One of the first experimental projects dealing with molten salt two-tank solar thermal energy storage for electricity generation was the CESA-I central receiver plant in Spain (1984) [133, 134]. There, the cylindrical storage tanks were placed horizontally, having their axes parallel to the ground. The upper bound heat loss for the hot tank was estimated to be 20 kW at its design temperature of 340 °C. Half of this value was estimated for the cold tank at 220 °C [134]. Through measurements, Andújar et al. [135] determined an overall heat transfer coefficient ($U_{overall}$) of 0.327 $\frac{W}{m^2K}$ for the hot tank, and 0.265 $\frac{W}{m^2K}$ for the cold tank, considering an external tank surface area of 213 m^2. Castro et al. [136] presented a comprehensive quasi-steady whole-system mathematical model of the CESA-I plant. They adjusted their model to real plant data and obtained a storage tank temperature drop of about 0.3 °C per hour.

Pacheco et al. [81] provided heat loss data that was measured at the Solar Two project. There, the total thermal losses of the hot tank (at 565 °C) and the cold tank (at 290 °C) amounted to about 102 ± 21 kW and 44 ± 6.6 kW, respectively. Herrmann et al. [80] developed the following empirical heat loss equation, based on measured values at the Solar Two project, where T_{salt} is the molten salt temperature (in °C) and $\dot{q}_{loss}$ is the specific heat loss in kW per area (valid for both the cold as well as for the hot tank):

$$\dot{q}_{loss} = 0.00017 \cdot T_{salt} + 0.012 \tag{4.1}$$

Al-Sulaiman et al. [137], Spelling et al. [52], as well as Powell & Edgar [64] use an overall heat transfer coefficient ($U_{overall}$) correlation for taking the storage tank heat losses into account. Spelling et al. [52] also consider the gas atmosphere above the storage medium in their storage tank model. Heat losses to the environment are obtained by evaluating the following equation, where T_m represents the temperature of the containing medium, T_a the ambient temperature, A the reference surface area (m^2) and $U_{overall}$ the overall heat transfer coefficient in $\frac{W}{m^2K}$:

$$\dot{Q}_{loss} = U_{overall} \cdot A \cdot (T_m - T_a) \tag{4.2}$$

[2]This section is entirely based on a previously published work [132] of the author. By citing the original work here at the beginning, a repeated referencing throughout the text is left aside.

Storage tank experience at a commercial parabolic trough collector plant has shown that the temperature decrease for the hot and the cold tank is less than 1 °C per day at the maximum molten salt level, and 5 – 6 °C at the minimum molten salt level [107]. Rovira et al. [138] used the data provided by Relloso & Delgado [107] and derived the following empirical correlation that depends on the tank fill factor χ as well as on the characteristic diameter D of the storage tank. This relationship is based on a dimensionless analysis and furthermore on the assumption that the same thermal insulation, the same geometry, as well as the same operating temperature differences are used. Under these conditions, the proposed relationship may be used for differently sized storage tanks:

$$\dot{Q}_{loss} = \left(\chi \cdot \dot{Q}_{loss,\,full} + (1-\chi) \cdot \dot{Q}_{loss,\,empty}\right) \cdot \frac{D}{D_{ref}} \tag{4.3}$$

$$\chi = \frac{m - m_{min}}{m_{max} - m_{min}} \tag{4.4}$$

The term $\dot{Q}_{loss,\,full}$ represents the heat loss of the full hot or cold tank that causes a temperature drop of 1 °C per day. This results in 488 kW and 483 kW for the hot and the cold tank, respectively, considering storage tank dimensions currently applied at commercial parabolic trough collector plants. The term $\dot{Q}_{loss,\,empty}$ represents the heat loss of the empty hot or cold tank that causes a temperature drop of 6 °C per day. This results in 230 kW and 225 kW for the hot and the cold tank, respectively [138].

Schulte-Fischedick et al. [139] accomplished a detailed CFD analysis of the cool-down behavior of such a molten salt thermal energy storage tank. They presented the ruling fluid mechanical effects that determine the molten salt cool-down behavior. This kind of study is important for improving and evaluating the storage tank design with high spatial resolution. It is crucial to identify locations where local freezing has to be expected first and to determine cool-down times until the onset of local solidifications. Good storage tank design avoids such "cold" spots that can be found where relatively high specific heat flows coincide with low molten salt flow velocities [139]. Schulte-Fischedick et al. [139] determined a cool-down rate for the cold tank of 0.47 K per day at the upper filling level, 0.95 K per day at the medium filling level and 13.4 K per day at the lower filling level.

Furthermore, Schulte-Fischedick et al. [139] provided the important information that a quite homogeneous salt inventory temperature profile can be expected. Even in storage system off-line mode, the heat loss to the environment offers enough driving force to establish a characteristic natural

convection flow profile within the tank. In regions close to the tank walls the molten salt cools down, its density increases and starts to move towards the tank bottom. Close to the bottom corner it reaches its maximum velocity that is according to [139] about 7 – 23 mm per second, depending on the filling level. Then it is decelerated and moves towards the tank bottom center. Its temperature rises again and begins moving towards the molten salt surface. This leads to good mixing of the relatively cool and hot salt, ensuring a homogeneous temperature distribution. Considering these results, it should be appropriate to model the molten salt inventory as an ideally mixed volume, having one representative fluid temperature T_{salt}.

This approach has also been chosen by the previously mentioned authors (e.g. [52], [64]) and may be considered as the up-to-date solution for performance oriented simulations. Furthermore, heat losses to the environment are typically taken into account using an empirical overall heat transfer coefficient applying a quasi-steady-state method for the heat transfer from the storage media to the environment (see Equation 4.2). Since the heat loss of the molten salt inventory also depends on the filling level of the storage tanks, fill-factor-dependent correlations shall be taken into account.

4.3 Active indirect single-tank thermocline TES modeling

The active indirect single-tank thermal energy storage system is similar to the active indirect two-tank thermal energy storage system, with the only difference that the two tanks are reduced to one tank of slightly larger dimensions. The hot and the cold molten salt are now stored in one single tank using the variation in density as a natural way of separation. Hence, temperature layers are stratified from the highest temperature at the top to the lowest temperature at the bottom. Studies have shown that the highest temperature gradient, thus the strongest temperature variation between these stratified layers, occurs in a rather limited zone within the total molten salt level height. For this reason, it is possible to provide almost constant molten salt outlet temperatures, during a reasonable part of the discharging process. And vice versa, the cold molten salt outlet temperature is almost constant during charging mode. About 69% of the total maximum molten salt level height can be used for the actual storage capacity. Hence, about 31% of the molten salt level height are required by the temperature gradient. Furthermore, in order to prevent convective mixing within the molten salt tank, and to increase the heat storage capacity, a low cost filler material is

necessary [75].

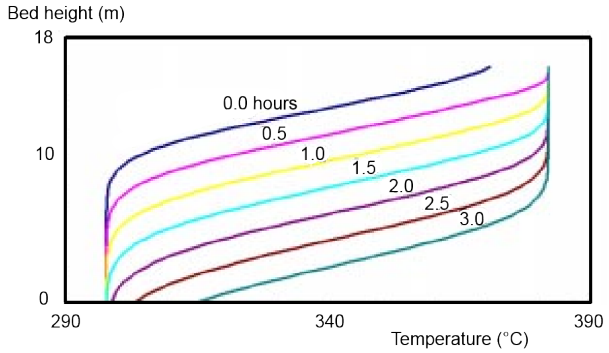

Figure 4.2: Temperature gradient for a charging cycle every 0.5 hours [75]

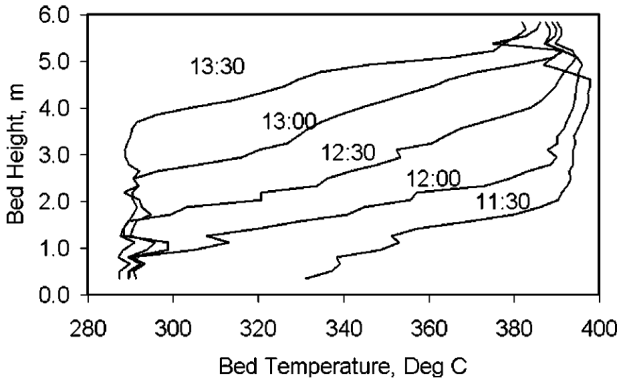

Figure 4.3: Measured thermocline temperature distribution for discharging mode [75]

The percentage of the storage medium level height that is required by the temperature gradient is determined by the heat transfer performance between the packed bed and the fluid. This performance can be described by the dimensionless number of transfer units (NTU). The number of transfer units is the product of the heat transfer coefficient and the total heat transfer area between solid and liquid phase, divided by the product of fluid mass flow and fluid heat capacity. This dimensionless number is related to the shape of the thermocline (temperature gradient) within the storage tank. The higher this number is, the higher is the temperature gradient and the higher is the effectiveness of the thermocline storage system due to a lower height required by the temperature gradient [140].

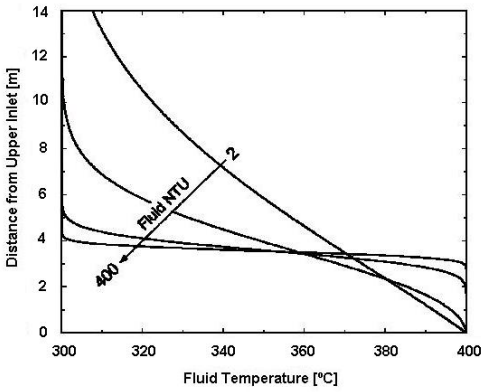

Figure 4.4: Thermocline as function of the number of transfer units (NTU) [140]

Concerning the dynamic modeling of active indirect single-tank thermocline storage systems, the modeling approach for the oil-to-salt heat exchanger stays the same as for the active indirect two-tank approach. While discharging, the hot molten salt is taken from the top of the storage tank, cooled in the oil-to-salt heat exchanger, and fed back to the bottom entry of the storage tank; and vice versa during charging mode. However, the storage tank itself will have to be considered in a different way.

As shown in Figure 4.5, a thermocline storage tank consists of the flow distributor, the actual storage space and the necessary piping for the cold and the hot salt flow. The storage space contains a low cost filler material and the stratified layers of molten salt. This concept is commonly known as packed bed storage layout. Quartzite rock has shown to be a good filler material option. The distributors at the inlet and the outlet of the packed bed storage tank ensure homogeneous flow conditions. According to Figure 4.5, h' characterizes the distributor height, and h the storage space height [74].

Referring to Figure 4.6, the thermocline storage space can be divided into three zones. Starting from the bottom, the first zone is a rather constant low temperature zone (i) ranging from the bottom area of the tank up to the beginning of the pronounced temperature gradient zone. This temperature gradient zone (ii) is characterized by significant temperature changes of the molten salt and the filler material. Finally, the temperature gradient zone is followed by the rather constant high temperature zone (iii) at the top of the tank [74].

While discharging and charging, the temperature gradient zone moves

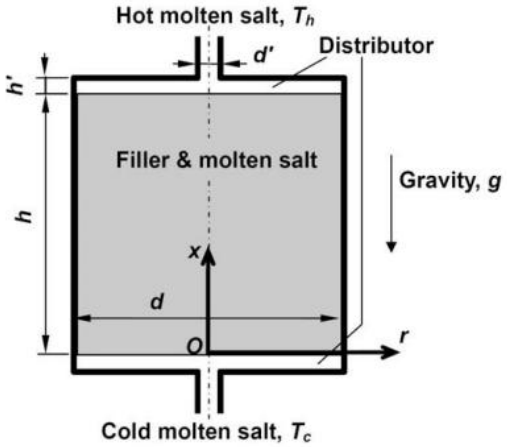

Figure 4.5: Thermocline storage tank scheme [74]

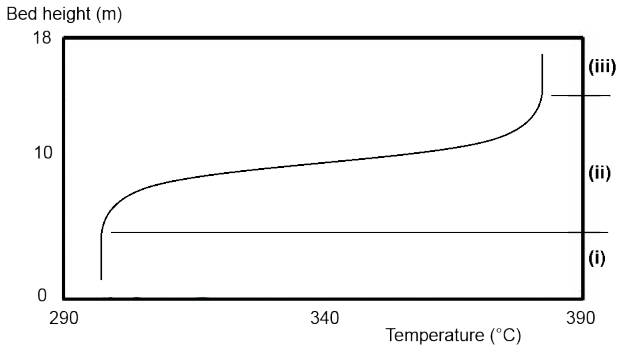

Figure 4.6: Thermocline zones (i), (ii) and (iii)

towards the exit piping, leaving behind an expanding constant low temperature zone (discharging), or high temperature zone (charging), respectively. In the constant temperature zones, the filler material is completely cooled or heated, hence, providing a thermodynamic equilibrium between the molten salt and the filler material. In the temperature gradient zone, the thermal energy is either transferred to the filler material (charging), or, in the case of discharging, to the molten salt. Hence, this zone is also referred to as heat exchange zone [74].

Several theoretical and practical studies have already been performed regarding the thermal behavior of liquid or gaseous fluid flow through solid porous media that occurs in thermocline packed bed storage tanks. One of the first works published, was that of Schumann in 1929. He presented an analytic solution for the one-dimensional thermal behavior of a liquid flowing through a porous prism under certain simplifying assumptions [141].

Schumann [142] assumed that lumps (the solid phase) within the prism are so small and have such high thermal diffusivity that any given lump may be considered as being at a uniform temperature at any instant. He neglected the transfer of heat by conduction in the fluid and in the solid phase. Furthermore he assumed that at any point, the heat transfer between fluid and solid is proportional to the average difference in temperature between the fluid and the solid. Additionally, he neglected the change in volume due to a change in temperature, and, assumed thermodynamic properties to be independent of temperature. Also, the prism's walls were assumed to be adiabatic, hence heat losses were neglected. According to these assumptions, he expressed the energy balance at an infinitesimal section (see Figure 4.7) of the prism in the following way (note, that he assumed a unit cross-sectional area, hence the volume of that infinitesimal section is 1 times dx):

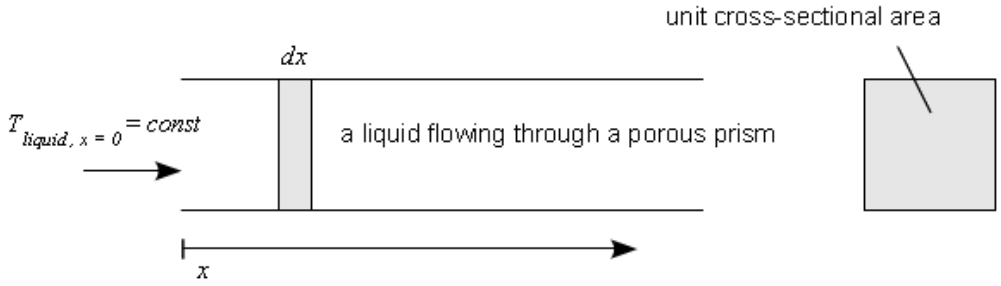

Figure 4.7: A liquid flowing through a porous prism [142]

$$\frac{\partial T_g}{\partial t} \cdot h_g \cdot f \cdot dx \cdot dt = -k \cdot (T_g - T_s) \cdot dx \cdot dt - \frac{\partial T_g}{\partial x} \cdot h_g \cdot v \cdot f \cdot dx \cdot dt \quad (4.5)$$

$$\frac{\partial T_s}{\partial t} \cdot h_s \cdot (1-f) \cdot dx \cdot dt = k \cdot (T_g - T_s) \cdot dx \cdot dt \tag{4.6}$$

Equation 4.5 states the energy balance for the fluid, Equation 4.6 states the energy balance for the solid, yielding the following governing partial differential equations [142]:

$$\frac{\partial T_g}{\partial t} + v \cdot \frac{\partial T_g}{\partial x} = -\frac{k}{h_g \cdot f} \cdot (T_g - T_s) \tag{4.7}$$

$$\frac{\partial T_s}{\partial t} = \frac{k}{h_s \cdot (1-f)} \cdot (T_g - T_s) \tag{4.8}$$

Schumann [142] solved these partial differential equations analytically under the assumption of a constant fluid entry temperature, i.e. $T_{g,\,x=0} = T_0$ for all time, and a porous prism start temperature $T_{s,\,t=0}$ of zero. However, under more realistic boundary conditions, the analytical solution becomes by far more complicated. Hence, in practical simulation applications numerical methods will have to be applied.

Mawire & McPherson [143] modeled an oil pebble bed thermal energy storage system for low to medium temperature solar applications, using the original and slightly modified Schumann equations. They also compared their simulation results with experimental data. Although the original Schumann equations provided good calculation results in low storage temperature ranges up to 140 °C, a larger deviation from experimental data has been detected at higher storage temperatures beyond 140 °C due to unaccounted heat loss correlations. The use of modified versions of the original Schumann equations provided better agreement between data from simulations and experiments at higher temperatures.

Hence, depending on the quality of the thermal insulation and the operating temperatures of thermocline systems that are proposed for solar thermal power applications, simulation models based on the original Schumann equations will have to be adapted accordingly. However, numerical investigations that have been performed by McMahan [140] showed that neglecting axial conduction and viscous dissipation within the thermocline storage as well as neglecting shell losses of the storage tank, are well-founded assumptions. He came to this conclusion by comparing thermocline calculation results with Solar One discharge data. According to this investigation, it is appropriate to neglect thermal losses to the environment during short-term discharge and charging cycles, since thermal losses are marginal compared to the energy

transfer from and to the tank. McMahan [140] performed numerical investigations using a one-dimensional thermocline storage tank model. Based on the energy balance of a storage tank slice with an infinitesimal height dx, which will be stated in the following, an explicit and implicit finite difference method was applied in order to solve the governing differential equations.

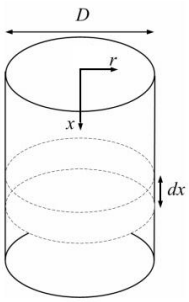

Figure 4.8: Infinitesimal storage tank slice [140]

The energy balance of the infinitesimal storage tank slice is given by the following partial differential equations, including the following simplifications [140]:

- The heat losses to the environment are neglected.
- The axial conduction along the storage tank height is neglected.
- The solid packed bed material is assumed to have uniform temperature, without temperature gradients inside particles. Hence the thermal conductivity is assumed to be ∼infinite. However, since solid materials that are proposed for solar thermal power applications have rather low thermal conductivity values, a modified heat transfer coefficient between solid and liquid phase is proposed, taking the Biot number into account.

$$\dot{m}_f \cdot C_f \cdot \frac{\partial T_f}{\partial x} + \rho_f \cdot \epsilon \cdot A_c \cdot C_f \cdot dx \frac{\partial T_f}{\partial t} = -h \cdot A_s \cdot (T_f - T_s) \tag{4.9}$$

$$\rho_s \cdot (1 - \epsilon) \cdot A_c \cdot C_s \cdot dx \cdot \frac{\partial T_s}{\partial t} = h \cdot A_s \cdot (T_f - T_s) \tag{4.10}$$

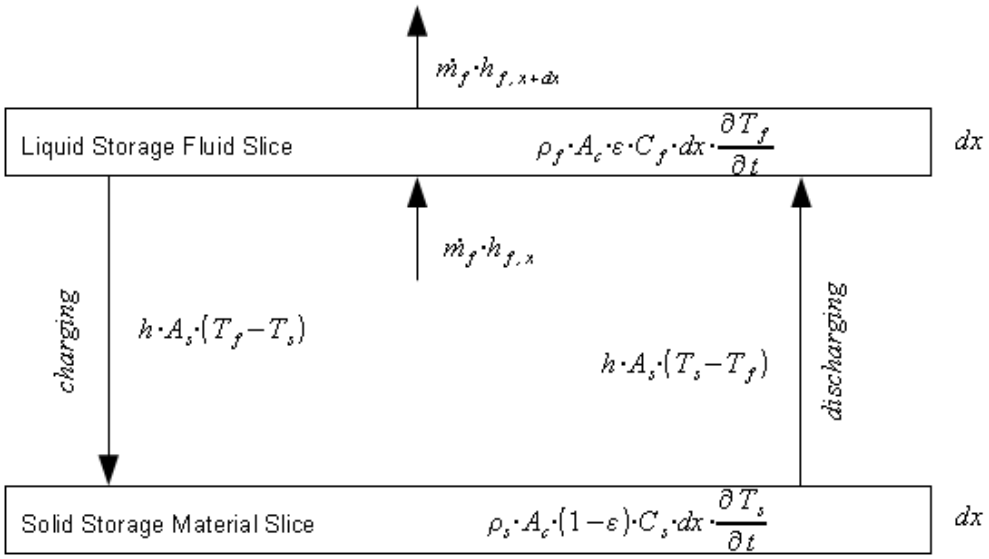

Figure 4.9: Infinitesimal storage tank slice energy balance

Van Lew et al. [144] also performed numerical investigations based on the energy balance mentioned above. Unlike McMahan [140], they transformed the governing partial differential equations into a dimensionless form, applying the method of characteristics for solving them. This provided a powerful solution with minimal computing time.

Considering long-term storage cycles, thermal losses to the environment cannot be neglected and have to be taken into account. Therefore, between charging and discharging mode, when the storage tank is in idle mode, the thermal conductivity as well as the thermal losses to the environment have to be taken into account. In order to model this, McMahan [140] divided the storage tank again into infinitesimal slices along its height, hence introducing a one-dimensional numerical grid. Thus, each infinitesimal slice (Figure 4.9) is assumed to have a uniform temperature since a model of higher dimension is not practical. Each infinitesimal mass element is defined by ϵ, which is the ratio of liquid phase volume to total volume, and the corresponding densities of the liquid phase and the solid phase. The energy balance for the infinitesimal slice is then defined considering an overall heat loss coefficient $h_{loss\,wall}$ and an effective thermal conductivity k_{eff} of the solid/liquid mass mixture. A_{wall} is the circumferential surface area of the slice.

Taking available data from a Solar One tank cool-down test, showed a general compliance with the model [140].

The assumptions from above yield the following partial differential equation:

$$(\rho_f \cdot \epsilon \cdot C_f + \rho_s \cdot (1-\epsilon) \cdot C_s) \cdot A_c \cdot dx \cdot \frac{\partial T}{\partial t} = k_{eff} \cdot A_c \cdot \frac{\partial^2 T}{\partial x^2} - h_{loss\,wall} \cdot A_{wall} \cdot (T - T_a) \tag{4.11}$$

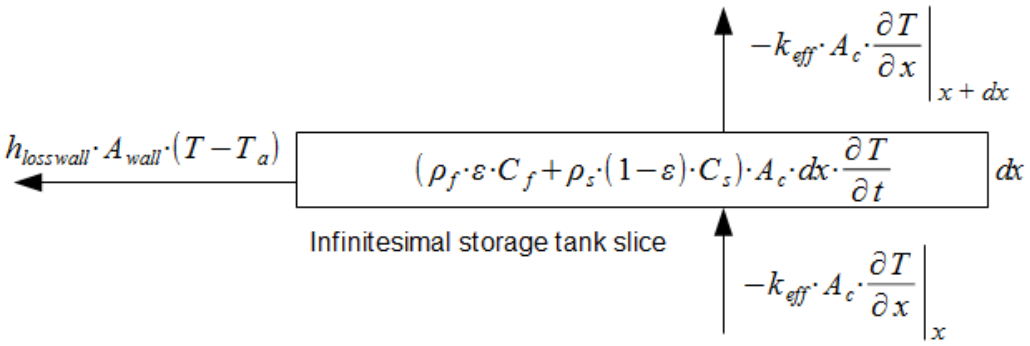

Figure 4.10: Infinitesimal storage tank slice energy balance

4.4 Active direct two-tank thermal energy storage modeling

The modeling of the active direct two-tank thermal energy storage concept is the same as for the active indirect two-tank approach. The only difference is the absence of the heat exchanger between the heat transfer fluid and the storage medium. This storage concept is the typical option for molten salt central receiver projects or molten salt parabolic trough collector power plants.

4.5 Active direct single-tank thermocline heat storage modeling

Correspondingly, the modeling of the active direct single-tank thermocline heat storage concept is the same as for the active indirect thermocline single-tank approach. Again, the only difference is the absence of the heat exchanger

between the heat transfer fluid and the storage medium. This storage concept could be applied at molten salt central receiver projects or molten salt parabolic trough collector power plants.

4.6 Passive sensible heat storage modeling

In passive sensible heat storage systems, the heat transfer fluid is pumped through a solid heat storage material where the thermal energy is stored or discharged in sensible form. Two concepts have been proposed so far; one for air-based central receiver power plants (air/rock – air/ceramic packed bed), and the second one for parabolic trough collector plants (casted blocks of concrete/ceramic containing tube bundles).

4.6.1 Passive sensible heat storage with concrete or ceramic for PTC plants

Concerning passive sensible heat storage for parabolic trough collector plants, either high temperature concrete or castable ceramics are proposed to serve best as storage materials. In particular, the high temperature concrete or the ceramics are casted in blocks containing tube bundles where the heat transfer fluid is pumped through. This passive sensible heat storage concept is a promising low cost alternative. Modular layouts that enable different setups for charging and discharging have been proposed in order to improve the efficiency and the ability to compete with conventional storage systems.

Due to the rather low thermal conductivity of the proposed storage materials, the temperature distribution within the storage block is not uniform and varies throughout the charging or discharging process. In order to take the low thermal conductivity into account, a two-dimensional model for the storage block was proposed. Since passive sensible heat storage units for parabolic trough collector plants are assemblies of parallel tubes where the remaining space between these tubes is filled with the storage material, the first modeling dimension would be in the direction of the steel tubes, and the second modeling dimension would be in the direction normal to these tubes. Furthermore, Steinmann et al. [145] assumed the storage unit to be composed of cylindrical storage masses that are concentrically placed to the parallel steel tubes (see Figure 4.11). One single simplified cylindrical storage unit is then discretized in the direction of heat transfer fluid flow and in radial direction, assuming a circumferentially uniform temperature distribution. In order to model the limited thermal conductivity of the storage volume a sufficient level of discretization has to be chosen. An arbitrary size

of the storage unit can be modeled via connecting these simplified storage units in parallel. Also the temperature distribution inside the steel tubes was assumed to be uniform in circumferential direction in order to avoid a three-dimensional model that would have required by far more computing time. The errors caused by this assumption seemed to be acceptable. The storage material and the tube was discretized into discrete sections that were connected with each other via elements with a certain thermal resistance or a heat transfer correlation in the case of the fluid-wall boundary. Then, for each discrete section the governing differential equations for the energy balance were solved numerically [145].

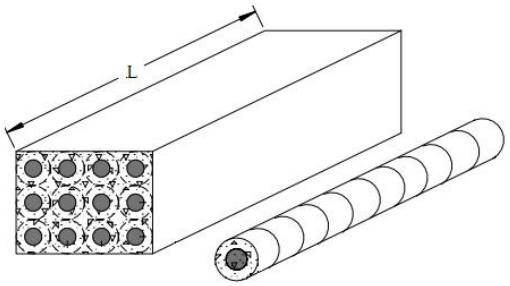

Figure 4.11: Passive sensible heat storage model scheme [146]

4.6.2 Air/rock – air/ceramic packed bed passive heat storage for central receiver plants

For volumetric central receiver power plants, an air/rock or air/ceramic heat storage system is proposed. There, the hot air, coming from the volumetric receiver, passes through a vessel containing a packed bed of an appropriate solid material that develops a characteristic thermocline temperature profile. This concept is similar to the single-tank molten salt thermocline approach that has already been mentioned before, but due to the rather low volumetric heat capacity of the air, the major part of the thermal energy is stored by the solid packed bed material.

Again, the modeling of the thermocline inside the storage vessel can be done by using the same equations that have already been mentioned in Section 4.3 of this work, commonly known as the Schumann equations [142, 88]. Hänchen et al. [88] extended the Schuman [142] equations by adding a term for the heat loss to the environment and a term for the thermal conduction within the solid packed bed material. Simplifying assumptions are:

- a uniformly packed bed that is defined by a certain constant void fraction,
- neglecting the radial (perpendicular to the air flow direction) temperature gradient within the storage vessel,
- a uniform temperature distribution within a single particle,
- neglecting the heat transfer via radiation,
- as well as neglecting the heat conduction within the fluid.

The governing partial differential equations were solved numerically applying an explicit forward difference scheme in time and an upwind difference scheme in space. The model was validated by using the experimental results obtained by Meier et al. [147].

4.7 Passive latent heat storage modeling for PTC plants

Passive latent heat storage is a thermal energy storage concept that is especially suitable for direct steam generation (DSG). While charging, the steam's thermal energy is transferred to the phase change storage material at almost constant temperature while condensing. Simultaneously, the phase change storage material changes from solid to liquid state. While discharging, the preheated water is evaporated by the previously stored latent heat of the phase change material. Now, the storage material changes from liquid to solid state. For preheating and superheating, additional passive sensible heat storage units have been proposed. Due to the almost constant temperature distribution along the evaporating and condensing sections of PCM storage units for direct steam generation, a rather rough level of discretization in flow direction is tolerable, simplifying the modeling considerably [148].

Proposed PCM storage unit layouts consist of assemblies of parallel steel tubes that are surrounded by the phase change material. In order to enhance the rather low thermal conductivity of suitable phase change materials aluminum or graphite fins placed perpendicular to the steel tubes are proposed. In Figure 4.12 a partial cross section of such a phase change material storage unit is shown, including a proposed two-dimensional modeling grid. In order to reduce the calculation time, and to improve the efficiency of the models, the circumferential temperature distribution is assumed to be uniform. Hence, the spatial discretization of a PCM storage unit is only proposed for

the direction of steam flow in the tubes and for the direction perpendicular to the tubes [148].

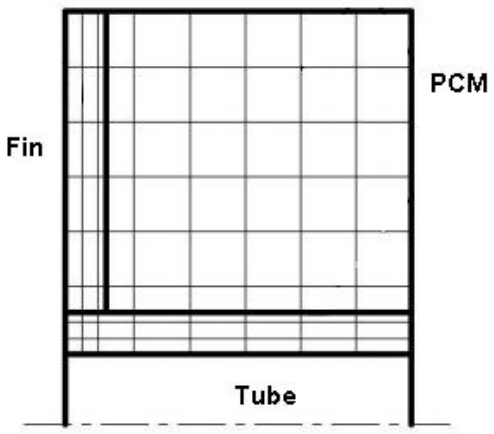

Figure 4.12: PCM storage unit partial cross section [148]

Stückle [148] used the finite volume method in order to solve the governing partial differential equations. One finite volume was represented by each of the squares, determined by the grid in Figure 4.12. The cylindrical shape of a single tube-storage-material unit was considered via a form factor. The mass and the heat capacity were lumped in each center point of the finite volumes. Furthermore, the state variables were only defined in these finite volume center points and the material properties were taken corresponding to these center point state variables. The resulting heat flows between the center points depended on the thermal conductivity of the corresponding materials, the temperature gradient and the finite volume surface areas. However, one has to keep in mind, that by only taking the thermal conductivity within the phase change material into account, a certain modeling error is made, as the convective heat transfer between the liquid and the solid phase is neglected.

In order to take the latent heat of fusion and solidification into account, Stückle [148] described the transfer of latent heat by introducing a specific heat capacity for melting and freezing, considering a temperature difference of 1 Kelvin (see Equation 4.12). The PCM was treated as a solid in solid state as well as in liquid state, neglecting the convective heat transfer mechanism.

$$C_{p\,melt} = \frac{h_{melt}}{\Delta T_{melt}} \tag{4.12}$$

Figure 4.13 shows a PCM storage section while charging. The heat transfer fluid passes through the PCM storage unit and transfers the carried heat through the fluid duct walls either directly to the PCM or indirectly via graphite fins. Hence, the PCM closest to the heat transfer fluid ducts and the graphite fins melts first, developing a characteristically shaped melting front.

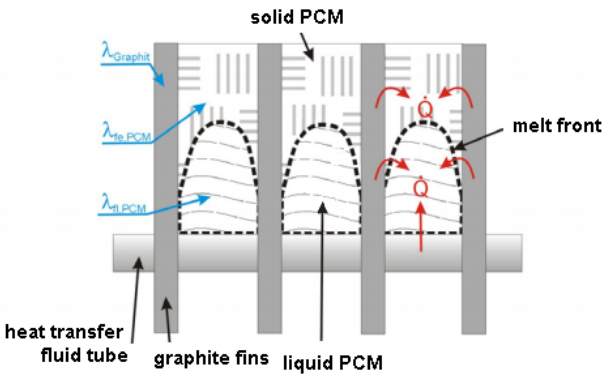

Figure 4.13: PCM storage charging heat transfer from steel tube and graphite fins [94]

Morisson et al. [149] also proposed a model for heat transfer and fluid flow within a PCM storage unit for direct steam generation. The governing equations were numerically solved. Starting from a detailed model, reasonable and justified assumptions for simplifications were introduced, resulting in a simplified model that provided fast and sufficient accurate solutions. The PCM storage unit analyzed consisted of a PCM block and the heat transfer fluid (water/steam) was passing through this block in a bundle of parallel tubes. But unlike the previously described setups, no thermal conductivity enhancing graphite or aluminum fins were used. Instead, a special graphite/binary eutectic $KNO_3/NaNO_3$ composite was used. This composite consisted of a porous graphite matrix that had been filled with the eutectic mixture of the nitrate salts. This increased the thermal conductivity to about 4 $\frac{W}{mK}$ and thus significantly improved the storage performance by increasing the charge and discharge rate as well as reducing the necessary overall length of the costly steel tubes.

The numerical model was based on Fourier's law in cylindrical coordinates, assuming a circumferentially uniform temperature distribution. Furthermore, the heat conduction within the heat transfer fluid was neglected and additionally, the heat transfer via convection within the PCM was neglected. Hence, the heat transfer within the PCM was only defined by con-

duction. Neglecting the convective heat transfer inside the PCM composite material was justified due to a strong viscosity of the salt in liquid state and its encapsulation in the graphite matrix [149].

As shown in Figure 4.14, the governing equations were only solved for one single tube, surrounded by the PCM composite. The whole storage unit was then represented by simply multiplying these single tube/PCM units according to the wanted storage capacity. This provided an efficient model that could be easily integrated into a solar thermal power plant model on system level, including the solar field and the power block [149].

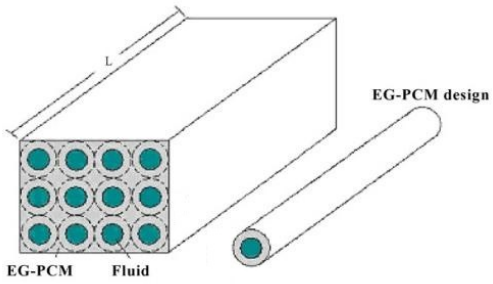

Figure 4.14: Enhanced graphite phase change material storage block model scheme [149]

Furthermore, Hoshi et al. [93] modeled the charging and the discharging characteristics of high melting point PCMs and analyzed them numerically. They proposed the integration of PCM storage modules in compact linear Fresnel receiver plants, although parabolic trough power plants would have been equally suitable. Again, they emphasized the importance of a high thermal conductivity within the PCM module regarding storage system performance. In order to compare the charging and the discharging performance of different PCMs, they assumed a double tube setup where the heat transfer fluid tube was placed concentrically to a surrounding tube having a larger diameter, containing the phase change material. They solved the governing partial differential equation (heat equations in cylindrical coordinates) numerically under the assumption of a negligible volumetric expansion during melting, a negligible heat transfer through convection in the liquid PCM region, and furthermore, constant physical properties.

Figure 4.15 displays the melting front $R_m(t)$ while charging, and the solidification front while discharging. The surrounding tube was assumed to be ideally insulated, hence the partial derivative of the temperature with respect to r at the position $r = r_1$ was set to zero.

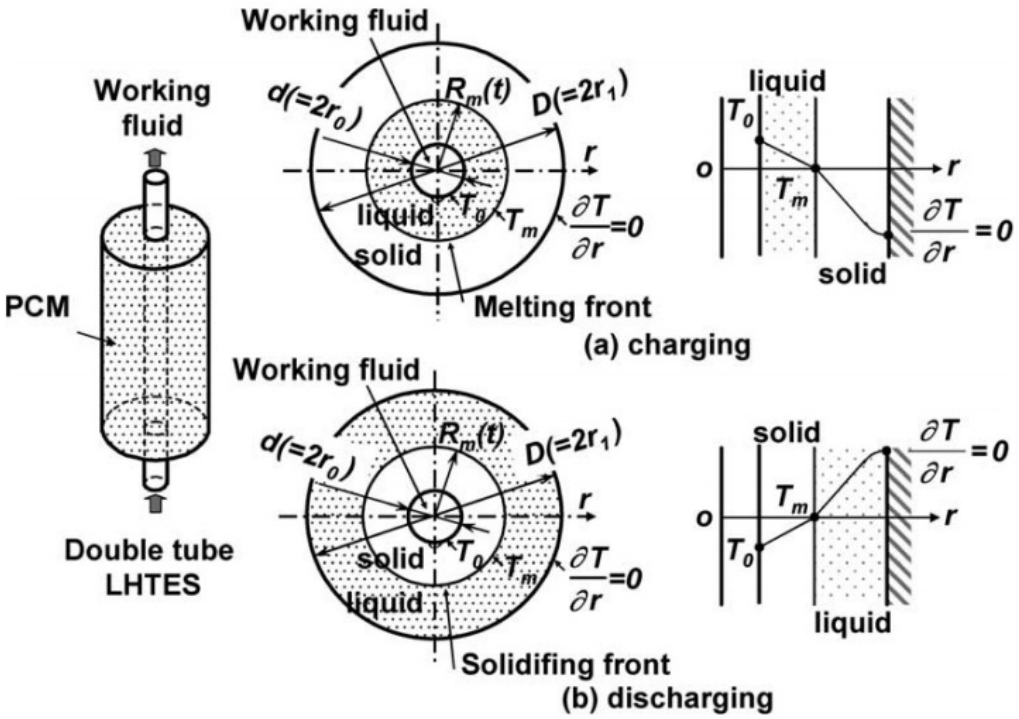

Figure 4.15: Double-tube latent heat thermal energy storage system model [93]

4.8 Thermochemical heat storage modeling

In order to predict the performance of thermochemical heat storage units, a model of the corresponding endothermic and exothermic reactors as well as a model of the relevant ducts, heat exchangers and storage vessels is required. A reactor model has to take simultaneous reaction mechanisms as well as heat and mass transfer mechanisms into account [101].

Kreetz & Lovegrove [101] adapted an already existing model for a steam/ methane reforming reactor in order to simulate the performance of an ammonia synthesis and dissociation reactor. The numerical calculation results heavily depended on semi-empirical correlations for mass and heat transfer parameters. In principle, the results agreed well with the obtained measurement data. Based on these results, it could be concluded that a reliable and effective tool for the performance prediction of similar reactor conditions had been obtained.

Skocypec et al. [150] improved an already existing model for a receiver/ reactor unit (shown in Figure 4.16) regarding the radiative as well as the convective heat transfer, and furthermore regarding catalyst loading and more realistic boundary conditions. The model took into account the incoming solar irradiation, heat losses due to radiation, conduction in the solid phase, heterogeneous chemical reaction, convection between the fluid and the solid phases and the interaction with the quartz reactor window. The resulting equations formed a system of coupled, non-linear, first-order ordinary differential equations. The predicted reactor efficiencies as well as the methane conversion agreed well with test data. However, further code validation was required in order to improve the ability to simulate large-scale reactor operation.

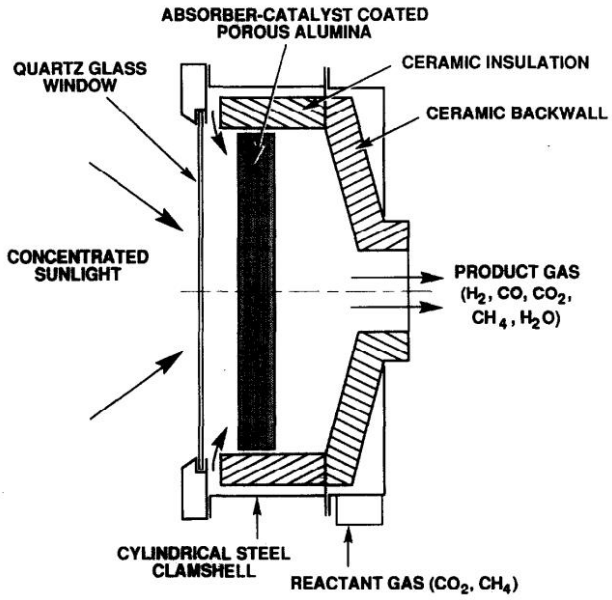

Figure 4.16: Catalytically enhanced solar absorption receiver scheme [150]

Chapter 5

The objectives of this work

The intention of the previous sections has been to give a good overview of the current state-of-the-art of concentrated solar power and its performance modeling, including the important topic of thermal energy storage. Having this in mind, it is now appropriate to formulate the objectives of this work that build upon already gathered knowledge in order to broaden the scientific horizon in the field of the modeling and simulation of solar thermal power plants.

It can be concluded that there is considerable research work left in the area of thermal energy storage. Many of the proposed technologies are in their first stage of development and not yet ready for their application at commercial level. Nevertheless, the molten-salt-based active direct and active indirect two-tank thermal energy storage technology has successfully been introduced at commercial level in the recent years. However, it has to be noted that the modeling and performance evaluation of these two-tank heat storage units has not yet been treated in the literature in sufficient detail. In particular, their transient performance evaluation is still due.

In general, the transient evaluation of thermal energy storage concepts is important since the variation in solar irradiance frequently causes transient operating conditions.

Thus, this work's intention is to extend the current state-of-the-art regarding the modeling of the active direct and the active indirect two-tank molten-salt-based thermal energy storage concept. The aim is to widen the knowledge about their thermal behavior and operational aspects. In particular, the developed models shall enable the evaluation of the storage system's transient behavior.

Specifically, the objectives of this work can be subdivided into two parts, namely (Part II) stating detailed examples and proposals of modeling approaches for the active direct two-tank and the active indirect two-tank con-

cept, and (Part III) implementing these approaches in an advanced transient performance model of a parabolic trough collector power plant on system level, enabling the theoretical analysis under transient operating conditions.

In particular, the main part (Part II) shall develop models for thermal energy storage system components that extend the current state-of-the-art. On the one hand, it shall focus on the modeling and the performance evaluation of oil-to-molten-salt heat exchangers for the active indirect thermal energy storage technology, applying molten salts as storage medium and thermal oil as heat transfer fluid. On the other hand, it shall treat the modeling of molten salt storage tanks for the two-tank concept, specifically focusing on the heat loss to the environment, a crucial factor considering the efficiency of thermal energy storage systems.

Subsequently, Part III shall treat the application of these thermal energy storage models in a solar thermal power plant model on system level.

In order to predict the behavior of solar thermal power plants, and to be able to improve their operation, sophisticated models are necessary. This especially includes start-up and shut-down procedures, which still have room for improvement. The required duration could be shortened, increasing the daily operating time. Also, more efficient emergency procedures are still under research. Although, the first large scale commercial solar thermal power plants started their operation in the 1980's, operating strategies can still be optimized. Since tests at real plants are expensive and in many cases impossible, reliable numerical models are therefore essential.

Thus, with the obtained model, it shall be possible to perform detailed simulations under transient conditions, such as evaluating the performance of a parabolic trough collector solar thermal power plant under strongly varying environmental boundary conditions (mainly regarding the current direct normal irradiance - DNI), or considering start-up and shut-down procedures, as well as giving emphasis to the usage of the thermal energy storage system. Consequently, the model shall enable to improve operation strategies, to establish operating directives, guidelines and emergency procedures. Additionally, the model shall enable the evaluation of the influence of various transient phenomena on the plant's energy yield.

5.1 The outline of this work

This work is organized as follows:

- Part II treats the modeling of the active indirect and the active direct two-tank thermal energy storage system as they are at the moment the

most relevant ones in practical applications, but do, so far, still lack in fully defined modeling recommendations.

Therefore, Chapter 6 of this work discusses the behavior of heat transfer and pressure drop for oil-to-molten-salt heat exchanger configurations for active indirect thermal energy storage systems under varying loads, indicating flow regimes, heat transfer coefficient and pressure drop ranges by using appropriate Nusselt number and pressure drop correlations. Since certain inefficient heat transfer conditions can be avoided by using separate heat exchanger trains in parallel that are switched on or off depending on the current load, two different heat exchanger setups are compared.

Chapter 7 of this work proposes a modeling approach for molten salt storage tanks that extends the current state-of-the-art. It proposes a transient storage tank model that features a degree of physical modeling that is able to provide more accurate results, but is at the same time still suitable for solar thermal power plant performance simulations. Furthermore, the total storage tank heat loss will be subdivided into its single parts, showing which mode of heat transfer contributes most. The model will be run at both currently applied temperature levels, hence at 386 °C and 292 °C (parabolic trough) as well as at 565 °C and 290 °C (power tower applications).

Chapter 8 of this work discusses a numerical shell-and-tube heat exchanger model for the transient performance evaluation of oil-to-molten-salt heat exchangers, as used in active indirect thermal energy storage systems. The model builds upon well proven methodologies (for a detailed literature review, the interested reader is referred to Section 4.2.2 of this work).

Chapter 9 of this work treats the transient behavior of a typical active indirect two-tank thermal energy storage system under varying load and abrupt changes between operating modes, by applying the previously developed models for the storage tank and the oil-to-molten-salt heat exchanger.

- Part III presents the implementation of a comprehensive transient parabolic trough collector power plant model on system level, giving emphasis to the consideration of thermal energy storage. It states typical simulation results, displaying the power plant's behavior under transient operating conditions.

  In particular, Chapter 10 of this work provides a detailed description of a numerical model of a typical parabolic trough collector power plant

using thermal oil as heat transfer fluid and applying the active indirect two-tank thermal energy storage concept. The modeling approach for all components is stated and referenced in detail. The modeling of the thermal energy storage system is based on Chapter 7 and Chapter 8 of this work. Finally, typical simulation results are discussed, showing the applicability of the developed model.

- Part IV summarizes this work's conclusions and gives recommendations for future work.

This page is intentionally left blank.

Part II

Detailed examples and proposals of modeling approaches for the active direct and the active indirect two-tank TES concept

Part two of this work gives detailed examples for the thermal energy storage modeling and proposes new approaches that have not been discussed so far. In particular, it focuses on the active direct and the active indirect two-tank TES concept.

Chapter 6

Part load behavior of oil-to-molten-salt heat exchanger configurations for active indirect thermal energy storage systems in CSP applications

This chapter focuses on the part load behavior of oil-to-molten-salt heat exchanger configurations for active indirect molten salt thermal energy storage systems. More precisely, the performance of a single-train shell-and-tube heat exchanger configuration is compared to the behavior of a parallel-train shell-and-tube heat exchanger setup. For the assumed heat exchanger dimensions and mass flow range, expected heat transfer coefficients, pressure drop ranges as well as duct outlet temperatures are given. Calculation results show that the parallel-train setup exceeds the single-train setup in thermal performance at low mass flow rates and furthermore significantly reduces the nominal load shell-side pressure drop.

6.1 Introduction

In active indirect two-tank thermal energy storage systems, surplus solar energy is stored using molten salts as sensible heat storage medium. Furthermore, as the name already implies, the heat storage system is charged and discharged indirectly via an oil-to-molten-salt heat exchanger. In order

to even fluctuations in incident solar irradiation throughout the day and to collect as much solar energy as possible, the storage unit often operates below design point conditions, which requires good part load behavior of the oil-to-molten-salt heat exchangers. However, depending on the actual charge or discharge rate, low mass flow rates limit the heat transfer in the heat exchanger, resulting in a higher mean temperature difference for a given heat duty.

This section discusses the behavior of heat transfer and pressure drop for oil-to-molten-salt heat exchanger configurations under varying storage system mass flow rates, indicating flow regimes, heat transfer coefficient and pressure drop ranges by using appropriate Nusselt number and pressure drop correlations, respectively. Since certain inefficient heat transfer conditions can be avoided by using separate heat exchanger trains in parallel that are switched on or off depending on the actual load, two different heat exchanger setups are compared. The performance of one single heat exchanger train (see Figure 6.1), the conventional setup, is compared to the behavior of two separate heat exchanger trains in parallel (see Figure 6.2) [151][1]. Note: The red question mark in the aforementioned figures, refers to the chosen heat exchanger setup. Does a parallel-train setup have advantages over the conventional single-train setup?

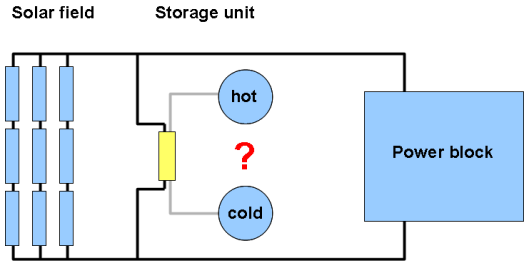

Figure 6.1: The conventional setup: One heat exchanger train

[1]This section is based on a work [151] originally presented at the SolarPACES conference in 2012 (Marrakech, Morocco). However, the boundary conditions for the storage system's discharging mode have been updated to the actually applied procedure. Thus, in discharging mode, the outlet temperature of the heat transfer fluid is controlled to a specified set point, which is determined by the steam generator. As a consequence, the feed temperature of the cold molten salt tank varies according to the thermal characteristic of the heat exchanger train and is not controlled. Hence, the corresponding calculation results, figures and conclusions for discharging mode differ from the originally stated ones.

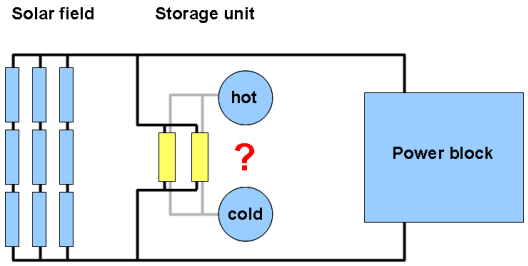

Figure 6.2: Two heat exchanger trains in parallel

6.2 The methodology

The intention of this chapter is to evaluate the part load behavior of two oil-to-molten-salt heat exchanger assemblies, suitable for solar thermal power active indirect storage system applications. This is done in a theoretical way by applying appropriate correlations for shell-and-tube heat exchanger design, shortly summarized in the following.

6.2.1 The heat transfer

The heat exchanger's thermal duty $\dot{Q}$ can be written as follows [110]:

$$\dot{Q} = U \cdot A \cdot \Delta T_m \tag{6.1}$$

where U is the heat exchanger's overall heat transfer coefficient, A is the heat exchanger's heat transfer area, and ΔT_m is the true mean temperature difference, also referred to as TMTD. Whereas the heat transfer area A is a given and fixed design parameter, the remaining factors are variables that depend on the actual storage system operating conditions, hence thermal oil and molten salt mass flow rates, temperature distributions and related fluid properties. In shell-and-tube heat exchangers, the overall heat transfer coefficient U is usually based on the outer tube surface area and is a function of the tube-side convective heat transfer coefficient h_i between the tube-side fluid and the inner tube wall, the tube wall's thermal conductive resistance, and the shell-side convective heat transfer coefficient h_o between the outer tube surface and the shell-side fluid. Neglecting the influence of any fouling resistances, the overall heat transfer coefficient can be defined as follows [152]:

$$U = \frac{1}{\frac{r_o}{h_i \cdot r_i} + \frac{r_o \cdot \ln(\frac{r_o}{r_i})}{k_{tube}} + \frac{1}{h_o}} \tag{6.2}$$

In the above relationship, the thermal resistance of the heat exchanger tubes is a function of the tubes' inner and outer radii (r_i,r_o) and the tube material's thermal conductivity k_{tube}. Its determination is straightforward, and additionally, its influence is usually negligible. However, the accurate determination of the important shell-side and tube-side convective heat transfer coefficients is rather challenging. In this work, appropriate Nusselt number correlations for forced convective flow within circular tubes as well as forced convective flow over tube bundles are used.

The tube-side mean heat transfer coefficient is estimated by using the following Nusselt number correlations, either valid for laminar (Nu_{la}) or turbulent (Nu_{tu}) flow in circular tubes.

Kreith et al. [152] published the following two correlations for laminar flow in circular tubes, valid for both the thermal entrance region as well as for fully developed conditions, where L is the tube length[2] and D is the tube's inner diameter:

$$Nu_{la} = \begin{cases} 1.953 \cdot [\frac{L}{D \cdot Re \cdot Pr}]^{\frac{1}{3}} & \text{for } [\frac{L}{D \cdot Re \cdot Pr}] \leq 0.03 \\ 4.364 + \frac{0.0722 \cdot D \cdot Re \cdot Pr}{L} & \text{for } [\frac{L}{D \cdot Re \cdot Pr}] > 0.03 \end{cases} \tag{6.3}$$

For fully developed turbulent flow in smooth tubes, Cengel [153] published the following Nusselt number correlation, proposed by Gnielinski (valid for $0.5 \leq Pr \leq 2000$ and $3 \cdot 10^3 < Re < 5 \cdot 10^6$):

$$Nu_{tu} = \frac{\frac{f}{8} \cdot (Re - 1000) \cdot Pr}{1 + 12.7 \cdot (\frac{f}{8})^{\frac{1}{2}} \cdot (Pr^{\frac{2}{3}} - 1)} \tag{6.4}$$

where the friction factor f can be obtained via the following equation, known as the first Petukhov equation [153]:

$$f = (0.79 \cdot \ln(Re) - 1.64)^{-2} \tag{6.5}$$

Note: The equations above for turbulent flow can also be used for obtaining rough estimates of the heat transfer coefficient in the transition region for Reynolds numbers between 2300 and 10000, especially when they are closer to 10000 than to 2300 [153].

In this study, the tube-side heat transfer coefficient h_i in the transition region is estimated by linearly interpolating between the heat transfer coefficient for laminar flow h_{la} and the heat transfer coefficient for turbulent flow h_{tu} in between the Reynolds numbers 2300 and 8000.

The shell-side heat transfer coefficient h_o is estimated according to Gnielinski [154] who provided Nusselt number correlations for tube bundles under

[2]For large values of L ($\rightarrow \infty$) the Nusselt number is simply obtained as 4.364.

cross flow, which are based on numerous measured values, valid for Reynolds numbers between 1 and 10^6, and Prandtl numbers between 0.7 and 700. Non-ideal cross flow over the tube bundle is considered via the Bell-Delaware method [110, 155].

Assuming pure counter-flow arrangement, the true mean temperature difference ΔT_m is estimated via the logarithmic mean temperature difference ΔT_{lm} [110], where ΔT_1 and ΔT_2 are the temperature differences between the thermal oil and the molten salt at the heat exchanger ends:

$$\Delta T_{lm} = \frac{\Delta T_1 - \Delta T_2}{\ln(\frac{\Delta T_1}{\Delta T_2})} \tag{6.6}$$

6.2.2 The pressure drop

The shell-side pressure drop is determined by dividing the shell-side flow volume in defined sections (entrance sections, cross-flow sections and window sections) and applying appropriate correlations for each of them as proposed by Gaddis & Gnielinski [156]. The pressure drop on the tube side is calculated via the well known correlation $\Delta p = \zeta \cdot \rho / 2 \cdot v^2$, providing appropriate pressure drop factor values for straight tube sections, tube bends, inlet and outlet nozzles as well as tube bundle tube sheet entrance and outlet sections [155, 157].

6.2.3 The fluid properties

The storage medium under consideration, the molten salt, is a mixture of 60% $NaNO_3$ and 40% KNO_3 (weight percent). The solar field heat transfer fluid (thermal oil) is a mixture of diphenyl ($C_{12}H_{10}$) and diphenyl oxide ($C_{12}H_{10}O$). Both fluids are modeled as incompressible fluids at liquid state and equation based fluid properties according to [158] and [11]. The fluid properties are evaluated at the arithmetic means between the heat exchanger duct inlet and outlet temperatures.

6.2.4 The heat exchanger setups under consideration

The first heat exchanger setup, the reference setup, is one single heat exchanger train (see Figure 6.3) having three shell-and-tube subunits connected in series, as shown in [108]. The thermal oil is pumped through the heat exchanger tube-side due to its relatively high vapor pressure (approximately 10 bar at the nominal solar field outlet temperature of 391 °C). The molten salt

is placed on the shell-side. Each shell-and-tube subunit is considered having two shell-side passes with a longitudinal baffle and two tube-side passes in U-tube design. Hence, the heat exchanger exhibits, in principle, pure counter-flow arrangement, when assuming a shell-side flow without baffles. The dimensions of each shell-and-tube subunit are assumed as follows: The inner shell diameter is set to 2 m, the mean total tube length contributing to the heat transfer area is set to 20 m, the tubes' outer and inner diameter is set to 19.05 mm and 15 mm, respectively. Furthermore, a staggered 45° square tube bundle arrangement is assumed and the tube pitch is set to 28.6 mm. This yields according to Shah & Sekulic [110] an estimated total number of tubes of about 3794 per subunit, which results in a total area of heat transfer of 13623.65 m^2 for the whole heat exchanger train. Finally, a vertical baffle cut of 40 cm is assumed. The baffle center spacing is set to 1 m, the baffle inlet and outlet spacing is set to 0.8 m.

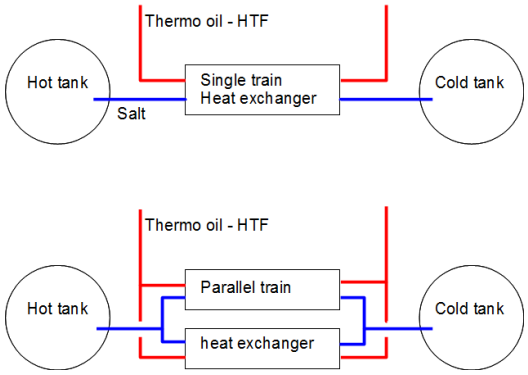

Figure 6.3: Upper scheme: Single train heat exchanger setup - Lower scheme: Parallel train heat exchanger setup

The second heat exchanger system under consideration features the same basic shell-and-tube subunit design but consists of two separate equally designed heat exchanger trains in parallel (see Figure 6.3), each having 3 subunits in series. Keeping the same total area of heat transfer (13623.65 m^2), hence reducing the number of tubes per subunit to 1897, the dimensions of each shell-and-tube subunit are assumed as follows: The inner shell diameter is set to 1.44 m, the mean total tube length contributing to the heat transfer area is again set to 20 m, the tubes' outer and inner diameter is set to 19.05 mm and 15 mm, respectively, as well. Furthermore, the same tube bundle arrangement is assumed, having a vertical baffle cut of 28 cm, a baffle center spacing of 1 m and a baffle inlet and outlet spacing of 0.8 m.

6.2.5 The temperature boundary conditions and the mass flow ranges

Considering an active indirect storage system as it is currently applied in commercial parabolic trough collector power plants, the thermal oil leaves the solar field at approximately 391 °C and is then pumped to the steam generator, or, in storage system charging mode, the hot thermal oil is pumped to the oil-to-molten-salt heat exchanger. There, the molten salt coming from the cold tank, approximately at 292 °C, is heated up to 386 °C, the design temperature level of the hot tank. Hence, for the storage system charging mode, three temperature boundary conditions are already given, i.e. the inlet temperature of the hot oil (391 °C), the inlet temperature of the salt (approximately 292 °C) and the outlet temperature of the salt (controlled to 386 °C). The remaining free variable is either the oil's outlet temperature or one of the two fluid mass flow rates. However, since the oil mass flow rate, pumped to the storage system, is set by the plant's operator, and the molten salt mass flow rate is adjusted by the control loop of the molten salt outlet temperature (which is controlled to 386 °C), the oil's outlet temperature (solar field return temperature) is the only free variable, which is, however, determined by the heat exchanger's thermal characteristic. Thus, in this study, the heat transfer fluid mass flow rate is set and the corresponding molten salt mass flow rate and the oil's outlet temperature (solar field return temperature) is calculated for steady-state operation.

For storage system discharging mode, three temperature boundary conditions are given as well. The oil's inlet temperature is defined by the steam generator's outlet temperature, which is assumed to be fixed at 285 °C. The salt's inlet temperature is given by the current inventory temperature of the hot storage tank (approximately 386 °C). Furthermore, the outlet temperature of the oil, the heat transfer fluid, is defined by the steam generator's inlet temperature and is usually controlled to a certain set point via adjusting the molten salt mass flow rate between the hot and the cold tank. In this work, this HTF outlet temperature set point is assumed to be 376 °C. Since the oil mass flow rate is again determined by the power plant's operator and the molten salt mass flow rate is adjusted by the control loop of the oil's outlet temperature, the remaining free variable, which is, however, determined by the thermal characteristic of the heat exchanger train, is the outlet temperature of the salt, i.e. the feed temperature of the cold tank. Thus, in this work, the heat transfer fluid mass flow rate is set and the corresponding molten salt mass flow rate and the salt's outlet temperature (the feed temperature of the cold tank) is calculated for steady-state operation.

The design charging and discharging heat transfer fluid mass flow rate is

assumed to be 600 $\frac{kg}{s}$. In order to investigate the part load behavior of the heat exchanger configurations mentioned above, the total storage system heat transfer fluid mass flow rate has been continuously varied from the design mass flow rate of 600 $\frac{kg}{s}$ down to 10 $\frac{kg}{s}$, for storage system charging as well as for storage system discharging mode.

6.2.6 The equation system solving

Applying the above described methodology for estimating the steady-state heat exchanger performance results in a non-linear system of equations that is typically solved numerically using a non-linear solver algorithm. For this study, the steady-state heat exchanger model has been programed using the Modelica modeling language. Therefore, the resulting system of equations has been solved using a state-of-the-art commercial Modelica tool, applying its standard algebraic system solver. It should be noted that a steady-state model of a heat exchanger is actually not the conventional application of Modelica that is primarily intended for the dynamic modeling and simulation. However, when thinking of system level models and the simulation of e.g. whole parabolic trough collector power plants, some components, whose dynamics are negligible for the specific simulation under consideration, may be modeled in steady state.

6.3 Calculation results

In this section, the steady-state performance of a single-train storage system heat exchanger configuration will be compared to a parallel-train storage system heat exchanger configuration (see Figure 6.3). The molten salt mass flow rates, overall heat transfer coefficients, heat transfer fluid outlet temperatures as well as heat exchanger duct pressure drops will be plotted over the total storage system heat transfer fluid mass flow rate. This will conveniently display the heat exchangers' part load behavior and will allow the fitting of much simpler models that are suitable for long-term solar thermal power plant yield simulations.

6.3.1 The single-train setup

Figure 6.4 shows the molten salt mass flow rate plotted versus the heat transfer fluid mass flow rate. For the assumed boundary conditions, the molten salt mass flow is always higher due to its lower specific heat capacity. Figure 6.5 displays the characteristic velocity for each heat exchanger duct

versus the heat transfer fluid mass flow rate. The tube-side characteristic velocity is simply obtained by dividing the total mass flow by the number of tubes, the mean fluid density and furthermore the tubes' inner cross sectional area. The shell-side characteristic velocity is the mean velocity of the fluid in the empty spaces between the tubes in a single tube row, which is obtained by dividing the free stream velocity (assuming a tube free inner shell cross section) by a void fraction factor, a function of the tubes' outer diameter and the tube pitch [154].

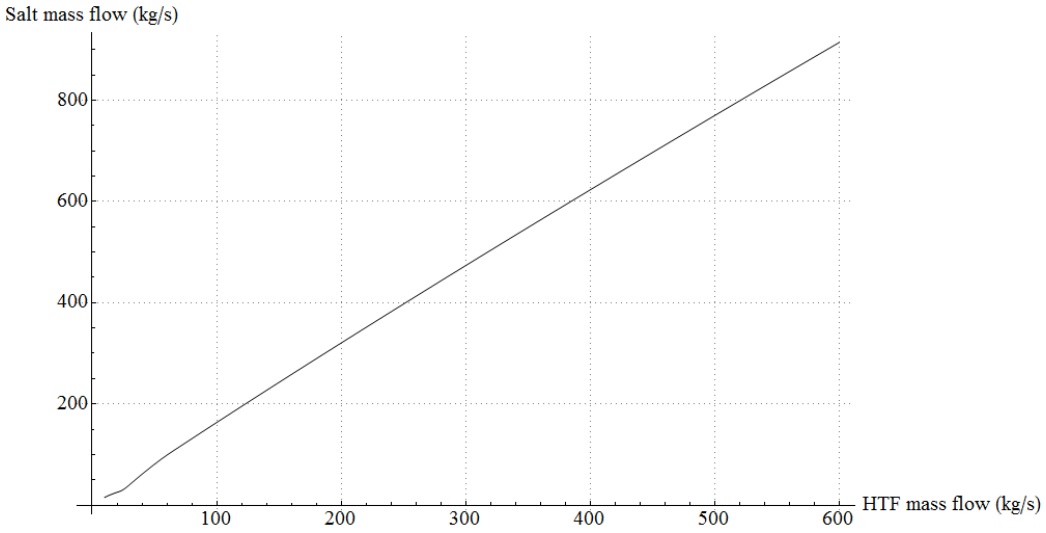

Figure 6.4: Molten salt mass flow rate versus oil mass flow rate (charging mode)

The corresponding heat exchanger duct Reynolds numbers are shown in Figure 6.6. The characteristic length on the tube-side is the tubes' inner diameter. On the shell-side, the characteristic length is set to the half of the tubes' outer perimeter, according to [154]. The laminar to turbulent transition region of the tube-side flow in between the Reynolds numbers of 2300 and 10000 is indicated by the two horizontal black dashed lines. According to the chosen heat exchanger dimensions, the tube-side flow stays in the fully turbulent regime for heat transfer fluid mass flow rates above 80 $\frac{kg}{s}$, whereas the shell-side flow reaches the transition region at a heat transfer fluid mass flow rate of about 360 $\frac{kg}{s}$ (according to [155], flow over tube bundles is laminar for Reynolds < 100 and turbulent for Reynolds $>$ 10000).

Figure 6.8 displays the heat exchanger duct heat transfer coefficients as well as the corresponding overall heat transfer coefficient U. It can be

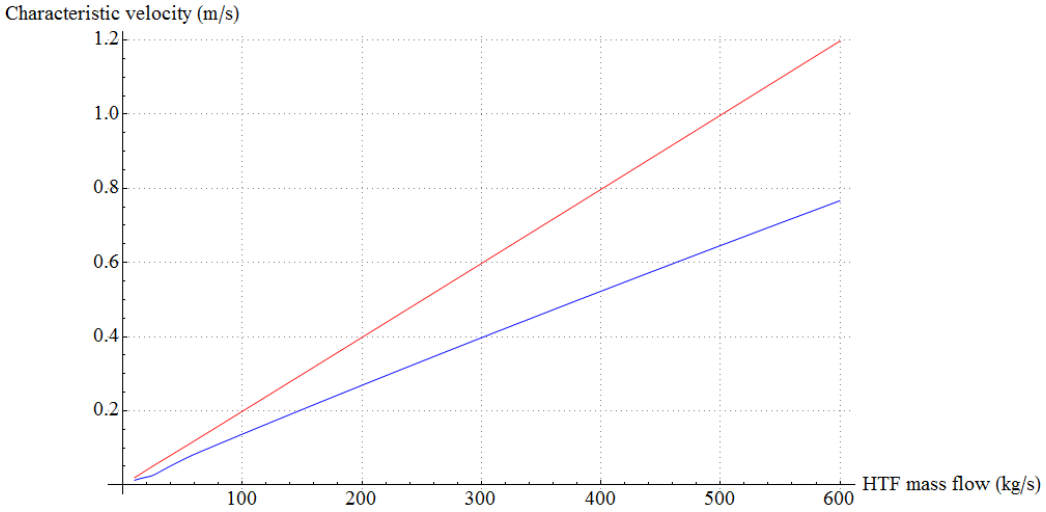

Figure 6.5: Characteristic flow velocities versus oil mass flow rate (charging mode); tube-side (thermal oil): red; shell-side (molten salt): blue

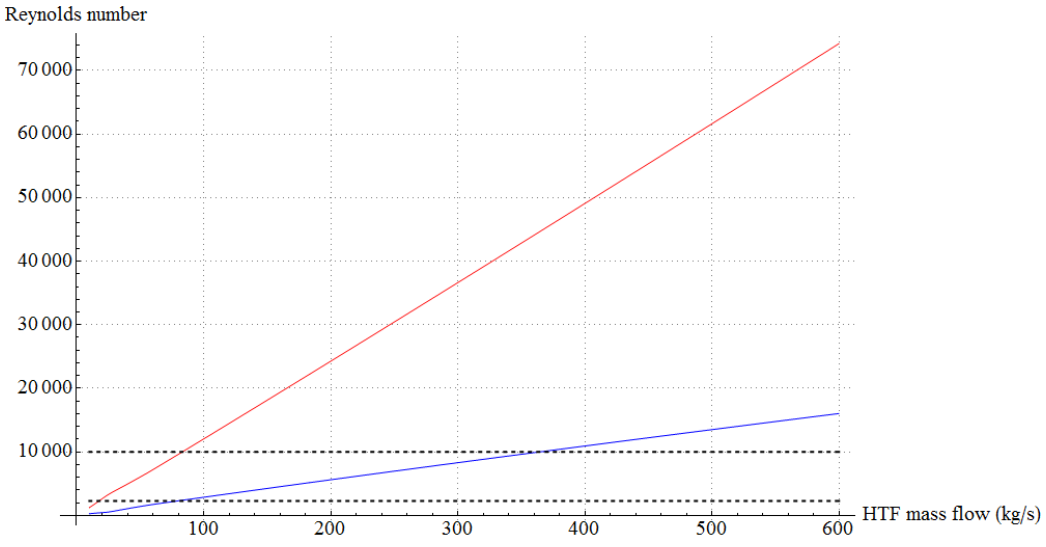

Figure 6.6: Heat exchanger duct Reynolds numbers versus oil mass flow rate (charging mode); tube-side (thermal oil): red; shell-side (molten salt): blue

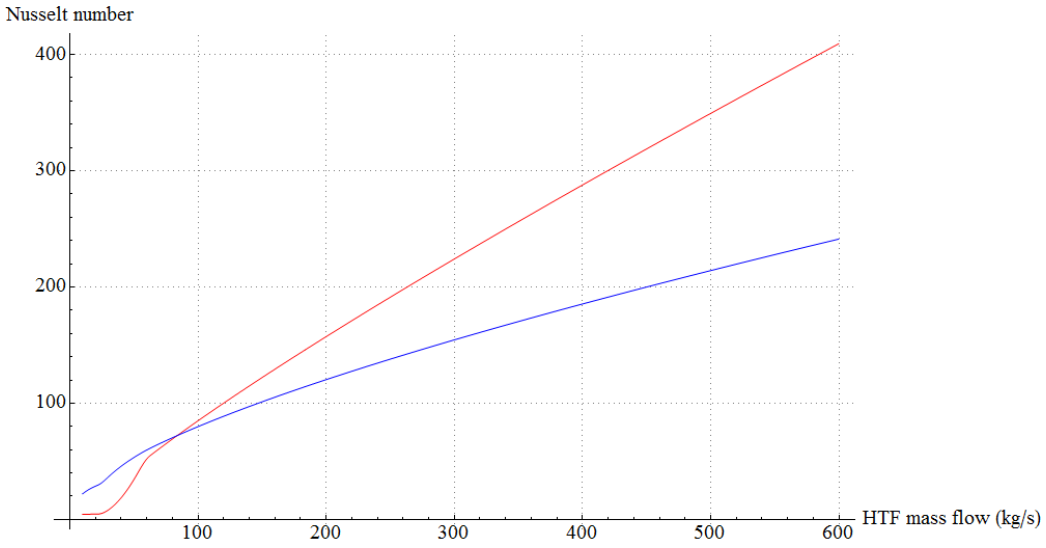

Figure 6.7: Heat exchanger duct Nusselt numbers versus oil mass flow rate (charging mode); tube-side (thermal oil): red; shell-side (molten salt): blue

observed that the tube-side heat transfer coefficient considerably decreases when reaching the laminar flow regime (see also Figure 6.7 for the corresponding Nusselt numbers). At the maximum heat transfer fluid mass flow rate of 600 $\frac{kg}{s}$ the tube-side heat transfer coefficient reaches approximately values around 2350 $\frac{W}{m^2K}$, whereas at the lower bound mass flow rate of 10 $\frac{kg}{s}$ it is reduced to approximately 26 $\frac{W}{m^2K}$. The shell-side heat transfer coefficient basically shows the same behavior but at a higher level. It reaches a maximum of about 4090 $\frac{W}{m^2K}$, and a minimum of about 375 $\frac{W}{m^2K}$. The corresponding overall heat transfer coefficient ranges between 1116 $\frac{W}{m^2K}$ and 19 $\frac{W}{m^2K}$.

Figure 6.9 shows the heat exchanger duct inlet and outlet temperatures in charging mode. According to the chosen boundary conditions, the thermal oil's inlet as well as the molten salt's inlet and outlet temperature is constant. The thermal oil's outlet temperature varies however due to the change in mass flow rate and overall heat transfer coefficient. According to Figure 6.9, the mean temperature difference decreases until a heat transfer fluid mass flow rate of about 60 $\frac{kg}{s}$ is reached (coming from nominal conditions). This can be explained by a relatively stronger decrease in heat duty (which is determined by the mass flow rate) than in overall heat transfer coefficient. Then, by reaching heat transfer fluid mass flow rates below that "critical" value of 60 $\frac{kg}{s}$, the mean temperature difference strongly increases until about 23 $\frac{kg}{s}$ where it reaches a maximum. Below a heat transfer fluid mass flow

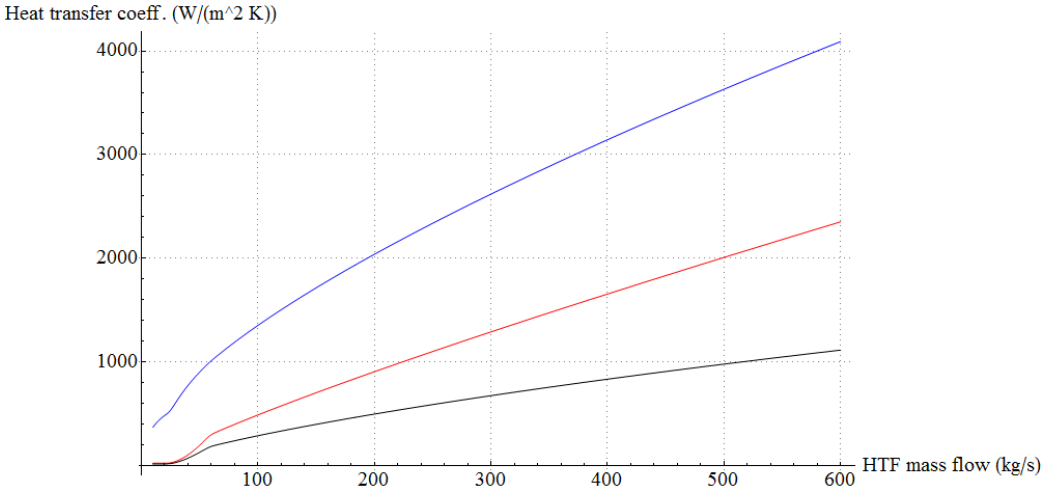

Figure 6.8: Heat exchanger duct heat transfer coefficients versus oil mass flow rate (charging mode); tube-side (thermal oil): red; shell-side (molten salt): blue; overall heat transfer coefficient U: black

rate of about 23 $\frac{kg}{s}$ the mean temperature difference decreases again. This sudden increase, the establishment of a maximum and the following decrease in mean temperature difference can be explained by the fact that by reaching the transition region between laminar and turbulent flow on the tube-side, the overall heat transfer coefficient suddenly shows a stronger decrease than the heat duty until at about 23 $\frac{kg}{s}$ of thermal oil mass flow rate, where the tube-side heat transfer coefficient approaches its minimum and consequently remains almost constant at laminar flow conditions. It has to be noted that the exact location and shape of the steep increase and the exact location of the establishment of the maximum in temperature difference, strongly depends on the chosen interpolation range for the tube-side heat transfer coefficient. Hence, in reality, a slight divergence from these calculation results may be observed.

Figure 6.10 shows the heat exchanger duct inlet and outlet temperatures in storage system discharging mode. Here, the same mean temperature difference to mass flow rate relationship can be seen. However, in this case, the free variable, which follows the thermal characteristic of the heat exchanger train, is the molten salt's outlet temperature, the feed temperature of the cold tank. It can be observed that the feed temperature of the cold tank considerably increases at lower storage system discharging mass flow rates, which consequently leads to an unwanted increase in temperature of the cold tank's inventory during longer discharging operation at low partial loads. A higher temperature of the cold tank leads to an increase of the heat transfer

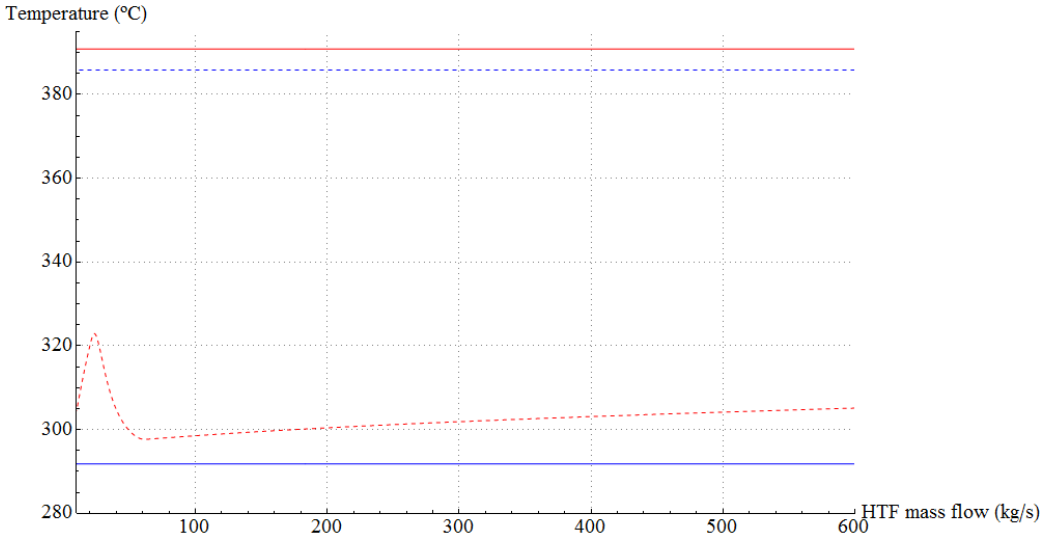

Figure 6.9: Heat exchanger duct inlet (continuous line) and outlet (dashed line) temperatures versus oil mass flow rate (charging mode); tube-side (thermal oil): red; shell-side (molten salt): blue

fluid's outlet temperature in charging mode, and thus reduces the possible charging rate due to a smaller temperature drop of the oil.

Figure 6.11 shows the heat exchanger duct pressure drops versus heat transfer fluid mass flow rate in charging mode. It can be observed that the pressure drop is considerably higher for the molten salt on the shell-side. The relatively strongly disturbed flow through a decent number of tube row cross flow sections as well as window sections increases not only the shell-side heat transfer coefficient, but also increases the caused pressure drop. As always in heat exchanger design, there exists a trade-off between good heat transfer and acceptable pumping power.

6.3.2 The parallel-train setup

As shown in the previous section, the assumed single-train heat exchanger setup reaches its heat transfer limits at low storage system mass flow rates, where the tube-side flow approaches the laminar regime. A parallel-train heat exchanger setup can improve the thermal performance at low storage system mass flow rates, since one train can be switched off, which results in a higher overall heat transfer coefficient for the same total storage system mass flow rate. However, it has to be kept in mind that also the area of heat transfer is reduced to the half of its value for the chosen setup if one

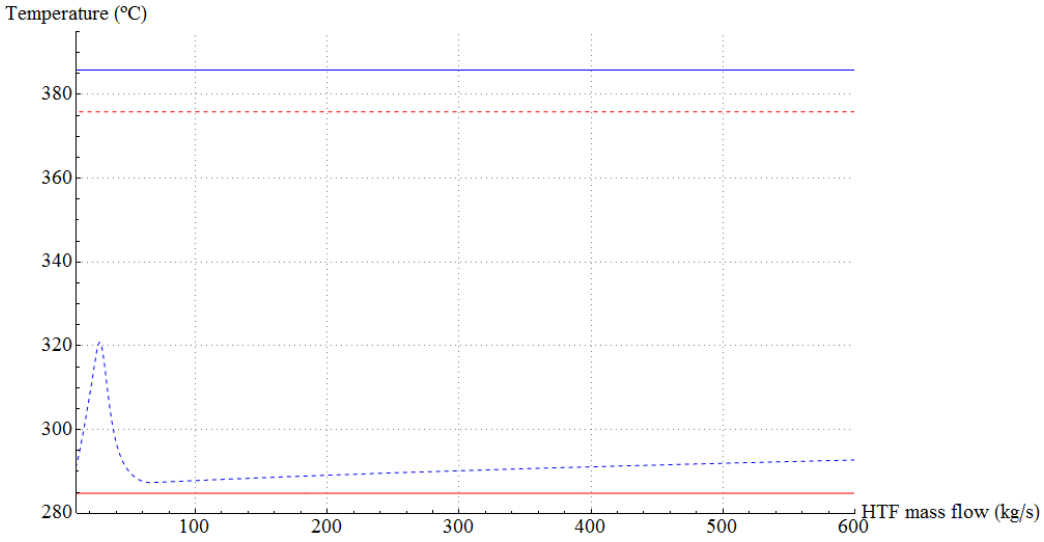

Figure 6.10: Heat exchanger duct inlet (continuous line) and outlet (dashed line) temperatures versus oil mass flow rate (discharging mode); tube-side (thermal oil): red; shell-side (molten salt): blue

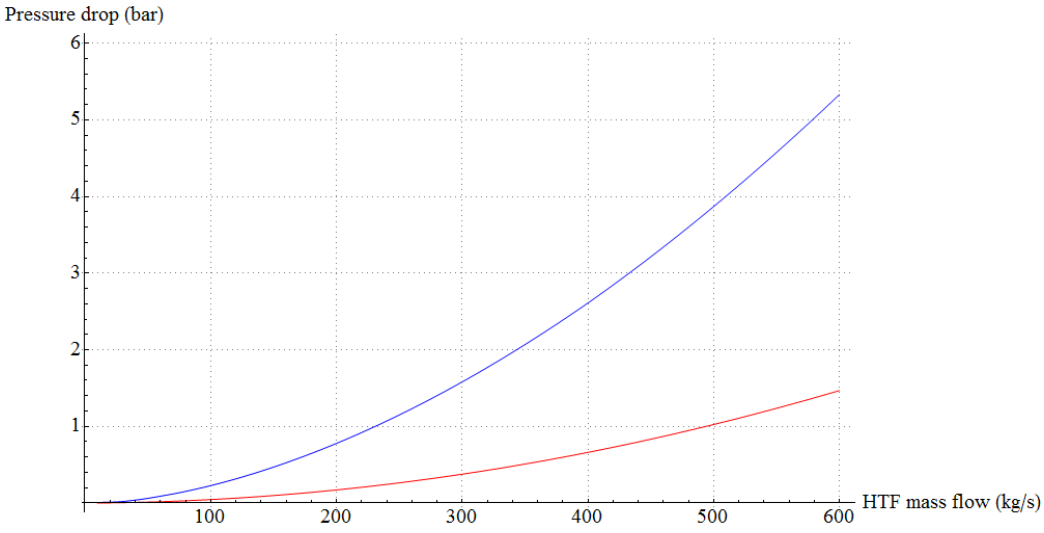

Figure 6.11: Heat exchanger duct pressure drops versus oil mass flow rate (charging mode); tube-side (thermal oil): red; shell-side (molten salt): blue

train is put offline. But this disadvantage is more than compensated by a considerably improved overall heat transfer coefficient. In order to evaluate the performance of a parallel-train heat exchanger setup having two equally designed parallel trains, the calculation results will be shown for the case where both trains are online, hence each of them receives half of the total storage system mass flow rate, and for the case where one train is put offline, hence one of the parallel trains receives the full storage system mass flow rate. In this way, it can be easily detected at which point one of the parallel trains has to be switched off, in order to improve the thermal performance at low mass flow rates.

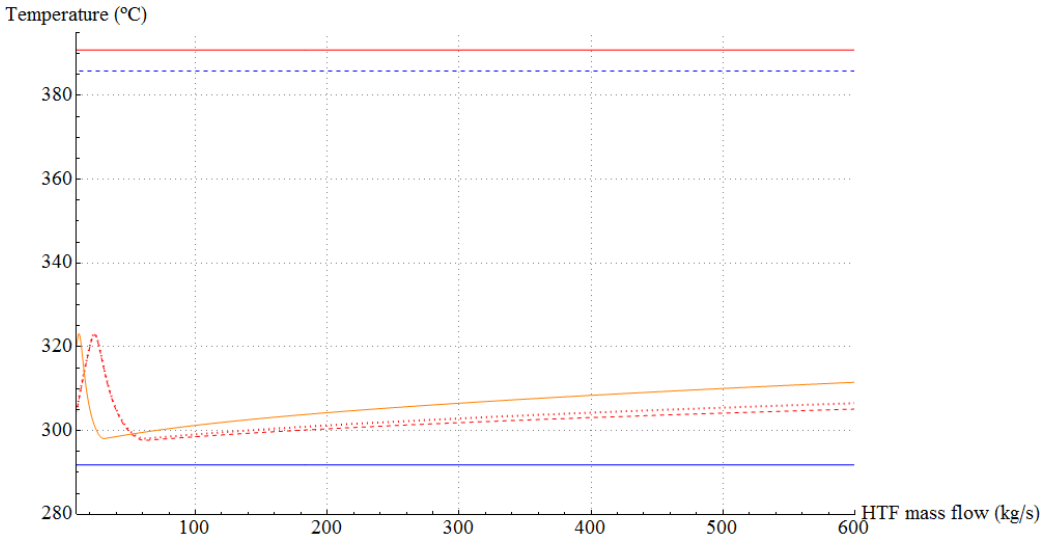

Figure 6.12: Heat exchanger duct inlet and outlet temperatures versus oil mass flow rate (charging mode); shell-side (molten salt): blue (inlet continuous, outlet dashed); tube-side (thermal oil) inlet: red continuous; tube-side outlet single train: red dashed; tube-side outlet parallel train both online: red dotted; tube-side outlet parallel train one offline: orange continuous

Figure 6.12 shows the heat exchanger duct inlet and outlet temperatures versus the thermal oil mass flow rate for the standard single-train setup as well as for the parallel-train setup for charging mode. The thermal behavior of the configurations under consideration can be well observed. In Figure 6.12, the tube-side outlet temperature of the standard single-train setup is displayed as red dashed line. The red dotted line represents the tube-side outlet temperature of the parallel-train heat exchanger setup, having both trains online. It can be observed that the resulting thermal performance of the parallel-train setup (red dotted line) is a little worse than that of the stan-

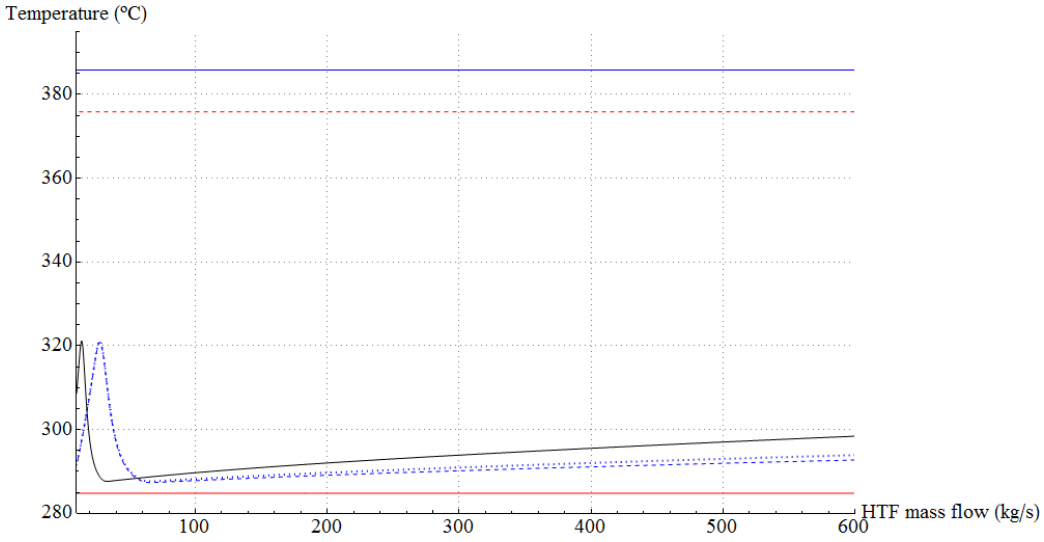

Figure 6.13: Heat exchanger duct inlet and outlet temperatures versus oil mass flow rate (discharging mode); tube-side (thermal oil): red (inlet continuous, outlet dashed); shell-side (molten salt) inlet: blue continuous; shell-side outlet single train: blue dashed; shell-side outlet parallel train both online: blue dotted; shell-side outlet parallel train one offline: black continuous

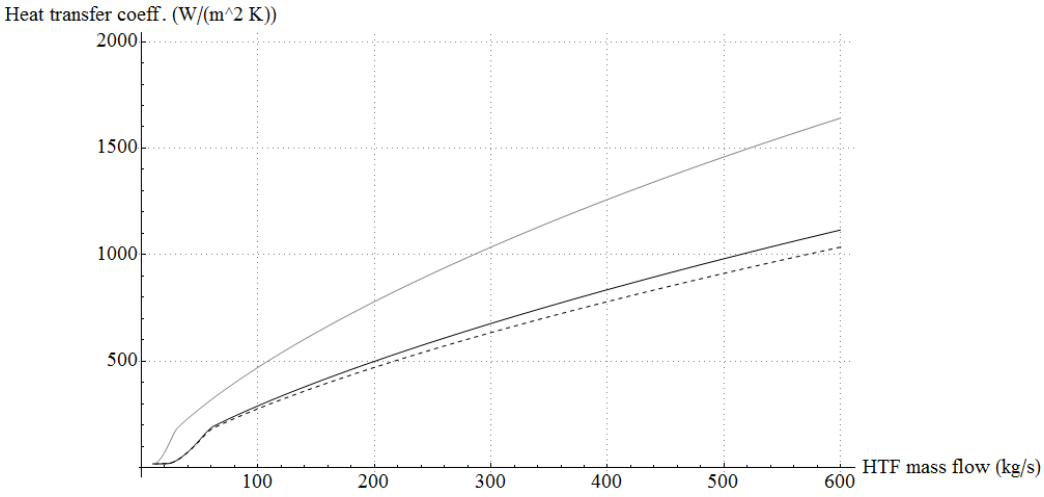

Figure 6.14: Heat exchanger setup overall heat transfer coefficients versus oil mass flow rate (charging mode); single-train setup: black continuous line; parallel-train setup both online: black dashed line; parallel-train setup one offline: gray continuous line

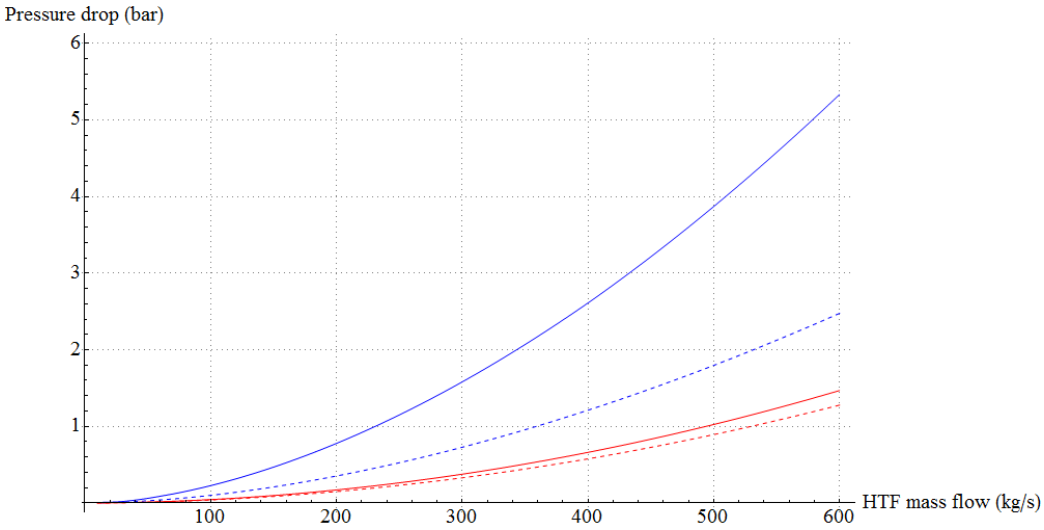

Figure 6.15: Heat exchanger duct pressure drops versus oil mass flow rate (charging mode); tube-side (thermal oil): red; shell-side (molten salt): blue; single-train setup: continuous lines; parallel-train setup both online: dashed lines

dard single-train setup at high mass flow rates (see also Figure 6.14). This is due to a lower shell-side heat transfer coefficient due to lower characteristic flow velocities. The orange continuous line represents the tube-side outlet temperature of the parallel-train setup, having one train offline. Here, the influence of the missing area of heat transfer can be observed at high mass flow rates. Although the reduced cross sectional flow areas lead to higher flow velocities and thus higher heat transfer coefficients, the reduction in total heat transfer area is not compensated at all at high mass flow rates. Additionally, a considerable increase in pressure drop makes this option of having the second parallel train always offline unacceptable. However, the opposite and also intended effect can be observed at low mass flow rates. As can be seen in Figure 6.12, the continuous orange line intersects the red dashed and dotted line at a heat transfer fluid mass flow rate of about 50 $\frac{kg}{s}$. Below this mass flow rate the parallel-train setup, where one heat exchanger train is switched off, exceeds the single-train setup in thermal performance. The pressure drop is a little higher, which, however, does not influence the overall performance significantly negative at such low mass flow rates.

Figure 6.13 displays the corresponding calculation results for discharging mode. The blue dashed line represents the shell-side (molten salt) outlet temperature of the standard single-train setup. The blue dotted line represents the shell-side outlet temperature of the parallel-train heat exchanger setup,

having both trains online. Again, the thermal performance of the parallel-train heat exchanger setup, having both trains online, is a little worse than that of the single-train setup, due to lower shell-side convective heat transfer coefficients. The black continuous line represents the shell-side outlet temperature of the parallel-train setup, having one train offline. At about 55 $\frac{kg}{s}$ the black solid line intersects the blue dashed and dotted lines, indicating the operating points where the parallel-train heat exchanger setup, having one train switched off, exceeds the other two configurations in thermal performance.

Figure 6.15 shows the heat exchanger duct pressure drops for the single-train setup and for the parallel-train setup having both trains online. It can be seen that the parallel-train setup reduces the shell-side pressure drop to half of the value estimated for the single-train setup. This is due to a reduced number of cross flow resistances as well as a lower characteristic flow velocity. Also the tube-side pressure drop is a little lower than that of the single-train setup. This is mainly due to relatively larger chosen nozzle diameters. The pressure drop induced in the straight tube sections is the same since the mass flow rate per tube stays the same.

6.4 Conclusions and outlook

Chapter 6 evaluates the part load performance of two heat exchanger configurations for the active indirect molten salt thermal energy storage concept. General overall heat transfer coefficient as well as pressure drop ranges are given. Calculation results show that the heat exchange becomes inefficient under low partial charging as well as low partial discharging loads, due to too low convective heat transfer coefficients. Hence, e.g., at partial charging loads where the thermal oil enters the heat exchanger at the nominal solar field outlet temperature but at a low mass flow rate, the full oil-side temperature drop cannot be reached due to a too low overall heat transfer coefficient that results in a higher mean temperature difference ΔT_m. Correspondingly, the same applies for storage system discharging mode at low mass flow rates, where higher molten salt outlet temperatures increase the inventory temperature of the cold molten salt tank, which e.g. reduces the achieved oil-side temperature drop during charging operation, and thus, reduces the heat transfer rate. By using two separate heat exchanger trains in parallel, one train can be switched off, providing acceptable heat transfer conditions within a wider range of storage system mass flow rates. Furthermore, a parallel-train heat exchanger setup reduces the nominal load shell-side pressure drop significantly.

This kind of study could especially be relevant for proposed high capacity solar thermal power plants, e.g., exceeding 100 MWe, where the two-tank concept is scaled up to a multiple of two-tank subunits. There, a combination of differently sized and centrally controlled heat exchanger trains could provide excellent thermal performance over a very wide range of mass flow rates, exceeding the performance of two-tank subunits having definitely assigned and equally sized heat exchanger configurations.

Chapter 7

Transient molten salt storage tank modeling for the two-tank thermal energy storage concept

This chapter focuses on the transient heat loss modeling of molten salt thermal energy storage tanks. More precisely, this chapter proposes a degree of physical modeling which describes the governing heat transfer mechanisms sufficiently accurate, obtaining a suitable tool for concentrating solar power (CSP) performance simulations, applicable for parabolic trough collector, as well as for central receiver plants. A fully transient storage tank model has been developed and simulated over 3 sets of 6 reference days, providing typical weather conditions of a solar thermal power plant location as model input. The model has been successfully compared to heat loss data that was observed at real application molten salt storage tanks. Several modeling assumptions, used heat transfer correlations and simplifications are outlined. Modelica [127] has been used as modeling language.

7.1 Introduction

This chapter is focused on the transient modeling of molten salt storage tanks. More precisely, it proposes levels of modeling detail which are suitable for solar thermal power plant performance simulations but still feature a reasonable physical detail. It shows which heat transfer mechanisms are important to be considered and identifies those which can be neglected by only introducing minor calculation errors. Accurate heat loss information is required to estimate the thermal energy storage efficiency, as well as the auxiliary heater power, in order to avoid freezing [80]. For a detailed literature

review, the interested reader is referred to Section 4.2.3 of this work.

The thermal evaluation of a high-temperature molten salt storage tank exposed to altering ambient conditions is a complex transient heat transfer problem. The molten salt inventory temperature depends not only on the heat loss to the environment, but also on the molten salt feed temperature as well as on the tank gas atmosphere temperature above the molten salt. At parabolic trough collector power plants, where nitrogen is used as inert gas for the thermal-oil circuit, the gas atmosphere of the tank usually consists of nitrogen at ambient pressure, whereas at power-tower applications, where nitrogen is not needed, the tank atmosphere consists of air at ambient pressure. In both cases, while charging or discharging, the gas is exchanged between the hot and the cold tank.

Of course, each of the influencing factors have different, and in some cases negligible levels of impact. It is the intention of this chapter to identify the most influencing mechanisms of heat transport that have to be considered, in order to obtain an efficient but still accurate and flexible storage tank simulation tool, suitable for CSP performance modeling.

This chapter is entirely based on a previously published work [132] of the author.

7.2 The methodology and the modeling approach

As stated in Section 4.2.3, the molten salt inventory can be modeled as ideally mixed, having one representative fluid temperature T_{salt}. By using this single-representative-temperature approach for the molten salt inventory volume, it seems to be self-evident to apply this approach to the gas atmosphere above the molten salt level as well. Also here, a characteristic natural convection velocity profile is to be expected that is slightly disturbed by the gas stream entering the tank volume, due to variations in molten salt level height. The gas temperature increases in regions close above the molten salt surface, hence its density decreases, which results in an upward fluid motion, while giving space for relatively cool gas that comes from the tank walls. For this study it is assumed that this heat loss induced velocity profile also provides good mixing of the gas atmosphere, ensuring a homogeneous temperature distribution. These assumptions lead to the basic model structure shown in Figure 7.1. In the following, the most detailed model features and boundary conditions will be explained. These are then considered as this study's reference model features. The calculation results of this reference setup represent

then the benchmark for the following more and more simplified models, indicating the introduced calculation error. The model simplification will be continued until mayor non-negligible errors are introduced, compared to the reference setup.

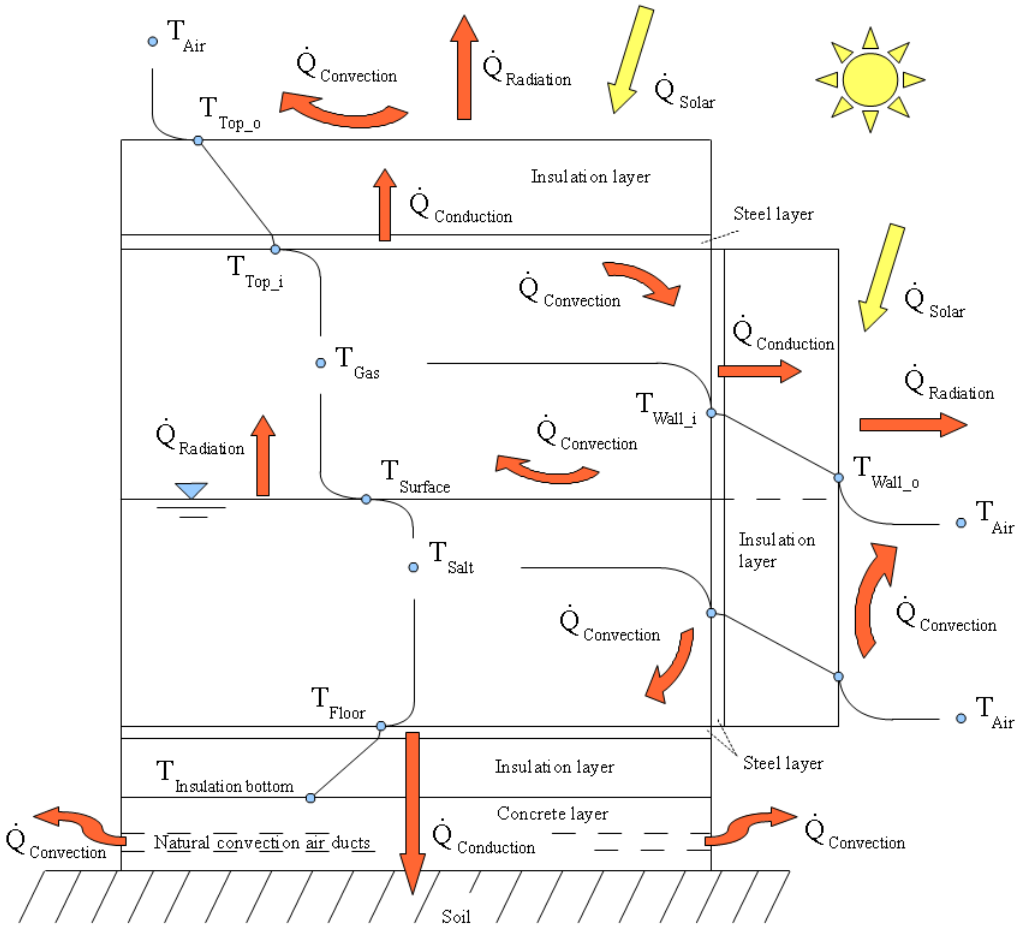

Figure 7.1: Molten salt storage tank model scheme – Temperature distributions and heat flows [132]

7.2.1 The storage tank design, materials and their properties

One of the most important steps in the modeling process is to correctly define the thermal properties of the storage tank materials. Especially the thermal conductivity of the insulation material is the governing factor for the

storage tank heat loss. In this study, the used insulation materials are mineral wool, foam glass and calcium silicate board. Since the thermal conductivity depends on the operating temperature, the relationship between temperature and thermal conductivity has to be known and implemented in the simulation code. In the following, each construction material used will be stated.

The typical tank base structure is a cylindrical steel container having a wall thickness of about 4 cm, as found in open literature [139]. This value has been chosen for all storage tank simulations. According to Pacheco et al. [81], 304 stainless steel was used at the Solar Two project for the hot tank. This type of steel has a chrome and nickel content of about 18-20% (Cr) and 8-12% (Ni). Peet et al. [159] provided thermal conductivity data as function of operating temperature for this kind of steel. A typical thermal conductivity value at 500 °C amounts to about 21 $\frac{W}{mK}$. The hot tank and the cold tank walls are assumed to be insulated with a layer of mineral wool. This insulation layer thickness was set to 30 cm for the cold tank and to 40 cm for the hot tank. These two insulation layer thicknesses were proposed by Schulte-Fischedick et al. [139], and are based on an optimization analysis of investment costs and revenues. Ochs & Müller-Steinhagen [160] proposed the following linear relationship between the operating temperature T in Kelvin and the insulation material thermal conductivity k in $\frac{W}{mK}$:

$$k = k_0 + k_1 \cdot (T - 273.15) \tag{7.1}$$

Typical values for the two parameters k_0 and k_1 for mineral wool would be 0.037 $\frac{W}{mK}$ and 2e-4 $\frac{W}{mK^2}$, respectively, according to [160]. These values are used hereafter. To complete the storage tank wall design, the mineral wool insulation layer is assumed to be followed by a thin protective layer of sheet metal (e.g. zinc/aluminium or galvanized steel). This outer protective layer is not explicitly modeled, as its thermal inertia and contribution to the thermal resistance is considered to be negligible. However, its optical properties contribute to the heat transfer via radiation and are considered in this work. Its solar absorptivity and long wave emissivity will be stated in Section 7.2.7.

The construction of the storage tank's roof is assumed to consist of an inner steel layer of 6 mm thickness (self-supporting dome, according to [161]), and an insulation layer of calcium silicate board, as proposed by Kelly et al. [161], again covered by a thin protective sheet metal layer. The insulation thickness is set to the same values used for the walls. Ebert & Hemberger [162] compared thermal conductivity measurements for calcium silicate insulation material and published the following polynomial relationship between

the thermal conductivity k in $\frac{W}{mK}$ and the operating temperature T in Kelvin:

$$k = 0.0674 + 4 \cdot 10^{-5} \cdot T + 6 \cdot 10^{-8} \cdot T^2 + 9 \cdot 10^{-12} \cdot T^3 \tag{7.2}$$

In this work, the relationship from above is used for estimating the roof insulation material's thermal conductivity.

The floor construction of the storage tank is assumed to be a steel layer like the walls and the roof. Its thickness is set to 4 cm as proposed by [139]. This steel layer is followed by a foam glass insulation layer of 30 cm and 40 cm thickness for the cold and the hot tank, respectively. Ochs & Müller-Steinhagen [160] also provided thermal conductivity values for foam glass insulation material. In this study, the same linear thermal conductivity correlation as for the mineral wool wall insulation is used (Equation 7.1). According to [160], the two linear correlation parameters k_0 and k_1 for foam glass are 0.043 $\frac{W}{mK}$ and 1.3e-4 $\frac{W}{mK^2}$, respectively. In order to complete the storage tank bottom construction design, the foam glass insulation layer is assumed to be followed by an air cooled concrete foundation, which is however not explicitly modeled in this work. The assumed model bottom end boundary condition will be outlined in Section 7.2.8.

Furthermore, the two remaining material properties, density and specific heat capacity, are set to 160 $\frac{kg}{m^3}$ and 840 $\frac{J}{kgK}$ for mineral wool, 255 $\frac{kg}{m^3}$ and 1000 $\frac{J}{kgK}$ for calcium silicate board, 150 $\frac{kg}{m^3}$ and 926 $\frac{J}{kgK}$ for foam glass, and 7800 $\frac{kg}{m^3}$ and 490 $\frac{J}{kgK}$ for steel. Additionally required design considerations are the tank dimensions as well as the height of the molten salt pump inlet, which defines the minimum molten salt level height. In this work, the height of the pump inlet is set to 0.7 m. Thus, an empty cold or hot tank has still an absolute molten salt level height of 0.7 m, which defines the remaining molten salt mass during cool-down simulations. The diameter and height of the inner storage tank steel container is set to 38.5 m and 14 m, respectively. The maximum absolute molten salt level height is set to 13 m.

7.2.2 The fluid control volumes and the general mass and energy balance

The Modelica modeling language has been chosen for this study. It is, in principle, open-source and enables developed models to be run under different simulation environments. Furthermore, by dividing the whole storage tank model into model subunits, categorized by the three basic modes of heat transfer, conduction, convection and radiation, many already existing freely available standard model structures and components can be reused,

reducing the necessary programing effort. Additionally, Modelica's object-oriented way of modeling leads to a clear model structure and maximizes the reusability of newly developed code.

As outlined above, the molten salt inventory as well as the gas atmosphere (nitrogen or air) is modeled as ideally mixed. Therefore, the Modelica Standard Library [163] (MSL) component "partial lumped volume" forms the base class of the molten salt model as well as of the tank atmosphere model. This Modelica base class formulates the general energy and mass balance for the corresponding control volume in terms of net mass flow, net enthalpy flow, net heat flow $\dot{Q}_{net}$ and net work flow $\dot{W}_{net}$. This can be written as follows:

$$\frac{dm}{dt} = \dot{m}_{in} - \dot{m}_{out} \tag{7.3}$$

$$U = m \cdot u \tag{7.4}$$

$$\frac{dU}{dt} = \dot{m}_{in} \cdot h_{in} - \dot{m}_{out} \cdot h_{out} + \dot{Q}_{net} + \dot{W}_{net} \tag{7.5}$$

where m is the control volume mass, $\dot{m}_{in}$ and $\dot{m}_{out}$ is the entering and the leaving mass flow, h_{in} is the specific enthalpy entering the control volume, h_{out} is the specific enthalpy leaving the control volume, U is the total internal energy, and u is the specific internal energy of the control volume.

7.2.3 Thermal conduction in the tank jacket

The storage tank walls, the roof and the bottom are modeled as 1-D multilayer conduction models (see Figure 7.1). The roof as well as the bottom are modeled as planar conduction models, consisting of one single element in direction normal to heat conduction. Hence, there is one temperature node available for each layer (i.e. one for the steel layer, and one for the insulation layer). The storage tank wall is modeled as a cylindrical conduction model. But unlike the roof and the bottom conduction model, the wall conduction model is separated into two sections, in direction normal to heat conduction (see dashed black line in Figure 7.1 that extends the gas-liquid level). This is done in order to account for the varying molten salt level height, hence assigning the correct thermal resistance to both, the molten salt control volume as well as the tank atmosphere control volume. Furthermore, this separation results in two characteristic wall temperatures, one for the wetted part, and one for the non-wetted part. Heat conduction in vertical direction is not

considered since only one-dimensional heat conduction equations are applied. These one-dimensional heat conduction equations are formulated in transient mode, by taking the thermal inertia of each layer into account. The thermal capacitance of each layer is assumed to be lumped in the single temperature node.

Finally, convection and radiation sub-models form the interfaces between the molten salt control volume, the tank atmosphere control volume, the tank jacket and the environment, completing the molten salt storage tank model itself as one comprehensive Modelica class. In the following, each of the used convection and radiation sub-models will be explained and their modeling assumptions outlined.

7.2.4 Natural convective heat transfer inside the tank

Neglecting fluid motion induced by the molten salt pump as well as the distribution header, the convective heat transfer between the molten salt inventory and the tank's inner steel surfaces can be described by dimensionless natural convection Nusselt number correlations that are available in published literature. Many correlations can be found for vertical and horizontal flat plates exposed to natural convection. Basically, the corresponding Nusselt (Nu) number is usually a function of the Prandtl (Pr) and the Grashof (Gr) number. Hence, $Nu = f(Pr, Gr)$ where

$$Pr = \frac{\eta \cdot c_p}{k} \tag{7.6}$$

and

$$Gr = \frac{g \cdot \beta \cdot (T_{surface} - T_\infty) \cdot L^3}{\nu^2} \tag{7.7}$$

In this work, the average natural convective heat transfer coefficient between the molten salt and the inner vertical steel wall of the tank is estimated by using the following two correlations for a vertical plate, published by Kreith et al. [152]. The first one is valid for $10 < Gr \cdot Pr < 10^8$ and the second one is valid for the turbulent region for $Gr > 10^9$. The fluid properties have to be evaluated at the arithmetic mean between the surface temperature $T_{surface}$ and the temperature of the undisturbed fluid T_∞:

$$Nu = \frac{h \cdot L}{k} = 0.68 \cdot Pr^{1/2} \cdot \frac{Gr^{1/4}}{(0.952 + Pr)^{1/4}} \tag{7.8}$$

$$Nu = \frac{h \cdot L}{k} = 0.13 \cdot (Gr \cdot Pr)^{1/3} \tag{7.9}$$

In order to get a continuous transition between the above correlations in the transition region a transformation of the following form is applied:

$$h = \varphi \cdot h_{laminar} + (1 - \varphi) \cdot h_{turbulent} \tag{7.10}$$

where φ is an auxiliary transition function $\varphi = f(Gr)$, which returns the value 1 for laminar region Grashof numbers and zero for turbulent region Grashof numbers. For a defined transition region around $Gr \approx 10^9$ the function smoothly varies between 1 and zero, allowing a numerically sound approximation of the heat transfer coefficient. A more detailed derivation of this method can be found in [164].

The average natural convective heat transfer coefficient between the molten salt and the tank steel bottom is approximated by the following correlation for horizontal and relatively cool plates facing upwards ($10^5 < Gr \cdot Pr < 10^{10}$) [152]: Note: The same correlation can be used for relatively hot plates facing downwards.

$$Nu = \frac{h \cdot L}{k} = 0.27 \cdot (Gr \cdot Pr)^{1/4} \tag{7.11}$$

Finally, the molten salt and the tank atmosphere control volume are coupled in the following way: By assuming a very thin plate with negligible mass and negligible thermal resistance between the molten salt and the gas atmosphere, the control volumes are linked via using a natural convection heat transfer correlation for a relatively cool surface facing downwards for the molten salt control volume and a correlation for a relatively hot surface facing upwards for the gas control volume. In both cases the following two Nusselt number correlations can be used, valid for $10^5 < Gr \cdot Pr < 10^7$ (Equation 7.12) and $10^7 < Gr \cdot Pr < 10^{10}$ (Equation 7.13), respectively [152]:

$$Nu = \frac{h \cdot L}{k} = 0.54 \cdot (Gr \cdot Pr)^{1/4} \tag{7.12}$$

$$Nu = \frac{h \cdot L}{k} = 0.15 \cdot (Gr \cdot Pr)^{1/3} \tag{7.13}$$

The resulting temperature of the imaginary thin plate is then assumed to represent the molten salt surface temperature. The correlations mentioned above are correspondingly applied to the remaining interfaces at the tank's inner roof surface (relatively cool plate facing downwards) and the non-wetted part of the tank's inner wall (relatively cool vertical plate).

7.2.5 Radiative heat transfer inside the tank

The second heat transfer mechanism that has to be considered inside the tank is the heat exchange via radiation between the molten salt surface and the non-wetted parts of the tank's inner steel jacket. Since elementary gases (nitrogen) and elementary gas mixtures (dry air) have a symmetrical molecular structure, and neither emit, nor absorb radiation in the temperature ranges under consideration [152], the heat transfer via radiation between the molten salt surface and the non-wetted inner steel surfaces of the tank can be modeled separately, by only considering the corresponding three surfaces, i.e. the molten salt surface, the tank's inner top surface, of circular planar shapes, and the non-wetted inner wall surface, of cylindrical shape.

In this work, the tank's inner steel surfaces are treated as gray surfaces. Furthermore, 18Cr-8Ni stainless steel has been chosen for the tank's inner wall material. In order to correctly estimate the heat transfer via radiation between the molten salt surface and the tank's inner walls, appropriate emissivity values have to be provided as model input. Cao et al. [165] performed emissivity measurements on various steel samples exposed to temperatures of 500 °C and 700 °C. Unlike polished stainless steel surfaces at room temperature, which provide rather low emissivity values e.g. around 0.18 [152], steel surfaces exposed to high temperatures tend to form emissivity increasing oxide layers. Cao et al. [165] concluded that the emissivity under high operating temperatures largely depends on the steel's chrome content, which limits the formation of oxide surface layers. Hence, alloys with lower chrome content and thus lower oxidation resistance tend to have higher emissivity values. Spectral emissivity values of heavily oxidized steel surfaces may reach values of 0.9 and even more. On the other hand, a tested stainless steel alloy sample having 17% chrome and 12% nickel content showed spectral emissivity values of around 0.35 at 500 °C and 0.5 at 700 °C [165]. According to these measurement results, and under the assumption that the spectral emissivity is rather independent of wavelength, the total emissivity value of the here modeled 18Cr-8Ni stainless steel surface was set to 0.35 in all presented simulations.

As molten salts are nearly transparent to infrared radiation [166], in this study, the molten salt surface is treated as quasi black body. Hence, its emissivity is close to one, that is, almost all the incoming radiation is absorbed by the liquid, either at the surface or as it is transparent, in deeper fluid zones. According to this, the molten salt surface emissivity is set to 0.95.

Finally, to fully define the radiation model of the corresponding enclosure of three gray surfaces, their shape-factors F_{j-i} have to be determined. This is done by calculating the shape-factors between the molten salt surface and

the tank's inner top surface, i.e. two parallel disks with a certain distance d between them, and consecutively determining the remaining shape-factors via shape-factor algebra, by obeying the principles of energy conservation [152]. The following correlation published by Kreith et al. [152] is used for determining the shape factors between the molten salt surface and the tank's inner top surface. This correlation represents the general case of two parallel disks of unequal radii and distance d apart with centers on the same normal to their planes:

$$F_{1-2} = \frac{1}{2 \cdot a^2} \cdot \left(d^2 + a^2 + b^2 - \sqrt{(d^2 + a^2 + b^2)^2 - 4 \cdot a^2 \cdot b^2} \right) \tag{7.14}$$

In the correlation above, a represents the radius of the smaller disk and b represents the radius of the larger disk. Of course, in this work, it is the special case of two disks of equal radii, i.e. the tank's inner radius.

7.2.6 Natural, forced and mixed convective heat transfer at the tank's outer surface

Now, having defined all heat transfer interfaces between the fluid control volumes and the tank jacket, the coupling to the environment will be stated in the following. The heat exchange between the tank's outer surface and the ambient happens via convection and radiation. Which of these two parts contributes most, depends on the current wind speed w, on the ambient air temperature T_{air}, and as well, on the current solar irradiance.

The convective part can be furthermore divided into heat transfer via natural convection and forced convection. The ratio between the Grashof number and the square power of the Reynolds number, i.e. $\frac{Gr}{Re^2}$, indicates whether natural or forced convection dominates the convective heat transfer. According to Kreith et al. [152], for a vertical flat plate exposed to natural convection as well as to forced parallel horizontal flow, forced convection dominates for $\frac{Gr}{Re^2} < 0.7$, whereas natural convection dominates for $\frac{Gr}{Re^2} > 10$. For values between 0.7 and 10, heat transfer occurs via mixed convection, where the resulting heat transfer coefficient can be obtained through superposition correlations that even consider flow directions of natural convective and forced convective fluid streams. However, in this study, a detailed consideration of the mixed convection region is left aside. The average convective heat transfer coefficient between the tank's outer surface and the ambient air is approximated by using again the continuous transition function method according to Equation 7.10. Thus, depending on the current Grashof-Reynolds

ratio the effective average heat transfer coefficient is obtained in the following way:

$$h = \varphi \cdot h_{natural} + (1 - \varphi) \cdot h_{forced} \tag{7.15}$$

where the transition function $\varphi = f\left(\frac{Gr}{Re^2}\right)$, and specifically:

$$\varphi = \begin{cases} 0 & \frac{Gr}{Re^2} < 0.7 \\ f\left(\frac{Gr}{Re^2}\right) & 0.7 \leq \frac{Gr}{Re^2} \leq 10 \\ 1 & \frac{Gr}{Re^2} > 10 \end{cases} \tag{7.16}$$

For the vertical outer surface, the natural convective heat transfer coefficient $h_{natural}$ is obtained by using the already mentioned correlations for a vertical wall (Equations 7.8 and 7.9). The average forced convective heat transfer coefficient h_{forced} for the vertical outer surface of the tank is determined by using the following Nusselt number correlation for cross flow over a cylinder, valid for $Re \cdot Pr > 0.2$ [153]:

$$Nu = \frac{h \cdot D}{k} = 0.3 + \frac{0.62 \cdot Re^{1/2} \cdot Pr^{1/3}}{\left(1 + \left(\frac{0.4}{Pr}\right)^{2/3}\right)^{1/4}} \cdot \left(1 + \left(\frac{Re}{282000}\right)^{5/8}\right)^{4/5} \tag{7.17}$$

where $Re = \frac{w \cdot D}{\nu}$. Again, fluid properties have to be evaluated at the arithmetic mean between the outer surface temperature and the free-stream, i.e. the ambient air temperature.

For the roof's outer surface, the average natural convective heat transfer coefficient $h_{natural}$ is obtained by applying the already mentioned Nusselt number correlations for relatively hot surfaces facing upwards (Equations 7.12 and 7.13). The average forced convective heat transfer coefficient h_{forced} for the roof's outer surface is approximated by using the following correlations for a horizontal plate exposed to forced parallel fluid flow, valid for $Re < 5{\cdot}10^5$ (Equation 7.18) and $0.6 \leq Pr \leq 60$ and $5 \cdot 10^5 \leq Re \leq 10^7$ (Equation 7.19) [153]:

$$Nu = \frac{h \cdot L}{k} = 0.664 \cdot Re^{1/2} \cdot Pr^{1/3} \tag{7.18}$$

$$Nu = \frac{h \cdot L}{k} = 0.037 \cdot Re^{0.8} \cdot Pr^{1/3} \tag{7.19}$$

7.2.7 Radiative heat transfer at the tank's outer surface

Besides the convective heat transfer, as explained in the previous section, also the heat transfer via radiation is taken into account, in this work. The tank's weather protection layer is assumed to consist of zinc/aluminium or galvanized steel sheet metal. At typical solar thermal power plant sites, this outer protective layer is exposed to high global solar irradiation, and thus, high fluctuations in temperature, almost every day. During times of high incident solar irradiation, the temperature of the tank's outer surface may reach more than 100 °C, of course depending on the current wind speed and the ambient air temperature. Hence, the absorbed solar irradiation as well as the emitted long wave radiation to the ambient influences the heat flow through the storage tank wall and the roof.

The global solar irradiation incident on the tank's roof is considered via the following equation:

$$\dot{Q}_{solar\,roof} = (DNI \cdot \cos(\Theta_{zenith}) + I_{diffuse\,horizontal}) \cdot \alpha_{surface} \cdot A_{roof} \quad (7.20)$$

The global solar irradiation incident on the outer wall is considered according to Liu & Jordan [167], assuming a uniform distribution of the diffuse radiation over the sky dome, and furthermore assuming an average ground reflectance ρ_{ground} of 0.2:

$$\begin{aligned} \dot{Q}_{solar\,wall} = (&DNI \cdot \sin(\Theta_{zenith}) \cdot A_{projection\,wall} \\ &+ I_{diffuse\,horizontal} \cdot \frac{1}{2} \cdot (1 + \cos\frac{\pi}{2}) \cdot A_{wall} \\ &+ I_{global\,horizontal} \cdot \rho_{ground} \cdot \frac{1}{2} \cdot (1 - \cos\frac{\pi}{2}) \cdot A_{wall}) \cdot \alpha_{surface} \end{aligned} \quad (7.21)$$

The long wave radiation heat exchange with the ambient is taken into account via Equations 7.22 and 7.23, considering the ambient as black body. At the roof's outer surface, the corresponding black body temperature is set to the current sky temperature T_{sky}, which is calculated according to Berdahl & Fromberg [168] and Buck [169] for clear skies, providing additional relative humidity measurements as model input. At the remaining vertical outer wall surface, the black body boundary temperature is set to the ambient air temperature T_{air}.

$$\dot{Q}_{radiation\,roof} = A_{roof} \cdot \sigma \cdot \epsilon_{surface} \cdot \left(T^4_{surface} - T^4_{sky}\right) \quad (7.22)$$

$$\dot{Q}_{radiation\,wall} = A_{wall} \cdot \sigma \cdot \epsilon_{surface} \cdot \left(T^4_{surface} - T^4_{air}\right) \tag{7.23}$$

Suehrcke et al. [170] provided good data for solar absorptivity and thermal emissivity values for various building roof materials. According to their published data, the outer surface material (weathered galvanized flat sheet metal) solar absorptivity and thermal emissivity is set to 0.66 and 0.3, respectively.

7.2.8 The boundary condition at the concrete foundation

As outlined in Section 7.2.3, the storage tank bottom construction is modeled as a one-dimensional planar multilayer conduction model, consisting of one steel layer, and one foam glass insulation layer. The following concrete foundation layer is not modeled explicitly. Since the compressive strength of concrete considerably decreases at high operating temperatures [171], built-in ducts enable natural convective air cooling at currently applied commercial plants. Hence, the total bottom heat loss of the tank can be subdivided into two main fractions, the heat loss via conduction from the concrete foundation into the soil, and the heat loss via natural convection from the concrete foundation to the ambient air (see Figure 7.1). However, an explicit modeling of the heat transfer to the ground and to the ambient air is left aside. In this work, the natural convective air cooling of the concrete foundation is assumed to be designed to keep the concrete foundation at a maximum temperature of about 90 °C. Thus, the bottom end insulation layer temperatures of both, the hot and the cold tank, are set to this value, applying a simple constant temperature boundary condition at the bottom end of the model.

Thus, this work's storage tank model can be graphically summarized as displayed in Figure 7.2.

7.2.9 The media properties

As already stated before, in this work, the proposed modeling concepts have been implemented using the Modelica language. Therefore, concerning the implementation of the medium properties it is kept to the MSL's modeling approach as well. Within the MSL, all specific media property functions are decoupled from the library components by defining a replaceable "medium package" in each of them. Basically, all fluid property function names and interfaces are declared within a base class called "partial medium". In order

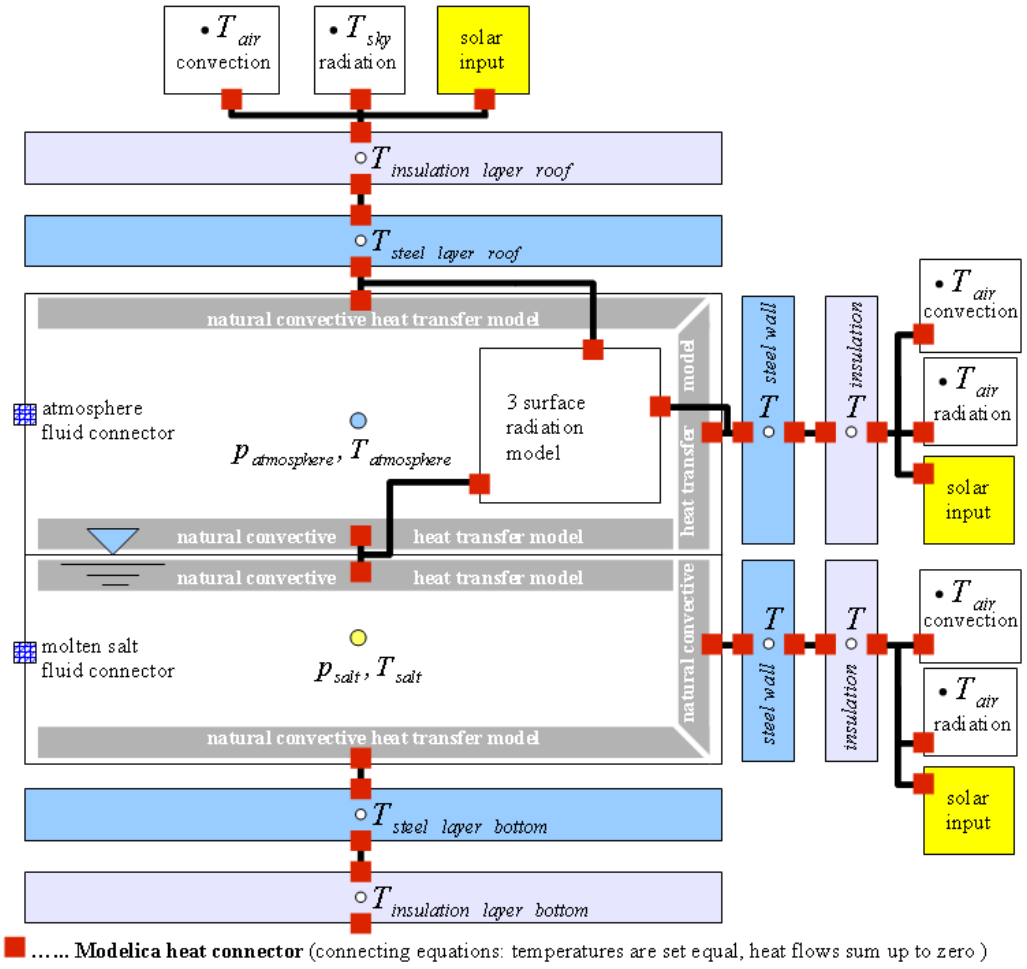

Figure 7.2: Molten salt storage tank model scheme - Model structure in Modelica

to allow for a full replaceability, each specific medium model extends from this "partial medium" base class and defines the specific medium behavior by re-declaring each necessary medium property function. Thus, every single component of the library which encompasses the modeling of fluid properties is not limited to a single medium. In fact, it can easily be adapted for the use of different fluids, by simply replacing the default medium package when instantiating the final model.

Since the media properties for solar salt are not yet available in open Modelica libraries, these features have been newly implemented. The solar salt is modeled as incompressible fluid at liquid state, using equation based fluid property data according to Zavoico [158] and Ferri et al. [172].

The two media for the tank atmosphere, either air or pure nitrogen, have been modeled according to the ideal gas law. Like in the Modelica Standard Library, the specific enthalpy and internal energy are calculated according to McBride et al. [173]. They provided polynomial based specific heat capacity data for a great variety of gases and for wide temperature ranges. Thus, by simply replacing the coefficients of the polynomials, the same code can be reused for many different kinds of gases. However, the transport properties, thermal conductivity and dynamic viscosity, had to be implemented additionally. This has been done according to Kadoya et al. [174], for the air model. They provided function based viscosity and thermal conductivity data for dry air in the gaseous phase for temperatures from 85 to 2000 Kelvin, and pressures up to 100 MPa. For the nitrogen model, function based viscosity and thermal conductivity data published by Stephan & Krauss [175] is used. Their data is valid for temperatures from 70 to 1100 Kelvin and pressures up to 100 MPa, as well [132].

In order to allow for efficient simulation code generation, inverse and derivative functions have been implemented as well. According to the Modelica Language Specification [176] each function definition can be accompanied by corresponding derivative and inverse functions. These additional function definitions enable a more efficient simulation code generation and thus may improve the simulation speed. Considering the implementation of the solar salt property functions the following example can be given to demonstrate the application of an additional derivative and inverse function. Equation 7.24 states the relationship between the density and the temperature of the solar salt [172]:

$$\rho_{salt} = 2263.723 - 0.636 \cdot T_{salt} \tag{7.24}$$

The corresponding Modelica function which returns the solar salt's den-

sity as function of its temperature would look like this:

```
function Density_t
    input Temperature temp "Fluid temperature (K)";
    output Density rho "Fluid density (kg/m3)";
 protected
    constant Real Density_c0 = 2263.723;
    constant Real Density_c1 = - 0.636;

 algorithm
    rho := Density_c0 + Density_c1 * temp;

    annotation(derivative = Density_dert,
               inverse(temp = Temperature_rho(rho)));
end Density_t;
```

As can be seen in the code above, an "annotation" is used to tell the model compiler that a derivative as well as an inverse function is available that can be used in the simulation code. In both cases the definition of the additionally required functions is straightforward. The inverse function is obtained by simply rearranging Equation 7.24 in order to solve for the temperature, i.e.:

$$T_{salt} = 3559.313 - 1.572 \cdot \rho_{salt} \tag{7.25}$$

Thus, the inverse function definition can be written as follows:

```
function Temperature_rho "Inverse of function Density_t"
    input Density rho "Fluid density (kg/m3)";
    output Temperature temp "Fluid temperature (K)";
 protected
    constant Real Temp_c0 = 3559.313;
    constant Real Temp_c1 = - 1.572;
 algorithm
    temp := Temp_c0 + Temp_c1*rho;

    annotation(derivative = Temperature_derrho,
               inverse(rho = Density_t(temp)));
end Temperature_rho;
```

The derivative function of "Density_t" is obtained in the following way by keeping to the information given in the Modelica Language Specification [176] on page 145. For each real-type function input variable a corresponding time derivative variable (also real-type) has to be added. The derivative function output is the time derivative of the original output variable, i.e. in this case the time derivative of the density of the solar salt. This can be written as follows:

```
function Density_dert "Derivative function of Density_t"
    input Temperature temp "Fluid temperature (K)";
    input Real der_temp "Fluid temperature time derivative (K/s)";
    output Real der_rho "Density time derivative (kg/(m3*s))";
 protected
    constant Real Density_c1 = -0.636;
 algorithm
    der_rho := Density_c1*der_temp;
end Density_dert;
```

Mathematically, this derivative function definition can be explained via the application of the so called "chain rule". In calculus, the chain rule is a method for computing the derivative of the composition of two or more functions. Hence, for the given example where the solar salt's temperature is a function g of time ($T_{salt} = g(t)$) and its density is a function of that temperature[1] and thus is a function f of time as well, i.e. $\rho_{salt} = f(T_{salt} = g(t))$, the chain rule has to be applied. Thus, the time derivative of the density is defined as follows:

$$\frac{d\rho_{salt}}{dt} = \frac{d\rho_{salt}}{dT_{salt}} \cdot \frac{dT_{salt}}{dt} \tag{7.26}$$

where according to Equation[2] 7.24 $\frac{d\rho_{salt}}{dT_{salt}} = -0.636$ and $\frac{dT_{salt}}{dt}$ is the additional derivative function input "der_temp" that is defined by the corresponding Modelica model compiler (simulation code generator), since this

[1] For compressible fluids, where the density is a function of temperature T and pressure p, the density's derivative function would have 4 input variables, namely (1) the temperature, (2) the pressure, (3) the temperature time derivative and (4) the pressure time derivative. In this case, the "chain rule" for functions of 2 independent variables has to be applied for calculating the density's time derivative, i.e. $\frac{d\rho}{dt} = \frac{\partial\rho}{\partial T} \cdot \frac{dT}{dt} + \frac{\partial\rho}{\partial p} \cdot \frac{dp}{dt}$ [177].

[2] For this special case, the definition of the derivative functions is rather straightforward. However, for more complicated relationships, where the computing of the derivative by hand is error-prone and a tedious job, it is recommended to use corresponding software packages as Mathematica or Maple.

additional input variable will be available only during the numerical integration.

The following example gives an idea how these derivative functions can be used in the simulation code. Let's consider a simple dynamic mass balance of a certain ideally mixed control volume of constant size having its temperature T as state variable[3]. The dynamic mass balance of that control volume can be written as follows:

$$m = V \cdot \rho \tag{7.27}$$

$$\frac{dm}{dt} = \dot{m}_{in} - \dot{m}_{out} \tag{7.28}$$

The corresponding lines of Modelica code would look like this:

```
fluidMass = fluidVolume * density;

der(fluidMass) = massFlowIn - massFlowOut;
```

During simulation code generation, Equations 7.27 and 7.28 would be expanded into the following form:

$$\frac{dm}{dt} = \frac{dV}{dt} \cdot \rho + V \cdot \frac{d\rho}{dt} = \dot{m}_{in} - \dot{m}_{out} \tag{7.29}$$

Since the size of the control volume is constant, the term $\frac{dV}{dt}$ equals zero, and Equation 7.29 is reduced to:

$$\frac{dm}{dt} = V \cdot \frac{d\rho}{dt} = \dot{m}_{in} - \dot{m}_{out} \tag{7.30}$$

Considering now the numerical integration of the resulting differential algebraic equation system (DAE-system) of the control volume model, it would be appropriate to substitute the term $\frac{d\rho}{dt}$ in Equation 7.30 by a relationship that only depended on the fluid temperature T, i.e. the state variable of the system. In this example, the Modelica compiler would use the density time derivative function "Density_dert" (see Modelica code section above), transforming Equation 7.30 into the following form:

[3]Assuming an incompressible fluid, its density does not depend on the current pressure, i.e. the termodynamic state vector that would normally be defined by the current fluid pressure and the fluid temperature is reduced to just one variable, i.e. the temperature only.

$$\frac{dm}{dt} = V \cdot \texttt{Density\_dert}(T, \frac{dT}{dt}) = \dot{m}_{in} - \dot{m}_{out} \tag{7.31}$$

Thus, for a given mass flow rate $\dot{m}_{in}$ entering the control volume, a certain fluid temperature T as well as a certain time derivative of that temperature ($\frac{dT}{dt}$) at a discrete point in time, the mass flow rate $\dot{m}_{out}$ leaving the control volume could be calculated directly by evaluating Equation 7.31 [4].

7.3 The environmental boundary conditions for the performed simulations

The above explained reference model, and the subsequently more and more simplified storage tank models have been simulated using BSRN (Baseline Surface Radiation Network) data for Desert Rock, Nevada, USA, as model input. Three different sets of 6 reference days have been chosen. Reference day set I and II provide data for summer. Reference day set III provides data for winter. The used simulation input data covers ambient air temperature, ambient pressure, relative humidity, wind speed, global horizontal solar irradiance, diffuse horizontal solar irradiance, and direct normal solar irradiance at time steps of 3 minutes. Values in between are continuously interpolated. Figures 7.3 to 7.7 show the solar irradiance data, the ambient air temperature as well as the wind speed for the 3 sets of 6 reference days.

The developed Modelica models have been simulated using a state-of-the-art commercial tool, applying its standard differential-algebraic system solver called DASSL [178, 179] (see also Section 8.2.7).

7.4 Comparison of reference model results with real application heat loss data

To evaluate the reference model described in Sections 7.2.1 to 7.2.9, the simulated heat loss values have been compared to data published by Relloso &

[4] If the DAE-system solver DASSL [178] was selected before simulating the model, the simulation code would apply an implicit method for the numerical integration of the governing ordinary differential equations. In particular, this algorithm approximates the derivatives using a k^{th} order backward differentiation formula, where k ranges from one to five. At every step it chooses the order and the step size based on the behavior of the solution. Newton's method is used to solve the resulting equations for the solutions at each discrete point in time.

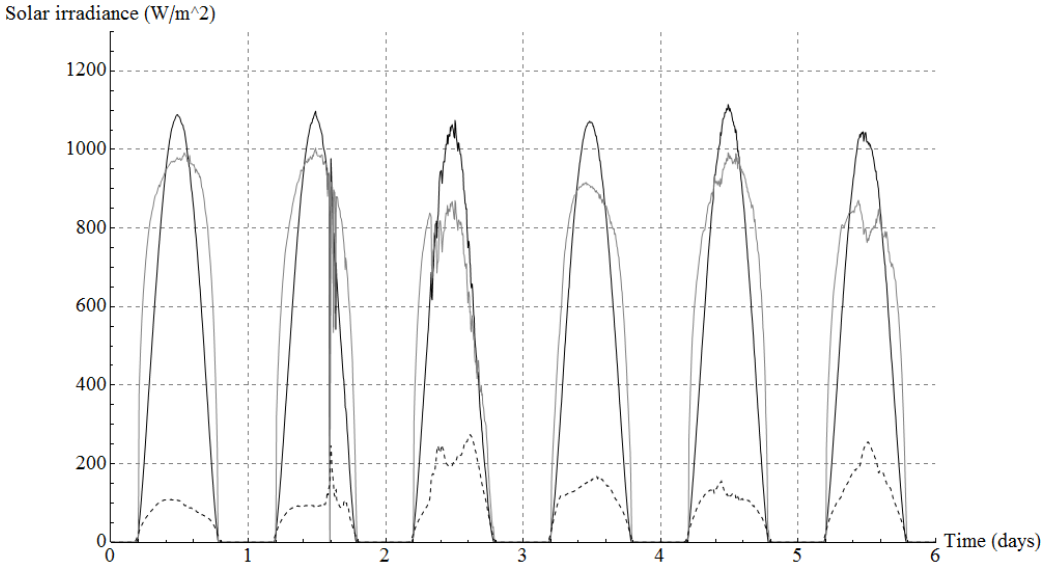

Figure 7.3: Solar irradiance data reference day set I (summer) – solid black line: global horizontal irradiance – solid gray line: direct normal irradiance – dashed black line: diffuse horizontal irradiance [132]

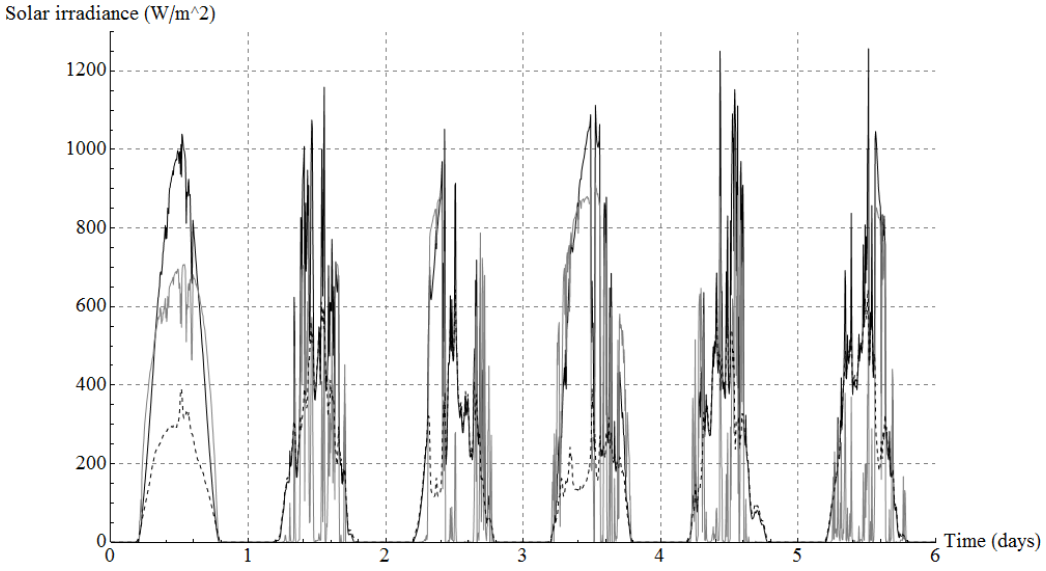

Figure 7.4: Solar irradiance data reference day set II (summer) – solid black line: global horizontal irradiance – solid gray line: direct normal irradiance – dashed black line: diffuse horizontal irradiance [132]

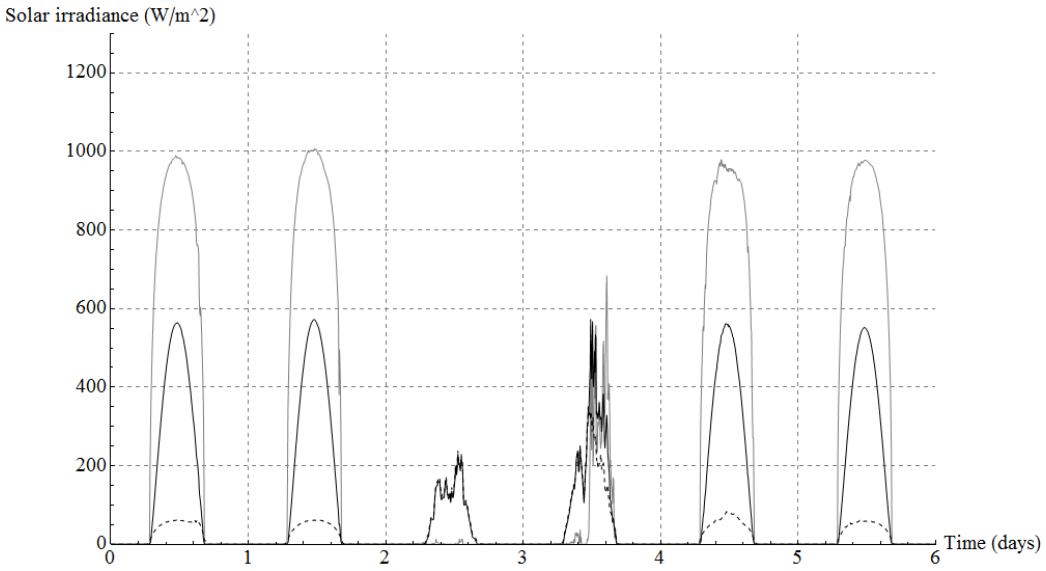

Figure 7.5: Solar irradiance data reference day set III (winter) – solid black line: global horizontal irradiance – solid gray line: direct normal irradiance – dashed black line: diffuse horizontal irradiance [132]

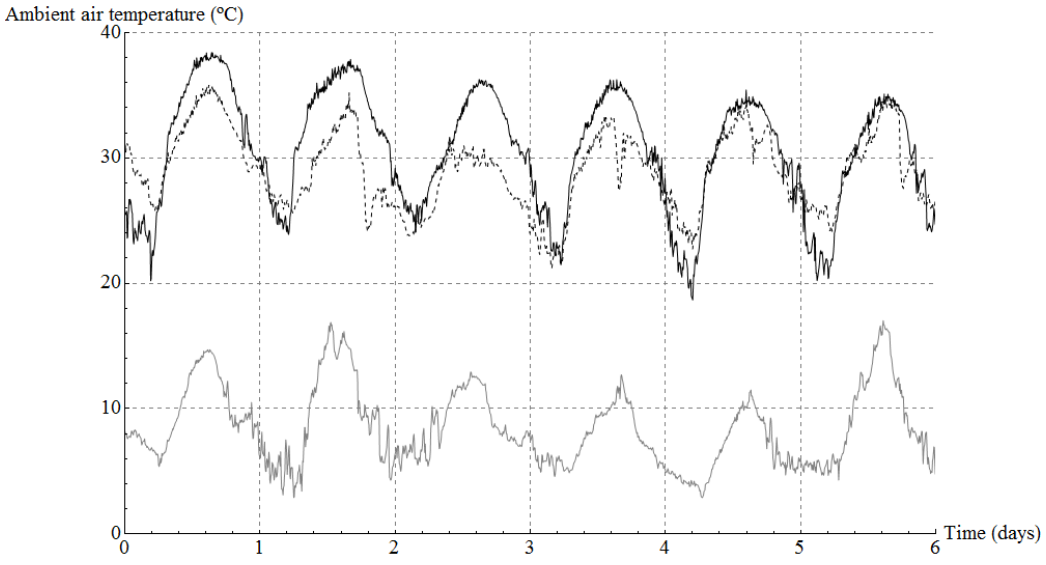

Figure 7.6: Ambient air temperature – solid black line: reference day set I – dashed black line: reference day set II – solid gray line: reference day set III [132]

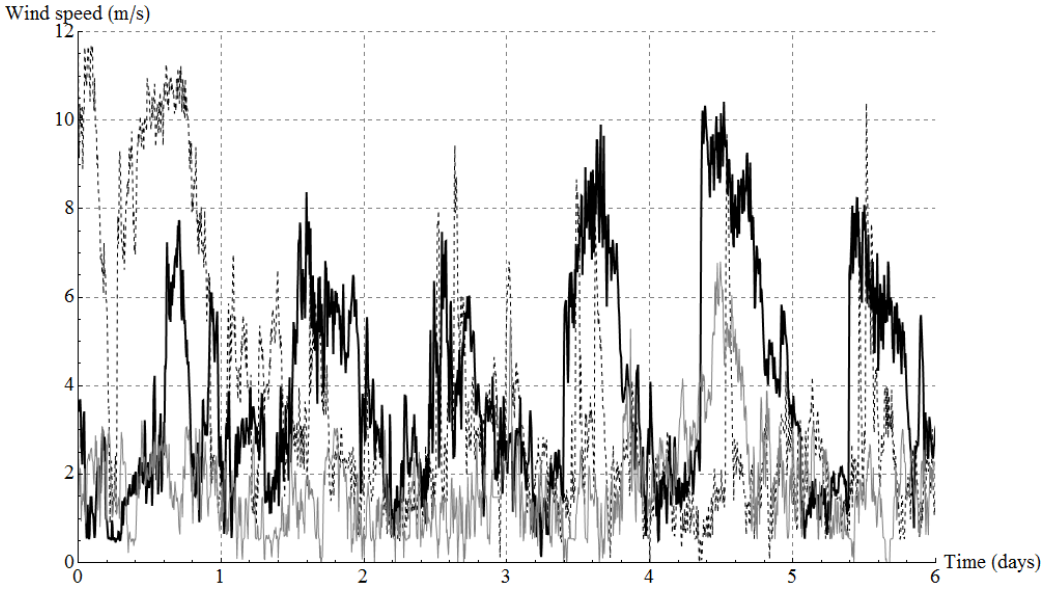

Figure 7.7: Wind speed – solid black line: reference day set I – dashed black line: reference day set II – solid gray line: reference day set III [132]

Delgado [107]. They provided molten salt inventory temperature drop values in Kelvin per day. These values were observed at a commercial parabolic trough collector plant, operated in Spain. In order to compare the reference model results with the data published in [107], the simulated 6-day temperature drop for each ambient conditions set has been divided by 6. In addition, the observed real application temperature drop values have been transformed into corresponding mean heat flows, by applying the following relationship:

$$\dot{Q}_{loss} = \frac{c_p \cdot m \cdot \Delta T}{\Delta t} \tag{7.32}$$

Figure 7.8 shows the comparison between the temperature drop data published in [107] and the mean values of the simulation results for a fully charged storage system. The black and the gray dots represent the data observed by Relloso & Delgado [107]. The black dots represent the observed temperature drop values for the full hot tank. The gray dots represent the observed temperature drop values for the empty cold tank. The dashed black line and the dashed gray line represent the mean values of the observed temperature drops for the hot tank (about 1.1 K/day) and the cold tank (about 5.4 K/day). The solid lines represent the mean values of the reference model simulation results (black for the full hot tank, and gray for the empty cold tank). The reference model has been run for the 3 sets of 6 reference

days. Thus, a molten salt inventory cool-down curve has been obtained for each of the three sets. As mentioned above, the shown temperature drop mean values have been obtained by dividing the full 6-day temperature drop by 6. The mean temperature drop for reference day set I (summer) amounts to 0.56 K/day for the full hot tank and 5.96 K/day for the empty cold tank. For the reference day sets II (summer) and III (winter) these values are 0.57 and 0.59 K/day, respectively, for the full hot tank, and 6.03 and 6.4 K/day, respectively, for the empty cold tank. All three values are shown for the cold tank (solid gray lines). However, only one value is shown for the hot tank (solid black line), since these values are too close together for being distinguishable in the graph. The boundary conditions of reference day set I lead to the lowest temperature drops. This is mainly due to the relatively high ambient temperature as well as the relatively high global solar irradiation. The boundary conditions of reference day set III lead to the highest temperature drops, which is mainly due to the relatively low ambient temperature.

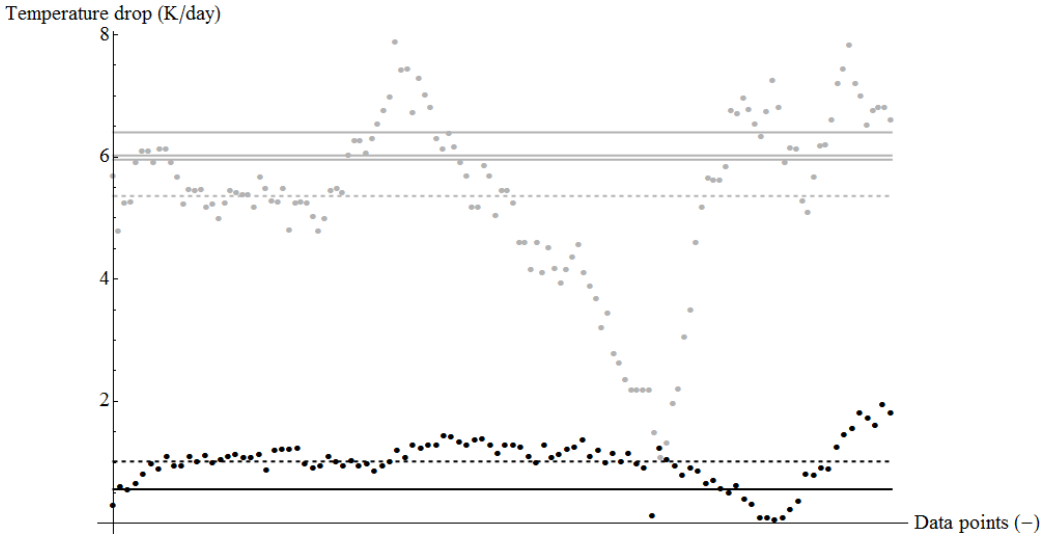

Figure 7.8: Molten salt inventory temperature drop in Kelvin per day for a fully charged storage system - cold tank empty (gray) and hot tank full (black) [132]

Figure 7.9 and Figure 7.10 show the simulated transient heat loss as solid lines and the observed real application data as points. As mentioned before, the temperature drop data presented in [107] has therefore been transformed into corresponding mean heat flow values. Figure 7.9 displays the data for the empty cold tank and Figure 7.10 displays the data for the full hot tank

(fully charged storage system).

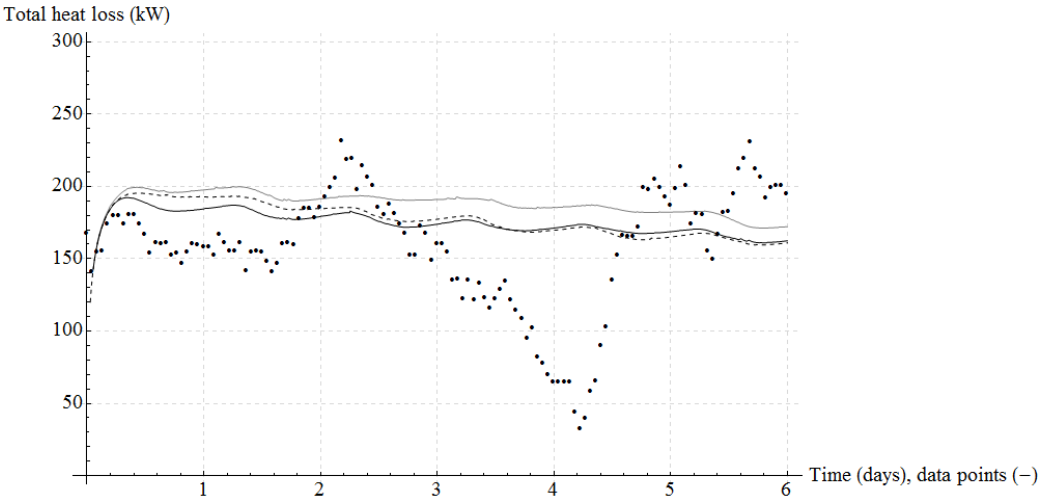

Figure 7.9: Simulated transient heat loss of the empty cold tank (solid lines) with the observations shown as points - black line: reference day set I – black dashed line: reference day set II – gray line: reference day set III [132]

To summarize the comparison, it can be said that the obtained simulation results of the reference model lie within the range of real application data that was observed by Relloso & Delgado [107]. The fact of having higher temperature drops at lower filling levels is captured well. This can be explained by a rather constant total heat loss that results in a larger temperature drop for smaller molten salt inventory masses. However, it has to be noted that this here presented comparison cannot be seen as model validation since neither the environmental boundary conditions, nor the real application storage tank construction details (e.g. insulation layer thicknesses) are known. Nevertheless, the reference model setup, as stated in Sections 7.2.1 to 7.2.9, is considered as an appropriate benchmark for the more and more simplified models that will be presented in the following.

7.5 Simulation results of the reference model

In order to perform acceptable model simplifications, the total heat loss has to be subdivided into its single parts, indicating which heat transfer mechanism influences the overall result most. This will be done for both currently applied temperature levels. Hence, for 386 °C and 292 °C, applied at parabolic trough collector plants, and for 565 °C and 290 °C, applied at power tower

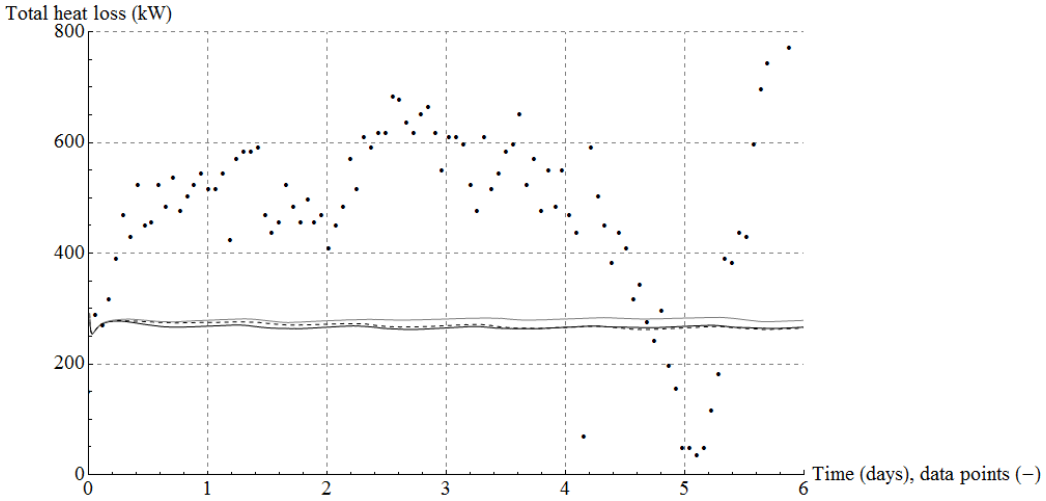

Figure 7.10: Simulated transient heat loss of the full hot tank (solid lines) with the observations shown as points - black line: reference day set I – black dashed line: reference day set II – gray line: reference day set III [132]

concepts. Thus, for both temperature levels, the reference model results will be discussed in the following.

7.5.0.1 Molten salt inventory heat loss fractions

Figure 7.11 shows the heat loss fractions for the hot, and the cold tank at the temperature levels of 386 °C and 292 °C, respectively. Displayed are the mean values of all three reference day sets. The left side of the chart shows the mean values for a fully charged storage system. The right side represents the mean values for a fully discharged storage system. The light-gray colored bars represent the heat loss values for the cold tank. The gray colored bars represent the heat loss values for the hot tank. As can be seen in the graph, the convective heat transfer between the molten salt surface and the nitrogen atmosphere contributes the least for full storage tanks. For empty storage tanks, the surface convective heat transfer reaches the order of magnitude of the convective heat transfer between the molten salt and the wetted inner wall. In both cases, the convective heat transfer at the molten salt surface stays relatively small, considering the total heat loss. On the other hand, a quite strong dependency can be seen between the molten salt filling level and the convective heat transfer between the molten salt and the wetted inner wall, and the heat exchange via radiation between the molten salt surface and the non-wetted inner surfaces of the steel jacket. The lower the filling level is, the higher is the heat loss via radiation, and the lower is the heat

loss via convection at the wetted inner surface of the wall. The convective heat transfer at the bottom seems to be rather independent of the state of charge, having slightly higher values at higher filling levels, though.

The same relationships can be observed in Figure 7.12, which shows the mean simulation results for the temperature levels applied at power tower applications. These results have been obtained by running the reference model at the temperature level of 565 °C for the hot tank, and 290 °C for the cold tank. Furthermore, the tank atmosphere nitrogen model has been replaced by the dry air model. Due to the higher temperature level of the hot tank, the total heat loss is almost doubled. It should be noted that the tank dimensions, as well as the insulation layer thicknesses have not been changed.

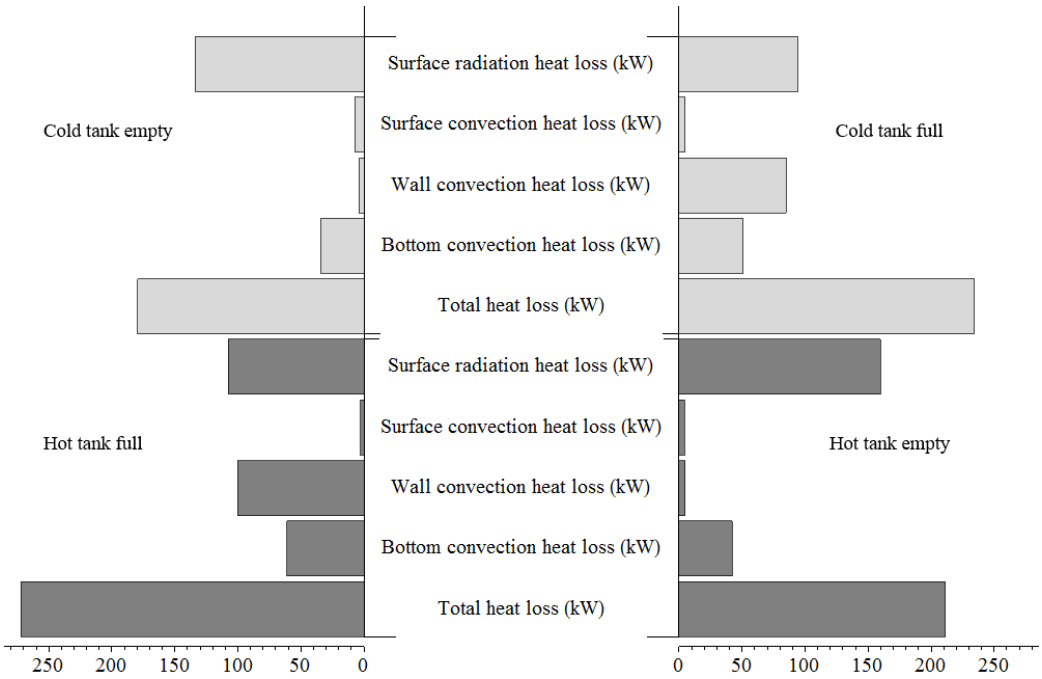

Figure 7.11: Storage tank heat loss fractions at temperature levels 386 °C / 292 °C – on the left: fully charged storage system (full hot tank, empty cold tank) – on the right: fully discharged storage system (empty hot tank, full cold tank) – hot tank gray – cold tank light-gray [132]

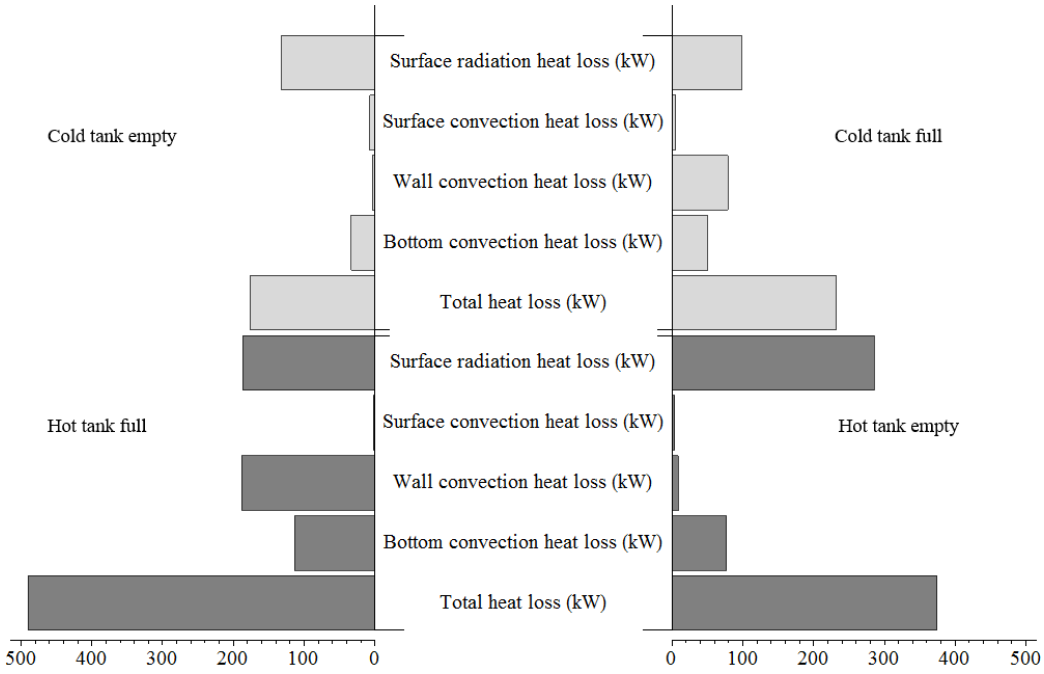

Figure 7.12: Storage tank heat loss fractions at temperature levels 565 °C / 290 °C – on the left: fully charged storage system (full hot tank, empty cold tank) – on the right: fully discharged storage system (empty hot tank, full cold tank) – hot tank gray – cold tank light-gray [132]

7.5.1 Wall temperatures and the heat exchange at the exterior surface

Considering the temperature distributions within the storage tank, it can be said that the inner steel wall temperatures keep very close to the molten salt bulk temperature. For the hot tank at 386 °C, the temperature differences between the steel wall surfaces and the molten salt ideally mixed bulk temperature range between 0.4 K, for the wetted inner wall, and 4.8 K, for the inner top surface of the tank. Figure 7.13 shows the cool down curve for the hot tank at the lower filling level, obtained for reference day set I. After a short transient effect at the simulation start, the temperature differences remain rather constant throughout the whole simulation.

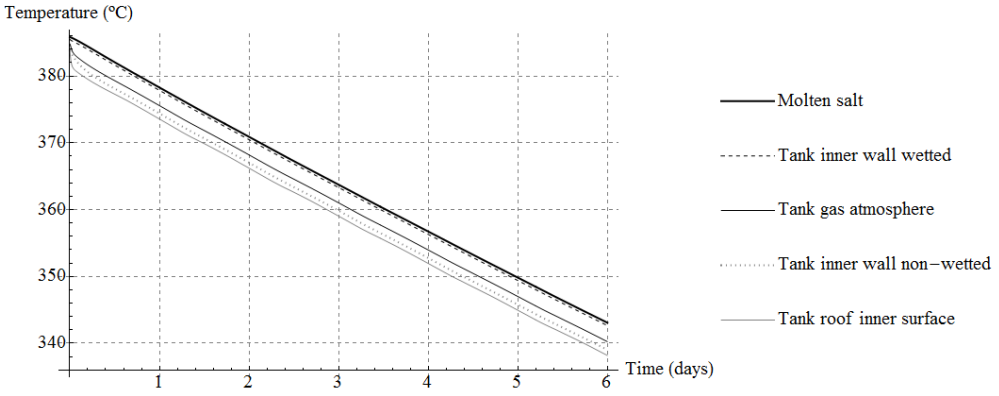

Figure 7.13: Molten salt (thick solid black line), tank atmosphere (thin solid black line) and steel jacket surface temperatures for the hot tank at lower filling level [132]

Due to the relatively high thermal conductivity of the steel walls, their node temperatures stay very close to their surface temperatures, also with a rather constant temperature difference between them. On the other hand, the node temperatures and the outer surface temperatures of the insulation layers show daily fluctuations due to the change in ambient air temperature and incident solar irradiance. Figure 7.14 shows the hot tank's roof temperatures and the ambient air temperature, also for reference day set I. As can be seen in the graph, the incident solar irradiance causes a large daily fluctuation of the roof's outer surface temperature. While having an outer surface temperature at around 34 °C during the nights, its value rises up to about 130 °C during moments of high incident solar irradiance ($\approx 1090 \frac{W}{m^2}$), high

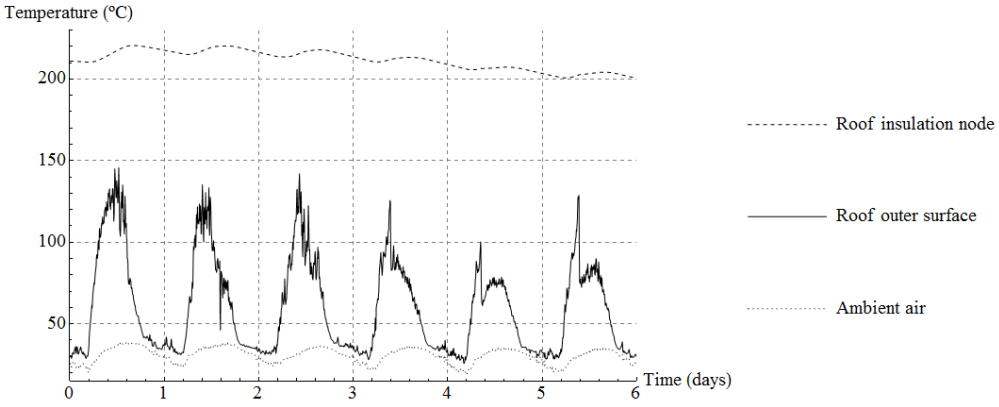

Figure 7.14: Storage tank roof insulation layer node temperature (dashed line), roof outer surface temperature (solid line), and ambient air temperature (dotted line), for the hot tank at lower filling level and reference day set I [132]

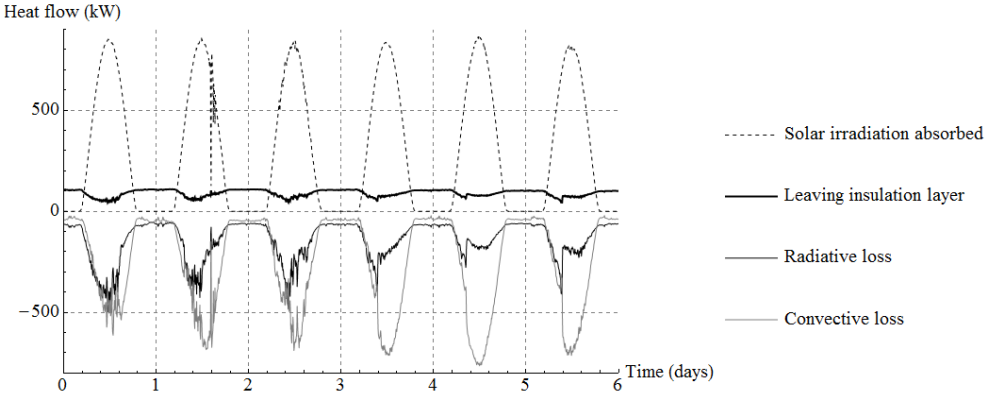

Figure 7.15: Heat flows at the exterior surface of the storage tank's roof – black dashed line: absorbed solar radiation – upper black solid line: heat flow leaving the insulation layer – lower solid black line: heat loss due to radiation – gray solid line: heat loss due to convection [132]

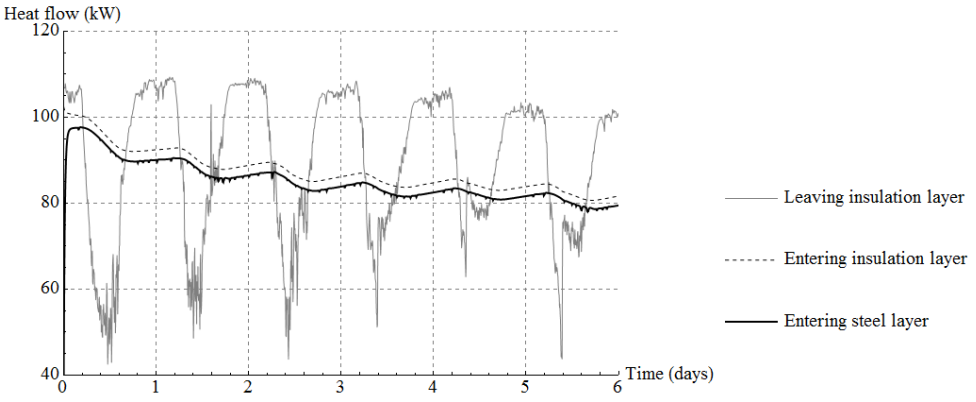

Figure 7.16: Heat flows between the temperature nodes of the storage tank's roof – black solid line: heat flow entering steel layer – black dashed line: heat flow between steel layer temperature node and insulation layer temperature node – gray solid line: heat flow leaving the insulation layer [132]

ambient air temperatures (≈ 40 °C) and low wind speeds ($\approx 1\frac{m}{s}$). A similar, but pronounced weaker relationship can be observed for the insulation layer node temperature, however, having a certain time lag due to the thermal inertia of the insulation material. Hence, the incident solar irradiance influences the heat flow through the storage tank walls. Figure 7.15 shows the heat flows at the roof's outer surface. Positive defined are heat flows "entering" the outer surface, i.e. the absorbed solar radiation (black dashed line) as well as the heat flow between the insulation layer temperature node and the exterior surface (upper black solid line). Negative defined are heat flows "leaving" the exterior surface, i.e. the convective heat loss to the ambient air (gray solid line) as well as the heat loss via radiation (lower black solid line). Of course, at each instant of time these heat flows sum up to zero.

As can be observed in Figure 7.15, the heat flow between the insulation layer temperature node and the exterior surface (upper black solid line) shows daily fluctuations reaching a periodic minimum at high solar irradiance values and thus relatively high exterior surface temperatures. This behavior can still be observed for the heat flows between the inner surface of the steel jacket and the containing media, however at a considerably damped level. Figure 7.16 shows the heat flow entering the inner roof construction steel layer (black solid line), the heat flow between the steel layer temperature node and the insulation layer temperature node (black dashed line), and the heat flow leaving the insulation layer (gray solid line). The latter curve corresponds to

the upper black solid line already shown in Figure 7.15, but at a larger scale. These heat flow fluctuations do also occur at the storage tank's side walls, but at lower amplitudes since the absorbed solar radiation is less, of course depending on the time of year.

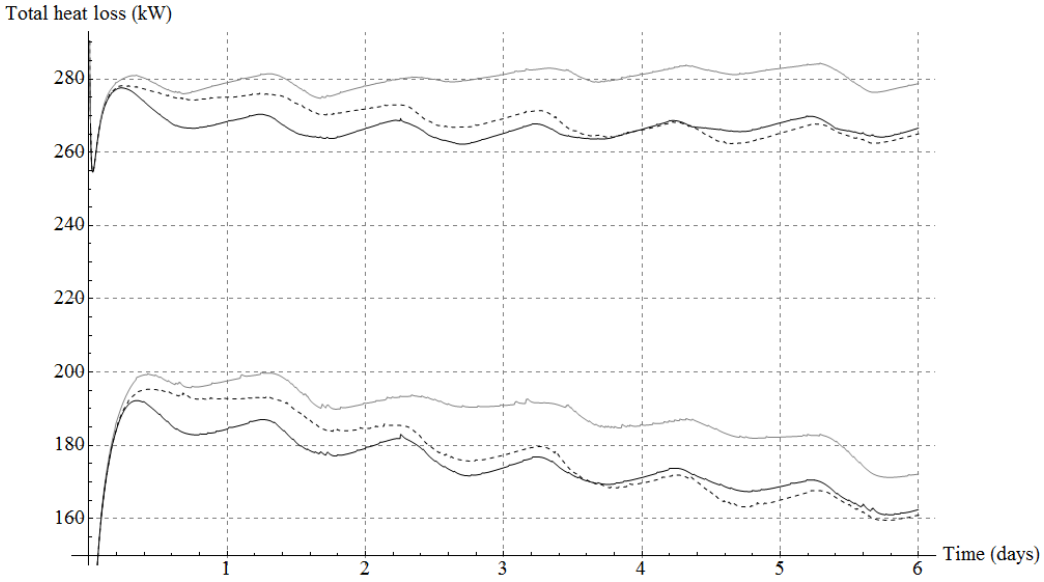

Figure 7.17: Reference model total heat loss in fully charged storage system mode at temperature levels 386 °C / 292 °C – upper lines: hot tank – lower lines: cold tank – black solid lines: reference day set I – black dashed lines: reference day set II – gray solid lines: reference day set III [132]

Figure 7.17 shows the reference model's total heat loss for all three reference day sets in fully charged storage system mode and at the temperature levels of 386 and 292 °C. The upper lines represent the heat loss of the full hot tank, the lower lines represent the heat loss of the empty cold tank. The black solid lines represent the calculation results of reference day set I, the black dashed lines represent reference day set II, and the gray solid lines represent reference day set III. From reference day set I to III, a consequently rising total heat loss can be observed. This is mainly due to the difference in ambient air temperature. Furthermore, the influence of the incident solar irradiation can be seen. The results of reference day set I show a continuous wave-like shape with pronounced local maximums and minimums. The results of reference day set III are similar, but show reduced amplitudes, though, especially during the two days of almost no incident solar irradiation (see Figure 7.5).

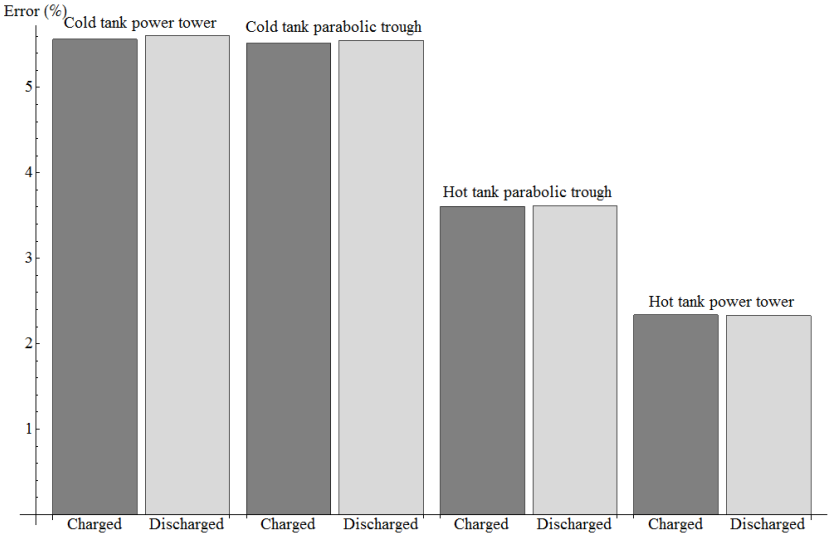

Figure 7.18: Relative errors in temperature drop for reference day set I in percent – rising molten salt inventory temperature from left to right [132]

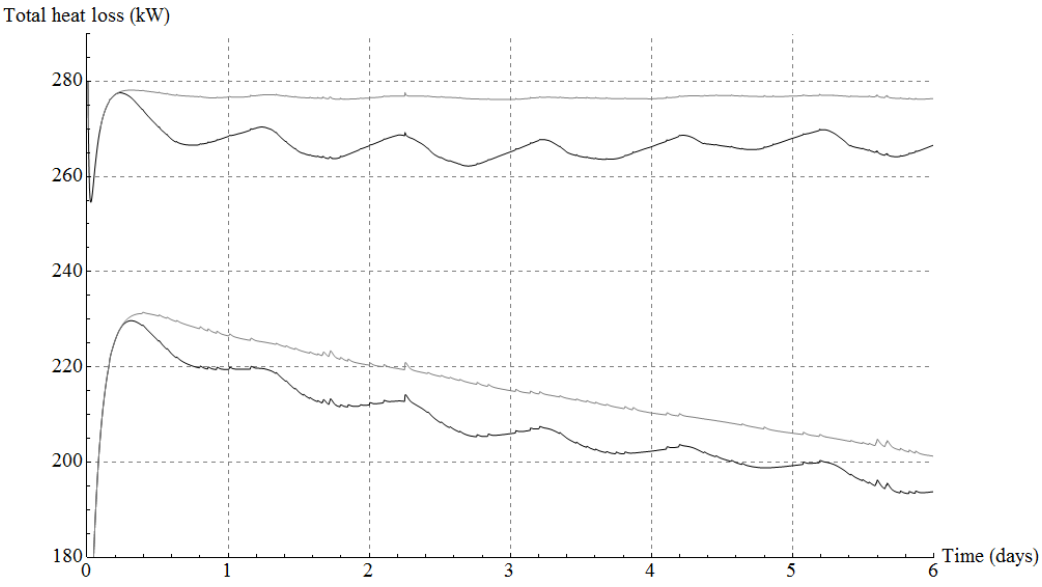

Figure 7.19: Total molten salt inventory heat loss for the hot tank with 386 °C simulation start temperature and reference day set I – gray lines: solar irradiation not considered – black lines: solar irradiation considered – upper lines: charged – lower lines: discharged [132]

7.5.2 The influence of the solar irradiation on the molten salt temperature drop

Considering the above, high solar irradiation incident on the storage tank's outer surface, temporally reduces the molten salt inventory heat loss, causing periodic fluctuations of the total heat loss. In the following, it will be shown up to which extent the incident solar irradiation influences the temperature drop over the 6 days of reference day set I. Therefore, the reference model has been run once more, but setting the solar irradiation to zero, only considering the ambient temperature boundary condition. This leads to considerably lower exterior surface temperatures, and thus, to an overprediction of the total heat loss. Since the reduction in temperature of the outer surface is rather equal for all molten salt temperature levels, the impact of not considering the solar irradiation will be lower for storage systems with higher molten salt temperatures. Thus, also the power tower storage tank models have been run without considering the incident solar irradiation. Figure 7.18 shows the relative error in temperature drop for reference day set I between the reference models considering the solar irradiation, and the reference models not considering the solar irradiation. The percentage is based on the total temperature drop obtained by the reference models that consider the solar irradiation. The error display sequence is based on the molten salt temperature levels, hence 290 °C (central receiver cold tank), 292 °C (parabolic trough cold tank), 386°C (parabolic trough hot tank) and 565°C (central receiver hot tank). The models have been run in fully charged mode and in fully discharged mode. Thus, each error is shown for storage system charged state and storage system discharged state. It can be observed that the error in heat loss does not depend on the filling level. At all temperature levels it is rather equal for fully charged and fully discharged systems. However, a quite strong temperature dependency can be seen. The relative error ranges between 5.6% for the cold tank with 290 °C simulation start temperature and 2.3% for the hot tank with 565 °C simulation start temperature.

Figure 7.19 shows the total heat loss of the hot tank with 386 °C simulation start temperature in charged (upper lines) and discharged (lower lines) storage system mode. The gray lines represent the heat loss obtained by the reference model not considering the incident solar irradiation. The black lines represent the heat loss obtained by the reference model considering the solar irradiation. The relative error amounts to about 3.6%.

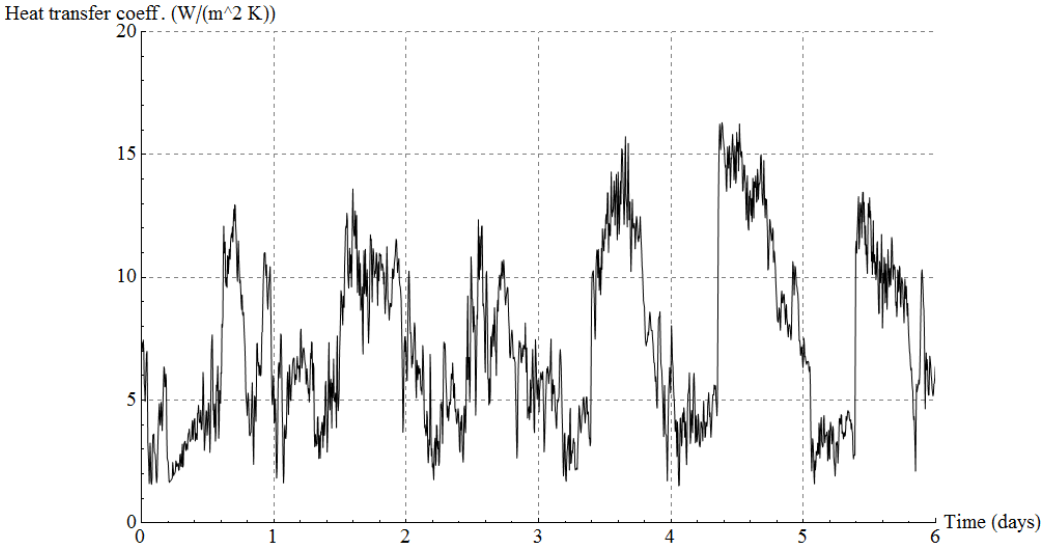

Figure 7.20: Convective heat transfer coefficient between the ambient air and the roof's exterior surface – reference day set I [132]

7.5.3 The convective heat transfer coefficient at the exterior surfaces

As outlined in Section 7.5.2, the solar irradiation has a reasonable impact on the storage tank's heat loss, especially at lower molten salt temperatures. This is due to a higher exterior surface temperature that reduces the overall temperature difference, the driving force for the heat loss. The reached surface temperature is a function of the radiative and the convective heat losses. If both the radiative heat loss and the convective heat loss are too low for the imposed heat flows determined by solar absorption and the molten salt temperature, the exterior wall temperature will rise until the equilibrium is reached. Thus, a sufficiently accurate approximation of the convective heat transfer coefficient between the ambient air and the tank's exterior surface is important. Figure 7.20 shows the convective heat transfer coefficient values obtained for reference day set I. It can be seen that during the last three days the convective heat transfer coefficient reaches its highest values, reducing the roof's exterior temperature considerably (see Figure 7.14 and Figure 7.15).

7.6 Simplified storage tank models and their simulation results

Considering the above presented results, the first obvious model simplification would be neglecting the convective heat transfer between the molten salt surface and the gas atmosphere. Thus, the whole gas atmosphere model has been removed, only considering the heat exchange via radiation between the molten salt surface and the non-wetted inner surfaces of the tank's steel jacket. As a next step, since the convective heat transfer coefficients at the wetted inner surfaces have been rather constant throughout the performed simulations, they will be set to their mean values.

7.6.1 Considering only the heat exchange via radiation at the molten salt surface

As can be seen in Figure 7.11 and Figure 7.12, the heat transport via convection to the gas atmosphere above the molten salt surface seems to have a negligible level of impact. Therefore, the reference model has been simplified by completely removing the gas atmosphere model. Thus, only the heat transfer via radiation is taken into account between the molten salt surface and the non-wetted steel container. Again, this simplified model has been run at both temperature levels for all three reference day sets. These simulations have shown that this simplification only introduces a minor heat loss error, for both temperature levels. The relative error based on the reference model results ranges between 0.1% and 0.01%, having relatively higher values for tanks at the lower filling levels. Hence, considering simulations of storage systems in off-line mode, the convective heat transfer can be safely neglected. However, strictly speaking, not modeling the gas atmosphere, may additionally introduce errors for simulations of storage systems during operation, where the gas is exchanged between the two tanks due to changes in volumes. For this reason, the influence of the gas exchange on the molten salt temperatures will be treated in the following.

7.6.1.1 The influence of the gas exchange between the hot and the cold tank during operation

During storage system operation, the gas above the molten salt surface, either nitrogen or air, is exchanged between the hot and the cold tank. While charging, the molten salt is pumped from the cold tank to the hot tank. This reduces the available space for the gas in the hot tank, and correspondingly,

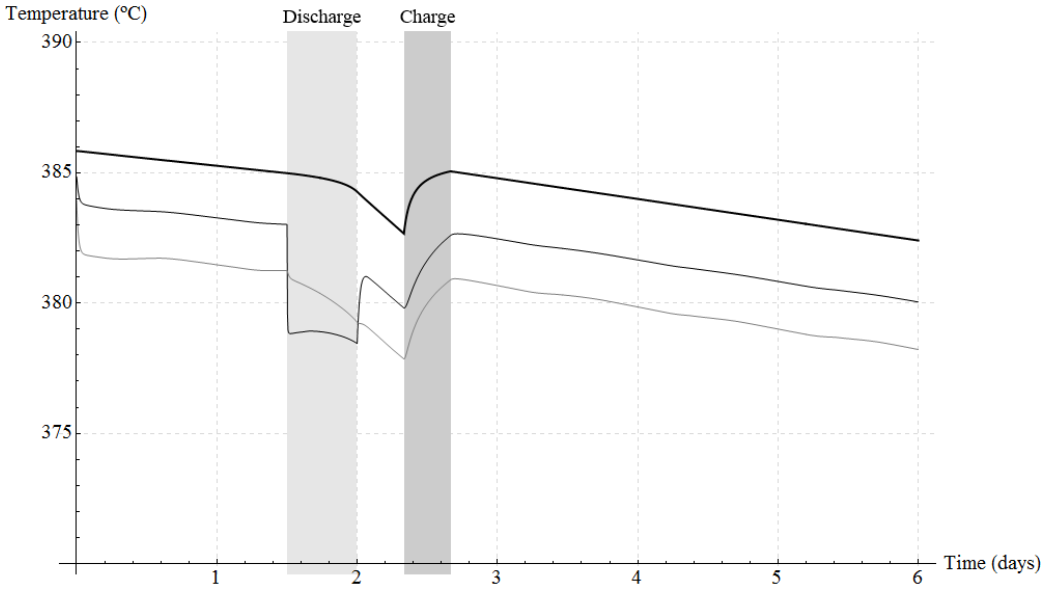

Figure 7.21: Hot tank charge and discharge simulation with 386 °C start temperature – thick black line: molten salt – thin black line: gas atmosphere – gray line: tank inner roof surface [132]

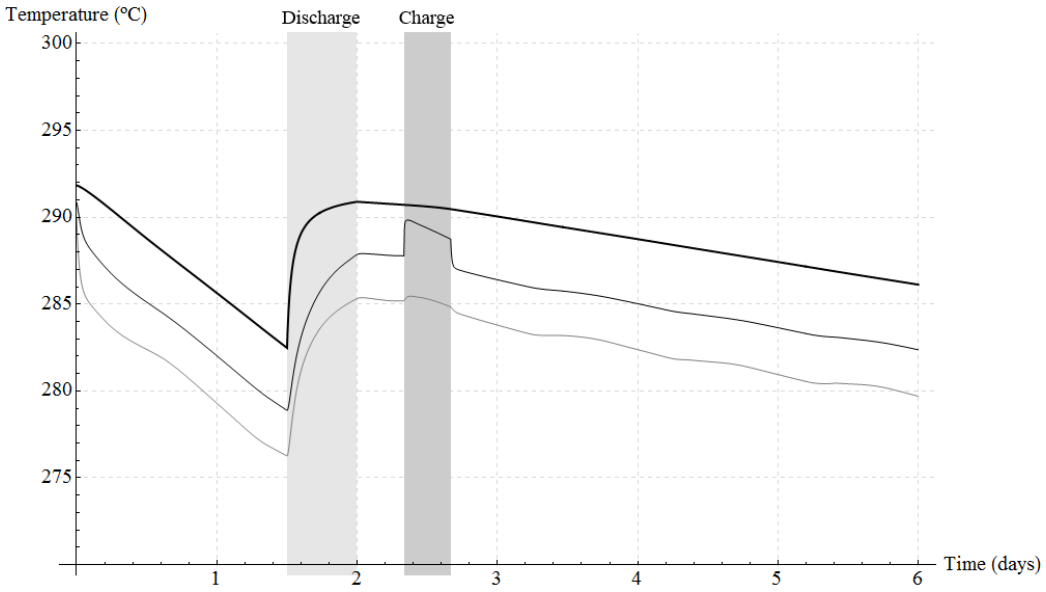

Figure 7.22: Cold tank charge and discharge simulation with 292 °C start temperature – thick black line: molten salt – thin black line: gas atmosphere – gray line: tank inner roof surface [132]

increases the available space in the cold tank, inducing a gas mass flow from the hot to the cold tank. Due to the relatively hot entering gas stream, the temperature of the cold tank's atmosphere increases temporarily, and consequently, also slightly reduces the convective heat loss of the cold molten salt inventory. While discharging, this gas exchange happens vice versa. Here, relatively cold gas enters the hot tank's atmosphere, and thus, temporarily reduces its temperature, which slightly increases the convective heat loss of the hot molten salt inventory. Figure 7.21 and Figure 7.22 show the temperatures of the storage tank media for a 6-day simulation (reference day set I), including a storage system discharge-charge cycle. During the charging process, as well as during the discharging process, the feed temperatures of both, the hot and the cold tank, have been set to their design temperatures, assuming an ideally controlled feed temperature. At simulation start, the storage system is fully charged (full hot tank, empty cold tank). During a 12 hours discharging process (light gray zone), which starts at day 2 at noon, the hot tank reaches its lower filling level. After an 8 hours charging process (gray zone), starting at day 3 in the morning, the storage system remains partially charged.

In order to justify the model simplification of not considering the gas atmosphere, the simulation shown in Figure 7.21 and Figure 7.22 has been performed with the simplified storage tank model as well, only considering the heat exchange via radiation. The comparison of these results, and additionally, the comparison of other simulation results during cyclic operation, has shown that the influence of the gas exchange is negligible as well. The relative error based on the reference model results stays below 0.1%. The same holds for central receiver type two-tank storage systems (565 °C, 290 °C).

7.6.2 Additionally assuming constant convective heat transfer coefficients at the wetted surfaces

Furthermore, the convective heat transfer coefficients between the molten salt and the wetted inner walls do not vary considerably. They do follow the temperature drop of the molten salt and slightly vary with the filling level. Since the temperature drops are generally only in the range of a few degrees, the convective heat transfer coefficients at the bottom and at the wetted walls can be safely set to constant values. In this work, they have been set to the mean values observed for both temperature and filling levels. For the hot tank at 386 °C and 565 °C, the mean convective heat transfer coefficients at the tank's bottom amount to about 30.8 and 39.8 $\frac{W}{m^2K}$, respectively. The

mean convective heat transfer coefficients at the hot tank's walls amount to about 125.2 and 176.9 $\frac{W}{m^2K}$, respectively. For the cold tank at 292 °C and 290 °C, the mean convective heat transfer coefficient at the bottom amounts to about 26 $\frac{W}{m^2K}$. The mean convective heat transfer coefficient at the cold tank's walls amounts to about 102 $\frac{W}{m^2K}$. The relative error observed based on the reference model results ranges between 0.13 and 0.03%, again having relatively higher values for tanks at lower filling levels.

7.7 The application of the proposed storage tank models

The above described molten salt storage tank models form a valuable basis for detailed two-tank thermal energy storage system simulations. They can be used to optimize design as well as operation. Efficient storage system operation and control strategies, which e.g. cause a minimum of electric power consumption of the auxiliary heating system, are not easy to elaborate. Reliable transient storage system component models are therefore needed. Furthermore, sensitivity studies can be performed, which identify design parameters that have a major impact on the storage system's overall behavior. The presented analysis of the dominant sources of heat loss gives useful information for optimizing the storage tank design. The ability of solar thermal power plants to store thermal energy is a great possibility to provide renewable energy on a constant basis. Therefore, detailed optimizations of thermal energy storage systems will definitely play a major role in making this emerging sector more competitive.

7.8 Conclusions and acknowledgments

Chapter 7 focuses on the modeling of molten salt thermal energy storage tanks for concentrating solar power performance simulations. A fully transient storage tank model has been developed and simulated over 3 sets of 6 reference days, providing typical weather conditions of a solar thermal power plant location as model input. The total storage tank heat loss has been subdivided into its single fractions, showing which mode of heat transfer contributes most. The convective heat transfer at the wetted inner surfaces of the tank's steel jacket and the radiative heat transfer between the molten salt surface and the non-wetted inner surfaces of the tank's steel jacket have been identified as the ruling factors. The convective heat loss via the gas atmosphere above the molten salt surface is negligible small and does not

have to be modeled in particular. Furthermore, the convective heat transfer coefficients between the molten salt and the wetted inner surfaces do not vary considerably. They may be set to constant values. The storage tank's outer surface temperature, and therefore the absorbed solar irradiation as well as the ambient air temperature influence the heat loss significantly. Thus, a good approximation of the heat transfer at the tank's exterior surface is strongly recommended in order to correctly estimate the exterior surface temperature and consequently define a reasonable temperature difference for the heat flow through the walls.

Taking these results into account, a reasonable simple transient high-temperature storage tank simulation tool is obtained, suitable for CSP performance simulations. Due to the transient modeling of the storage tank walls and a detailed estimation of the exterior surface temperature, the influence of altering environmental boundary conditions can be captured more accurately than by quasi-steady-state methods that only account for the current ambient air temperature. It has been shown that the temperature distributions and heat flows within the walls do not experience a steady state.

The author would like to thank the BSRN for maintaining and providing a comprehensive and reliable solar irradiation data base. Especially, the author would like to thank the people involved at the station Desert Rock, Nevada, USA.

Chapter 8

Object-oriented modeling for the transient response simulation of multi-pass shell-and-tube heat exchangers as applied in active indirect thermal energy storage systems for concentrated solar power

This chapter focuses on the transient numerical modeling of multi-pass shell-and-tube heat exchangers that apply single-phase fluids. A one-dimensional modeling approach is used for the heat exchanger ducts. The governing partial differential equations are solved numerically by applying the finite volume method. In particular, the commonly applied cell-method is used, which is presented in a flexible, intuitive and simulation-platform-independent way. Simulation results are checked for consistency by comparing them to theoretical as well as experimental data available in the literature. Subsequently, the presented modeling approach is used for a specific case study, showing the transient behavior of a typical heat exchanger train configuration currently used at active indirect thermal energy storage systems for concentrated solar power (CSP). Typical process parameters (process gain, dead time and time constant) are given for charging as well as for discharging mode at different heat exchanger loads. Furthermore, transient response simulation results are discussed in detail, providing all used

boundary conditions and assumed heat exchanger specifications, thus enabling future model comparison studies. Finally, suitable degrees of discretization are discussed for transient CSP performance simulations on system level, offering a good trade-off between simulation speed and accuracy. Modelica [127] is used as modeling language.

8.1 Introduction

The active indirect two-tank thermal energy storage system (having one hot molten salt tank and one cold molten salt tank) is at the moment the state-of-the-art solution at commercial plants. However, in order to reduce costs a thermocline single-tank approach has been proposed by various authors. In this concept, the hot molten salt tank and the cold molten salt tank is replaced by just one tank containing the hot and the cold salt separated by a thermocline zone, i.e. a temperature gradient zone. A low-cost filler material (packed bed) should prevent convective mixing of the hot and the cold fluid, and furthermore, should provide the bulk of the thermal capacitance of the thermal energy storage [75]. Nevertheless, thermal ratcheting of the storage tank walls remains a significant design concern and further research is required in order to make the thermocline concept applicable at commercial level [84].

In both cases, either the active indirect two-tank or the active indirect single-tank (thermocline) approach, the heat transfer from the thermal oil (the HTF) to the molten salt (the storage medium) and vice versa is accomplished via the use of an oil-to-molten-salt heat exchanger, i.e. as the name already implies, the storage system is charged or discharged indirectly.

The typical heat exchanger setup used at commercial parabolic trough collector plants is a counter-flow shell-and-tube heat exchanger design having the thermal oil on the tube-side and the molten salt on the shell-side [80]. This fluid assignment is primarily due to the relatively high system pressure of the thermal oil (HTF) circuit. The vapor pressure of the thermal oil is approximately 10 bar at the nominal solar field outlet temperature of 391 °C. Thus, taking the piping and solar field pressure drop into account, the maximum system pressure of the thermal oil circuit is usually around 25 to 30 bar. On the other hand, the molten salt features a very low vapor pressure. It can be stored in the tanks at ambient air pressure, and is thus placed on the heat exchanger's shell-side. The applied temperature levels for the molten salt are typically 292°C (cold end) and 386°C (hot end), due to the relatively high liquidus temperature of the salt mixture and the thermal stability limit of the thermal oil at about 400 °C.

This chapter focuses on the transient numerical modeling of oil-to-molten-salt heat exchangers used in CSP active indirect thermal energy storage systems. It proposes an object-oriented, Modelica-based, distributed parameter model, suitable for storage system performance simulations that allow for testing, evaluating and improving of operating and control strategies. Furthermore, by using a simplified model setup and an optimized spatial resolution that should be as low as possible, i.e. keeping the necessary computational effort at a minimum, the proposed model is also appropriate for CSP plant performance simulations on system level. The developed model is based on a detailed literature review, and the interested reader is thus referred to Section 4.2.2 of this work to obtain useful information about modeling approaches that have already been proposed.

Note: This chapter is entirely based on a work [111] published in Elsevier's journal Energy. For simplicity, the citation throughout this chapter is left aside.

8.2 The methodology and the modeling approach

This work presents a Modelica-based, transient shell-and-tube heat exchanger model for the application in CSP. Modelica is a multi-purpose physical system modeling language and has been developed in an international effort in order to unify already existing similar modeling approaches and to enable developed models and model libraries to be easily exchanged. The concept is based on non-causal models featuring true ordinary differential and algebraic equations, i.e. differential-algebraic equation (DAE) systems [127]. The object-oriented approach, the possibility of multiple inheritance and the re-declaration feature lead to a clear model structure, avoid multiple definitions of frequently used code and offer an incredible model flexibility. The code syntax and application guidelines are defined in the regularly updated Modelica Language Specification [176]. Furthermore, the use of Modelica clearly decouples the modeler from the equation system solving. Instead of developing a specific solving algorithm for each modeling task, the Modelica tool reads the developed Modelica code, performs symbolic manipulations of equations and translates the Modelica model into numerical simulation code, using state-of-the-art algorithms developed for general application. Thus, developed models and model libraries are exchangeable, i.e. can be read and simulated using different Modelica environments. Today, commercial, as well as open-source Modelica environments are available [180, 181].

8.2.1 1-D fluid flow modeling according to the Modelica Standard Library

In this work, the fluid ducts of the shell-and-tube heat exchanger are modeled according to the MSL's concept. Since this one-dimensional fluid flow modeling approach forms the core feature of the here presented transient heat exchanger model, it will be explained in the following. However, the full transient implementation will not be used, since a simplified version will be more efficient for this study's intentions. Therefore, several simplifications will be explained and justified. The MSL offers a rigorous implementation of a one-dimensional fluid flow model according to the finite volume method (FVM) [182]. The total flow volume is discretized in finite control volumes along the flow direction. In order to avoid a multiple definition of the basic mass and energy balances, the one-dimensional flow model extends from the MSL's base class "partial distributed volume". This generic base class defines the mass and energy balances in terms of net mass flow, net enthalpy flow, net heat flow $\dot{Q}_{net}$ and net work flow $\dot{W}_{net}$, for each control volume i (see Figure 8.1). This can be written as follows:

$$m_i = V_i \cdot \rho_i \tag{8.1}$$

$$\frac{dm_i}{dt} = \dot{m}_{a,i} - \dot{m}_{b,i} \tag{8.2}$$

$$U_i = m_i \cdot u_i \tag{8.3}$$

$$\frac{dU_i}{dt} = \dot{m}_{a,i} \cdot h_{a,i} - \dot{m}_{b,i} \cdot h_{b,i} + \dot{Q}_{net,i} + \dot{W}_{net,i} \tag{8.4}$$

Note: For a positive mass flow at the right control volume boundary ($\dot{m}_{b,i} > 0$, see Figure 8.1), $h_{b,i}$ is the specific enthalpy leaving the control volume, which corresponds to the specific enthalpy h_i of control volume i; for $\dot{m}_{b,i} < 0$, $h_{b,i}$ is the specific enthalpy h_{i+1} of the corresponding adjacent control volume upstream; for $\dot{m}_{a,i} > 0$, $h_{a,i}$ is the specific enthalpy h_{i-1} of the corresponding adjacent control volume upstream; for $\dot{m}_{a,i} < 0$, $h_{a,i}$ is the specific enthalpy h_i of the control volume i; the net work flows $\dot{W}_{net,i}$ are set to zero in the heat exchanger model.

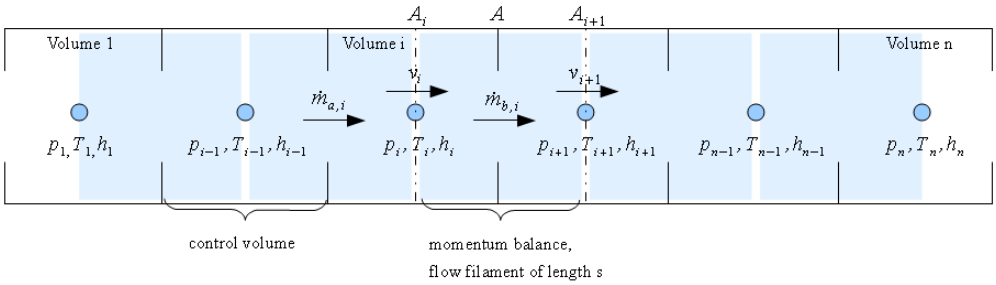

Figure 8.1: Finite volume discretization scheme according to the staggered grid approach [183]

Having formulated the general mass and energy balances, the momentum balances have to be defined as well, in order to provide the missing relationship between the pressure states and the mass flow rates between the neighboring volumes. This is implemented according to the staggered grid approach [183], hence the grid of the momentum balances and the grid of the finite control volumes are displaced relative to each other (see Figure 8.1), i.e. resulting in an alternating concept of momentum balances (shaded squares) and control volumes (black solid lines). The shaded dots in the centers of the control volumes represent the thermodynamic state vectors, i.e. either pressure and specific enthalpy, or pressure and temperature, depending on the selected states.

According to Newton's second law of motion, the net force $\vec{F}$ acting on a body equals the time derivative of the body's momentum $\vec{I}$:

$$\vec{F} = \frac{d\vec{I}}{dt} \tag{8.5}$$

Applying this relationship to an infinitesimal straight flow filament, having the cross-sectional area A and length ds, and furthermore assuming that the velocity vector does only point in direction of that straight flow filament (avoiding the vector notation), the infinitesimal momentum can be written as follows:

$$dI = v \cdot \rho \cdot A \cdot ds \tag{8.6}$$

Integrating this infinitesimal momentum dI from position s_1 to position s_2, stating its time derivative, hence F, and applying the Leibniz integral rule [184], yields:

$$I = \int_{s_1}^{s_2} v(s,t) \cdot \rho(s,t) \cdot A(s,t)\, ds \tag{8.7}$$

$$F = \frac{d}{dt} \int_{s_1}^{s_2} v(s,t) \cdot \rho(s,t) \cdot A(s,t)\, ds \tag{8.8}$$

$$F = v_2 \cdot v_2 \cdot \rho_2 \cdot A_2 - v_1 \cdot v_1 \cdot \rho_1 \cdot A_1 + \int_{s_1}^{s_2} \frac{\partial}{\partial t} v \cdot \rho \cdot A\, ds \tag{8.9}$$

Now, applying Equation 8.9 to the discrete flow filament of length $s = s_2 - s_1$, indicated in Figure 8.1, i.e. the shaded section between the control volume i, and control volume $i+1$, and assuming that the variables velocity v, density ρ, and the cross-sectional area A do not depend on the position s, i.e. do have the same but time dependent values along the discrete flow filament, the equation can be written as follows:

$$F = v_2 \cdot v_2 \cdot \rho_2 \cdot A_2 - v_1 \cdot v_1 \cdot \rho_1 \cdot A_1 + \frac{d}{dt} (v \cdot \rho \cdot A \cdot s) \tag{8.10}$$

Furthermore, replacing v_1 by v_i, and v_2 by v_{i+1}, and replacing the product $v \cdot \rho \cdot A$ by $\dot{m}_{b,i}$ gives:

$$F = v_{i+1}^2 \cdot \rho_{i+1} \cdot A_{i+1} - v_i^2 \cdot \rho_i \cdot A_i + \frac{d}{dt} (\dot{m}_{b,i} \cdot s) \tag{8.11}$$

According to the above, F represents the net force acting on the fluid along the flow filament of length s. This net force can be also written as the sum of 3 factors, namely, the gravitational force F_g, the external pressure forces F_p, acting on the cross-sectional areas A_1 and A_2 at the ends of the discrete flow filament, and the force due to friction F_f. Hence, inserting these three terms into the equation above, and rearranging it in order to have the time derivative on the left-hand side, yields:

$$\frac{d}{dt} (\dot{m}_{b,i} \cdot s) = v_i^2 \cdot \rho_i \cdot A_i - v_{i+1}^2 \cdot \rho_{i+1} \cdot A_{i+1} - F_p - F_f - F_g \tag{8.12}$$

Note: Any force F acting on the fluid is defined positive in the direction of positive flow, i.e. is positive when pointing from position s_1 to position s_2, or from area A_i to area A_{i+1}. Thus, the three forces F_p, F_f, and F_g have a negative prefix in the equation above, when assuming F_p positive for a positive pressure gradient in flow direction, F_f positive when acting against direction of flow, and assuming F_g positive for an increasing height difference in direction of positive flow.

The implementation of Equation 8.12 is accomplished in the MSL's base class "partial distributed flow". However, since in this work, the thermal performance modeling is of main concern and the evaluation of pressure wave

propagations within the heat exchanger ducts is not of interest, the momentum balance has been reduced to its steady-state formulation, by furthermore neglecting differences in velocity and the influence of the gravitational force. These assumptions lead to the equation $F_p = -F_f$, which states that the pressure difference between two neighboring control volumes is the pressure drop due to friction.

8.2.2 The shell-and-tube heat exchanger setup under consideration

A possible design option for an oil-to-molten-salt heat exchanger applicable for CSP active indirect thermal energy storage systems, is a TEMA-F [185] type design (see Figure 8.2). This heat exchanger type has two shell passes and two tube passes in U-tube design. The two shell passes are defined by installing a longitudinal baffle that separates the shell volume into two sections. Furthermore, a certain number of equally spaced vertical segmental baffles, having also a vertical baffle cut, force the shell side fluid flow along a "s-shaped" path, beginning at the shell-side inlet nozzle, passing through the two shell-side passes, and ending at the shell-side exit nozzle. The "s-shaped" flow is induced in order to increase the shell-side heat transfer coefficient, which is largest for ideal cross flow over the tube bundle. On Figure 8.2 on the left-hand side, section A-A displays the cross-sectional view of the heat exchanger. Due to installed baffles and the vertical baffle cut, 2 distinct and alternating tube bundle regions can be identified, namely the window zone (triangular-shaped shaded area) and the cross-flow zone (square-shaped shaded area). Examples for these two zones are also indicated on the right-hand side view of Figure 8.2 (shaded squares). Within the cross-flow zone, the shell-side convective heat transfer coefficient reaches its highest values since almost ideal cross-flow over the tube bundle occurs. However, within the window zone, the shell-side flow changes its flow direction by 180 degrees and flow conditions vary between pure parallel flow along the tubes and flow in a certain angle to the tubes, which usually stays far below the ideal 90 degrees (90 degrees would be ideal cross-flow). Compared to the "s-shaped" shell-side flow, the tube-side flow is relatively simple. As can be seen in Figure 8.2, the tube-side flow enters the heat exchanger via the tube-side inlet nozzle, passes through the inlet channel, and is distributed over a certain number (n_t) of U-tubes at the tube sheet. In each tube, the flow passes the upper straight tube section, goes through the bend, passes the lower straight tube section, and is mixed in the outlet channel before entering the tube-side outlet nozzle.

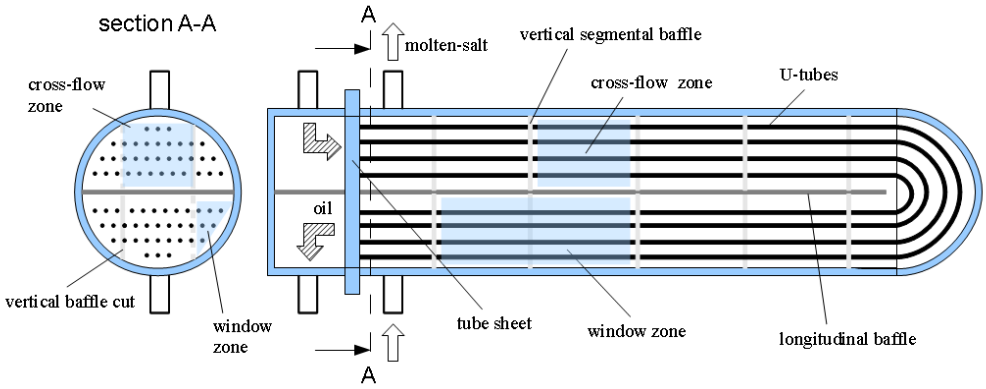

Figure 8.2: Front view of a TEMA-F type shell-and-tube heat exchanger - vertical segmental baffles - vertical baffle cut [111]

In order to achieve a clear and flexible model structure that is not limited to the single heat exchanger setup explained above, the final heat exchanger model will be composed of several generic sub-models. Each of the heat exchanger sub-models will be explained in the following.

8.2.3 The tube bundle model

The basic element of the heat exchanger's tube bundle is one single metal tube or pipe containing the tube-side fluid. Therefore, a dynamic pipe model, also containing a dynamic model of the pipe's steel wall, forms the base model of the tube bundle. As already explained in Section 8.2.1, the pipe flow itself is modeled according to the finite volume method formulating the momentum balance in steady state. The pipe's steel wall is modeled as a cylindrical one-dimensional conduction model, having one temperature node in radial direction. The wall's capacitance is assumed to be lumped together at this single temperature node. Heat conduction in flow direction is neglected. However, the cylindrical conduction model is divided into discrete sections in flow direction, so that each control volume of the pipe flow can be coupled to the corresponding wall segment. This gives one characteristic wall surface temperature for each finite pipe flow control volume. Figure 8.3 displays a scheme of one discrete section of the applied cylindrical conduction model. Note: The red squares represent a Modelica heat connector, i.e. the boundary between sub-models. At the connecting points, the heat flows sum up to zero and the temperatures are set equal. The model is based on the so-called "single layer cylinder" model of the free Modelica Buildings Library [186]. The governing equations for each discrete longitudinal section can be

described as follows:

$$R_1 = \frac{\ln\left(r_{center}/r_{inner}\right)}{2 \cdot \pi \cdot L_i \cdot k_{tube}} \tag{8.13}$$

$$R_2 = \frac{\ln\left(r_{outer}/r_{center}\right)}{2 \cdot \pi \cdot L_i \cdot k_{tube}} \tag{8.14}$$

$$\dot{Q}_1 = \frac{T_{tube\ inner\ i} - T_{tube\ i}}{R_1} \tag{8.15}$$

$$\dot{Q}_2 = \frac{T_{tube\ i} - T_{tube\ outer\ i}}{R_2} \tag{8.16}$$

$$C_{tube\ i} \cdot \frac{dT_{tube\ i}}{dt} = \dot{Q}_1 - \dot{Q}_2 \tag{8.17}$$

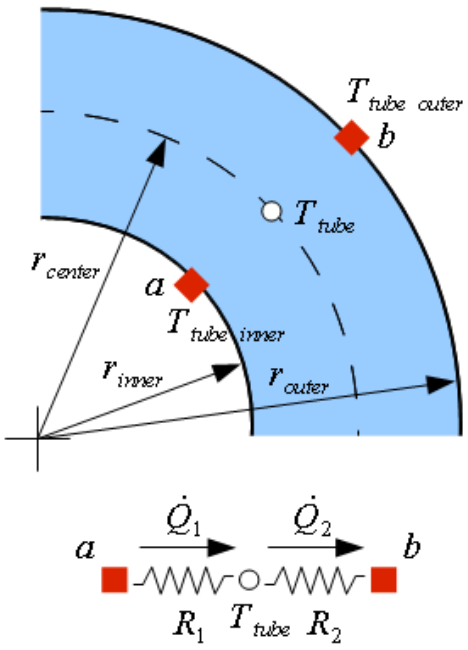

Figure 8.3: Cylindrical 1-D conduction model scheme (one discrete section) [111]

8.2.3.1 The heat transfer between the tube-side fluid and the tubes' inner walls

According to the MSL, the convective heat transfer is defined via a replaceable wall heat transfer model, which defines the relationship between the tube's inner wall temperatures, the fluid bulk temperatures (see Figure 8.1, T_1 to T_n) and the net heat flows $\dot{Q}_{net\,i}$. Thus, the tube bundle model can easily be adapted for different flow conditions, by simply replacing the heat transfer sub-model, which basically means that the heat transfer coefficient is estimated by using different Nusselt number correlations, fulfilling Newton's convective heat transfer law:

$$\dot{Q}_{net\,i} = h_{fluid\,i} \cdot A_{tube\,inner\,i} \cdot (T_{tube\,inner\,i} - T_i) \tag{8.18}$$

To correctly estimate the heat transfer for turbulent pipe flow, which occurs during typical operation, the following Nusselt number correlation for smooth pipes, as proposed by Gnielinski [187], is used:

$$Nu = \frac{h_{fluid} \cdot D_{inner}}{k} = \frac{(f/8) \cdot (Re - 1000) \cdot Pr}{1 + 12.7 \cdot \sqrt{f/8} \cdot (Pr^{2/3} - 1)} \cdot \left[1 + (D_{inner}/L)^{2/3}\right] \cdot \left[\frac{Pr}{Pr_{wall}}\right]^{0.11} \tag{8.19}$$

where:

$$f = (1.82 \cdot \log Re - 1.64)^{-2} \tag{8.20}$$

Equation 8.19 is regarded to be valid for Reynolds numbers between 2300 and 1e6 ($2300 < Re < 1e6$) and Prandtl numbers between 0.6 and 1e5 ($0.6 < Pr < 1e5$) [187]. Abraham et al. [188], reassured the validity of Equation 8.19 for the transition region for Reynolds numbers above 3100.

8.2.3.2 The pressure drop due to wall friction in straight pipe sections

Within straight pipe sections of the tube bundle, the pressure drop due to wall friction is calculated according to the well known correlations published by Moody [189]. Since the MSL does already feature a thorough implementation of pressure drop functions that are valid for the whole flow regime ("detailed wall friction package"), these are used throughout this work.

8.2.3.3 Adapting the pipe model in order to obtain the tube bundle's equivalent thermal behavior

Now, having defined the basic pipe model (see Figure 8.4), the first idea that comes into mind would be the definition of a Modelica array whose size equaled the number of tubes (n_t). Although this approach might work for very small heat exchangers, it is definitely not suitable for larger ones where the number of tubes (n_t) easily exceeds 3000. Thus, tubes that have similar thermal boundary conditions must be lumped together to one single "tube-like" object, having the equivalent fluid flow volume, the equivalent tube wall mass, as well as the equivalent thermal resistance. This can easily be achieved by instantiating the dynamic tube model explained above, but multiplying each control volume size V_i and each wall section length L_i, and each area of heat transfer ($A_{tube\ inner\ i}$ and $A_{tube\ outer\ i}$ of the distributed wall heat transfer models) by the number of lumped tubes ($n_{t\ lumped}$). Note: The tubes' inner radius and the tubes' wall thickness stay the same, i.e. the real tubes' radius and the real tubes' wall thickness.

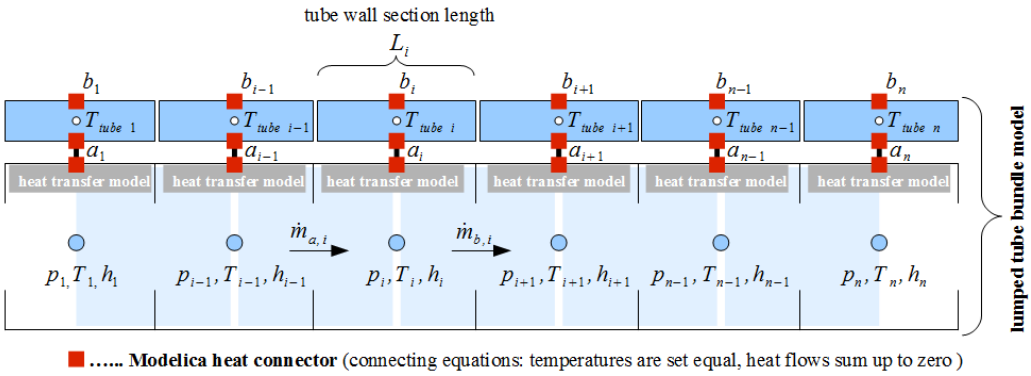

Figure 8.4: Scheme of the lumped tube bundle model [111]

8.2.4 The shell-side flow model

Using the above described tube bundle sub-model, tubes of bundle sections that have similar thermal boundary conditions can be lumped together, obtaining a relatively simple transient model of the tube-side flow and the tube wall. In order to obtain a corresponding model for the remaining shell-side volume, the "s-shaped" shell-side flow is also discretized using a certain number of control volumes, i.e. according to the well proven cell-method [118, 119, 120, 121, 123, 131]. Again, the basic governing equations are those

as described in Section 8.2.1. The total shell-side flow volume can be subdivided into two alternating main zones that have considerably different flow conditions, namely the window zones and the cross-flow zones. By also taking the shell-side inlet and outlet regions into account (right after and before the inlet/outlet nozzles), the shell-side flow may be described by a row of discrete zones, which can be written as follows: inlet zone – window zone – cross-flow zone – window zone – cross-flow zone – window zone – etc. – outlet zone. Hence, the shell-side flow is modeled by assigning to each zone one finite control volume.

8.2.4.1 The heat transfer between the shell-side fluid and the tubes' outer walls

As stated before, the ideal shell-side flow follows a "s-shaped" path, which is determined by the vertical segmental baffles. However, in reality, these ideal flow conditions are not reached due to leakage and bypass streams [110]. Furthermore, eddies, induced by the vertical segmental baffles, prevent the flow within the cross-flow zones from reaching ideal conditions [114]. Therefore, the estimation of the average shell-side heat transfer coefficient is rather difficult. A detailed empirical method to estimate the average shell-side heat transfer coefficient was proposed by Bell, who performed numerous experiments with shell-and-tube heat exchangers at the University of Delaware [110]. This heat exchanger rating procedure is widely known as the Bell-Delaware method and estimates the shell-side heat transfer coefficient by multiplying the ideal value for cross-flow over a tube bundle by correction factors, which take into account baffle configuration, baffle leakages, bypass streams, baffle inlet and outlet spacing, as well as adverse temperature gradients in laminar flow [110]. This methodology is well established and recently, its validity has been reconfirmed by CFD simulations [114]. Thus, also for this study, the Bell-Delaware method is used to estimate the shell-side heat transfer coefficient for each of the discrete shell-side control volumes. This is realized as follows: For each control volume, the ideal cross-flow heat transfer coefficient is calculated according to the local fluid properties and the local flow velocity. Then, for each control volume the final heat transfer coefficient is obtained by multiplying the ideal cross-flow coefficient by the Bell-Delaware factor. The heat transfer relationship as stated by Equation 8.18 is correspondingly applied to the shell-side flow. The ideal shell-side heat transfer coefficient for cross-flow over a tube bundle is evaluated according to Gnielinski [154], who provided Nusselt number correlations for single tube rows and tube bundles under cross-flow, which are based on numerous measured values, valid for Reynolds numbers between 1 and 1e6, and

Prandtl numbers between 0.7 and 700. These correlations depend on several tube bundle geometry parameters, such as tube pitch, outer tube diameter, and tube bundle arrangement (e.g. staggered or in-line). Thus, a detailed citation of these correlations is out of scope and it is referred to the original manuscript [154].

8.2.4.2 The pressure drop on the shell side

The pressure drop on the shell side is caused by several factors. In the first place, one part of the pressure drop is caused by the shell-side inlet and outlet nozzles, which lead to a sudden expansion, or a sudden contraction of the flow. Furthermore, the flow passes a certain number of tube rows and is periodically contracted at the narrowest sections of the window zones (baffle cut). Also here, it is a common practice to estimate the shell-side pressure drop according to empirical correlations. In this work, correlations proposed by Gaddis & Gnielinski [156] are used. Since these correlations are rather complicated and depend on several geometrical parameters as well, a detailed citation is left aside. It is therefore also referred to the original manuscript [156], or to its detailed citation in the VDI Heat Atlas [155]. Finally, it should be noted that a lumped pressure drop approach is used for the shell-side flow model, i.e. the whole shell-side pressure drop is lumped together, either at the inlet, or at the outlet, assigning all shell-side control volumes the same pressure level.

8.2.5 The final shell-and-tube heat exchanger model

The final shell-and-tube heat exchanger model is composed of one or more instances of each of the sub-models described above. In the case of a TEMA-F type heat exchanger, which is considered in this work, 6 instances of the tube bundle flow model and 1 instance of the shell side flow model can be used. Figure 8.5 displays the top view of the shell-and-tube heat exchanger under consideration. According to section B-B, the whole tube bundle can be divided into 2 tube bundle sections that only consist of cross-flow zones (shaded squares, c and d), and 4 tube bundle sections that only consist of window zones (shaded triangles, a, b, e and f). The tube bundle model instance d is also indicated on the right-hand side sketch on Figure 8.5 (“d.1” to “d.6”). Of course, the entrance/outlet sections as well as the tube bend sections have slightly different flow conditions, but are added to either the window tube bundle sections or the cross-flow tube bundle sections (e.g. shaded squares “d.1” and “d.6” in Figure 8.5). In the case of this heat exchanger scheme, the tube bundle model d consists of 6 finite control volumes, i.e. “d.1” to

"d.6". The same applies to tube bundle model instance c. Correspondingly, the tube bundle model instance b has 4 finite control volumes, where the length of "b.1" equals the length of "d.1", but the length of "b.2" equals the sum of the lengths of "d.2" and "d.3", etc. To complete the upper shell side volume, the tube bundle model instance f consists of 3 finite control volumes, where the length of volume "f.1" equals the sum of the lengths of "d.1" and "d.2", etc. In order to complete the tube-side flow, the upper tube bundle models (b, d and f) are connected with the lower tube bundle models (a, c and e) via 3 instances of a tube bend model, which calculates the corresponding pressure drop induced by a 180° tube bend having the mean radius of curvature of the bundle. Since a general implementation of a tube bend is already available in the MSL package "fluid dissipation", which was implemented according to Idelchik [157], the corresponding pressure drop functions are used throughout this work. Finally, two additional control volumes are added, which represent the tube-side inlet channel, and the tube-side outlet channel, a crucial model feature in order to accurately reproduce the relevant dynamics [116, 121]. The pressure drops induced by the tube-side inlet and outlet nozzle as well as by the tube sheet inlet and outlet (sudden contractions and sudden expansions) are considered via the well known relationship $\Delta p = \zeta \cdot \rho/2 \cdot v^2$, providing appropriate pressure drop factors ζ according to Gaddis & Gnielinski [156] and the VDI Heat Atlas [155], respectively.

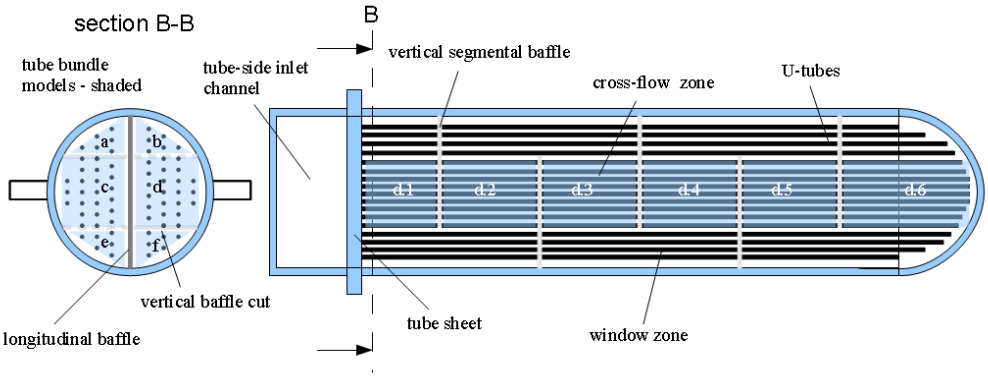

Figure 8.5: Top view of a TEMA-F type shell-and-tube heat exchanger - vertical segmental baffles - vertical baffle cut [111]

Figure 8.6 also displays the top view of the heat exchanger setup under consideration. But unlike Figure 8.5, Figure 8.6 indicates the upper part of the shell side flow model, i.e. its finite control volumes "shell.1" to "shell.11" (shaded squares). Here, the "s-shaped" path can be well identified. In order to finish the shell-and-tube heat exchanger model itself as one comprehensive

Modelica class, the tube bundle models' heat connectors are correspondingly connected to the shell-side flow model's heat connectors. For example, considering the scheme in Figure 8.5 and Figure 8.6, the control volume "shell.2" is connected to the pipe wall segment of tube bundle model "f.1", the control volume "shell.3" is connected to the pipe wall segment of tube bundle model "d.2", and the control volume "shell.4" is connected to the wall segment of tube bundle model "b.2", etc.

The whole fluid flow within the heat exchanger model is considered as incompressible, i.e. several pressure drops are calculated as function of mass flows. Finally, it has to be noted, that the above described shell-and-tube heat exchanger model is just one example among many possibilities. Due to the clear separation into distinct sub-models, arbitrary shell-and-tube heat exchanger flow setups can be described in an object-oriented and intuitive way, by simply modifying the couplings between shell-side control volumes and pipe wall segments.

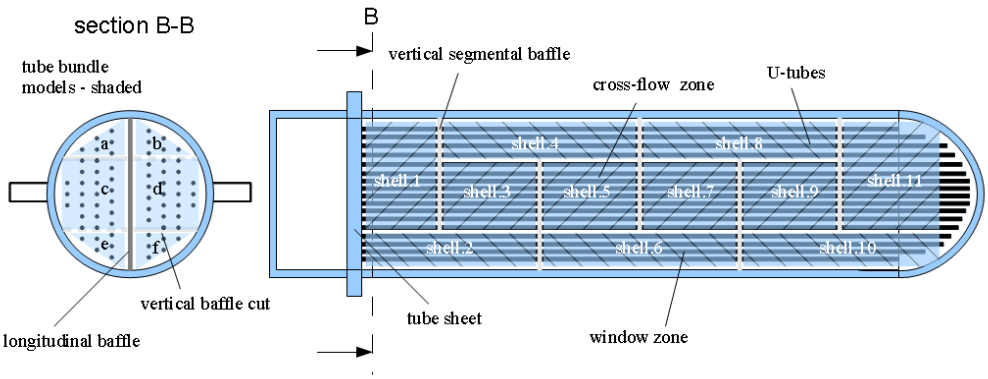

Figure 8.6: Top view of a TEMA-F type shell-and-tube heat exchanger - vertical segmental baffles - vertical baffle cut; upper shell-side flow model control volumes are indicated on the right-hand side (shell.1 to shell.11) [111]

8.2.6 The fluid properties

Within the MSL, all specific media property functions are decoupled from the library components by defining a replaceable "Medium package" in each of them. Basically, all fluid property function names and interfaces are defined within the base class "partial medium". In order to allow a full replaceability, each specific medium model extends from this base class the "partial medium" and defines the specific media related relationships by re-declaring each necessary medium property function. Thus, every single component of

the library is not limited to a single medium. In fact, it can easily be adapted for the use of different fluids, by simply replacing the default medium package when instantiating the final model.

Since the media properties for solar salt, as well as that for thermal oil are not yet available in open Modelica libraries, these features have been newly implemented. Both liquids are modeled as incompressible fluids according to [12], and [158, 172], respectively. In order to allow for efficient simulation code generation, several inverse and derivative functions are implemented as well.

8.2.7 The model's translation and its numerical integration, i.e. simulation

In this work, the developed Modelica code has been translated into numerical simulation code using a state-of-the-art commercial Modelica tool, applying its differential-algebraic system solver DASSL [178, 179]. This algorithm applies an implicit method for the numerical integration of the governing ordinary differential equations. In particular, it approximates the derivatives using a k^{th} order backward differentiation formula, where k ranges from 1 to 5. At every step it chooses the order and the step size based on the behavior of the solution. Newton's method is used to solve the resulting equations for the solutions at each discrete point in time [178, 179]. A detailed description of the code DASSL and its usage was provided by Brenan et al. [179]. Thus, for a detailed derivation of the numerical method applied, the interested reader is referred to this work.

8.3 The model validation

The validation of the above presented heat exchanger modeling methodology has been performed using theoretical as well as experimental data available in open literature.

8.3.1 The theoretical model validation via a model comparison

In order to check the simulation results for consistency, the above explained tube bundle sub-model (Section 8.2.3) and the shell-side sub-model (Section 8.2.4) have been used to reproduce a reference case available in the literature. In particular, the heat exchanger setup according to case II, as defined by Correa & Marchetti [121], has been chosen as the reference case. Correa &

Marchetti [121] provided transient response data for a shell-and-tube heat exchanger having 2 tube-side passes and 1 shell-side pass (TEMA-E [185] type shell) and water as fluid on both sides. The specific heat exchanger setup is shown in Figure 8.7. The geometrical and technical details of this reference setup are given in Table 8.1.

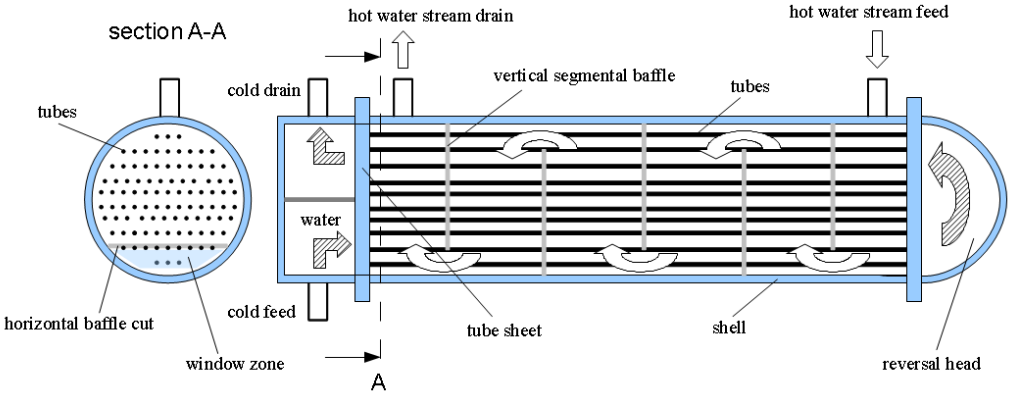

Figure 8.7: Shell-and-tube heat exchanger scheme having 1 shell-side pass and 2 tube-side passes – According to case II of Correa & Marchetti [121]

This work's model of the reference case heat exchanger consists of one tube bundle sub-model instance and one shell-side sub-model instance, having 32 control volumes (or cells) in each case. The cells have been correspondingly connected in order to reproduce the flow setup as displayed in Figure 8.7. Like in [121], the tube-side inlet/outlet channel as well as the tube-side reversal head (see Figure 8.7) are not considered. The water is modeled according to the state-of-the-art IAPWS-IF97 [190] standard (which is already part of the Modelica Standard Library), by simply replacing the default media packages during model instantiation.

The entry conditions of the tube-side fluid and the shell-side fluid, water in both cases, during the start-up simulation [121], are as follows: The hot stream enters on the shell side, at a mass flow rate of 22.05 $\frac{kg}{s}$, a temperature of 34 °C and a pressure of 2 bar. The cold stream enters on the tube side, at a mass flow rate of 35.3 $\frac{kg}{s}$, a temperature of 24 °C and a pressure of 2 bar as well. The initial conditions of each control volume or cell (initialization problem) of the reference simulation are the boundary mass flow rates, as stated above, and the entry temperature of the cold water stream, i.e. each control volume is initialized with 24 °C at simulation start. After completing the heat exchanger's start-up, i.e. both fluid outlet temperatures have converged to their corresponding steady-state values, the shell-side stream is subjected to a sudden inlet temperature step, from 34 °C up to 36.5 °C at

simulation time 13.5 s. The simulation results are shown in Figure 8.8. The simulated shell-side outlet temperature of this work's model is represented by the black thin solid line. Its corresponding counterpart obtained by Correa & Marchetti [121] is indicated by the black dashed line. For the case of the tube-side fluid's outlet temperature, this work's simulation result is displayed by the gray thin solid line, and the result obtained by Correa & Marchetti [121] is represented by the gray dotted line. It can be said, that the simulation results obtained by the two different models correlate quite well. The root-mean-square errors calculated according to Equation 8.21 between the two simulation results, constitute about 0.26 °C for the shell-side stream, and 0.25 °C for the tube-side stream, which is about 4.8% and 7% based on the final steady-state temperature decrease (shell side) and increase (tube side), respectively. As already stated by Correa & Marchetti [121] in their original work, it is interesting to note that there are unequal time delays for the fluid streams, and additionally, during a significant time interval, the cold fluid stream (tube side) leaving the heat exchanger is hotter than the "will-be" hot stream (shell side), which can be explained by the specific flow arrangement (see also Figure 8.7).

$$RMSE = \sqrt{\frac{\sum_{j=1}^{z} \left(simulated_j - simulated\,CM_j\right)^2}{z}} \tag{8.21}$$

Table 8.1: Shell-and-tube heat exchanger data [111]

Design parameters	Case II [121]	Case II-1 [116]	TEMA-F oil-salt
Area of heat transfer (m)	46.6	5.84	4995.34
Mean overall heat transfer coefficient ($Wm^{-2}K^{-1}$)	1470	$\approx$ 1430	$\approx$ 1120 (nominal load)
Tube side volume (m^3)	0.14	0.03	13.41
Shell side volume (m^3)	0.14	0.053	11.46
Shell inner diameter *) (m)	0.454	0.205	2.02
Outer center line diameter of tube bundle *) (m)	0.434	0.195	2
Total number of tubes *) (-)	470	40	3794
Tube bundle layout (-)	staggered 45° square	triangular	staggered 45° square
Tube outer diameter (m)	0.0158	0.019	0.01905
Tube inner diameter (m)	0.0138	0.0148	0.015
Tube pitch (m)	0.018	0.0238	0.0286
Tube length per pass, or distance between tube sheets (TEMA-E) (m)	2	2.44	10
Number of shell-side passes (-)	1	1	2
Number of tube-side passes (-)	2	4	2
Number of baffles (-)	15	14	30
Baffle cut (%)	20	35	20
Baffle center spacing (m)	0.125	0.163	0.5
Baffle inlet/outlet spacing (m)	0.125	0.163	0.8

*) Corresponding design parameter estimates according to Shah & Sekulic [110] if not explicitly stated.

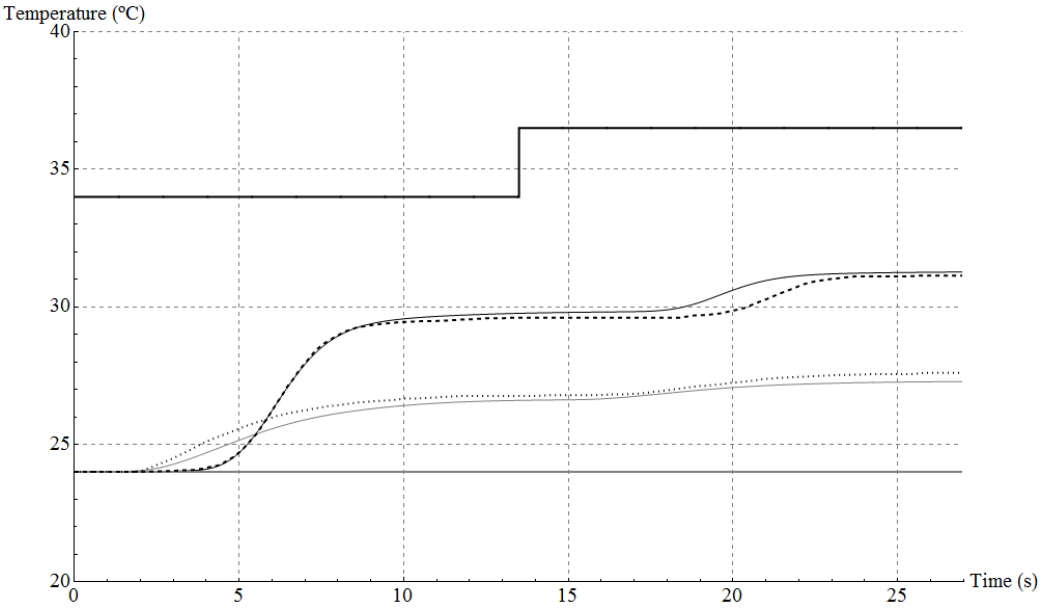

Figure 8.8: TEMA-E start-up simulation including an inlet temperature step response – black thick solid line: shell-side inlet temperature, black thin solid line: simulated shell-side outlet temperature of this work, black dashed line: simulated shell-side outlet temperature by Correa & Marchetti [121], gray thick solid line: tube-side inlet temperature, gray thin solid line: simulated tube-side outlet temperature of this work, gray dotted line: simulated tube-side outlet temperature by Correa & Marchetti [121]

8.3.2 The experimental model validation

Besides the simulation presented in Section 8.3.1, the heat exchanger sub-models have also been validated against experimentally obtained data. In particular, experiments originally presented by Morris [116] have been used, specifically case II-1 [116]. The used experimental data is displayed in Figure 4 of his original work. Morris [116] performed measurements on industrial size shell-and-tube heat exchangers having 1 shell-side pass and 4 tube-side passes (see Figure 8.9). The heat exchanger details are given in Table 8.1 (Case II-1).

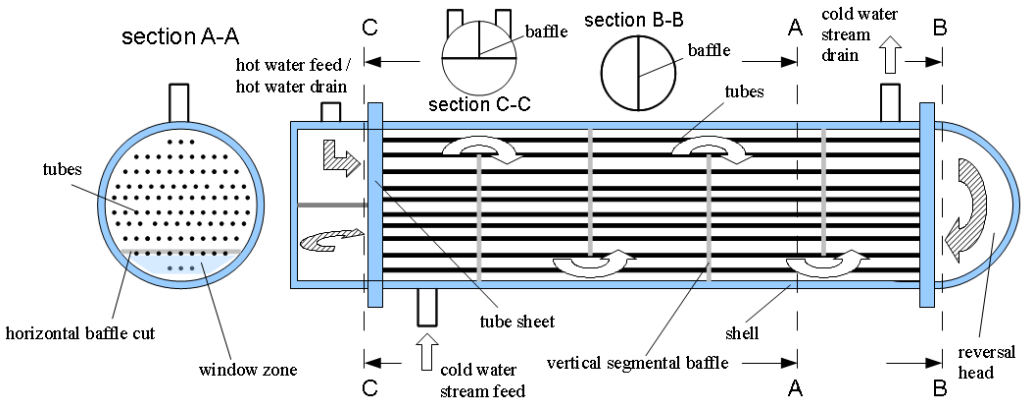

Figure 8.9: Shell-and-tube heat exchanger scheme having 1 shell-side pass and 4 tube-side passes – According to heat exchanger setup II of Morris [116]

The heat exchanger setup as displayed in Figure 8.9 has been reproduced using 4 instances of the tube bundle sub-model, one instance of the shell-side flow sub-model and 5 additional ideally mixed volumes, representing the tube-side inlet/outlet channels as well as the reversal head volumes. These 5 additional tube-side volumes are sized as follows (in sequence of the tube-side flow): 2.5 dm^3, 2.0 dm^3, 4.1 dm^3, 2.0 dm^3, 2.5 dm^3 [116]. The control volumes (15 CVs for each tube bundle model, and 30 CVs for the shell-side flow) have been correspondingly linked in order to reproduce the given flow setup as shown in Figure 8.9. Morris [116] used resistance thermometers for the temperature measurement, which were directly installed in the heat exchanger nozzles. The temperature recordings were made on a high speed oscillograph so that the measuring and the recording equipment had a negligible effect on the dynamic measurements. Dynamic data were obtained by introducing a temperature pulse to the tube-side inlet (through the injection of steam into city tap water) and recording the time history of that

temperature and the tube-side outlet temperature [116]. He converted the experimental pulse information into frequency response data using a pulse technique based on the Fourier transformation.

The boundary conditions of the specific experiment reproduced in this work are as follows: The hot water stream enters on the tube side at a temperature of 38.2 °C and a volumetric flow rate of 13.9 $\frac{m^3}{h}$. The cold water stream enters on the shell side at a temperature of 19.2 °C and a volumetric flow rate of 4.5 $\frac{m^3}{h}$. The inlet pressure levels were set to 2 bar. The water is again modeled according to the state-of-the-art IAPWS-IF97 [190] standard.

Superposing a sinusoidal temperature signal having an amplitude of 10 °C on the tube-side inlet temperature of 38.2 °C, and running a set of simulations at different excitation frequencies ω, yielded the Bode diagram as shown in Figures 8.10 and 8.11 (solid lines). In particular, Figure 8.10 shows the normalized amplitude ratio between the output temperature amplitude at the tube-side outlet and the excitation temperature amplitude at the tube-side inlet. Since the steady-state gain is constant (≈ 0.78) and equals the amplitude ratio at an excitation frequency of zero it has been used to normalize the amplitude ratio via division. Hence, the normalized amplitude ratio approaches the value 1 for low excitation frequencies. Furthermore, the comparison between the theoretical and the experimental data is not obscured by small deviations in steady-state results. As can be observed in Figures 8.10 and 8.11, the simulated data of this work (solid lines) agrees well with the experimental data obtained by Morris [116] (dots).

Thus, summarizing the model validation, it can be said that this work's model formulation has been accomplished correctly, since the obtained simulation results correlate well with simulated data and experimental measurements from available literature. There is thus confidence that the model also yields reasonable results for different flow arrangements and other single-phase fluids, of course, given that all dimensionless correlations are evaluated within their ranges of validity.

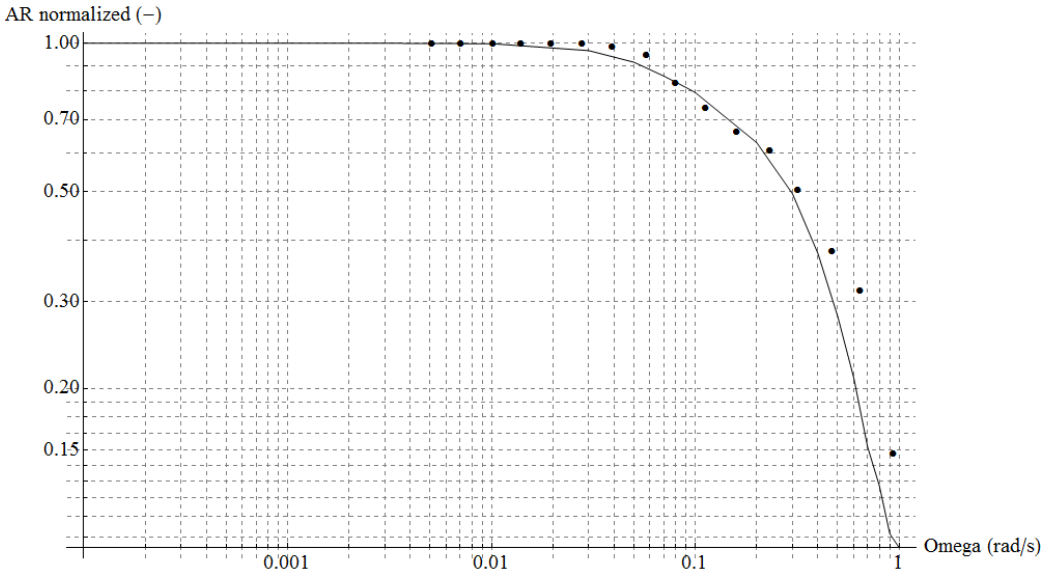

Figure 8.10: Log-log plot of the normalized amplitude ratio versus ω – solid line: simulation results, dots: experimental data according to Morris [116]

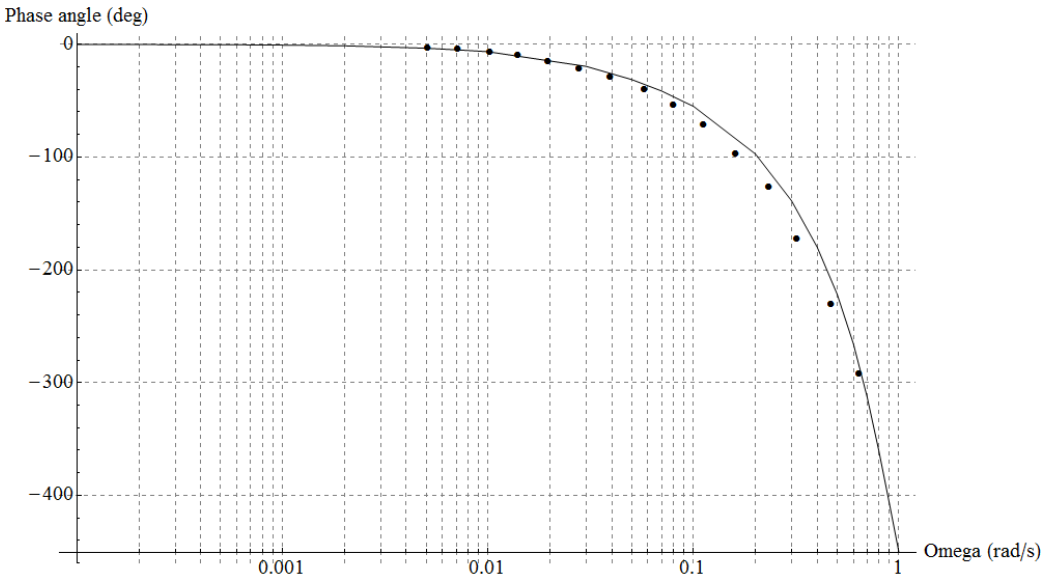

Figure 8.11: Semi-log plot of the phase shift versus ω – solid line: simulation results, dots: experimental data according to Morris [116]

8.4 Transient response simulations of a typical oil-to-molten-salt heat exchanger train configuration used in CSP thermal energy storage systems

Figure 8.12 shows the general setup of an active indirect two-tank thermal energy storage system for CSP. The basic components are the molten salt storage tanks (the hot tank and the cold tank) and the oil-to-molten-salt heat exchanger train, which typically consists of 3 shell-and-tube subunits connected in series [108]. Each shell-and-tube subunit is considered to have two shell passes with a longitudinal baffle and two tube passes in U-tube design as described in Section 8.2.2 of this work. The assumed design details of one single subunit are given in Table 8.1 (TEMA-F oil-salt).

In the following, the results of transient response simulations of such a heat exchanger train, as depicted in Figure 8.12, will be presented. It should be noted that the final model class of this heat exchanger train features 21433 equations and a simulation of a 2 h experiment typically takes around 8 min on a standard desktop computer (3.10 GHz), of course depending on the performed simulation and the number of grid points.

In general, a heat exchanger in operation can be seen as a self-regulating processes that features first-order-plus-time-delay behavior, i.e. it can be described by the three parameters as process gain K_s, dead time Θ and time constant τ (see Equation 8.22), however, due to non-linearities, only in the range close to a certain operating point.

$$G(s) = \frac{K_s \, e^{-\Theta \, s}}{\tau \, s + 1} \tag{8.22}$$

As it is a self-regulating process, the heat exchanger's process variables settle at their new steady-state values after any arbitrary change in any input variable. However, in order to achieve the desired behavior, i.e. in order to reach the desired outlet temperatures for a given operating point, the mass flow rates have to be controlled correspondingly. This is usually done via standard PI feedback control loops, due to their easy implementation.

During the operation of the thermal energy storage system as depicted in Figure 8.12, the HTF mass flow rate is a given boundary condition of the storage system and the major disturbance variable of the controlled system, due to abrupt changes in load, and particularly, due to changes between charging and discharging mode (HTF flow reversal). Furthermore, also the HTF inlet temperatures are given boundary conditions and are disturbance

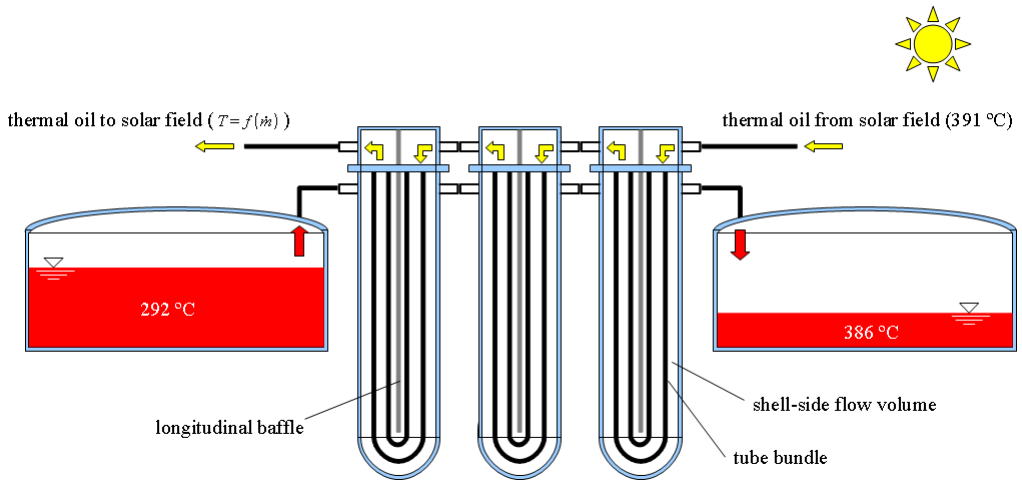

Figure 8.12: Active indirect two-tank thermal energy storage system scheme (charging mode) [111]

variables as well, as, e.g., during charging mode, the solar field's outlet temperature cannot be perfectly controlled to the design value of typically 391 °C. In addition, having the molten salt within the storage tanks at a certain temperature (around 386 °C and 292 °C depending on thermal losses and operation), which also defines the molten salt inlet temperatures of the heat exchanger train, the molten salt mass flow rate is the only free process variable that needs to be controlled in such a way that either the molten salt outlet temperature (charging), or the HTF outlet temperature (discharging) keeps to the assigned set-point. In particular, during storage system charging mode, the molten salt outlet temperature is kept to the hot tank's design temperature. On the other hand, during storage system discharging mode, the HTF outlet temperature is kept to the desired feed temperature of the CSP plant's steam generator, which is assumed to be 376 °C, in this work. In this way, the feed temperature of the cold molten salt tank varies according to the thermal characteristic of the heat exchanger train, i.e. it is not controlled to keep to the cold tank's design temperature of 292 °C.

In order to state typical heat exchanger process parameters for a active indirect two-tank thermal energy storage configuration, the three parameters as process gain K_s, dead time Θ and time constant τ have been obtained via the so-called process reaction curve method. Thus, evaluating step response simulations at different load conditions and applying the tangent method at the point of inflection [191], yielded the data given in Table 8.2. Note: The heat exchanger input variable that is subjected to the step changes is the

molten salt mass flow for charging and discharging mode. The corresponding output variable is the HTF outlet temperature in discharging mode, and the molten salt outlet temperature in charging mode. Furthermore, it must be kept in mind that the so-obtained process parameters are only representative for the given heat exchanger load conditions and mass flow step height. Due to process non-linearities, results typically vary for different step sizes and load conditions.

Table 8.2: Process parameters of a typical oil-to-molten-salt heat exchanger train configuration for CSP [111]

Operating mode	HTF mass flow (kg/s)	Δ mass flow salt (kg/s)	Process gain K_s $(K\ s\ kg^{-1})$	Dead time Θ (s)	Time constant τ (s)
Charging	600	50	-0.046	≈ 0	100
Charging	300	50	-0.12	≈ 0	201
Charging	150	50	-0.24	≈ 0	395
Discharging	600	50	0.042	2.7	113
Discharging	300	50	0.082	4.7	194
Discharging	150	50	0.14	8.5	298

The task of the control design is to define an appropriate control algorithm that keeps the hot tank's feed temperature (during charging mode) as close as possible to its design temperature regardless of occurring disturbances, capturing as much solar energy as possible. On the other hand, during discharging mode, the HTF inlet temperature of the steam generator should be kept as constant as possible in order to avoid fatigue caused by thermal stresses in thick-walled components due to too large temperature gradients. Typical rate-of-change limits in temperature for CSP steam generators constitute about 2-3 °C per minute.

Besides the step response simulations as presented in Table 8.2, the numerical model of the heat exchanger train has also been subjected to sinusoidal molten salt mass flow input signals at different excitation frequencies ω, thus obtaining the frequency response of the system at nominal load conditions in discharging mode. In particular, the molten salt mass flow input has been obtained via superposing a sinusoidal signal (with 50 $\frac{kg}{s}$ in amplitude) on the nominal molten salt mass flow. The remaining input variables have been set to constant values (nominal conditions). The corresponding output variable, having a certain variation in amplitude and phase, is the outlet temperature of the HTF. The resulting Bode plot is shown in Figures 8.13 and 8.14. Basically, the expected first-order-plus-time-delay behavior can be observed. Hence, for very low excitation frequencies, the system approaches the steady state and the normalized amplitude ratio (normalized by the steady-state gain) approaches the value one. For high frequencies, the

output deviations are completely attenuated. Due to the time delay (dead time), the phase shift is unbounded for high frequencies.

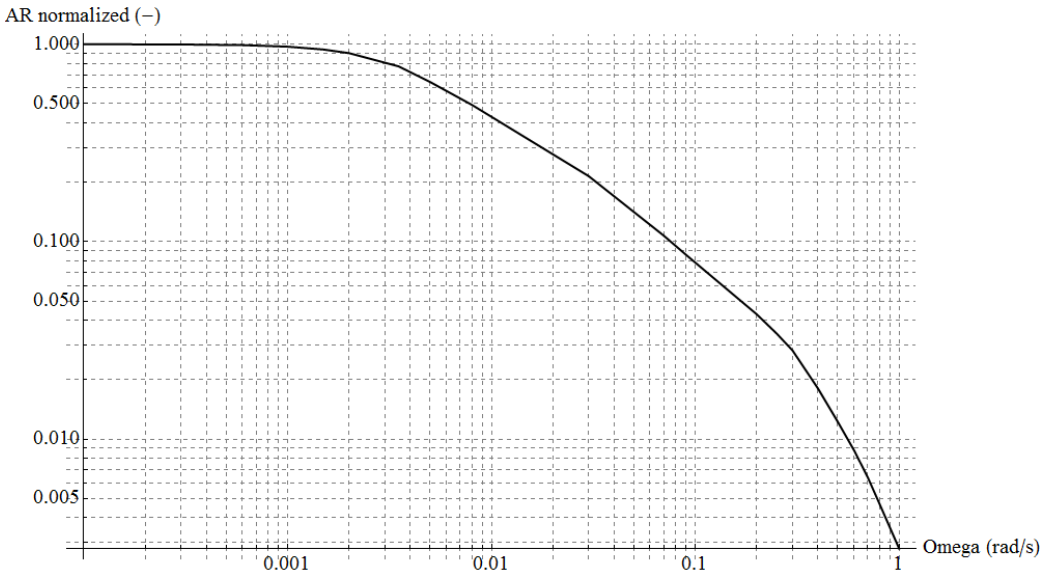

Figure 8.13: Log-log plot of the normalized amplitude ratio versus ω – Oil-to-molten-salt heat exchanger under nominal conditions (discharging) [111]

Additionally, the heat exchanger train has also been subjected to step changes in HTF mass flow rate, and to step changes in HTF inlet temperature, in both cases for storage system charging mode, i.e. the HTF stream is the hot stream, entering at 391 °C at simulation start, which is assumed to be the ideally controlled solar field outlet temperature. The molten salt enters the heat exchanger at a temperature of 292 °C, the temperature level of the cold molten salt tank. In all presented simulations, the molten salt mass flow rate has been set to the corresponding constant value that leads to a molten salt outlet temperature of 386 °C (the hot tank's design temperature) in steady-state conditions for the initial HTF mass flow rate. Table 8.3 states the boundary conditions of the performed simulations.

Figure 8.15 displays the simulation results of case A according to Table 8.3. Starting from steady-state conditions, the HTF mass flow rate is subjected to a negative step change at simulation time t = 2500 s, from 600 $\frac{kg}{s}$ down to 300 $\frac{kg}{s}$. The remaining boundary conditions remain constant. As expected for this case of a self-regulating process, it can be well observed that both fluid duct outlet temperatures converge to their new steady-state values. The HTF outlet temperature reaches its new steady state after about 10 min, almost reaching the inlet temperature of the cold stream. The outlet

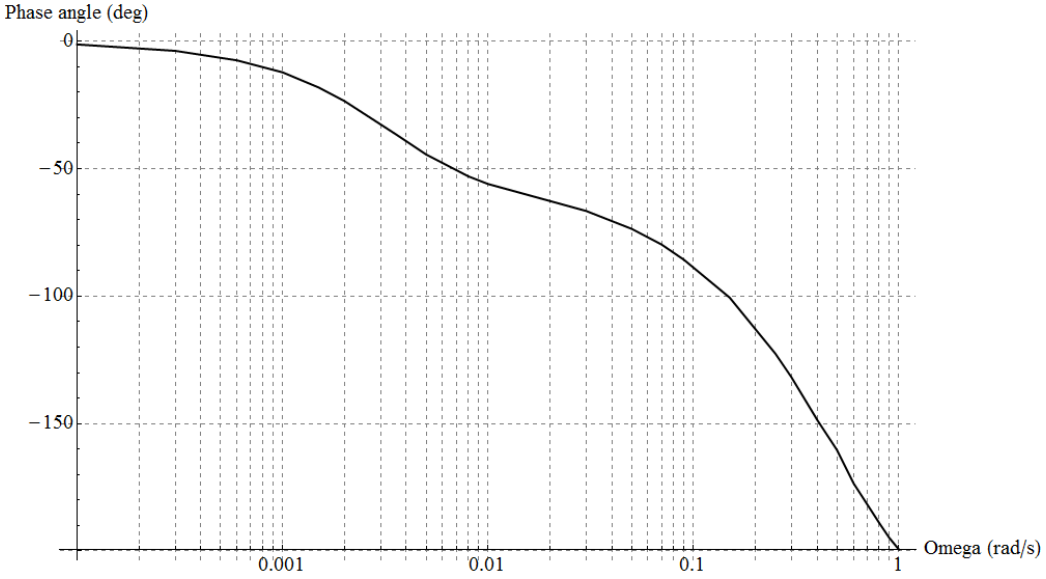

Figure 8.14: Semi-log plot of the phase shift versus ω - Oil-to-molten-salt heat exchanger under nominal conditions (discharging) [111]

Table 8.3: Experiment definitions [111]

Index	Experiment	Tube-side (HTF) inlet temperature (^oC)	Shell-side (salt) inlet temperature (^oC)	Tube-side (HTF) mass flow rate (kg/s)	Shell-side (salt) mass flow rate (kg/s)
A	HTF mass flow step 100% - 50% load	391	292	600 until t = 2500 s 300 until t = 5000 s 600 remaining time	899
B	HTF mass flow step 50% - 25% load	391	292	300 until t = 3500 s 150 until t = 7000 s 300 remaining time	470
C	HTF inlet temperature step at 100% load	391 until t = 2500 s 371 until t = 5000 s 391 remaining time	292	600	899
D	HTF inlet temperature step at 50% load	391 until t = 3500 s 371 until t = 7000 s 391 remaining time	292	300	470

temperature of the molten salt, however, converges to its new steady state about 6 min later. At simulation time t = 5000, the HTF mass flow rate is subjected to a positive step change, from 300 $\frac{kg}{s}$ up to 600 $\frac{kg}{s}$ again. It is interesting to note, that now both fluid streams approach approximately at the same time their new steady-state conditions (after about 19 min).

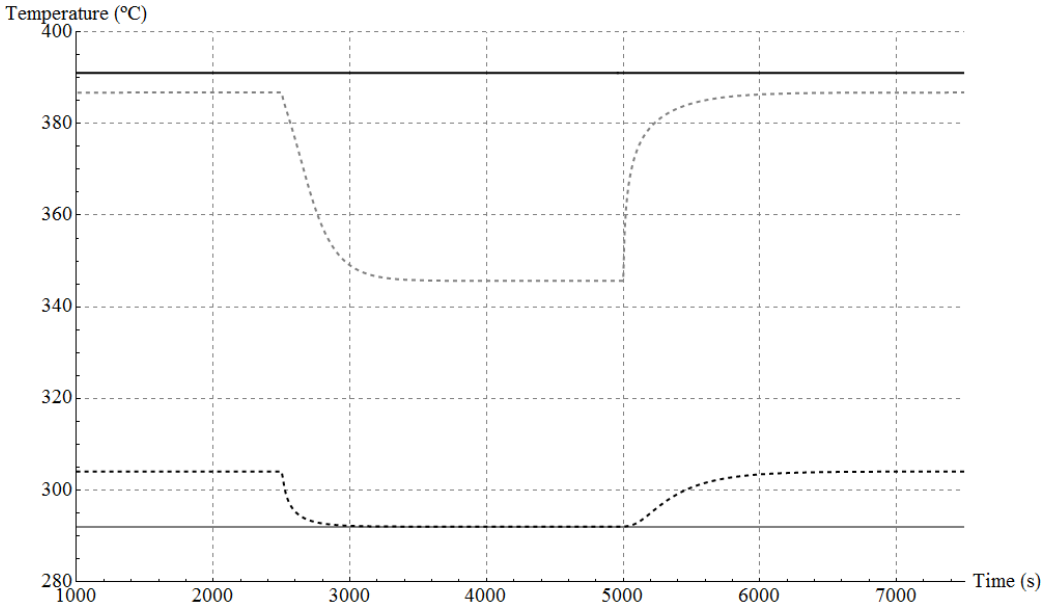

Figure 8.15: HTF mass flow rate step response simulation according to experiment A in Table 8.3 – black solid line: HTF inlet, black dashed line: HTF outlet, gray solid line: molten salt inlet, gray dashed line: molten salt outlet [111]

Figure 8.16 treats the corresponding case at lower mass flow rates (Case B of Table 8.3). Again, starting from steady-state conditions, the HTF mass flow rate is subjected to a negative step change at simulation time t = 3500 s, from 300 $\frac{kg}{s}$ down to 150 $\frac{kg}{s}$. In principle, the outlet temperature responses experience the same transients like in case A. However, due to the lower mass flow rate and non-linearities of the process, its characteristic parameters change. As can be well observed in Figure 8.16, the time constants increase considerably, since it takes the fluid outlet temperatures approximately 42 min to reach their new steady-state conditions after the positive step change in HTF mass flow rate at simulation time t = 7000.

Figures 8.17 and 8.18 display the transient responses to inlet temperature steps of the HTF stream, corresponding to case C and D (see Table 8.3), respectively. In particular, the HTF inlet stream is subjected to negative

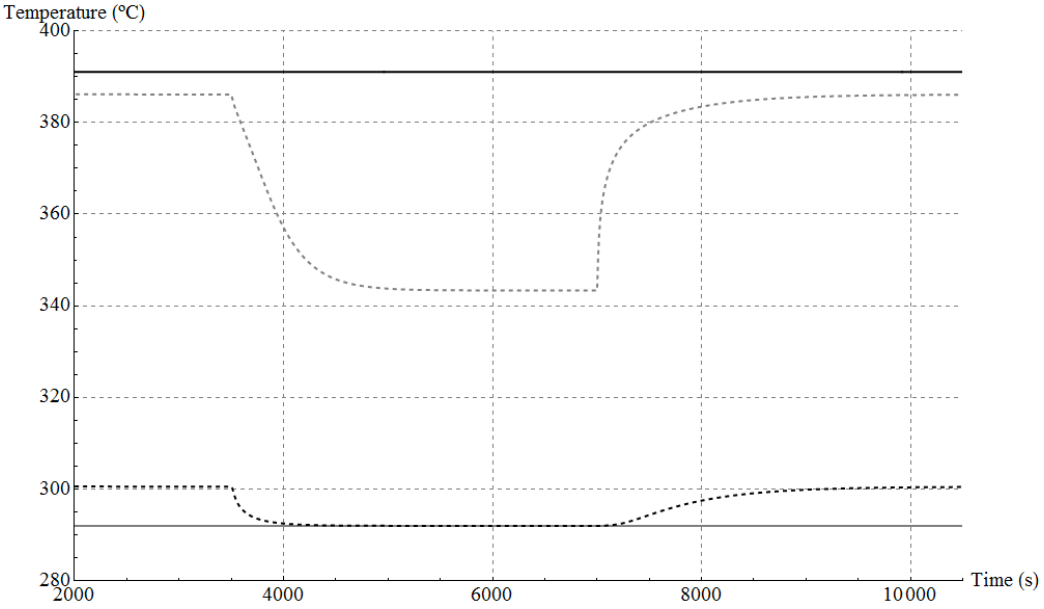

Figure 8.16: HTF mass flow rate step response simulation according to experiment B in Table 8.3 – black solid line: HTF inlet, black dashed line: HTF outlet, gray solid line: molten salt inlet, gray dashed line: molten salt outlet [111]

and positive step changes of 20 °C at two different load conditions. Figure 8.17 represents the case for nominal load, Figure 8.18 represents the case for 50% load. As expected, also here, the time constants increase considerably at lower mass flow rates. Whereas at nominal load conditions (Figure 8.17) the fluid outlet temperatures approach their new steady-state values after about 16 min, at 50% load (Figure 8.18), almost twice as much time is required.

Summarizing the performed simulations, it can be said that the thermal inertia of such a shell-and-tube heat exchanger is considerable and forms a major obstacle for rapid load changes that are crucial for capturing as much solar energy as possible, and to supply the power block with constant thermal power, independently of the current solar irradiance. Obviously, the performance will strongly depend on the control methodology applied.

The presented model forms a flexible tool for the performance analysis of any shell-and-tube heat exchanger configuration, either for rating or control oriented studies. However, the model is by far too complex for simulations on system level, i.e. considering the performance of an entire solar thermal power plant. Thus, Section 8.5 will deal with a much simpler model, representing a good trade-off between computational effort and accuracy.

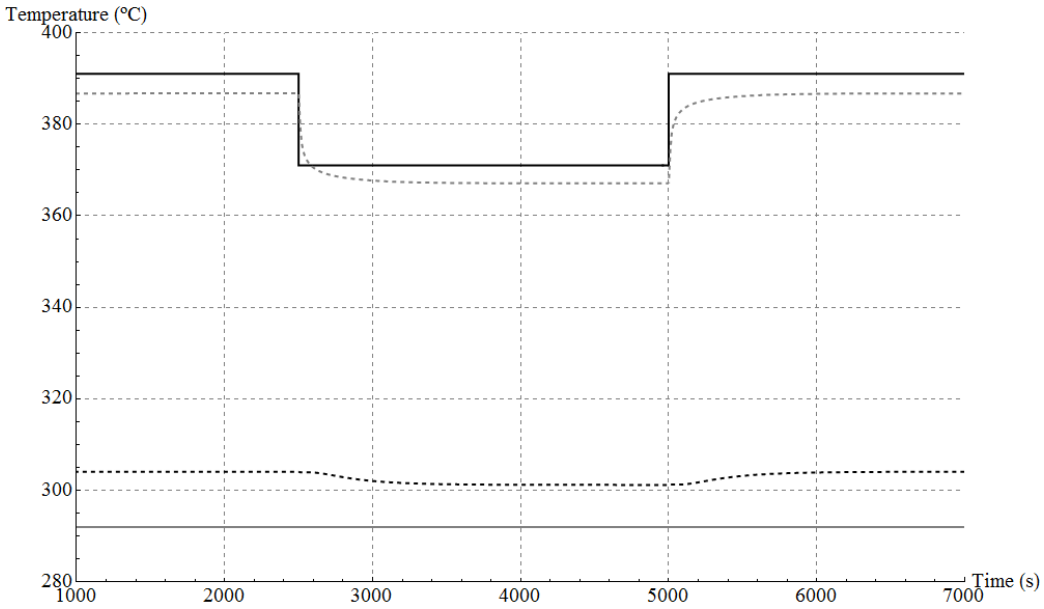

Figure 8.17: HTF inlet temperature step response simulation according to experiment C in Table 8.3 – black solid line: HTF inlet, black dashed line: HTF outlet, gray solid line: molten salt inlet, gray dashed line: molten salt outlet [111]

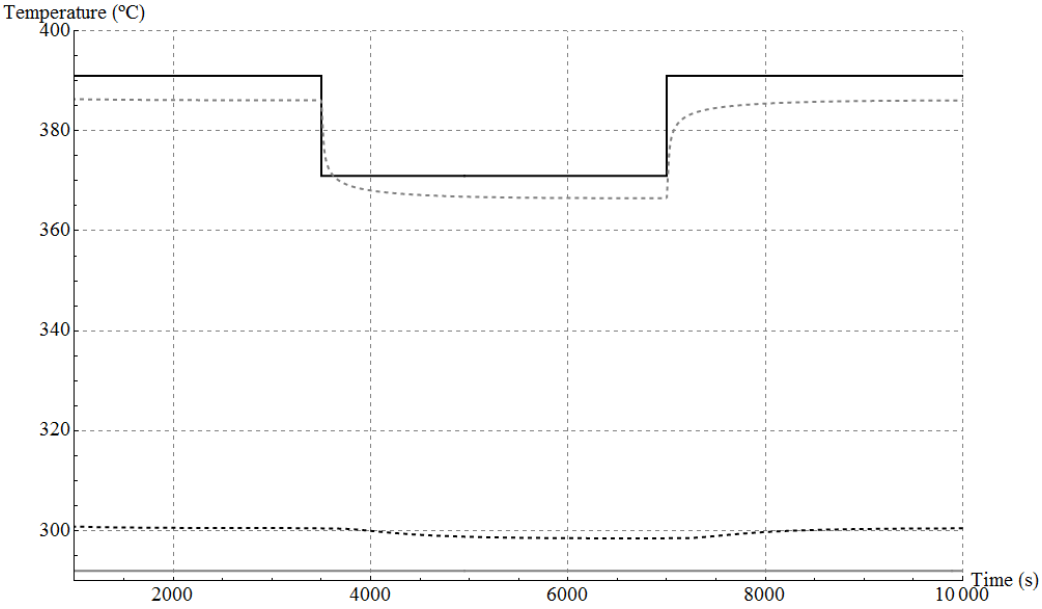

Figure 8.18: HTF inlet temperature step response simulation according to experiment D in Table 8.3 – black solid line: HTF inlet, black dashed line: HTF outlet, gray solid line: molten salt inlet, gray dashed line: molten salt outlet [111]

8.5 A simplified model for CSP performance simulations

Since the modeling approach of Section 8.2.5 may lead to a relatively large number of equations, especially for large heat exchangers with many vertical segmental baffles and tight baffle spacing, the calculation results will be compared to a simplified shell-and-tube heat exchanger model, where the tube-side stream only features one single tube bundle model, i.e. the tube bundle models b, d and f, as well as the tube bundle models a, c and e are lumped together. Consequently, the real "s-shaped" flow cannot be modeled any more. Nevertheless, the model's complexity is considerably reduced, also leading to a more flexible control volume size definition, since it is independent of the baffle spacing now. Since the aim of an efficient model, for system-level simulations, is to reproduce the dominant dynamics as best as possible, while keeping the computational effort at an acceptable minimum, the total number of control volumes will be decreased step by step, monitoring the transient as well as the steady-state model performance. The heat exchanger model according to Section 8.2.5 is considered as this study's reference model. Figure 8.19 represents the scheme of the simplified shell-and-tube heat exchanger model. In principle, this setup corresponds to the method already proposed by Mattsson [126] or Skoglund et al. [130], and can be seen as the standard approach in Modelica.

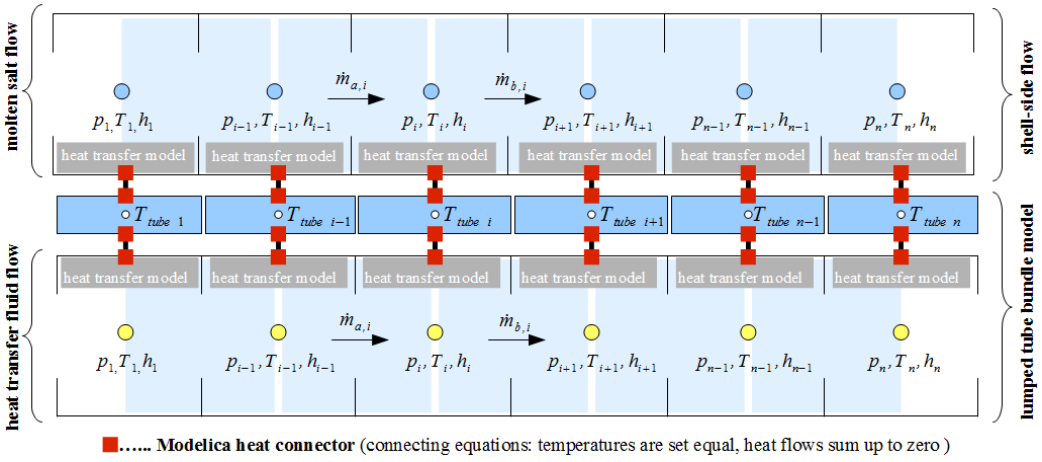

Figure 8.19: Simplified shell-and-tube heat exchanger model scheme [111]

In order to evaluate the performance of this simplified model, its simulation results are compared to the reference setup. The number of control volumes per fluid stream has been varied according to the following sequence:

160 CVs, 80 CVs, 40 CVs and finally 20 CVs. This corresponds to spatial resolutions of 0.375 m, 0.75 m, 1.5 m and 3 m, assuming a total heat exchanger length of 60 m. Since the temperature profiles along the heat exchanger are typically non-linear, a too small number of control volumes will lead to a considerably wrong approximation of the steady-state solution. Additionally, the models' transient behavior will be modified, making too simple models unsuitable for control oriented studies. Thus, the finally chosen number of control volumes will be the one that reproduces the non-linear temperature profile as well as the dominant dynamics accurately enough.

Figure 8.20 represents the discrete approximations of the steady-state temperature profiles along the heat exchanger's length. The upper curve represents the tube-side temperature profile, the lower curve represents the shell-side temperature profile. The results correspond to case A in Table 8.3 (nominal load, steady state). It should be noted that the difference in steady-state solution between the model having 160 control volumes (black) and the model having 80 control volumes (red) can be considered to be negligible. The difference in outlet temperature approximation is approximately 0.5 °C (see also Table 8.4). Also the transient responses keep very close to the reference model explained in Section 8.2.5. The simplified model, having 160 control volumes, shows a RMSE of about 0.8 °C. The RMSE increases to about 1.1 °C when using a simplified model having 80 control volumes. Considering the notable advance in calculation speed, 80 control volumes, i.e. a spatial resolution of about 0.75 m should be sufficiently accurate for transient CSP performance simulations on system-level. Lower spatial resolutions lead to relatively large steady-state errors (see Table 8.4 and Figures 8.20 and 8.21).

8.6 Conclusions

This work presents a Modelica-based transient shell-and-tube heat exchanger model for single-phase flow in both fluid ducts and multiple shell-side and tube-side passes. The model is based on the nowadays well established cell-method, which was originally proposed by Gaddis & Schlünder [118, 120]. It is a specific case of the finite volume method. Subsequently, the model is used for a specific case study, in particular, for the transient evaluation of a heat exchanger for active indirect thermal energy storage systems for CSP, applying molten salt (60% $NaNO_3$, 40% KNO_3 by weight) and thermal oil ($C_{12}H_{10}$, $C_{12}H_{10}O$) as fluids. The model is subjected to changes in mass flow rate and inlet temperature, showing the transient behavior of a typical shell-and-tube heat exchanger train, as currently used at CSP active indirect

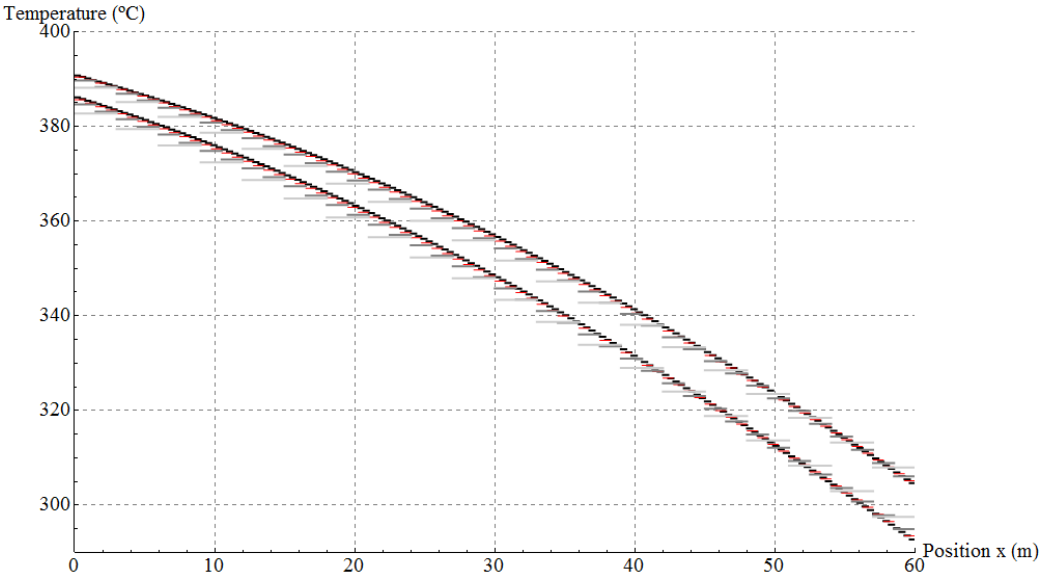

Figure 8.20: Steady state temperature profile along the oil-to-molten-salt heat exchanger train in charging mode and nominal load – black: 160 CVs, red: 80 CVs, gray: 40 CVs, light gray: 20 CVs [111]

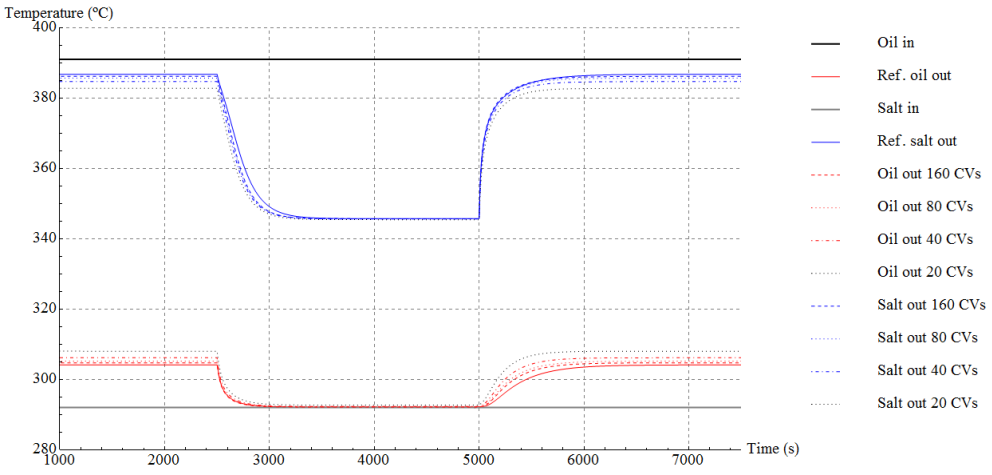

Figure 8.21: Control volume variation and the comparison to the reference case (experiment A according to Table 8.3) [111]

Table 8.4: Errors induced by the reduction in spatial resolution compared to the reference setup, assuming a total heat exchanger flow length of 60 m (experiment A according to Table 8.3) [111]

	160 CVs	80 CVs	40 CVs	20 CVs
Spatial resolution (m)	0.375	0.75	1.5	3
Number of variables (-)	17400	8760	4440	2280
CPU time (s/h of experiment)	≈ 144	≈ 40	≈ 11	≈ 3
Shell side				
Steady state error (^oC)	0.6	1.1	2.1	4.0
RMSE (^oC)	0.8	1.1	1.9	3.4
Tube side				
Steady state error (^oC)	0.6	1.1	2.0	3.9
RMSE (^oC)	0.7	1.1	1.9	3.5

two-tank thermal energy storage systems. It is shown that the thermal inertia of such a shell-and-tube heat exchanger is considerable and forms a major obstacle for rapid load changes that are crucial for efficient power plant operation. It is obvious that the final performance of the thermal energy storage system will strongly depend on the control methodology applied.

Additionally, for the specific heat exchanger setup under consideration, a study of the required discretization level for a simplified pure counter-flow model setup is performed, in order to obtain an efficient simulation code that still features reasonable steady-state as well as transient behavior. It has been shown that a spatial resolution of about 0.75 m represents a good trade-off between computational effort and accuracy for heat exchanger simulations on system level.

For detailed transient response or rating studies, where the number of equations and simulation time do not matter, the modeling method as described in Section 8.2.5 forms a flexible approach for the performance analysis of any shell-and-tube heat exchanger configuration. Last but not least, the proposed implementation in Modelica provides a flexible and intuitive design tool, which is not limited to a single simulation platform.

Chapter 9

Transient behavior of an active indirect two-tank thermal energy storage system during changes in operating mode

This chapter focuses on the transient response simulation of an entire active indirect two-tank thermal energy storage system during changes in operating mode, combining the models presented in Chapter 7 and Chapter 8. Standard PI feedback control loops with constant tuning parameters are used for the molten salt mass flow control. Simulation results show that there are certain limitations regarding instantaneous thermal power demand or supply, which still requires small HTF buffer storage in order to provide the thermodynamic power cycle of the plant with a continuous thermal power input.

9.1 Introduction

A thermal energy storage system for CSP is designed to even fluctuations of the currently available solar thermal power on the one hand, and to shift/extend the operation of the plant to/during hours where no solar irradiation is available. Whereas in the latter application, the storage system mainly operates under steady-state conditions, transients frequently occur during short-term buffering throughout the day, which makes the evaluation of the storage system's transient behavior indispensable.

In this context, this chapter describes the transient responses of the oil-to-molten-salt heat exchanger train to transitions between charging and discharging mode, as well as the dynamics of the storage system as a whole.

The molten salt storage tank model applied is based on Section 7.6 of this work. The shell-and-tube heat exchanger model is based on Section 8.2.5 of this work. The content of this chapter is based on the work originally presented by Zaversky et al. [192].

9.2 The storage system layout

Figure 8.12 shows the general setup of an active indirect two-tank thermal energy storage system for CSP. The basic components are the molten salt storage tanks (the hot tank and the cold tank) and the oil-to-molten-salt heat exchanger train, which typically consists of 3 shell-and-tube subunits connected in series [108]. Each shell-and-tube subunit is considered having two shell passes with a longitudinal baffle and two tube passes in U-tube design, which corresponds to a TEMA-F [185] type design. Note that the molten salt suction pumps as well as the distribution headers are not displayed in the storage tank schemes.

The dimensions of the system are set to values currently applied at 50 MWe parabolic trough collector plants operated in Spain. The diameter and height of the storage tank's steel container is set to 38.5 m and 14 m, respectively. The maximum absolute molten salt level height is set to 13 m. The height of the suction pump inlet is set to 0.7 m. Thus, an empty cold or hot tank has still an absolute molten salt level height of 0.7 m, which defines the remaining molten salt mass during cool-down. The assumed dimensions of one of the three shell-and-tube subunits are given in Table 8.1 (TEMA-F oil-salt).

9.3 The storage system model and its control

The final storage system model consists of 2 instances of the molten salt storage tank model class (i.e. one for the hot tank and one for the cold tank), and 3 instances of a shell-and-tube heat exchanger model class that are connected in series (see Figure 8.12) [1]. All connecting pipes are assumed to be ideally insulated.

The HTF mass flow rate is a given boundary condition of the model. The same holds for the HTF inlet temperatures. They are set to the constant values of 391 °C, for charging (solar field outlet temperature), and 285 °C, for discharging (power block outlet temperature). The molten salt mass flow

[1] For a detailed model description, the interested reader is referred to Sections 7.6 and 8.2.5 of this work.

rate is controlled in such a way that either the molten salt outlet temperature (charging), or the HTF outlet temperature (discharging) keeps to the assigned set-point. In particular, during storage system charging mode, the molten salt outlet temperature is kept to the hot tank's design temperature. On the other hand, during storage system discharging mode, the HTF outlet temperature is kept to the desired feed temperature of the CSP plant's steam generator (in this work 376 °C). In this way, the feed temperature of the cold molten salt tank varies according to the thermal characteristic of the heat exchanger train, i.e. it is not controlled to keep to the cold tank's design temperature of 292 °C. Continuous PI controllers are applied for both the charging, and the discharging mass flow control. The inertia of the control system's actuator circuit (including the molten salt pumps) is modeled via an instance of a first-order block having a gain of 1 and a time constant of 30 s, i.e. 63,2% of the final molten salt mass flow rate value is reached after 30 s assuming a step-change in the control signal.

Since the HTF inlet temperatures are assumed to be constant while charging and discharging, the HTF mass flow rate variation is the only major disturbance caused. This also includes changes in flow direction when switching from charging to discharging mode, or vice versa.

The controller settings have been obtained via a so-called process reaction curve method, which can be applied to self-regulating processes that feature first-order-plus-time-delay behavior, i.e. that can be described by the three parameters as process gain K_s, dead time Θ and time constant τ, as it is the case for the here considered heat exchanger in the range close to a certain operating point. In particular, the controller settings have been obtained applying the Chien-Hrones-Reswick method for the aperiodic case and set point step [193]. Evaluating open-loop step response simulations and applying the tangent method at the point of inflection [191], yields approximately 0.031 $K\,s\,kg^{-1}$ for the process gain K_s, 12.3 s for the dead time Θ and 345.6 s for the time constant τ for charging mode, and 0.056 $K\,s\,kg^{-1}$ for the process gain K_s, 12.6 s for the dead time Θ and 251.6 s for the time constant τ for discharging mode. This gives a controller gain K_p of 317.1 $kg\,s^{-1}\,K^{-1}$ for the charge controller, and a controller gain K_p of 124 $kg\,s^{-1}\,K^{-1}$ for the discharge controller [2]. The integral time τ_i results in 414.7 s for the charge controller, and in 302 s for the discharge controller.

It has to be noted that the controller output in the model is a direct mass flow signal and not a valve position or molten salt pump speed as it is the case in reality. Furthermore, the controller settings, stated above, have been obtained for flow conditions that are close to the nominal ones.

[2]Note that, for simplicity, all gains are given in absolute values.

However, due to non-linearities of the behavior of the heat exchanger train, its process parameters, on which the controller settings are based, typically vary depending on the actual load (HTF mass flow rate) and may not be ideal for the operation at partial loads.

9.4 Discussion of simulation results

Again, the developed Modelica code has been translated into numerical simulation code using a state-of-the-art commercial Modelica tool, applying its differential-algebraic system solver DASSL [178] (see Section 8.2.7).

It should be noted that the final model class of this active indirect two-tank thermal energy storage system features 22291 equations and a simulation of a 5 h experiment typically takes around 10 min on a standard desktop computer (3.10 GHz).

In order to show the transient behavior of the thermal energy storage system, the numerical model has been subjected to step changes in HTF mass flow rate. In particular, 4 simulations treat step changes in HTF mass flow rate during charging and discharging mode, respectively (step changes between nominal load and 50% load, and step changes between 50% load and 25% load). In addition to that, 4 simulations treat the complete change in operating mode, including the flow reversal within the heat exchanger ducts, i.e. the switching between storage system charging and discharging mode. These simulations have been performed for 4 load cases (100%, 75%, 50% and 25% load).

Figures 9.1 and 9.2 display results of the 4 simulations during that no operating mode switching occurs, i.e. there occurs no flow reversal within the heat exchanger ducts, only the mass flow rates change between nominal load (100% load) and 50% load (solid lines), and between 50% load and 25% load (dashed lines). More precisely, the HTF mass flow rate (red) is subjected to ideal step changes between these loads, after 500 s and after 8000 s. Note, that the mass flows are defined positive for charging mode and negative for discharging mode. As can be well observed, the controllers adjust the molten salt mass flow rates (blue) to the new steady-state values in order to reach the desired set points. In charging mode, the outlet temperature of the molten salt has to follow its set point, i.e. the hot tank's design temperature. On the other hand, in discharging mode, the outlet temperature of the HTF has to follow its set point, i.e. the steam generator's inlet temperature. Thus, while discharging, the feed temperature of the cold molten salt tank is not controlled and varies according to the heat exchanger's thermal characteristic.

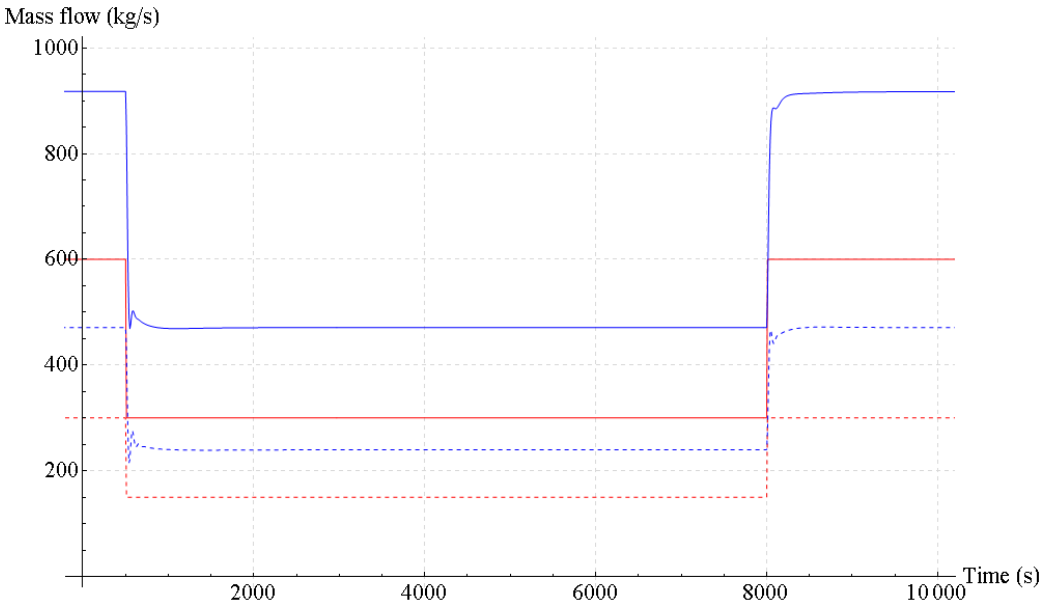

Figure 9.1: Mass flow step changes charging mode; 100% - 50% load steps: solid, 50% - 25% load steps: dashed

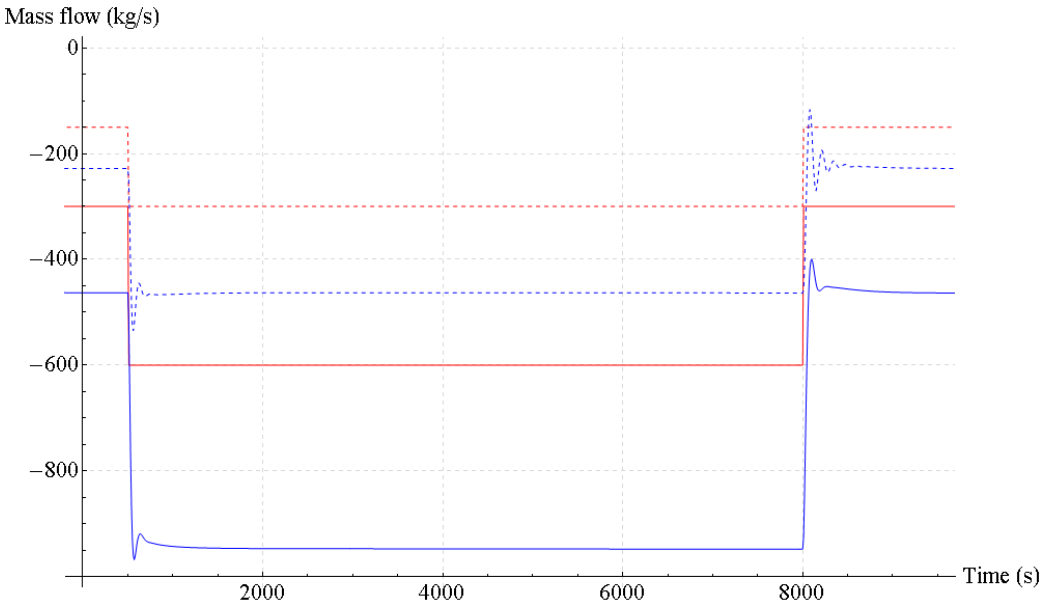

Figure 9.2: Mass flow step changes discharging mode; 100% - 50% load steps: solid, 50% - 25% load steps: dashed

Figures 9.3 and 9.4 show the corresponding heat exchanger duct outlet temperatures in charging mode (molten salt: blue, HTF: red), and the corresponding ideally mixed inventory temperature of the hot molten salt tank (gray). As can be well observed, with the aforementioned controller settings, it takes approximately 25 min to control the system to the steady-state conditions of the new operating point. Note, that the difference in temperature response (depending on the load) also slightly influences the molten salt inventory temperature trend. The offset between the solid and the dashed line (gray) is due to different filling levels (Figure 9.3), since the initial value of the storage system's state of charge is the same for each simulation run. Lower molten salt filling levels lead to higher temperature drops, due to higher specific heat losses [132].

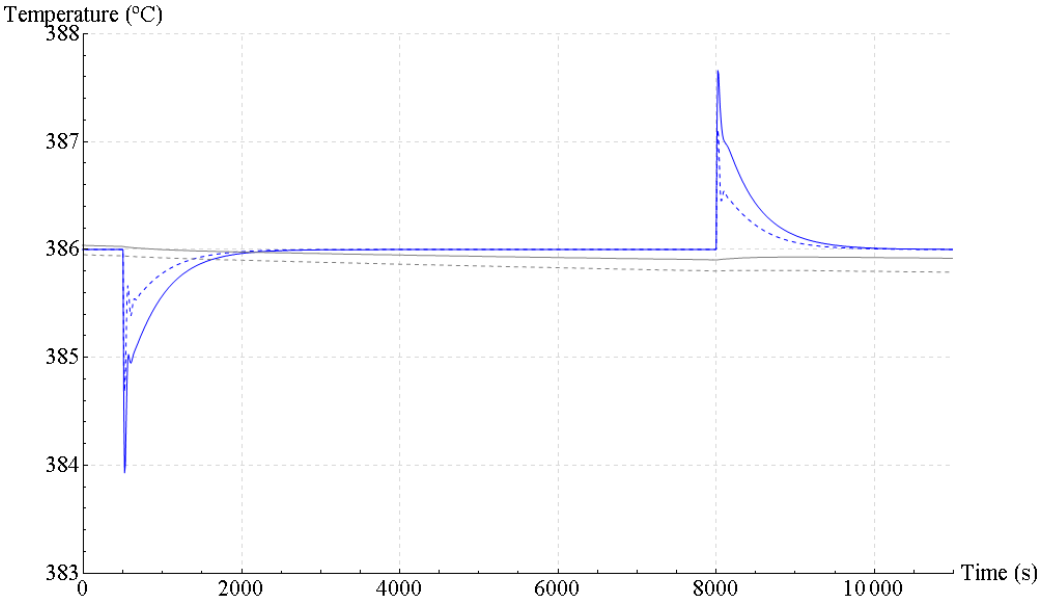

Figure 9.3: Hot tank feed (blue) and inventory (gray) temperatures (charging mode); 100% - 50% load steps: solid, 50% - 25% load steps: dashed

Figures 9.5 and 9.6 show the heat exchanger duct outlet temperatures in discharging mode (molten salt: blue, HTF: red), and the ideally mixed inventory temperature of the cold molten salt tank (gray). As already mentioned above, in this operating mode, the aim of the controller is to keep the HTF outlet temperature (steam generator feed temperature) at the desired set point. As can be seen in Figure 9.5, it takes about 17 min until the HTF outlet temperatures settle at the set point, reaching the new steady-state conditions after the step change in HTF mass flow rate (see Figures 9.1 and 9.2). Figure 9.6 displays the resulting feed temperatures of the cold molten

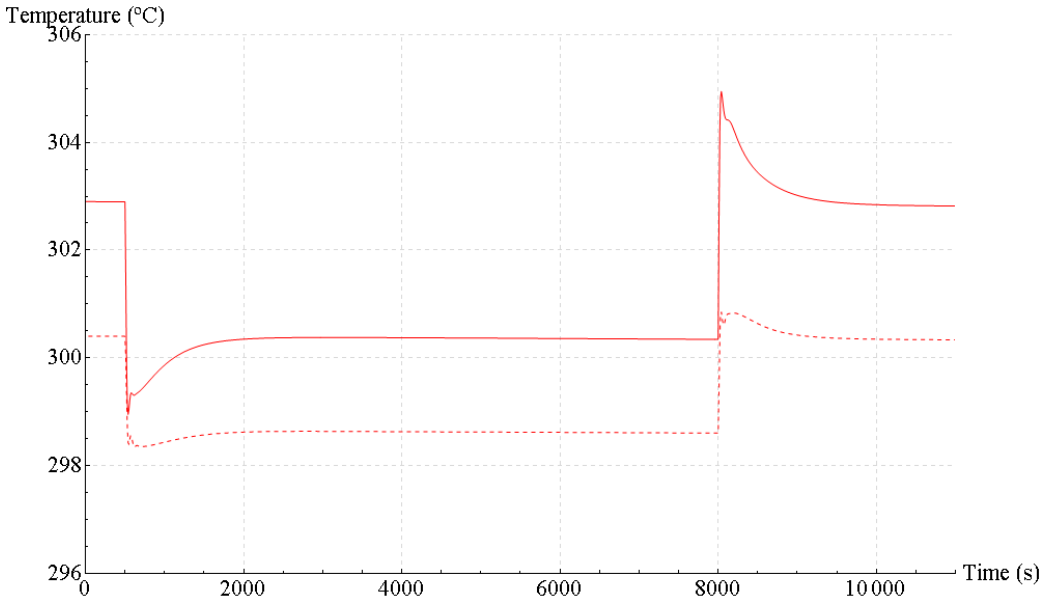

Figure 9.4: HTF outlet temperature (charging mode); 100% - 50% load steps: solid, 50% - 25% load steps: dashed

salt tank during discharging mode. The cold tank's feed temperature is not controlled and depends thus on the operating point. During nominal discharge conditions, the feed temperature of the cold molten salt tank is about 1.5 °C higher than its design temperature of 292 °C, which leads to a slight increase in molten salt inventory temperature (gray solid line). On the other hand, at 25% load, the resulting feed temperature of the cold tank is about 2 °C below its design value, which shows, that the actual temperature of the cold tank's molten salt inventory varies during operation within a certain range around its design value.

Figures 9.7 and 9.8 display the simulation results of changes between charging and discharging mode. In particular, starting from steady-state charging conditions (positive mass flows), the HTF mass flow is inverted at simulation time t = 500 s, which initiates the discharging mode. Then the discharge controller acts in such a way, that the molten salt mass flow also changes its sign in order to settle the HTF outlet temperature at the desired set point, the steam generator's feed temperature. About 25 min after the flow reversal, the HTF outlet temperature reaches its set point. At t = 8000 s, the HTF mass flow is inverted again, initiating the charging process. With the given controller settings (see Section 9.3), the molten salt mass flow shows damped oscillations at low partial loads (dotted blue line) when switching from discharging to charging mode, which disappear

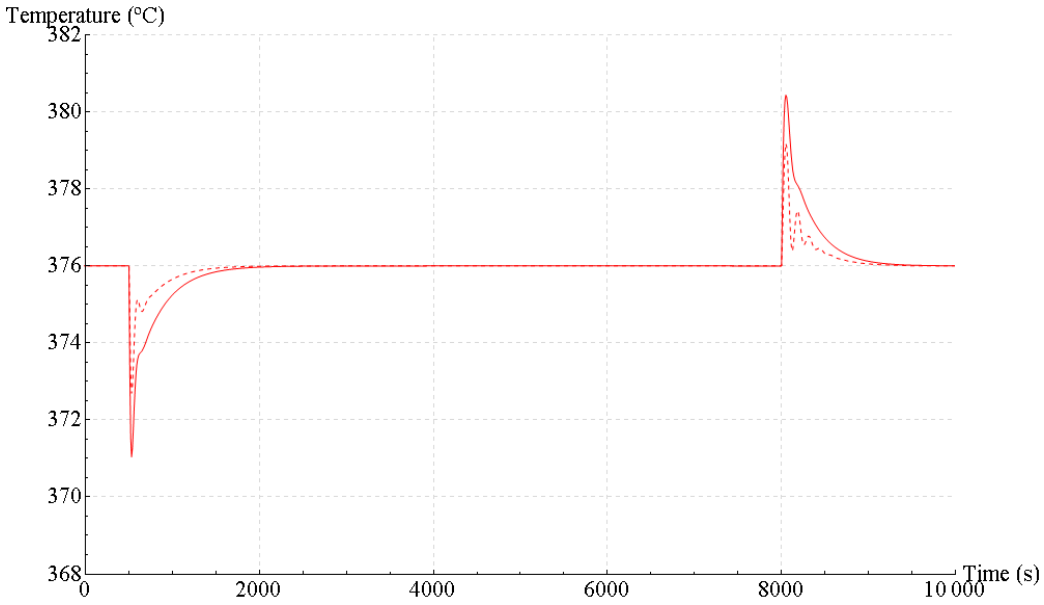

Figure 9.5: HTF outlet temperature (discharging mode); 100% - 50% load steps: solid, 50% - 25% load steps: dashed

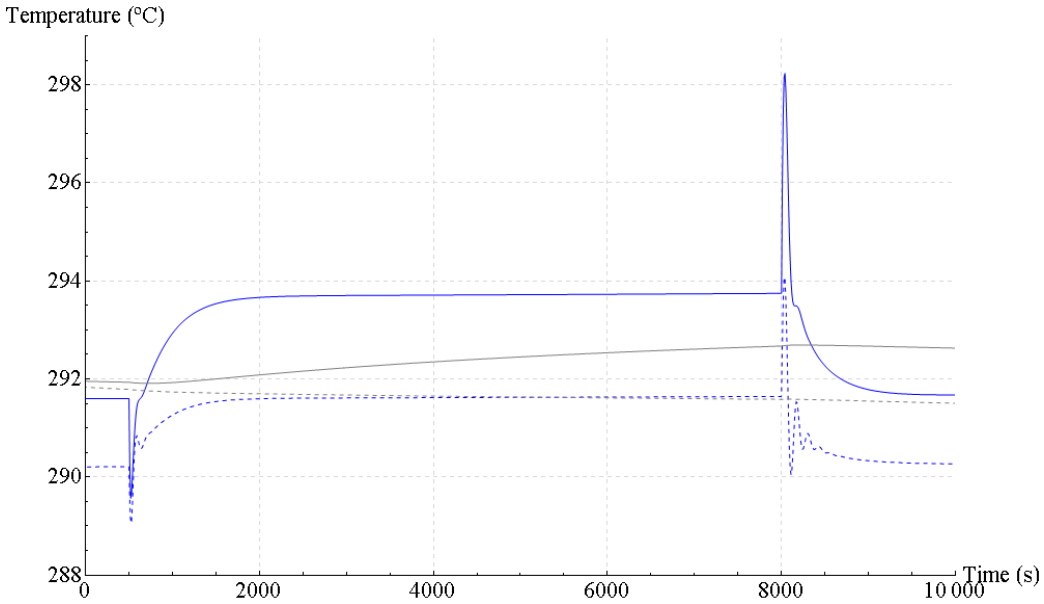

Figure 9.6: Cold tank feed (blue) and inventory (gray) temperatures (discharging mode); 100% - 50% load steps: solid, 50% - 25% load steps: dashed

at higher loads. However, in this case (Figure 9.7) about 30% of overshoot remain, also at nominal loads, which causes the molten salt mass flow rate to be limited to the assumed maximum value of 950 $\frac{kg}{s}$.

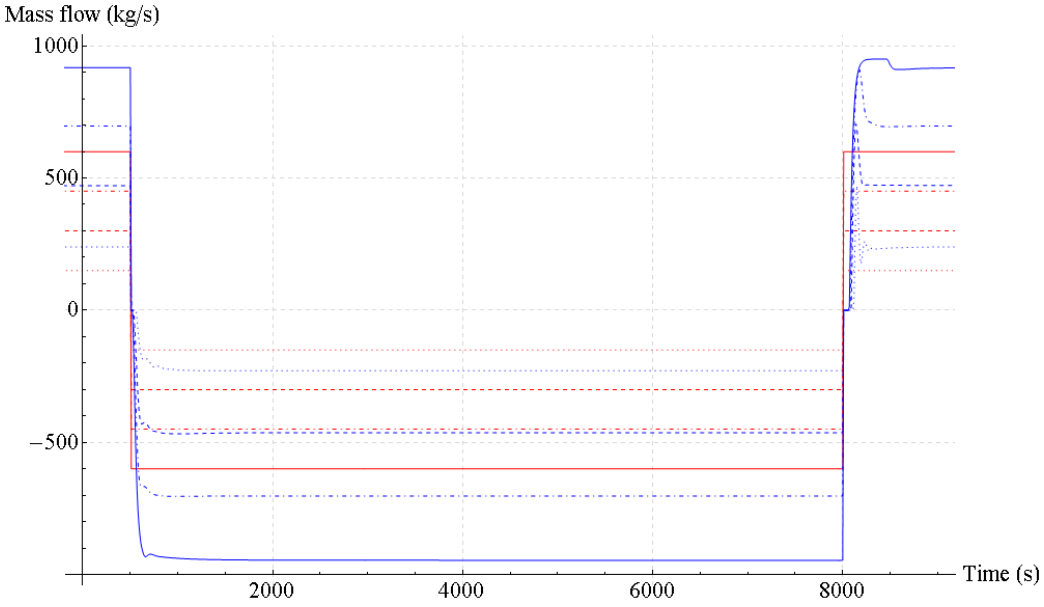

Figure 9.7: Mass flows during changes in operating mode; HTF: red, molten salt: blue; 100% load: solid lines, 75% load: dot-dashed lines, 50% load: dashed lines, 25% load: dotted lines

Summarizing the above presented simulations, it can be said that the thermal inertia of the storage system's fluid circuit limits the performance during abrupt changes in operating mode, of course, depending on the applied control methodology. Thus, in order to provide the power block with a constant thermal power supply independently of the current solar irradiance, and, to store as much thermal energy as possible when solar irradiation is available in excess, the optimization of control methods and additional HTF buffer storage plays an important role.

9.5 Conclusions and outlook

This chapter presents the application of a detailed one-dimensional numerical model of an active indirect two-tank thermal energy storage system for solar thermal power generation. The applied model is typically suitable for the evaluation of transient responses caused by the storage system's disturbance

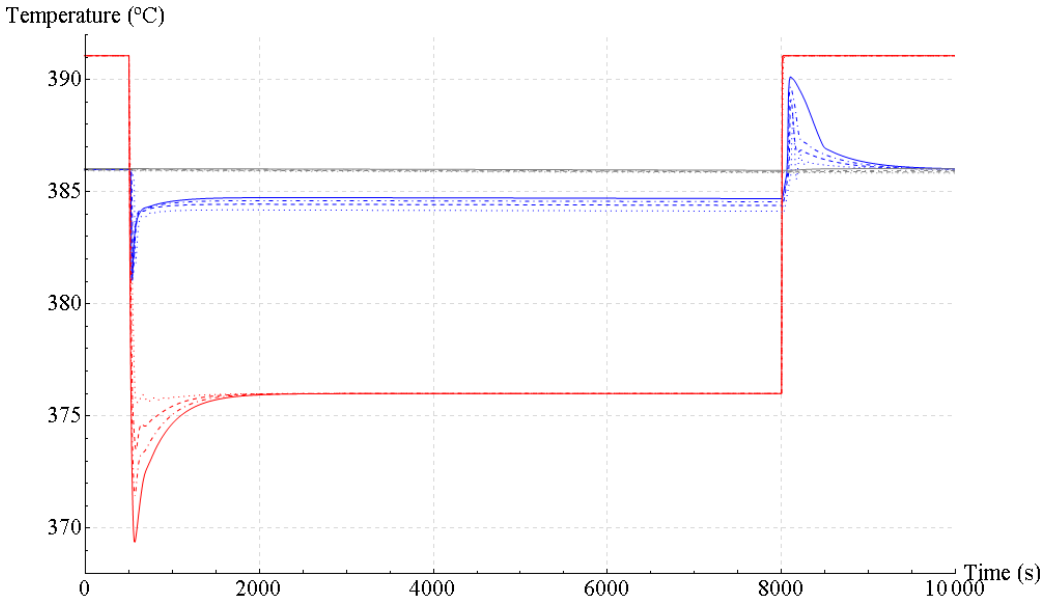

Figure 9.8: Temperatures at the hot end of the heat exchanger train during changes in operating mode (last control volumes); HTF: red, molten salt: blue, inventory temperature of the hot tank: gray; 100% load: solid lines, 75% load: dot-dashed lines, 50% load: dashed lines, 25% load: dotted lines

variables as HTF mass flow rate, HTF inlet temperature or molten salt temperatures within the tanks. It thus forms a valuable basis for improving and optimizing the storage system's operation and control strategy, important tasks related to cost-competitiveness of CSP.

It has been shown that there are certain limitations regarding the storage system's charging and discharging performance during abrupt changes in operating mode, due to the thermal inertia of the storage system's fluid circuit. The active indirect two-tank thermal energy storage concept has certain limitations regarding instantaneous thermal power demand or supply. Hence, additional small buffer storage in terms of excess HTF piping volume or small vessels is still important in order to provide the thermodynamic power cycle of the plant with a continuous thermal power input, regardless of the current solar irradiance.

Furthermore, it has to be emphasized, that the storage system's performance strongly depends on the oil-to-molten-salt heat exchanger's control methodology. Since this study only considers standard PI feedback control loops with constant tuning parameters, the potential of advanced control methods should be treated in future works.

Part III

A transient parabolic trough collector power plant model on system level and its numerical simulation

Part three of this work presents an implementation of a transient parabolic trough collector power plant model on system level. It describes a numerical model and presents simulation results of power plant operation under transient conditions.

Chapter 10

A transient PTC power plant model on system level

This chapter describes a transient, object-oriented and Modelica-based PTC power plant model on system level and presents its numerical simulation. In particular, this chapter is devoted to the application of the modeling approaches that have been proposed and discussed in detail in Part II of this work. Thus, the molten salt based active indirect two-tank thermal energy storage concept plays an important role in the model. It will be combined with a solar field model and a model of the plant's power block. Whereas the power plant's HTF circuit (including the thermal energy storage) is entirely modeled according to the finite volume method, the modeling of the power block is considered in a different way. On the one hand, for detailed transient short-term simulations, the power block model is a combination of a transient 1-D distributed parameter model of the steam generator (according to the finite volume method) and a quasi-steady zero-dimensional fluid circuit model including the turbine, the condenser and the feed water preheaters. On the other hand, for transient long-term simulations, the power block is entirely considered as a quasi-steady zero-dimensional fluid circuit model. In order to capture basic dynamics during plant start-up and shut-down, the latter power block model concept is coupled with an equivalent thermal inertia.

10.1 Introduction

This chapter discusses a numerical model of a parabolic trough collector power plant on system level that is able to perform detailed simulations of the entire power plant under transient operating conditions. It is thus possible to

analyze the start-up and shut-down behavior as well as the plant's transient response to disturbances throughout the day, caused by variations in incident solar direct normal irradiation.

Detailed transient performance simulations of solar thermal power plants are, for instance, important to establish operational strategies that do not cause unwanted component overloading during large variations in incident solar direct normal radiation.

Besides the transient model of the solar field and the thermal energy storage system, the consideration of the power block's steam generator is another important issue regarding the behavior of the entire power plant.

A crucial constraint in plant operation is the maximum allowed rate of change in temperature of thick-walled components (maximum allowed thermal stress) like the steam drum of natural or forced circulation boilers that are commonly applied in commercial CSP plants. An exceeding of these operating limits will inevitably lead to life time reductions of critical components [194]. It is thus important to study different operating strategies of the plant during transient conditions in order to optimize the life-time of individual components, or to develop an efficient emergency handling.

Typical rate-of-change limits in temperature for CSP steam generators constitute about 2-3 °C per minute in order to keep the induced thermal stress in thick walled components as low as possible. Ramp-up limitations and hold times for thick walled components are therefore obstacles considering start-up time reductions of solar thermal power plants. Thus, during power plant start-up, it is an important task to accurately control the heat transfer fluid recirculation mass flow rate (steam generator by-pass), in order to avoid a too high drum pressure gradient (i.e. the saturation temperature variation exceeds the rate-of-change limit) due to a too high heat input.

However, in order to be able to analyze the transient behavior of the steam generator, a sufficiently accurate numerical model is required, whose development is not a trivial task at all, when compared to the rather straightforward modeling of incompressible fluid circuits, as applied for the solar field as well as for the thermal energy storage system. Nevertheless, Section 10.4.1.1 will describe a modeling approach that is able to capture the basic boiler dynamics as the response of the drum pressure to changes in heat input, or steam mas flow rate (i.e. the response of the drum pressure to changes in "firing rate"[1] or turbine valve opening).

Unfortunately, a transient steam generator model as described in Section 10.4.1.1, is relatively complex and practically not suitable for long-term so-

[1]In CSP plants, the so-called "firing rate" corresponds to the HTF mass flow rate entering the steam generator.

lar plant simulations covering several weeks, not to mention years (at least considering current state-of-the-art Modelica tools). Thus, in this work, two types of power block models will be treated. One including a transient distributed parameter model of a CSP steam generator (10.4.1.1), suitable for detailed short-term simulations, and a second one, much simpler in its concept, but therefore feasible for transient long-term solar power plant simulations. Complementing each other, the results of the detailed model can be used for adjusting parameters of the simpler model, suitable for transient energy yield calculations over longer periods of time.

Basically, the described modeling approach is similar to that already presented by Hirsch & Schenk [195]. However, in this work, the power block is treated in more detail.

In the following, each sub-model of the considered solar thermal power plant will be described.

10.2 The PTC solar field sub-model

The solar field of a parabolic trough collector plant is usually composed of several identical sub-fields, which in turn consist of many identical solar collector loops connected in parallel (see Figure 1.5). These loops are fed by the cold header pipe and drain into the hot header pipe. Each loop consists of solar collector assemblies (SCAs) that are connected in series. Finally, each solar collector assembly is composed of the basic solar collector components, as the parabolic mirrors and the solar absorber tubes (as shown in Figure 1.3), i.e. the heat collector elements (HCEs).

The number of collectors per loop, and thus the final length of one loop, is defined by the plant's operating conditions, such as the solar field's nominal inlet and outlet temperature and the desired HTF mass flow rate for a given solar irradiance level. Another important design aspect when it comes to the definition of the collector loop's length, is the solar field's pressure drop, since the pumping power required for circulating the heat transfer fluid is usually around 5% of the plant's gross output. Typical loop lengths at today's parabolic trough collector plants are in the range between 600 and 800 m.

The total number of loops per power plant depends on the solar multiple. For instance the 30 MWe SEGS plants in California, USA, feature 50 loops per plant. Nevada Soler One has 96 collector loops for a nominal power block output of 64 MWe. Thus, for plants without thermal energy storage, the number of installed collector loops per MW of electric plant output is typically around 1.5. Hence, considering these rather huge dimensions of parabolic trough solar fields, a certain abstraction has to be made when

developing the model, since a complete reproduction of the field would lead to huge models having thousands of variables featuring not practicable simulation times. Of course, the best model structure depends on the type of simulations to be performed. For instance, studies that investigate the influence of partial shading of the solar field, or analyze the effect of scattering of the performance parameters within the field, definitely demand higher model resolutions than simple energy yield calculations.

When it comes to steady-state or transient power plant performance simulations where partial shading of the solar field or performance parameter scattering do not need to be considered, it is a common practice to model one representative solar collector loop only. For transient models, the additional consideration of the supply and the return header pipe (the cold and the hot header) will be representative for the whole solar field dynamics. This modeling abstraction is furthermore supported by the fact that the solar irradiance data is usually only available for one single point per location, i.e. the physical location of the DNI measurement device. Thus, implementing a high resolution model of the solar field and finally assigning exactly the same solar irradiance value to each virtual receiver tube would definitely be a computational overhead.

Figure 10.1 shows a scheme of this work's solar field model. It consists of one representative solar collector loop, two mass flow gains, and two additional dynamic pipe models that represent the cold and the hot header. A detailed description of the solar collector model is given in Section 10.2.1 of this work. Basically, the model is based on a 1-D approach according to Forristall [41]. It discretizes the solar collector loop into a certain number of control volumes according to the finite volume method. To correctly reproduce the dominant dynamics and the steady-state behavior, a certain minimum number of control volumes per loop is required. According to Zaversky et al. [34], a discretization level of 3 control volumes per solar collector of about 50 m length is considered to be accurate enough for transient performance simulations. Since in this work, the collector loop's length is assumed to be 600 m (see Table 10.3), the number of control volumes per loop has been set to 36.

The total thermal power of the solar field is simply achieved via multiplying the mass flow of one loop by the number of total parallel loops (see Figure 10.1).

However, it has to be noted that this approach leads to considerable differences in control volume sizes, i.e. having relatively small volumes in the model of the solar absorber but relatively big volumes in the header pipes,

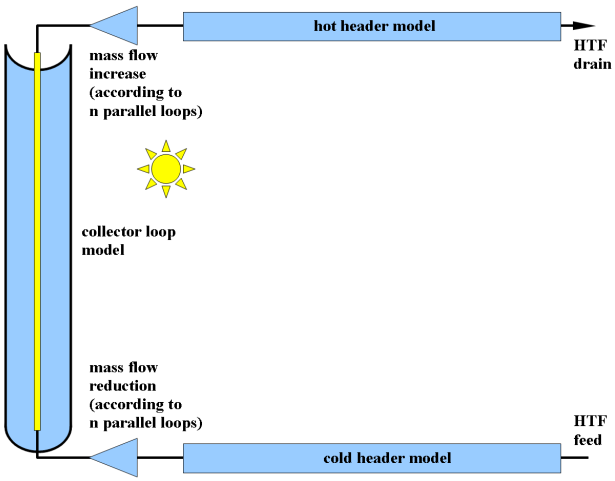

Figure 10.1: The end-loop model of the parabolic trough collector field

which in turn results in a stiff system[2] of equations that may cause problems during simulation.

A better (because more robust) approach would be to take advantage of the fact that a solar field consists of many identical parallel solar absorber pipes. Thus, all the absorber pipes could be lumped together to one single equivalent "tube-like" object, having the equivalent fluid volume, the equivalent metal mass and the equivalent thermal resistance. This would be in complete accordance with the concept of the lumped tube bundle model as explained in Section 8.2.3.

[2]One may speak about a stiff system of equations when there are greatly differing time constants within the modeled system [196]. For instance, small control volumes react very fast to changes in net heat flow or net enthalpy flow, hence they approach very fast their new steady state and have thus relatively small time constants when compared to large fluid volumes whose temperature changes slowly due to the difference in mass. Generally, the term time constant is used by engineers and physicists to refer to the rate of decay of state variables [196]. The differences between the rates of decay of the state variables of the system have a strong influence on the stability of the numerical method applied. Typically, the fastest rates of decay control the stability of the numerical method used to solve the system of equations [196].

However, the term "stiff" has been used by various authors with quite different meanings [197]. Spijker [197] gave a good review about the different meanings of stiff systems. One of the prominent features of stiff initial-value problems is that they are extremely hard to solve using standard explicit step-by-step methods [197]. Significantly better perform methods that are based on the backward differentiation formula, which is a basic ingredient of some highly successful modern software packages [197].

10.2.1 The object-oriented model of a parabolic trough collector

Given today's importance of parabolic trough solar collectors, their modeling has already been subject of numerous publications. Thus, this work's model is based on a thorough literature review and furthermore on a well structured and flexible modeling approach as proposed by the Modelica Standard Library [163]. For a detailed summary of already proposed PTC models, the interested reader is referred to Section 2.1 of this work.

Note: Like the review of already existing PTC models (Section 2.1), also this section is entirely based on a previously published work [34] of the author. It has to be emphasized, that the presented experimental model validation (see Section 10.2.2) is a corrected republication of the work first published in Elsevier's journal Solar Energy [34]. Unfortunately, Figures 17, 18 and 19 of the original work [34] display wrong results and have thus been corrected.

10.2.1.1 The model of the linear solar absorber

The linear absorber of a parabolic trough collector is basically a straight steel pipe featuring a selective coating at the tube's outer surface in order to maximize the solar energy absorbed and to minimize the thermal losses via radiation. The general approach in such a case is to discretize the pipe into a number of finite control volumes, and to solve the basic equations for mass and energy conservation for each of them.

In this work, once again, the model is based on the Modelica Standard Library's 1-D finite volume method (see Section 8.2 for a detailed description of the method). Thus, Equations 8.1 to 8.4 describe the basic mass and energy balances for each finite control volume. The momentum balance is considered according to Equation 8.12, however, once again it has been reduced to its steady-state formulation, by furthermore neglecting differences in velocity and the influence of the gravitational force.

Hence, the HTF flow within the absorber tube is discretized using n finite control volumes of equal size. This approach corresponds to that already proposed by previously mentioned authors (e.g. Edenburn [35], Forristall [41], Larraín et al. [45] or Yebra et al. [62, 63]) and can be seen as the standard approach. Since the influence of longitudinal heat conduction within the absorber metal tube is considered to be negligible, the one-dimensional HTF flow model is extended by an instance of a one-dimensional cylindrical conduction model, which has already been used and explained in Section 8.2.3 of this work.

In order to fully define the absorber tube model as one single Modelica

class, the convective heat transfer between the HTF and the absorber tube's inner wall has to be formulated.

10.2.1.1.1 The convective heat transfer model According to the MSL, this is done by using a replaceable wall heat transfer model, which defines the relationship between the tube's inner wall temperatures, the fluid bulk temperatures (see Figure 8.1, T_1 to T_n) and the heat flows $\dot{Q}_{net\,i}$. Thus, the absorber tube model can easily be adapted for different flow conditions, by simply exchanging the heat transfer sub-model, which basically means that the heat transfer coefficient is estimated by using different Nusselt number correlations, fulfilling Newton's convective heat transfer law according to Equation 8.18.

A so-called "ideal" heat transfer model would represent the simplest case. This "ideal" heat transfer model sets the fluid bulk temperatures (T_1 to T_n) equal to the absorber tube's inner wall temperatures ($T_{tube\,inner\,1}$ to $T_{tube\,inner\,n}$). Whereas this model represented a good approximation for the boiling heat transfer in the case of direct steam generation, in the present study, which considers single-phase flow of the HTF, a more detailed implementation according to Equation 8.18 is necessary.

In this work, the convective heat transfer coefficient is approximated by using the widely accepted Gnielinski correlation for turbulent flow in smooth tubes, as already given by Equations 8.19 and 8.20.

Abraham et al. [188] reconfirmed the validity of Equation 8.19 for the transition region for Reynolds numbers above 3100. Since Reynolds numbers below that value, and especially laminar flow conditions ($Re < 2300$) are not relevant for the parabolic trough collector's operation, the modeling of the heat transfer over the entire flow regime is left aside.

10.2.1.1.2 The pressure drop model Now, having stated the convective heat transfer sub-model, the missing relationship between the HTF mass flow and the pressure drop due to friction has to be defined. The pressure drop due to friction within the heat collector elements, which are basically straight pipe sections, can be calculated according to the well known correlations published by Moody [189]. Since the MSL does already feature a thorough implementation of pressure drop functions that are valid for the whole flow regime ("detailed wall friction package"), these are used throughout this work.

10.2.1.1.3 The fluid properties Since the PTC model has been experimentally validated at the SOLTERM facility in Italy, two different media

models are used in this work, in particular, one for solar salt (validation) and one for thermal oil (final power plant model).

For the model validation, the solar salt is modeled as incompressible fluid at liquid state, using equation based fluid property data as published by Zavoico [158] or Ferri et al. [172]. On the other hand, for the final power plant simulations on system level, the thermal oil is modeled in the same manner as the solar salt, but using the data given in [12]. In order to allow for efficient simulation code generation, inverse and derivative functions are implemented as well.

The above stated one-dimensional fluid flow sub-model, coupled with the instance of a distributed one-dimensional cylindrical conduction model, using a replaceable convective heat transfer model, forms the basic Modelica class of the solar absorber, which can be seen in Figure 10.2.

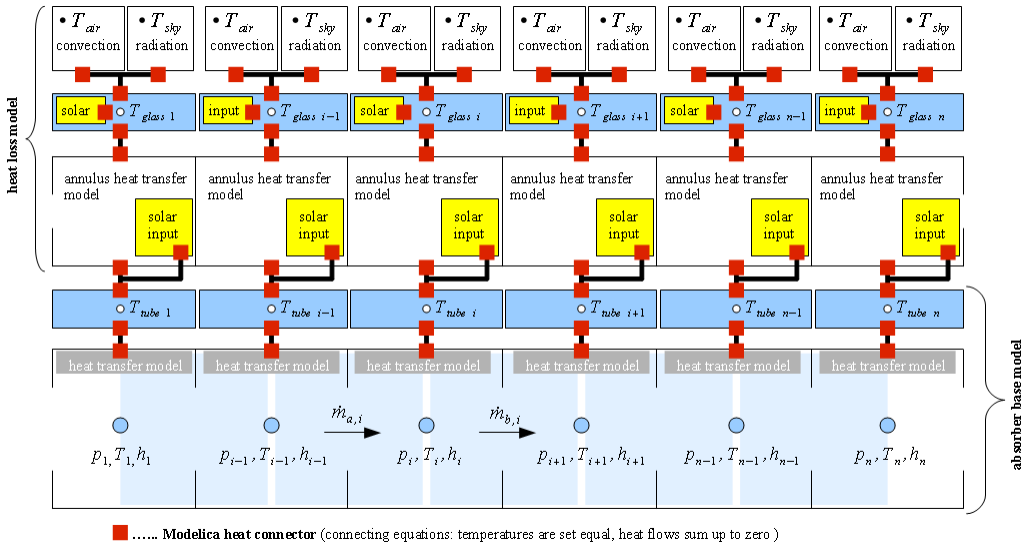

Figure 10.2: The object-oriented parabolic trough collector model scheme according to Forristall [41]

In order to complete the model of the heat collector element (HCE) and the parabolic trough collector (PTC), the heat loss model as well as the model of the solar heat input due to absorption has to be defined.

10.2.1.2 The heat loss model

Figure 10.2 displays the model of the heat collector element, featuring a detailed heat loss model according to Forristall [41]. As can be seen in the figure, the instance of the absorber tube model is coupled with a distributed annulus

heat transfer model, which accounts for radiative and free-molecular convective or natural convective heat transfer, depending on whether the annulus is evacuated or not. The upper boundary of the annulus heat transfer model is coupled with an additional instance of a distributed one-dimensional cylindrical conduction model according to Section 8.2.3, representing the glass envelope. Finally, instances of distributed convection and radiation models represent the environmental boundary conditions. These are connected to the glass envelope's outer surface, completing the heat loss model as one Modelica class. In order to make Forristall's modeling concept suitable for transient simulations in Modelica some modifications have been performed, and are outlined in the following.

Besides the transient formulation of all heat conduction equations for the absorber tube as well as for the glass envelope, the convective heat transfer model to the ambient air has been modified in order to allow for a smooth transition between the so-called "no-wind case" and the "wind case". This basically means that both Nusselt number correlations, i.e. that for natural convection, and that for forced convection, are always evaluated, but the finally used heat transfer coefficient, either that for natural convection, or that for forced convection, is chosen as a function of the current Grashof to Reynolds number ratio ($\frac{Gr}{Re^2}$). In particular, if $\frac{Gr}{Re^2} < 0.7$ the forced convective heat transfer coefficient is chosen, and if $\frac{Gr}{Re^2} > 10$ the natural convective heat transfer coefficient is taken. For values between 0.7 and 10 a smooth transformation is applied, using a continuous transition function as already stated by Equations 7.15 and 7.16.

However, it has to be noted that the transition interval [0.7, 10] was originally proposed for a vertical flat plate [152], and it is thus assumed that it is a reasonable approximation for the case of a horizontal cylinder, as well. Furthermore, the wind direction is not included in the model. Thus, neither shielding effects of the parabolic mirrors, nor deviations from ideal cross flow over the heat collector element can be considered. The ambient air is modeled as ideal gas using polynomial based specific heat capacity data as published by McBride et al. [173], and thermal conductivity and dynamic viscosity functions as published by Kadoya et al. [174].

The PTC model proposed in this work, has been validated at the SOLTERM facility in Italy. Thus, the relationship between the selective coating emittance and its temperature has to be estimated for the specific collectors installed at the facility. Hence, the information given on the manufacturer's product data sheet [198] has been used to obtain a relationship between the selective coating emittance and its temperature. The HCE product data sheet [198] provides emittance values at three absorber tube surface temperature levels (0.1 at 400 °C, 0.14 at 550 °C, and 0.15 at 580 °C). Since these

three values are not enough to construct a reliable emittance curve, it is assumed that the behavior of the selective coating, considered in this work, can be approximated by a polynomial relationship, already known for other receiver selective coatings. Thus, it is assumed that the relationship between the emittance and the absorber tube's surface temperature can be described by the following equation, as published by Burkholder & Kutscher [199]:

$$\epsilon_{abs} = a_0 + a_2 \cdot (T_{tube\ outer} - 273.15)^2 \tag{10.1}$$

The parameters a_0 and a_2 have been obtained via least squares curve fitting using the emittance data published in [198], resulting in a value of 0.0547 for parameter a_0, and a value of 2.826e-7 K^{-2} for parameter a_2. Figure 10.3 shows the three emittance values published in [198] (black points), the fitted curve (solid black line), and the emittance relationship published by Burkholder & Kutscher [199] (dashed black line).

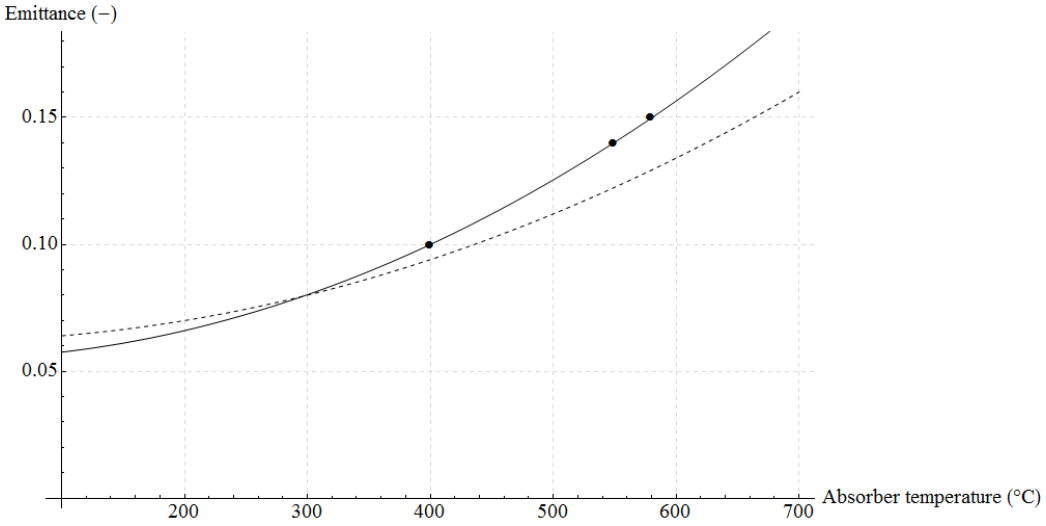

Figure 10.3: Absorber tube selective coating emittance – black points: data published in [198], solid black line: fitted emittance curve, dashed black line: emittance relationship published in [199]

10.2.1.3 The solar heat input model

In order to complete the final PTC model, the solar heat input sub-model has to be defined. This sub-model is then connected to the HCE model, and represents the relationship between the incident direct normal irradiation and the solar energy absorbed.

The basic solar heat input model structure is again of array type, having the same longitudinal level of discretization as the 1-D fluid flow sub-model. Thus, each discrete absorber tube section is coupled with one solar heat input model element (see Figure 10.2) that basically applies the standard PTC modeling approach, which has already been explained and summarized by several previously mentioned authors (e.g. Clark [36] or Edenburn [35] for earlier works, and Manzolini et al. [46] for a recent summary). In general, the solar heat input model accounts for the cosine effect loss, the shading loss, and the optical efficiency, including an empirical correlation for the incidence angle modifier (ζ_{IAM}). This can be written as follows:

$$\dot{Q}_{solar\ input\ i} = DNI \cdot \zeta_{shading} \cdot \eta_{opt} \cdot A_{coll\ i} \tag{10.2}$$

where the optical efficiency can be determined according to Equations 10.3 and 10.4 [48].

$$\eta_{opt} = \eta_{opt\ peak} \cdot \zeta_{IAM} \tag{10.3}$$

$$\zeta_{IAM} = \cos(\Theta) + 0.000884 \cdot \Theta - 0.00005369 \cdot \Theta^2 \tag{10.4}$$

In order to also account for the solar absorption within the glass envelope, which is determined by the solar absorptance of the glass ($\alpha_{glass} \approx 0.02$ [41]), the solar heat input model is split into two parallel parts, i.e. one for the solar absorptance at the receiver tube, and one for the solar absorptance at the glass envelope (see Figure 10.2), each applying the corresponding optical efficiency. Furthermore, since the solar absorption at the glass envelope can be considered as a volumetric effect, which does not only happen at the outer surface, the transient heat conduction equations of the glass envelope have been modified by adding a simple source term that acts at the central temperature node ($T_{glass\ 1}$ to $T_{glass\ n}$). Thus, Equation 8.17, specifically adapted for the glass envelope conduction model, can be written as follows:

$$C_{glass\ i} \cdot \frac{dT_{glass\ i}}{dt} = \dot{Q}_1 - \dot{Q}_2 + \dot{Q}_{solar\ input\ glass} \tag{10.5}$$

Where applicable, replaceable sub-models are used to make the PTC Modelica class as adaptable as possible. In addition, the current direct normal irradiance (DNI) is accessed via an ambient conditions model that is

declared as an "inner/outer" model instance (see Modelica Language Specification [176]), i.e. all ambient condition variables, such as the direct normal irradiance, the ambient air temperature, the wind speed and the sun position [200] are easily accessible within each sub-model, without using additional connecting equations.

10.2.1.4 A possible HCE model simplification – An empirical heat loss model

In order to improve the simulation efficiency, a possible HCE model simplification would be the replacement of the detailed heat loss model, as proposed by Forristall [41], by an empirical heat loss model, only based on the temperature difference between the outer absorber tube surface and the ambient air and the sky temperature, respectively. This possible type of HCE model is displayed in Figure 10.4, and would represent the modeling approaches presented by, e.g., Odeh et al. [39] or Larraín et al. [45]. Since no empirical heat loss model is available in open literature for the HCE type installed at the validation facility, this model concept will not be treated in further detail in this work though. However, it should be shown that the presented PTC model can be easily adapted by simply replacing sub-models.

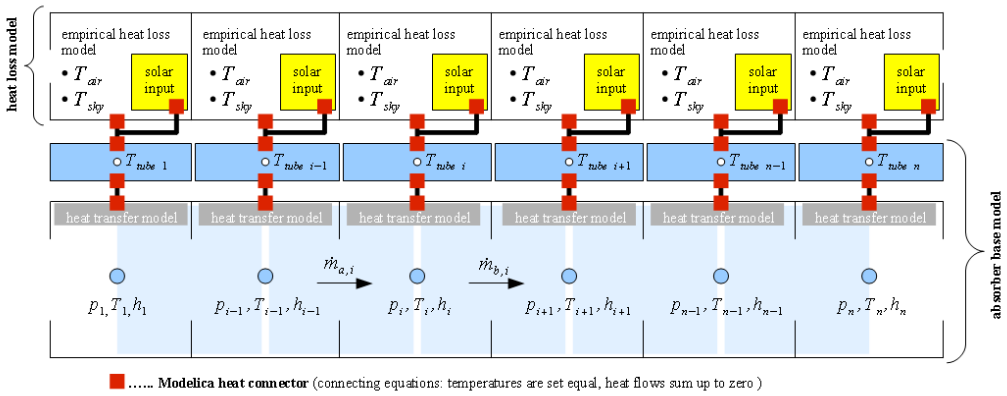

Figure 10.4: Heat collector element (HCE) model scheme, featuring an empirical heat loss model

10.2.1.5 A summary of modeling assumptions

The resulting modeling assumptions can be summarized as follows:

- All finite control volumes are modeled as ideally mixed.

- Heat transfer fluid properties are functions of temperature only.
- All solid material properties, thermal conductivity, density, and specific heat capacity are assumed to be constant and homogeneous.
- The absorber tube as well as the glass envelope are divided in discrete sections that have uniform surface temperatures and one representative node temperature ($T_{tube\,1}$ to $T_{tube\,n}$, or $T_{glass\,1}$ to $T_{glass\,n}$) in the center of the tube's wall.
- The whole thermal capacitance of each discrete tube or discrete glass envelope section is assumed to be lumped at these central temperature nodes ($T_{tube\,1}$ to $T_{tube\,n}$, or $T_{glass\,1}$ to $T_{glass\,n}$).
- The absorber tube as well as the glass envelope is assumed to have uniform circumferential temperatures and a uniform circumferential solar heat input. Strictly speaking, this is definitely not the case in reality, since the absorber tube is only heated in the regions facing the reflecting mirror surface.
- The glass envelope is assumed to be opaque to infrared radiation.
- The heat conduction in longitudinal direction within the absorber tube and the glass envelope is neglected.
- The heat loss via the expansion bellows at the ends of each HCE is neglected.
- Furthermore, any heat loss caused by the HCE support brackets is neglected, too. Strictly speaking, this additional loss term can be approximated by treating the brackets as infinite fins [41, 68]. However, taking other accuracy limiting modeling assumptions into account (e.g. only one-dimensional radial heat conduction equations for the absorber tube, no heat loss model for the expansion bellows) the author considers this as a good compromise regarding model complexity.

Basically, these assumptions correspond with already proposed modeling approaches (as outlined in Section 2.1), for transient PTC performance simulations as well as for solar field control design, as they provide a good trade-off between calculation effort and accuracy.

10.2.2 The experimental validation of the parabolic trough collector model

In this section, the validation of the transient PTC model is presented. In order to validate the model, measurement data obtained at the SOLTERM facility, located in Casaccia, Italy, is used and compared to simulation results. The presented measurement data was obtained during a test campaign of the VAMOSS project: VAlidation of a dynamic model for MOlten Salts Solar facilities, granted to the National Renewable Energy Center (CENER, Spain) within the European SFERA (Solar Facilities for the European Research Area) program. In the following, the SOLTERM facility and the performed experiment will be briefly described.

Note: This section is a corrected[3] republication of the work first published in Elsevier's journal Solar Energy [34]. Unfortunately, Figures 17, 18 and 19 of the original work [34] display wrong results and have thus been corrected and must be replaced by the Figures 10.16, 10.18 and 10.19 of this work.

10.2.2.1 The SOLTERM facility and the performed experiment

The SOLTERM facility ("Progetto SOLare TERModinamico") is located in Casaccia (Rome), Italy, and is operated by the Italian National Agency for New Technologies (ENEA). Basically, this facility is a closed molten salt test loop, consisting of one storage tank and two PTC assemblies (east-west orientation). In order to allow for temperature regulation of the circulated molten salt, the facility features an electric heater as well as convective air coolers. In addition, all connecting pipes as well as the absorber tubes are heat traced, keeping the circuit at all times above a certain temperature level (270 – 300 °C), ensuring liquid state of the containing salt mixture. During operation, the molten salt is drained from the storage tank and pumped through the circuit, i.e. it passes through the electric heater, the two PTC assemblies and the air coolers, and finally returns to the storage tank. A scheme of the facility can be found in [172].

Figure 10.5 shows a scheme of the two PTC assemblies installed at the SOLTERM facility. This section of two PTCs is taken for the transient model

[3]Unfortunately, a wrongly placed parenthesis in the Nusselt number correlation for the natural convective heat transfer coefficient at the glass envelope's outer surface made three figures and a certain part of the simulation completely useless - *To err is human* [201, 202]. However, despite this severe implementation error, it turns out that the final difference in outlet temperature is negligible, which is also the reason why it was not detected during the model's validation procedure. Only Figures 17, 18 and 19 of the original work [34] are useless. The other simulations have been performed with higher wind speed values, thus being in the range of forced convection only.

validation. Each assembly consists of 12 heat collector elements of 4.06 m length. Thus, one solar collector assembly has a total length of 48.72 m. Furthermore, the total tube length of the insulated and flexible connecting joint amounts to about 4 m as well. This value is used throughout this work.

The signals of the temperature sensors located at the inlet of the PTC assembly number one and at the outlet of the PTC assembly number two (see Figure 10.5) have been used for the model validation. Both temperature sensors are calibrated thermocouples providing an accuracy of ± 2 °C (the accuracies of all used measurement devices are stated in Table 10.1).

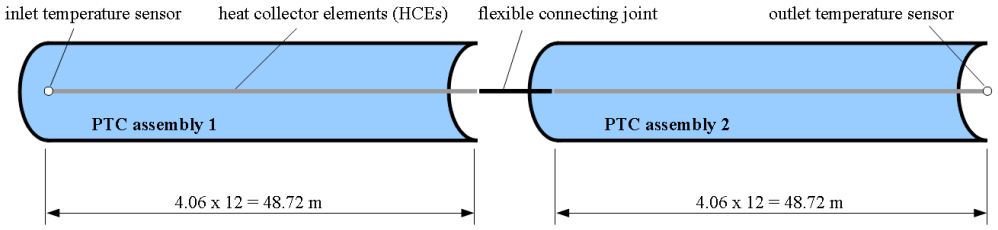

Figure 10.5: Scheme of the two PTC assemblies at ENEA, consisting of 12 HCEs each [34]

Table 10.1: Accuracies of all used measurement devices

Measurement device	Accuracy of measurement (Range)
HTF temperature sensors (thermocouples)	±2 °C / ±0.5 °C
HTF flow rate sensor (orifice plate + differential pressure transmitter)	±1% (3 – 9 kg/s)
DNI sensor (pyrheliometer)	±2% (0 – 1400 $\frac{W}{m^2}$)
Air temperature sensor (resistance temperature detector)	±0.3 °C
Wind speed sensor (cup anemometer)	±2% (0.15 – 10.3 m/s)*)
	*) wind speed threshold ≈ 0.15 m/s

The experiment used for the here presented model validation was performed on the 4th of October, 2012, starting at about 9:00 am, and lasting until about 2:30 pm (local solar time). Throughout the whole experiment the molten salt mass flow was set to certain pre-defined values. Thus, the solar collector outlet temperature was not controlled and the resulting temperature drop or rise depended on the current incident solar irradiance, and the heat loss to the ambient. Furthermore, both collectors were defocused (zero solar input) at the beginning of the experiment until about 9:40 am. From then on, both collectors remained focused, tracking the sun until the end of the experiment.

Figure 10.6 displays the molten salt mass flow rate. Basically, the intention was to perform the experiment at different levels of constant mass

flow rates. However, due to the absence of a HTF mass flow control loop at the SOLTERM facility, the actual mass flow was determined via manually adjusting a valve. Therefore, as can be seen in the graph, the measured mass flow significantly deviates from ideal step signals.

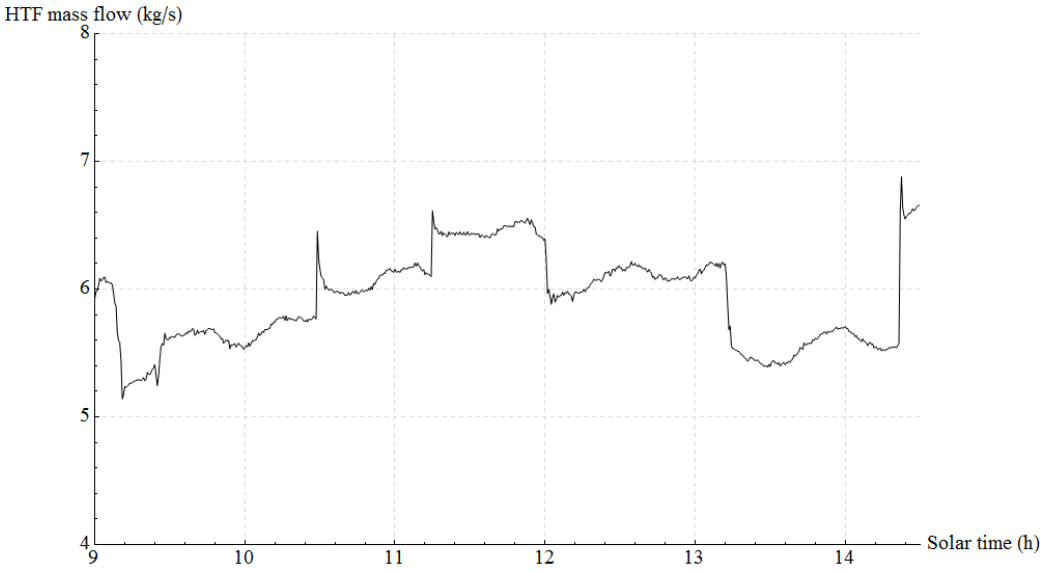

Figure 10.6: HTF mass flow rate of the validation experiment [34]

The remaining boundary conditions needed for the simulation are the measured temperature at the inlet of the solar collector assembly (see inlet temperature sensor indicated in Figure 10.5) and the ambient conditions, i.e. the measured direct normal irradiance, the measured ambient air temperature as well as the measured wind speed. Since the molten salt is modeled as incompressible fluid, its density does not depend on the pressure, i.e. the pressure level within the molten salt circuit can be arbitrarily set. It has to be noted that it was impossible to obtain reliable pressure drop measurement data for the PTC assembly. Therefore, the validation of the previously described pressure drop sub-model is not included in this work.

Figure 10.7 displays the direct normal irradiance (solid gray line), and the direct normal irradiance multiplied by the cosine of the incidence angle (solid black line), i.e. the effectively usable fraction of the incident solar irradiance. As can be seen in the graph, the incident solar irradiance is relatively undisturbed from 9 am until right before 11 am. From then on, the incident solar irradiance is considerably disturbed by passing clouds throughout the remaining experiment, representing excellent boundary conditions for simulations under transient conditions.

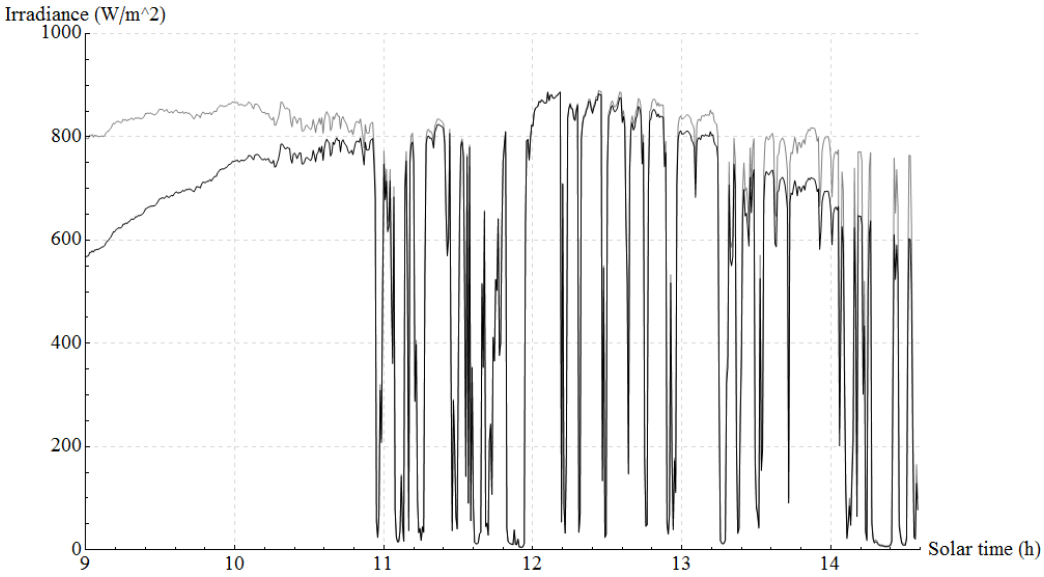

Figure 10.7: Incident solar irradiance during the validation experiment – solid gray line: DNI, solid black line: DNI multiplied by the cosine of the incidence angle [34]

Figure 10.8 and Figure 10.9 show the ambient air temperature and the wind speed, respectively.

10.2.2.2 Simulated collector outlet temperature versus measured outlet temperature

During the performed experiment, the solar collector assembly inlet temperature as well as the solar collector assembly outlet temperature was measured (see the indicated sensors in Figure 10.5). The measured inlet temperature was provided as boundary condition for the simulation. Hence, the aim of the model validation was to reproduce the outlet temperature of the solar collector assembly. Thus, in this section, the simulated outlet temperature will be compared with the measured outlet temperature, proving the validity of the model. It has to be noted that the collector inlet temperature measurement signal was assumed to be "ideal", hence neglecting the uncertainty range of $\pm$ 2 °C. The same applied for the remaining boundary conditions as mass flow, solar irradiance, ambient air temperature and wind speed. They were implemented in the model via a Modelica table ("combi table 1-Ds"). The model was simulated using a state-of-the-art commercial tool applying the differential algebraic system solver DASSL [178] (see Section 8.2.7).

It should be noted, that a previous model adjustment was needed to be

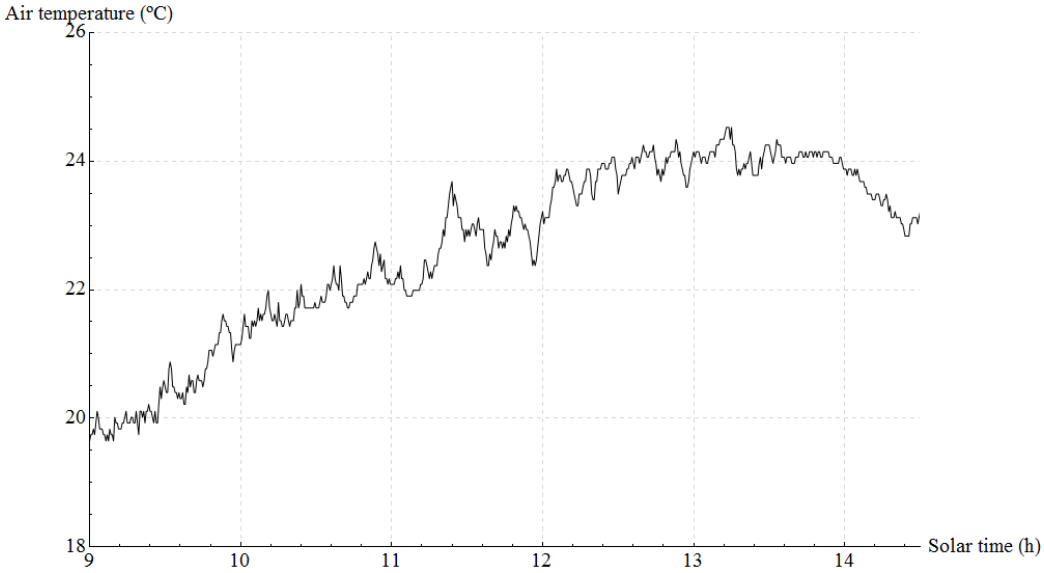

Figure 10.8: Ambient air temperature during the validation experiment [34]

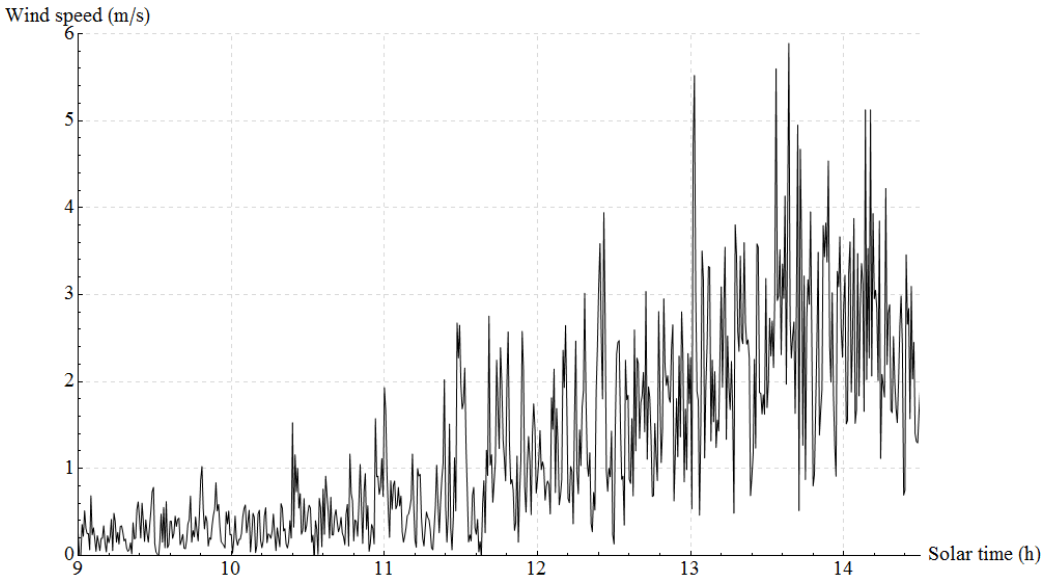

Figure 10.9: Wind speed during the validation experiment [34]

able to fit the measured data satisfactorily well. In this work, the cleanliness factor of the parabolic mirrors was the only parameter adjusted. In particular, it was adjusted to steady-state measurement data of another experiment, performed on the 5th of October 2012, ensuring the decoupling of the validation and the adjustment data sets. The cleanliness factor value obtained constitutes 0.948. This value was obtained by adjusting the model to the measured outlet temperature, without considering the uncertainty range of $\pm$ 2 °C.

For both the adjustment and the validation process, the number of control volumes (n) per heat collector element was set to 2, resulting in 24 control volumes per solar collector, and thus, 48 control volumes for the whole modeled collector assembly.

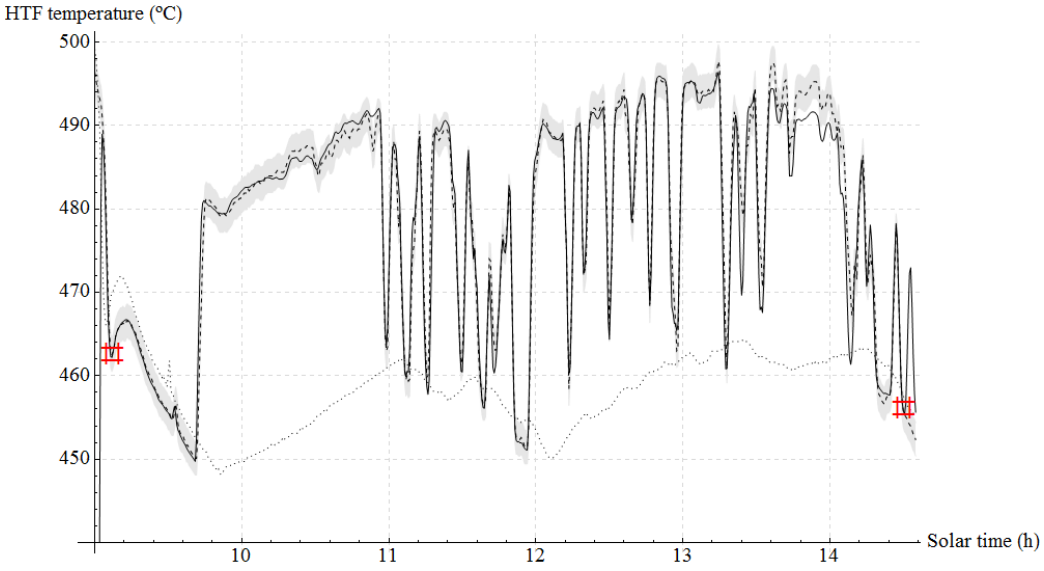

Figure 10.10: Simulated HTF outlet temperature versus measured outlet temperature – dotted line: measured inlet temperature, dashed line: measured outlet temperature (uncertainty range shaded), solid line: simulated outlet temperature

Figure 10.10 shows the measured inlet temperature (dotted line), the measured outlet temperature (dashed line) as well as the simulated outlet temperature (solid line). In addition, the uncertainty range of $\pm$ 2 °C of the measured collector outlet temperature is indicated via the shaded gray area. In general, a good correlation can be observed between the measured and the simulated outlet temperature. For the most part of the experiment the deviation remains within the measurement uncertainty range. However, larger deviations do occur, especially between about 1:20 pm and 2 pm. This can

be explained by the fact that the solar irradiance is assumed to be uniformly distributed along the whole collector length, while in reality, partial shading of the solar collectors occurs, which is neither measured nor considered in the simulation. In principle, this partial shading could be considered in the model, since the solar heat input variable is an array of size n (see Figure 10.2), thus being able to assign different solar heat inputs to each discrete section. However, the solar irradiance measurements are only available for one single location of the facility, since there is only one measurement device installed, so that this non-uniform solar irradiance boundary condition is not possible to implement with the current equipment.

In order to give an idea of the accuracy of the model, the root-mean-square error (RMSE) between the measured and the simulated outlet temperature values was calculated. The RMSE was calculated according to the following equation, considering the measurement data as "ideal", neglecting the uncertainty range of ± 2 °C:

$$RMSE = \sqrt{\frac{\sum_{j=1}^{z} \left(simulated_j - measured_j\right)^2}{z}} \tag{10.6}$$

Measurements as well as simulation results were taken at time steps of 30 seconds. The considered starting and end points of the interval for the root-mean-square error calculation is indicated by the hash marks in Figure 10.10 (starting at about 9:10 am, until about 2:30 pm). This "ideal" root-mean-square error constitutes 2.32 °C. This is about 5.8%, based on the maximum temperature increase in the collector assembly during the experiment. However, considering the relatively large measurement uncertainty range of ± 2 °C, it does not make sense to state a RMSE showing two decimal places. Thus, it can only be said that the accuracy of the model does approximately correspond with the uncertainty range of the measurements. Furthermore, with Figure 10.10 it can only be shown that the general dynamics are reproduced well; a validation of, e.g., the heat loss model would be impossible, since the uncertainty ranges of the measured inlet temperature and the measured outlet temperature do overlap during the defocussed part of the experiment.

Besides the dynamics caused by the varying solar irradiance, the model also reproduces "step" changes in the inlet temperature very well. An example for this can be seen in Figure 10.10 in the first part of the experiment. At about 9:30 am, a sudden increase and decrease in collector inlet temperature can be seen, which has the shape of a "spike". This sudden inlet temperature change was caused by the electric heater of the molten salt loop, which

was switched on for a short period of time. As can be seen in the graph, the abrupt change in inlet temperature propagated through the whole collector assembly, appearing at the outlet slightly damped. This part of the experiment clearly shows the dead time of the collector assembly, which is determined by the current HTF mass flow rate.

In order to show that the presented PTC model is able to reproduce any kind of experiment performed at the SOLTERM facility, two additional simulations for two additional measurement data sets, obtained on the 27th of September and on the 5th of December 2012, were accomplished. It has to be emphasized that the model was not adjusted to the new data, only the boundary conditions were replaced. Furthermore, before the experiment on the 5th of December, both thermocouples at the collector assembly inlet and the collector assembly outlet were replaced by more accurate ones, reducing the temperature measurement uncertainty range to $\pm$ 0.5 °C.

Figure 10.11 displays the simulation results for an experiment performed on the 27th of September, 2012. There, both solar collectors were defocused from the start of the experiment until about 9:54 am (solar time). From then on, both collectors kept tracking the sun throughout the remaining experiment. As can be observed, continuously passing clouds caused a remarkable transient behavior of the collector outlet temperature.

Figure 10.12 shows the simulation results of an additional experiment, performed on the 5th of December, 2012, featuring newly installed thermocouples with an improved accuracy ($\pm$ 0.5 °C). The mass flow was set to certain pre-defined values as well, but unlike the experiments explained before, both solar collectors were kept defocussed during the whole test interval. Thus, the difference between the inlet and the outlet temperature was only determined by the heat loss to the environment.

Again, the "ideal" root-mean-square errors between the simulation results and the measurements were calculated. This was done for the intervals indicated by the hash marks in Figure 10.11 and 10.12. The root-mean-square errors constitute about 1.8 °C and 0.5 °C, respectively. These values are about 6.3% and 6.4% respectively, based on the maximum temperature increase/decrease in the collector assembly during the experiments. Again, it can be said that the accuracy of the model does approximately correspond with the uncertainty range of the measurements.

Summarizing the model validation, it can be stated that the simulation results show a very good correlation with the measured data, reproducing a large variety of phenomena. The only advisable model improvement would be a non-uniform solar heat input boundary condition over the whole solar collector length, the validation of which is, however, not possible with the above presented data set.

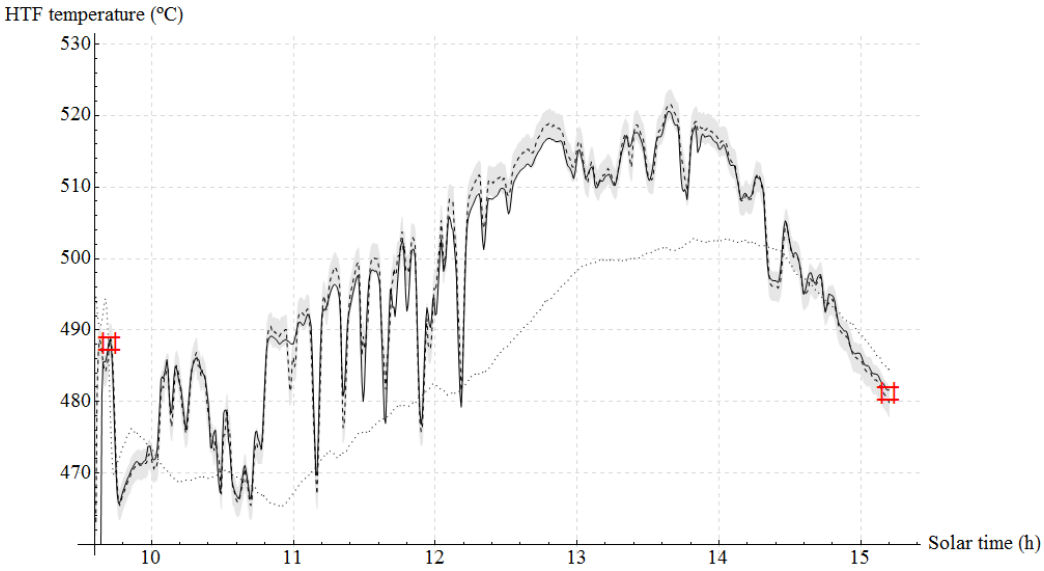

Figure 10.11: Simulated HTF outlet temperature versus measured outlet temperature – dotted line: measured inlet temperature, dashed line: measured outlet temperature (uncertainty range shaded), solid line: simulated outlet temperature [34]

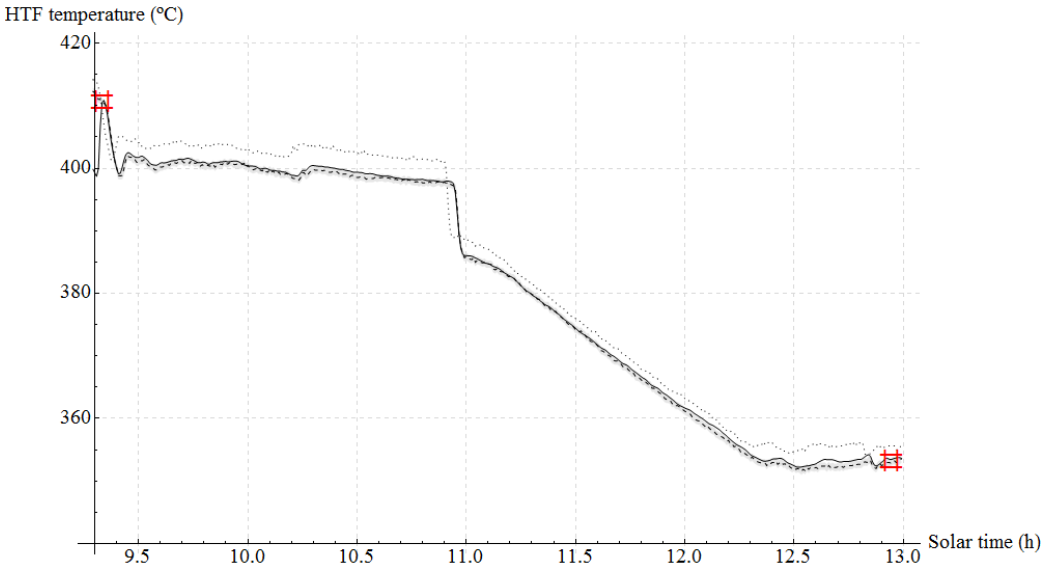

Figure 10.12: Simulated HTF outlet temperature versus measured outlet temperature – dotted line: measured inlet temperature, dashed line: measured outlet temperature (uncertainty range shaded), solid line: simulated outlet temperature [34]

It has to be noted that the validation process of the presented model was only performed for a rather small operating window and a limited loop length of about 100 m, caused by constraints of the SOLTERM facility. However, many dependencies are highly non-linear and it has to be clarified whether the obtained results do also apply when modeling a representative full-size loop of a solar plant. The HTF temperatures observed during the validation process range between 352 and 520 °C (see Table 10.2). The HTF mass flow ranges between 3.8 and 6.9 $\frac{kg}{s}$ (see Table 10.2). Thus, strictly speaking, the model's results are only verified for these operating conditions and solar salt as HTF. However, since it is a detailed physical model that considers all three modes of heat transfer (conduction, convection and radiation), there is also confidence in its correctness beyond the validation window and other single-phase fluids, considering, of course, that all dimensionless correlations are evaluated within their range of validity. Nevertheless, since the model only considers one-dimensional heat transfer and thus assumes each discrete pipe and glass envelope element to have uniform longitudinal temperatures, a certain minimum number of elements is required to correctly estimate the non-linear temperature profile of the solar absorber. Also the transient behavior of the model depends on the chosen level of discretization. These issues were dealt with in Section 4 of the original work [34] of the author.

Table 10.2: Validity range of the validation tests at the SOLTERM facility

	Min. value observed	Max. value observed	Range
HTF mass flow (kg/s)	3.8	6.9	3.1
HTF Temperature $(°C)$	352	520	168
HTF Prandtl number	3.6	6.8	3.2
HTF Reynolds number	37 974	104 063	66 089
Ambient air temperature $(°C)$	6	28	22
Wind speed (m/s)	0	6	6
Reynolds number ambient air *)	0	43 131	43 131
Grashof number ambient air *)	6.04964e6	1.45644e7	8.514760e6
Prandtl number ambient air *)	0.7	0.71	0.01
Gr/Re^2 ambient air *)	0.0043	2818	$\approx$ 2818

*) evaluated at film temperature (arithmetic mean between envelope surface and air bulk temperature)

10.2.2.3 Analysis of important simulation results

In this section some important simulation results will be presented, indicating the governing mechanisms of heat transfer and providing suitable data for future model comparison studies. As outlined above, the number of discrete sections per solar collector was set to 24, for the purpose of model validation. In the following, specific simulation results of the experiment displayed in

Figure 10.10 will be plotted for the last discrete element of the whole collector assembly. Hence, all important model variables will be plotted for the 24th discrete section of solar collector number 2.

Figure 10.13 shows the absorber tube's outer surface temperature (black solid line), i.e. the selective coating temperature, the absorber tube's inner wall temperature (black dashed line), and the HTF bulk temperature (solid gray line) of control volume number 24 of collector number 2. The resulting temperature differences, determined by the solar absorption and the heat loss to the ambient can be observed. For the given absorber tube parameters as thermal conductivity and geometry, the temperature difference across the absorber tube's wall reaches a maximum of about 2.3 K, during times of high solar irradiance. It has to be emphasized that this maximum in temperature difference is based on the modeling assumption of having a circumferentially uniform temperature and heat flux distribution. In reality, the temperature differences will be higher in zones oriented towards the mirror. The maximum temperature difference between the HTF bulk temperature and the absorber tube's inner wall amounts to about 6.4 K.

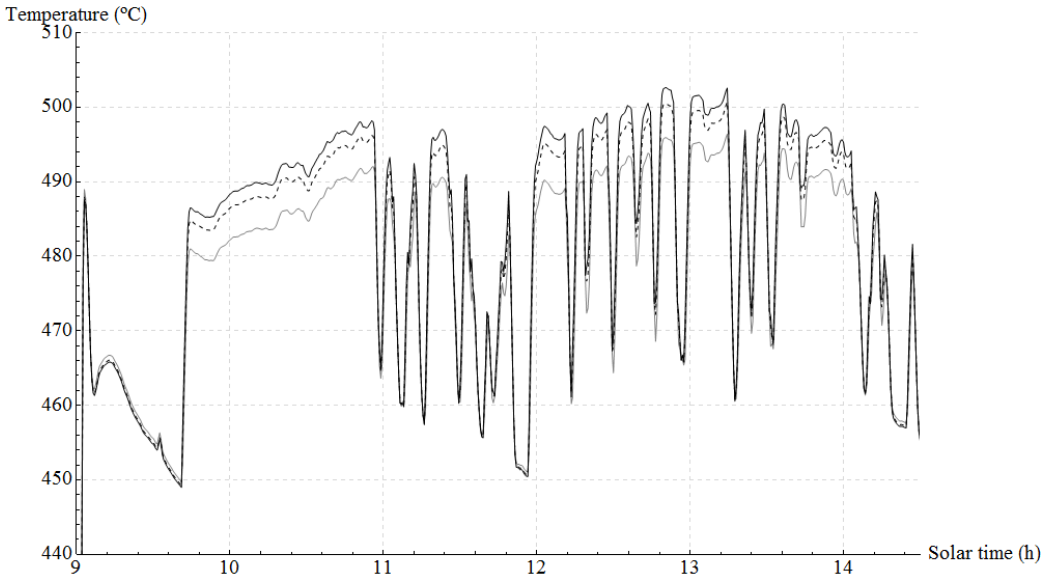

Figure 10.13: Temperatures of the last discrete absorber tube element of collector number 2 – black solid line: outer surface temperature of absorber, black dashed line: inner surface temperature of absorber, gray solid line: HTF bulk temperature

The Reynolds number and the forced convective heat transfer coefficient between the HTF and the absorber tube's inner wall are displayed in Fig-

ures 10.14 and 10.15 respectively. Throughout the whole simulation, the heat transfer fluid flow clearly stays within the turbulent regime. The corresponding forced convective heat transfer coefficient, i.e. the result of the local evaluation of Equation 8.19, ranges between 2986 and 3786 $\frac{W}{m^2\,K}$.

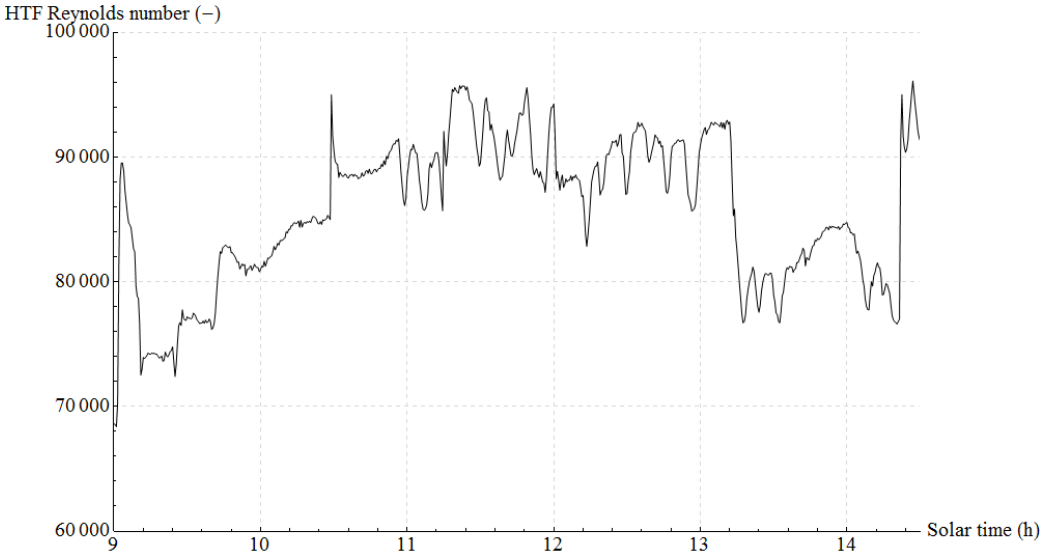

Figure 10.14: HTF flow Reynolds number (24th control volume of solar collector 2)

Figure 10.16 shows the outer (solid line) and the inner (dashed line) surface temperature of the glass envelope. It can be well observed that the temperature of the glass envelope is considerably reduced during the period of intermittent direct normal solar irradiance and higher wind speeds. While being in the range of 120 °C between 10 and 11 am, the temperature of the glass envelope steadily decreases from then on, due to higher wind speeds and several passing clouds.

The impact of higher wind speeds on the convective heat transfer coefficient can be seen in Figure 10.17. While being at around 6 $\frac{W}{m^2\,K}$ at low wind speeds and thus temporarily dominating natural convection (rather straight and smooth sections), its values rise up to about 26 $\frac{W}{m^2\,K}$ at higher wind speeds and dominating forced convection.

Figure 10.18 displays the total heat loss to the ambient at the outer surface of the glass envelope per meter of collector length, of course, again for the last discrete element of solar collector number 2. This total heat loss can be subdivided into the convective and the radiative part, which are shown in Figure 10.19. As expected, the convective heat loss (gray line) correlates with the wind speed (Figure 10.9). The higher the wind speed

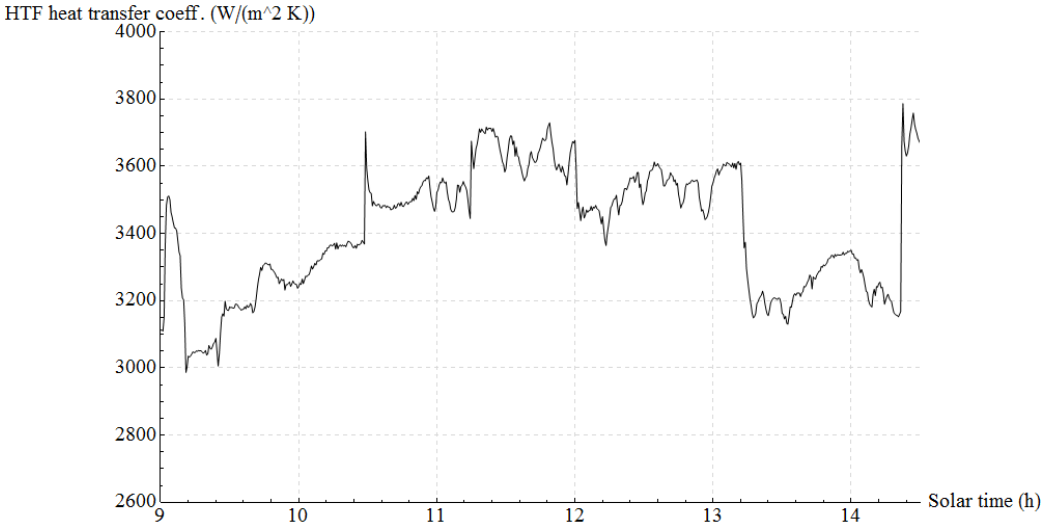

Figure 10.15: Convective heat transfer coefficient between the HTF and the absorber tube's inner wall (24th control volume of solar collector 2)

is, the higher is also the heat loss caused by convection. The radiative heat loss (black line) shows its expected behavior as well, hence being larger for higher glass envelope surface temperatures. Since the glass envelope cools down after about 11 am, also the radiative heat loss steadily decreases.

10.2.2.4 Acknowledgments

The author would like to thank the SFERA (Solar Facilities for the European Research Area) project and all the people related to it. The author would, especially, like to thank the people working at the SOLTERM facility in Italy (Casaccia, Rome), which is operated by the Italian National Agency for New Technologies (ENEA). In particular, the authors are grateful to Rita D' Adamio, Fabrizio Fabrizi, Walter Gaggioli, Primo Di Ascenzi, Antonio De Luca and Massimo Falchetta for the pleasant and informative stay.

10.3 The thermal energy storage system submodel

This section describes the thermal energy storage model used for the subsequently presented simulations of the parabolic trough collector plant on system level. The thermal energy storage concept considered is a typical

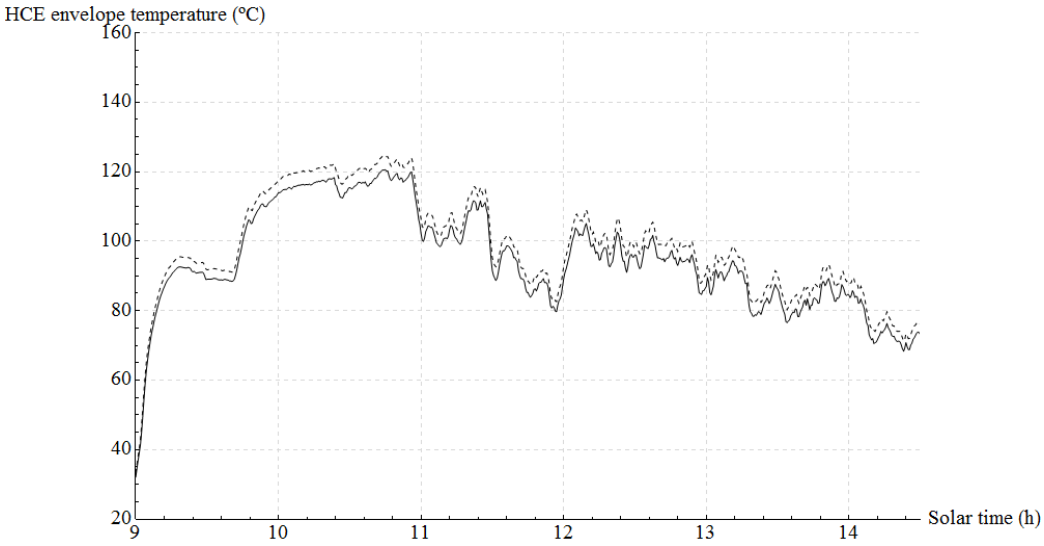

Figure 10.16: Heat collector element envelope surface temperatures (24th section of collector number 2) – solid line: outer surface, dashed line: inner surface

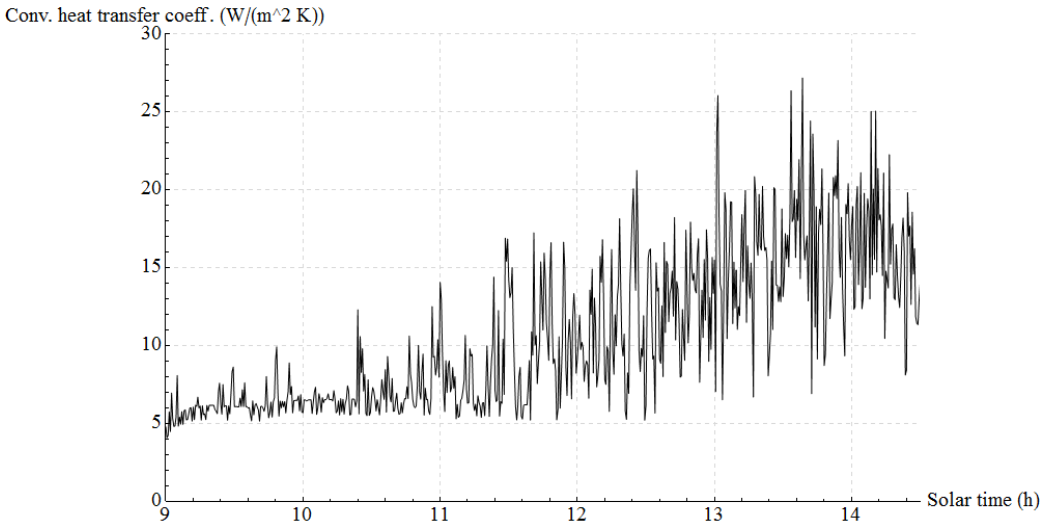

Figure 10.17: Convective heat transfer coefficient at the envelope's outer surface (24th section of collector number 2)

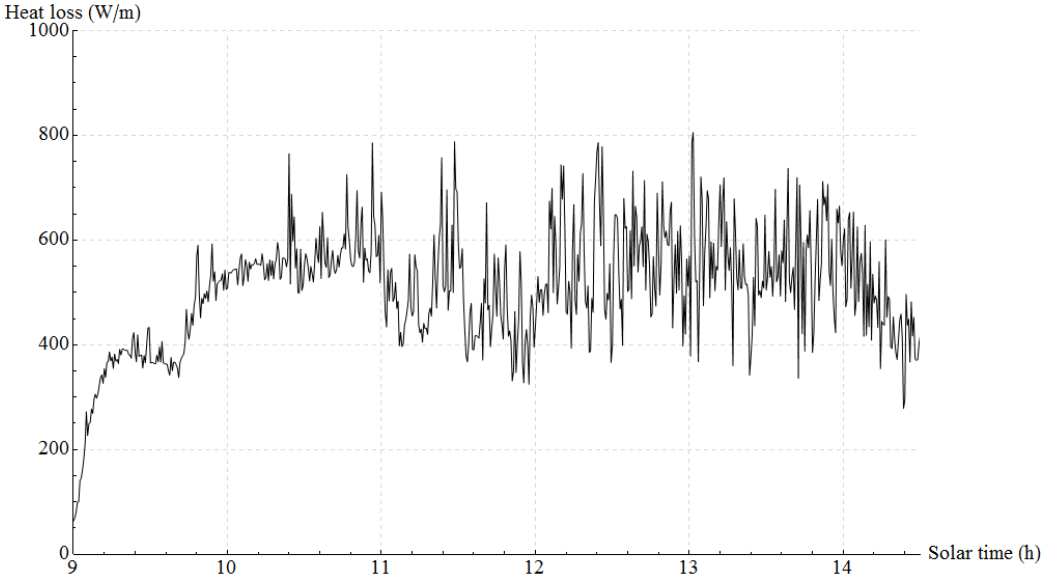

Figure 10.18: Total heat loss to the ambient at the outer surface of the glass envelope (24th section of solar collector number 2)

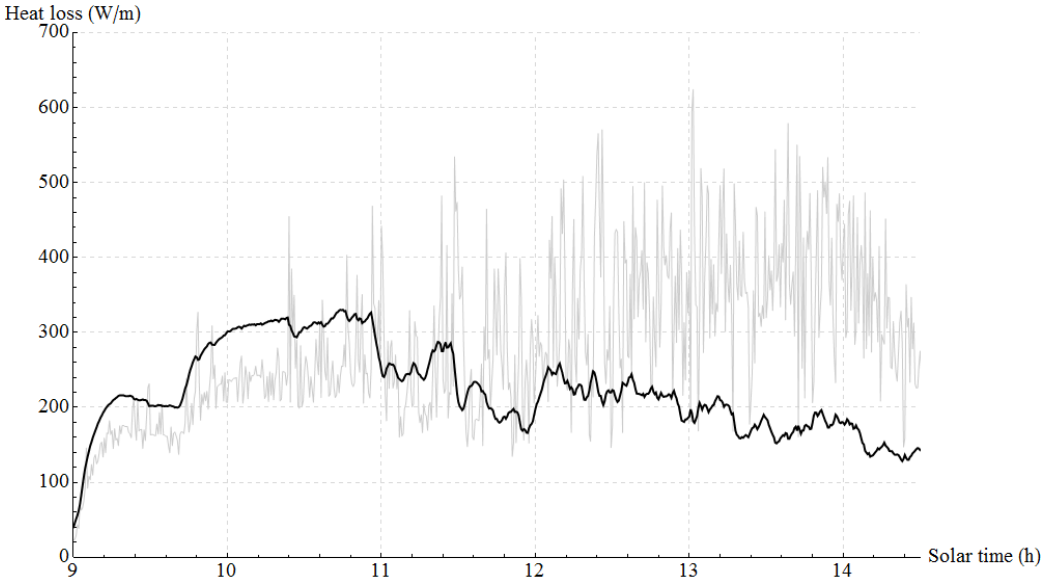

Figure 10.19: Convective (gray line) and radiative (black line) heat loss to the ambient at the outer surface of the glass envelope (24th section of solar collector number 2)

active indirect two-tank system, using molten salts as storage medium, as it is currently applied at commercial power plants.

Detailed modeling approaches for this type of thermal energy storage have been derived in Part II of this work, also indicating feasible model simplifications that have negligible impacts on the simulation results. Thus, this section combines all these simplifications proposed, obtaining a reasonable simple transient performance model of an active indirect two-tank thermal energy storage system.

The general system layout is shown in Figure 8.12 of this work. The basic components are the molten salt storage tanks (the hot tank and the cold tank) and the oil-to-molten-salt heat exchanger train, which typically consists of 3 shell-and-tube subunits connected in series.

The dimensions of the system are set to the same values as discussed in Part II of this work (see Section 9).

The storage tank model is based on the assumption of having one representative molten salt temperature. Hence, the molten salt inventory within the tank is modeled via a single lumped control volume, defining an ideally mixed energy balance. The heat loss to the ambient is modeled in transient mode, by taking the thermal inertia of the tank's steel container as well as that of the insulation material into account. Convective heat losses via the tank's gas atmosphere (nitrogen at ambient pressure) above the molten salt surface are neglected. The important radiative heat transfer between the surface of the molten salt and the non-wetted parts of the tank's steel jacket is considered assuming an ideal cylindrical geometry. The convective heat transfer coefficients at the wetted inner surfaces of the tank's steel jacket are assumed to be constant. The heat transfer at the tank's outer surfaces is split into the convective and the radiative part, also considering the solar absorption, which allows for a reasonable approximation of the influence of altering environmental boundary conditions.

The 3 shell-and-tube subunits connected in series are considered applying an equivalent axial double-pipe heat exchanger model setup in counter-flow arrangement, as discussed in Section 8.5 of this work. The longitudinal discretization level has been set to 80 control volumes per fluid duct. Furthermore, the detailed pressure drop models, as e.g. discussed in Section 8.2.4.2 of this work, are replaced by a simple quadratic relationship (see Equation 10.13) that has been fitted to detailed simulation results under different load conditions. It has to be noted that the replacement of individual sub-models can easily be achieved via the re-declaration feature of the Modelica language during model instantiation.

Standard PI feedback control loops are applied for the control of the molten salt flow rate. The controller settings correspond to the values given

in Section 9.3 of this work.

Figure 10.20 displays the final scheme of the thermal energy storage model for system level simulations. Note: The drawings of the molten salt tanks have to be associated with the scheme displayed in Figure 7.2 of this work.

The molten salt pumps (one for discharging mode, and one for charging mode) are considered according to Equation 10.19.

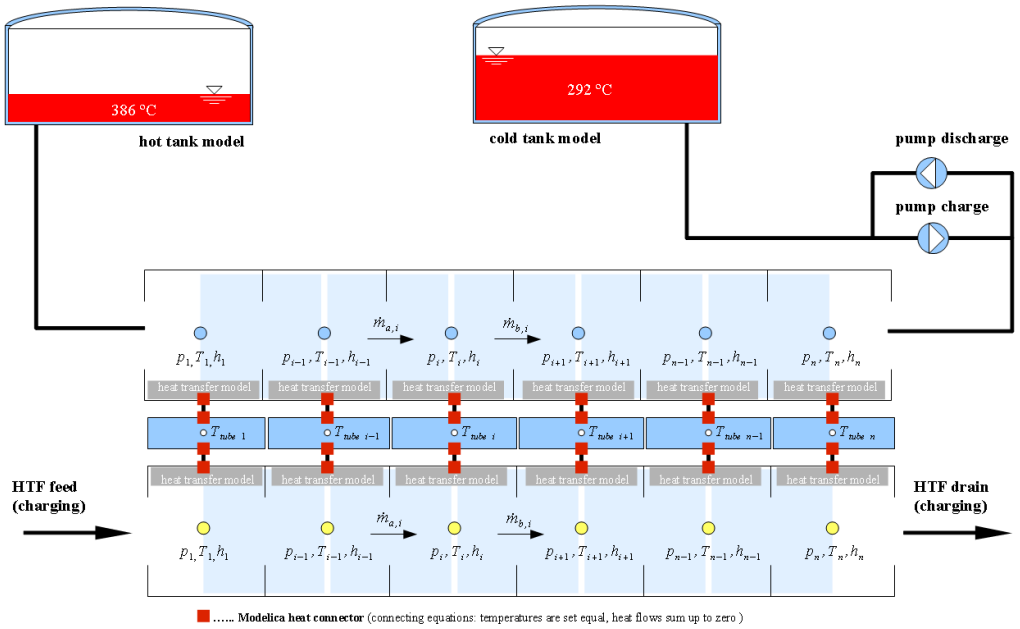

Figure 10.20: The thermal energy storage model scheme for system-level simulations

10.4 The power block sub-models

Power block models for CSP performance simulations range from simple efficiency-correlation-based polynomial models (i) (where the current electric output is a function of the entering HTF mass flow rate or thermal power input only), over multi-dimensional performance maps or tables (ii) (where the current electric output is a function of, e.g., the HTF mass flow rate, the HTF inlet temperature and the condenser pressure), to detailed quasi-steady zero-dimensional physical models (iii) having several hundreds of variables. Of course the best model is always the fastest having the wanted accuracy level. Thus, given the availability of a corresponding state-of-the-art process simulation tool [29], the best option for CSP performance simulations is

usually to obtain a multi-dimensional performance map of the power block by running a detailed physical zero-dimensional model multiple times, performing a systematic parameter variation. However, when many different process setups have to be investigated, it can be more efficient, including a sufficiently detailed physical zero-dimensional model of the power block in the solar thermal power plant performance model.

For example, Gracia et al. [49] applied model type (i) in their study, based on a polynomial efficiency correlation having the supplied thermal power of the solar field as input. Model type (ii) was used, amongst others, by Hirsch & Schenk [195] and Patnode [42]. Patnode [42] derived a linear regression equation, based on a zero-dimensional physical model, having the HTF mass flow rate, the HTF inlet temperature and the condensing pressure as inputs of the linear regression model. Detailed zero-dimensional physical power block models, i.e. model category (iii), directly incorporated into the solar plant's performance model, were for example applied by Stuetzle et al. [58], Rheinländer et al. [43], Zaversky at al. [203] or Manzolini et al. [46, 47].

This work applies two separate power block model concepts. Model type A is a combination of a transient steam generator model with a quasi-steady turbine-condenser-preheater-pump circuit, assuming that the transients of the steam generator are the dominant ones. Model type B applies a full quasi-steady zero-dimensional model coupled with a simple thermal inertia that has to be heated up in the morning before the power block delivers power to the grid. This is conceptually similar to the models presented by Stuetzle et al. [58] or Hirsch & Schenk [195].

In the following, both power block models (A and B) will be explained in detail.

10.4.1 The power block model type A (transient and quasi-steady)

Unlike the other solar plant sub-models as the solar field and the storage model that feature a complete transient formulation, the power block model type A is a combination of transient lumped or distributed parameter models and steady-state models. In particular, the steam generator (the economiser, the evaporator and the superheater) is modeled in transient mode considering the containing water and the steam as compressible fluid, i.e. the drum pressure is a function of heat input and steam extraction (turbine valve opening). The remaining components as steam turbines, condenser, feed water preheaters, deaerator, valves and pumps are modeled in steady state as their transient responses are usually negligible when compared to the

dynamics of the boiler. This should result in a reasonable trade-off between model complexity and the exact representation of the dominant dynamic behavior of the power block. The transient behavior of the steam generator and its limitations concerning rapid changes in temperature (considering the maximum thermal stress allowed) are a key issue for the power plant's start-up. Thus, a transient steam generator model is essential for detailed solar thermal power plant short-term simulations. Besides thorough considerations of the power plant's start-up, shut-down, or emergency simulations, such a detailed model can be used for the adjusting and fitting of much simpler models that are, e.g., suitable for long-term performance simulations.

10.4.1.1 The transient steam generator model

The aim of this section's modeling task is to implement a transient steam generator model that is able to capture the basic boiler dynamics as the response of the drum pressure to changes in heat input and steam flow rate (i.e. the response of the drum pressure to changes in HTF mass flow rate, or in turbine valve opening). Additionally, the model should allow for an estimation of component wall temperatures and their corresponding rates of change. Due to the high operating pressure of steam generators, which typically constitutes about 100 bar in CSP applications, the estimation of wall temperature distributions and wall temperature time derivatives play an important role considering component fatigue and thus life time. The knowledge of wall temperatures is important since besides the strain caused by the operating pressure, also the thermal stress in the component walls has to be considered. An exceeding of the maximum allowed component wall surface temperature or an exceeding of the maximum allowed temperature difference within the component wall may lead to damage and, in the worst case, to component failure [204]. Additionally, during steam generator start-up and shut-down procedures, a certain limit of the rate-of-change in wall temperature (wall temperature time derivative) must not be exceeded, since the thermal stress in thick component walls (steam drum wall) must not surpass a certain limit [204]. This rate-of-change limit is especially relevant for solar thermal power plants since frequent start-up and shut-down procedures as well as large changes in load are quite common due to the intermittent nature of solar energy. Steam generator designs that allow higher rates of change in wall temperature can considerable shorten start-up times and thus increase the operating time of solar thermal power plants. Typical rate-of-change limits for CSP steam generators constitute about 2-3 °C per minute. Improved designs may allow 9-12 °C per minute [205].

Despite the rather complex system layout of a real natural recirculation

evaporator used in CSP applications as shown in Figure 10.21, it turns out that its dynamic gross behavior can be well captured by global mass and energy balances [206]. According to Aström & Bell [206], all parts of the system that are in contact with the saturated liquid-vapor mixture can be considered to be in thermal equilibrium, due to the very efficient heat transfer via boiling and condensation. The energy stored in the steam and the water is released or absorbed rapidly during changes of drum pressure. Surprisingly, for a system having that large physical dimensions, it seems to be the case that most of the distributed effects can be neglected in the model. However, models that must account for drum level dynamics have to include relationships for the distribution of the steam and the water in the evaporator's fluid circuit, i.e. the drum and the riser tubes. Figure 10.22 shows the basic fluid circuit model scheme of a natural recirculation boiler. Aström & Bell [206] presented a relatively simple lumped parameter model of a natural recirculation boiler, also accounting for drum level dynamics. Their model agreed well with experimental data. Nevertheless, this work's intention is to reproduce the dynamic gross behavior of a natural circulation boiler as described before, by neglecting any drum level dynamics also known as the shrink-and-swell effects that may e.g. occur during a fast drop in drum pressure that causes a swelling of the steam bubbles below the drum's water level. Hence, in this work, the evaporator, i.e. the drum, the downcomers and the risers are considered as one lumped volume. The distribution of the steam and the water in the evaporator's fluid circuit is not modeled.

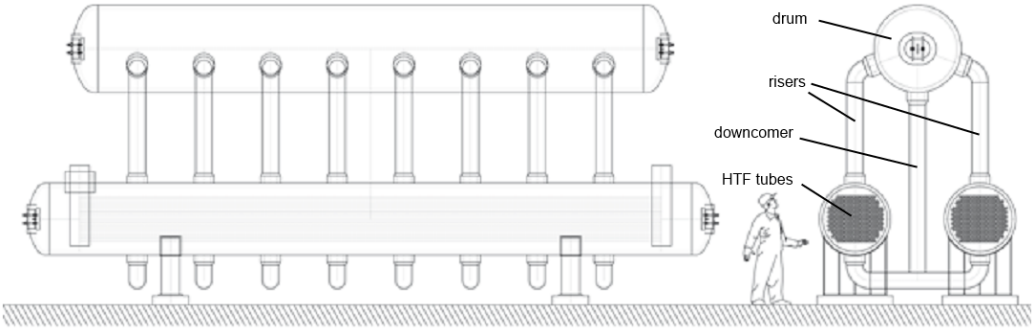

Figure 10.21: CSP evaporator scheme [207]

Basically, the model of the steam generator is based on the transient distributed parameter model of a heat exchanger as described in Chapter 8. The steam generator model is divided into three sub-models, the economiser, the evaporator and the superheater. Each of them is formulated according to the finite volume method as proposed by the Modelica Standard Library's

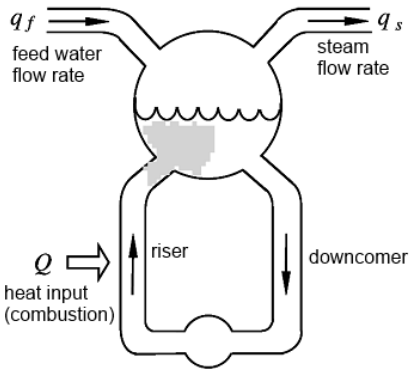

Figure 10.22: Standard natural circulation boiler scheme [206]

1-D fluid flow concept. The generic heat exchanger model, featuring two 1-D distributed fluid flow models that are connected via a corresponding distributed cylindrical 1-D conduction model, is adapted for the steam generator sub-models by simply replacing the medium models as well as the wall heat transfer models at instantiation. The medium model of the water and the steam is defined according to the IAPWS (International Association for the Properties of Water and Steam) Industrial Formulation 1997 [190], i.e. the accepted industrial standard and best compromise between accuracy and computation time. The IAPWS water package has been part of the ThermoFluid Modelica library and has been extended, reorganized and documented to become part of the Modelica Standard Library [163]. An important feature of this implementation of the IAPWS 97 standard is that it has been explicitly designed to work well in dynamic simulations [183, 163]. From the three possible pairs of independent variables, pressure and specific enthalpy have been chosen, in this work. It is the most natural choice for general applications, in particular for power plants.

Each 1-D flow model extends from the Modelica base class "partial distributed volume" which defines the distributed mass and energy balance according to Equations 8.1 to 8.4. However, since the partial derivatives of the density with respect to pressure and enthalpy are explicitly available as functions of pressure and enthalpy ($\frac{\partial \rho}{\partial p} = f(p,h)$ and $\frac{\partial \rho}{\partial h} = f(p,h)$), the definition of the mass balance has been modified according to the following:

Considering Equation 8.1, and assuming constant finite volumes, the mass balance can be written as:

$$\frac{dm}{dt} = V \cdot \frac{d\rho}{dt} = V \cdot \left(\frac{\partial \rho}{\partial p} \cdot \frac{dp}{dt} + \frac{\partial \rho}{\partial h} \cdot \frac{dh}{dt} \right) \tag{10.7}$$

This yields a clear definition of the mass balance using the state variables of the system, i.e. the pressure p and the specific enthalpy h.

However, a Modelica tool might do the above transformation automatically from Equations number 8.1 and 8.2, if the explicit partial derivative equations are detected when loading the medium package.

The model scheme of the economiser and the superheater is shown in Figure 10.23. Since in both cases, single-phase fluid flow occurs in both heat exchanger ducts, the economiser and the superheater can be modeled in the same way. The convective heat transfer sub-model on the water/steam side corresponds in principle to that described by Equations 8.19 and 8.20. To avoid numerical problems when approaching the two-phase boundary due to sudden changes in fluid properties (e.g. density), the fluid properties are simply kept at their saturation values when approaching or surpassing a vapor quality of 0 or 1 (approach from outside the two-phase dome).

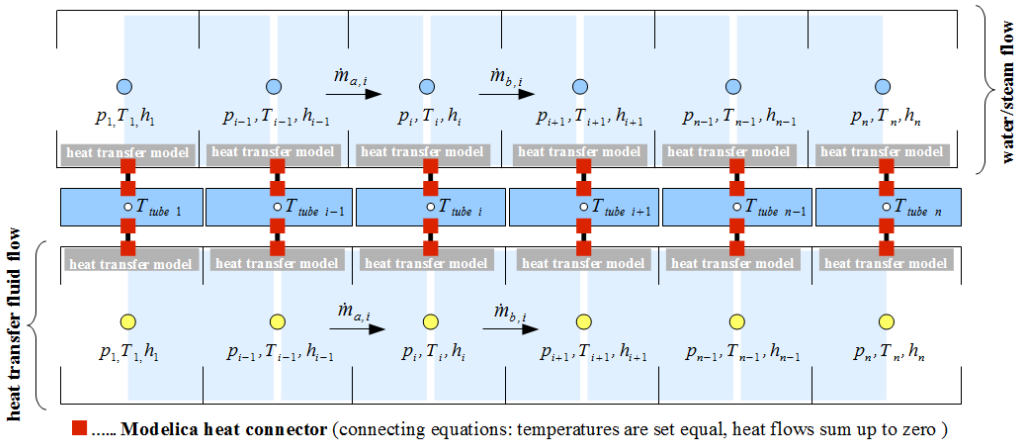

Figure 10.23: Economiser and superheater model scheme

Figure 10.24 displays the model scheme of a natural circulation evaporator. The heat transfer fluid flow model is a distributed parameter model as used in the economiser and the superheater model. Each finite control volume of the heat transfer fluid flow is coupled to a corresponding 1-D conduction model instance that represents the thermal behavior of the tube bundle[4] placed inside the riser tubes of the evaporator (see Figure 10.21). The riser and the downcomer tubes are not modeled explicitly. Their piping volume is, however, added to the total drum volume to correctly model the total fluid mass inside the evaporator. Furthermore, the total mass of the solid drum material (metal) and the mass of all riser and downcomer

[4]See Section 8.2.3 for a detailed explanation of the used tube bundle model.

pipes is lumped together in the model and is represented by a cylindrical conduction model having one representative temperature node $T_{drum\ wall}$ (see Figure 10.24). This model of the evaporator metal masses is assumed to be ideally insulated, i.e. the heat flow at the boundary is set to zero. Also the economiser as well as the superheater is assumed to be ideally insulated. The heat exchange with the ambient is not considered in the steam generator model.

The drum's water-steam model is a lumped parameter model and extends from the base class "partial lumped volume". The water steam mixture is assumed to be saturated and in thermodynamic equilibrium at all time. The state variables are the drum pressure and the current liquid volume inside the drum. This lumped steam drum model is connected to the heat transfer fluid flow model via one heat input connector (see Figure 10.24). Thus, the outer temperature of the tube bundle model is set equal to the current saturation temperature of the water-steam mixture inside the drum, i.e. the convective heat transfer (boiling heat transfer) between the saturated water and the tube bundle is assumed to be ideal. The natural recirculation is not modeled. It is assumed that the evaporator is correctly designed causing the required recirculation rate at all time, thus avoiding the departure from nucleate boiling, also known as boiling crisis. This simplified model scheme should represent a good trade-off between modeling detail and simulation speed.

10.4.1.2 The turbine valve model

The turbine valve opening typically controls the steam generator's pressure level via defining a certain mass flow rate of live steam entering the turbine section of the Rankine cycle. The resulting live steam mass flow is defined by the valve's cross sectional area and the imposed pressure difference across the valve. This problem is typically modeled assuming ideal gas behavior for the super-heated steam, and in general, assuming the following points [155]:

- The model assumes adiabatic operation (no heat losses to the ambient).
- Changes in kinetic energy from inlet to outlet are neglected in the energy balance.
- Friction between fluid and wall is neglected.
- The state transformation is assumed to be sufficiently well described by the ideal gas law.

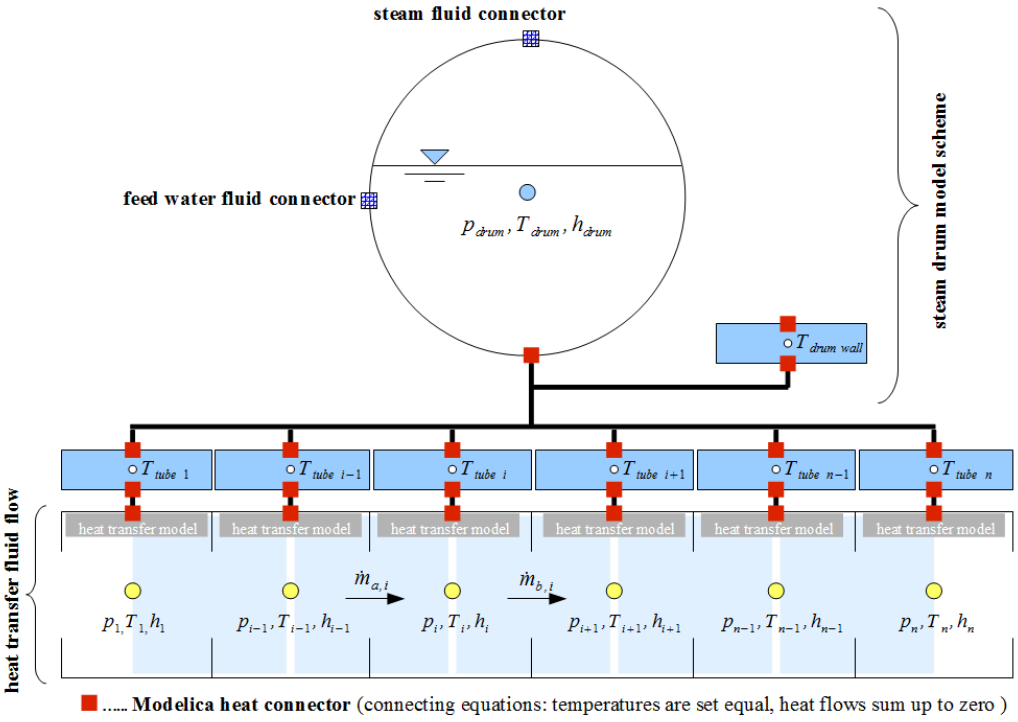

Figure 10.24: Natural circulation evaporator model scheme

- No friction and adiabatic conditions imply an isentropic state transformation.

Under these assumptions the mass flow rate across the valve can be described as a function of the valve's cross sectional area A_{valve}, the so-called outflow function function Ψ, the upstream pressure p_0 and the upstream density ρ_0:

$$\dot{m}_{valve} = A_{valve} \cdot \Psi \cdot \sqrt{2 \cdot p_0 \cdot \rho_0} \tag{10.8}$$

The outflow function Ψ is defined as follows, where p_1 is the pressure at the valve cross section which is equal to the downstream pressure p_2 for not-chocked flow, and equal to the critical pressure p_c for chocked flow conditions ($p_1 = p_2$ if $p_2 > p_c$ and $p_1 = p_c$ if $p_2 \leq p_c$).

$$\Psi = \sqrt{\frac{\kappa}{\kappa - 1} \cdot \left[\left(\frac{p_1}{p_0} \right)^{\frac{2}{\kappa}} - \left(\frac{p_1}{p_0} \right)^{\frac{\kappa+1}{\kappa}} \right]} \tag{10.9}$$

The critical pressure ratio η_c at which chocked flow (the outflow velocity is limited to the local sonic speed) begins, is defined according to the following equation:

$$\eta_c = \frac{p_c}{p_0} = \left(\frac{2}{\kappa + 1} \right)^{\frac{\kappa}{\kappa - 1}} \tag{10.10}$$

However, considering the intention of connecting the quasi-steady-state model of the turbine-condenser-preheater fluid circuit, in this work, the turbine valve of the finally used power block model is considered in a much simpler way. In particular, the turbine valve is represented by a mass flow sink whose mass flow rate is determined by a feedback drum pressure control loop (see Sections 10.4.1.2.1 and 10.6.4). Nevertheless, the corresponding boundary settings for using the transient steam generator model in combination with a turbine valve model (according to Equations 10.8 to 10.10) are explained in Section 10.4.1.2.1 as well.

10.4.1.2.1 The flow model structure and the fluid circuit boundary settings For compressible fluid flow modeling where the fluid properties depend on the current pressure as well as on the temperature, it is important to define a correct flow-model-volume structure. Furthermore,

also the boundary conditions at the outermost fluid connectors are slightly different when compared to an incompressible fluid circuit.

When modeling fluid circuit systems, they are typically separated into components that store mass and energy (large volume equipment as tanks and piping) and components of high power densities (turbines, pumps, valves and orifices) that usually have a negligible storage of mass and energy but cause large changes in pressure or kinetic energy. This results in two basic model types, (i) control volumes that model the dynamic mass and energy balance, and (ii) flow models that model the relationship between mass flow and imposed pressure difference, either according to a quasi-steady-state approach or a rigorous implementation of the 1-D dynamic momentum balance. In addition to that, these two basic model types are typically connected in an alternating manner in order to avoid unnecessary high index differential algebraic equations and furthermore unpleasant non-linear equation systems. This modeling abstraction can be seen as the typical standard approach for simulations of thermo-fluid systems [183].

According to the Modelica Standard Library [163], the flow model structure of each component is defined via a Modelica enumeration [176] having the following options:

- av_b
- av_vb
- a_vb
- a_v_b

where, the letters "a" and "b" represent the fluid connectors at port a (upstream port) and port b (downstream port), respectively, letter "v" represents a control volume, and the underscore "_" represents a flow model. Basically, these enumerations refer to the model structure at component boundaries, i.e. at the fluid connectors. Hence, it is important that a model having structure "av_b" does not necessarily have just one volume (one "v") and one flow model (one "_") inside. It is rather referred to the structure at the boundaries that has to be known when connecting different component models using Modelica's "connect" statement. Thus, model structure "av_b" does end with one control volume at the upstream boundary (port a), i.e. the pressure variable of fluid connector a is set equal to the medium pressure inside that last upstream control volume. In this case it is also said that the fluid connector a exposes the state, which does mean that it exposes the pressure variable that is one state variable of the last control volume at fluid

connector a. In order to keep to the alternating concept of volumes and flow models in this case, fluid connector a has to be connected to another component model that provides a flow model at fluid connector b (e.g. "a_v_b" or "av_b"), yielding the following layout (Note: The dash "-" represents the Modelica "connect" statement):

```
a_v_b - av_b
```

or

```
av_b - av_b
```

It is thus obvious that a model having structure "av_b", does provide one flow model between the pressure variable of fluid connector b and its last downstream control volume, i.e. in this case, the pressure variable of fluid connector b does not expose a state variable.

Another related and important topic is the correct definition of the fluid circuit boundaries, usually also referred to as mass flow sources or pressure sources. Considering incompressible fluid circuit modeling where the fluid properties do not depend on the pressure, the pressure level of the circuit can be arbitrarily set somewhere in the circuit and the remaining pressure variables will be calculated according to the given mass flows, i.e. the pressure drop in every component model or between adjacent finite control volumes is a function of the corresponding mass flow variable ($\Delta p = f(\dot{m})$). Thus a possible and quite intuitive way of defining the fluid boundaries is to define a source and a sink, and to set the pressure level and the mass flow in the so-called source model. This source and sink model for the incompressible case is a combination of the mass flow source and the pressure source since both fluid connector variables (pressure and mass flow) of the source are defined boundary conditions. For the compressible case, where the mass flow between two adjacent finite control volumes is a function of the imposed pressure difference ($\dot{m} = f(\Delta p)$), which is determined by the two corresponding pressure states, it has to be distinguished between mass flow sources and pressure sources where both of them have to provide one free variable. In the case of the mass flow source, the free variable is the source's fluid connector's pressure variable, and in the case of the pressure source, the free variable is the source's fluid connector's mass flow variable. This has two basic reasons:

- The pressure variable of the fluid connector has to be decoupled from the source's or sink's medium[5] pressure. Otherwise, the outstream enthalpy would vary as a function of the resulting circuit pressure.

[5]Inside each fluid boundary model, the so-called "outstream" fluid properties are de-

- Apart from the fact above, setting the pressure and the mass flow in the same boundary of a compressible fluid circuit model would be impossible as the given mass flow (that was set) required a certain pressure difference. This pressure difference, however, would already be set as well, since the boundary pressure was set and the pressure in the adjacent volume was a state variable, specified by the initial conditions.

Now, coming back to actual problem of defining the flow-model-structure and the boundaries for the steam generator model, the lumped parameter model of the drum (see Figure 10.24) exposes its thermodynamic state, i.e. the feed water fluid connector as well as the steam fluid connector exposes the current drum pressure, a state variable of the system. Hence, in order to keep to the alternating concept, the economiser's distributed feed water model must finish with a flow model, which defines the mass flow between the economiser's last feed water duct volume and the drum volume as a function of the pressure difference that is defined by the current medium[6] pressures. Correspondingly, the distributed steam model of the superheater must start with a flow model as well.

The feed water mass flow entering the economiser is defined via a mass flow source whose pressure variable at the fluid connector has been freed. Furthermore, the mass flow source is directly connected to the first volume of the economiser's distributed feed water model. Thus, the economiser's flow model structure is of "av_b" type, where the mass flow source is connected at fluid connector a and the drum model is connected at fluid connector b. The steam outlet of the superheater can either be connected with a model of the turbine valve (see Section 10.4.1.2), or, with a simple mass flow sink. In reality, the steam pressure of the steam generator is controlled via the turbine valve opening that defines the live steam mass flow rate as a function of the imposed pressure difference (pressure difference between turbine entry and steam generator exit). Valves are typically pure flow models that can be

fined. The outstream fluid properties are propagated to the adjacent model component whenever the mass flow variable of the source's or sink's fluid connector becomes negative, i.e. the mass flow is leaving the boundary and enters the adjacent component model. See also the definition of the so-called Modelica "stream" variable [176].

[6]According to the Modelica Standard Library's modeling approach, each finite volume comes with a sub-model called "medium" that calculates all basic fluid properties as a function of the thermodynamic state vector (usually pressure p and specific enthalpy h, or pressure p and temperature T). This sub-model is an instance of a Modelica model class called "base properties" and calculates the density ρ, the specific enthalpy h as well as the specific internal energy u. For two-phase flow, also the current saturation temperature of the pressure input variable is calculated.

directly connected to models that expose their pressure states.

For this reason, when using a model of the compressible fluid flow through a valve, the superheater's steam duct model must end with a volume at its fluid connector b, which results in "a_vb" as flow model type. In order to completely define the boundary conditions on the water-steam side, the turbine valve model is connected to a pressure sink that sets the turbine entry pressure and provides a free mass flow variable at its fluid connector, since the mass flow is a result of the pressure difference across the turbine valve.

On the other hand, when using a simple mass flow sink as turbine valve model, as it is applied in this work, the mass flow sink is directly connected to the superheater's steam duct model that exposes its state (flow model structure "a_vb"). Thus, the mass flow sink (i.e. the live steam sink) must provide a free pressure variable at its fluid connector in order to set the current live steam mass flow in the model. Of course, in this case, it is assumed that the imaginary valve's cross-sectional area is correspondingly adjusted according to the current available pressure difference (which is determined by the linked quasi-steady turbine-condenser-preheater model).

The heat transfer fluid flow is modeled as incompressible, hence the fluid properties do not depend on the pressure and the pressure level can be arbitrarily set. The corresponding fluid connector boundary conditions are rather straightforward. An intuitive possibility is to set the pressure and the mass flow at the steam generator's heat transfer fluid entry source.

Note: In order to define the outstream[7] enthalpies at every fluid boundary as well, all temperature variables of the boundaries have to be set. In the case of the feed water boundary, also the pressure has to be set in order to define the outstream enthalpy (free pressure variable at the fluid connector).

10.4.1.3 The steady-state heat exchanger models

Apart from the economiser, the evaporator and the superheater, that are transient models (power block model type A), all remaining heat exchangers (the feed water preheater and the reheater) are modeled in steady state[8]. To allow for an efficient definition of a steady-state fluid circuit model that does not have to cope with reversible flow, i.e. all mass flow directions do always correspond with the design direction, a simple Modelica "fluid connector" has been defined. This simple fluid connector does only have 3 basic variables,

[7] See the definition of the Modelica "stream" variable [176].

[8] In the case of power block model type B, also the heat exchangers of the steam generator are modeled according to this section

the pressure, the enthalpy and the mass flow, without the definition of a "flow" or "stream" type variable[9]:

```
connector StaticFluidConnector
 "Fluid Connector for steady-state fluid circuits
   without stream and flow variables - NO flow reversal"

  //Medium
  replaceable package Medium = Media.Fluid.WaterIF97
              constrainedby Media.Fluid.Partial.PartialFluidMedium
              "Medium model of the connector";

  Medium.MassFlowRate massFlow
   "mass flow rate from connector a to connector b - always positive";
  Medium.Pressure pressure
   "pressure at connecting point";
  Medium.SpecificEnthalpy enthalpy
   "specific enthalpy at connecting point";

end StaticFluidConnector;
```

Thus, by connecting two fluid models with each other via the Modelica "connect" statement, all three variables are set equal at the connecting point, i.e. the outlet pressure and enthalpy of the previous model will be the inlet pressure and enthalpy of the succeeding one, furthermore, the mass flow rates will be the same.

Basically, the steady-state heat exchanger model contains two medium models ("MediumOne" and "MediumTwo") that are defined via two replaceable Modelica "packages". Furthermore, it instantiates four steady-state fluid connector objects, namely "fluidConnectorOne_a", "fluidConnectorOne_b", "fluidConnectorTwo_a" and "fluidConnectorTwo_b".

The energy balance is formulated according to the mean temperature difference method according to Equation 6.1 by approximating the true mean temperature difference as proposed by Paterson [208]. Paterson [208] provided a relationship that approximates the logarithmic mean temperature difference (Equation 6.6) in a mathematically more applicable way, having a defined value when ΔT_1 equals ΔT_2. Also the derivatives with respect to ΔT_1 and ΔT_2 are well defined, which is required for Newton iterative solutions of non-linear equations. This approximation of the logarithmic mean temperature difference can be written as follows:

[9]See the Modelica Language Specification [176] for the definition of a "flow" or "stream" type variable.

$$\Delta T_{lm} \approx \frac{2}{3} \cdot \sqrt{\Delta T_1 \cdot \Delta T_2} + \frac{1}{3} \cdot \frac{\Delta T_1 + \Delta T_2}{2} \tag{10.11}$$

and can be seen as a serious replacement for the logarithmic mean in many applications [208].

The overall heat transfer coefficient U and its part load behavior is approximated via the following simple relationship, only as a function of the overall heat transfer coefficient at nominal conditions U_{nom}, the mass flow rate of one fluid stream at nominal conditions $\dot{m}_{nom}$, and the corresponding current mass flow rate $\dot{m}$, of course assuming that the ratio between the hot and the cold fluid's mass flow rate stays the same:

$$\frac{U}{U_{nom}} = \left(\frac{\dot{m}}{\dot{m}_{nom}} \right)^{0.8} \tag{10.12}$$

The pressure drop in each of the two fluid ducts is modeled according to the following relationship, taking only a constant pressure drop factor into account:

$$\Delta p = k_{pressure\,drop} \cdot \dot{m}^2 \tag{10.13}$$

Furthermore, it has to be noted that a pure counter flow arrangement is assumed for all heat exchangers.

10.4.1.4 The steady-state steam turbine model

The steam turbine stages are assumed to react very fast to changes in steam mass flow rate and temperature. Thus, their real behavior is approximated in a quasi-steady manner. The turbine power is calculated assuming an isentropic efficiency for each stage. Furthermore, in order to cover the part load behavior as well, the isentropic efficiencies of the turbine stages are functions of the current steam mass flow rate. The relationship between the pressure difference across the turbine and the steam mass flow rate is described applying Aurel Stodola's Law of the Ellipse, also known as Stodola's Cone Law.

The isentropic efficiency of a steam turbine stage is defined as the ratio between the real enthalpy difference across the turbine and the enthalpy difference achieved during an ideal isentropic expansion. This can be written as follows:

$$\eta_s = \frac{h_1 - h_2}{h_1 - h_{2s}} \tag{10.14}$$

The power[10] of one turbine stage can then be written as follows:

$$\dot{W}_{turbine} = (h_1 - h_2) \cdot \dot{m} \tag{10.15}$$

However, for calculating the power of each turbine stage according to Equations 10.14 and 10.15, the pressure level at the inlet and the outlet of each stage has to be known. An intuitive approach is to set the condenser's pressure level, which basically depends on the current ambient air temperature since a certain temperature difference is required to reject the low temperature waste heat to the environment. Setting the condensing pressure defines the outlet pressure of the last low pressure turbine stage. Thus, the inlet pressure of each stage is calculated backwards applying Aurel Stodola's Cone Law, which can be written in temperature form as follows [209]:

$$\sqrt{\frac{p_i^2 - p_o^2}{T_i}} = \frac{\dot{m}}{\dot{m}_0} \cdot \sqrt{\frac{p_{i0}^2 - p_{o0}^2}{T_{i0}}} \tag{10.16}$$

10.4.1.5 The steady-state model of the air-cooled condenser

As a matter of its thermodynamic principles, the Rankine power cycle has to reject a large amount of low temperature waste heat to the environment. At conventional power plants, this low temperature heat rejection to the environment is usually done via evaporative wet cooling towers that, however, need large amounts of make-up water. At typical locations of solar thermal power plants, water is a rare resource and thus cannot be used for the cooling of the power plant. The water needed for cleaning the mirrors of the solar field already nearly exhausts the water resources at certain locations. For this reason, dry air-cooled condensers are the standard solution for concentrated solar power applications. Due to the relatively high ambient air temperatures, the condensing pressure has to be increased compared to wet cooled plants, which slightly reduces the Rankine cycle's efficiency. Furthermore, due to a limiting convective heat transfer coefficient on the air side of the condenser, the heat transfer area has to be very large in order to keep the fan power and thus the condenser's parasitic power consumption at an acceptable level. In order to achieve the required heat transfer area, many smaller air-cooled condenser (ACC) subunits are usually connected in series

[10] To obtain the finally useful power input of the generator, the mechanical efficiency of the turbine's drive train has to be taken into account.

and in parallel and combined in large arrays. A typical design is the so-called forced-draft direct air-cooled condenser in A-frame arrangement (see Figure 10.25) [210].

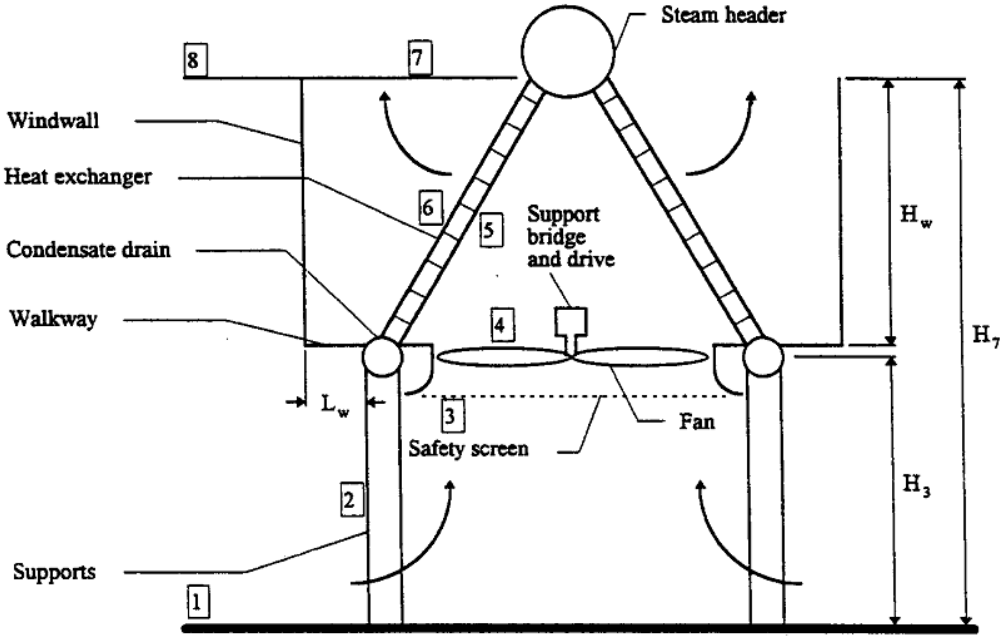

Figure 10.25: Forced-draft direct air-cooled condenser unit [210]

Fan diameters of such an A-frame air-cooled condenser design are typically around 9 meters which leads to condenser unit dimensions of about 10 times 10 meters. Figure 10.26 shows an example for an array of 30 A-frame condenser subunits (6 times 5 units).

In this work, the heat exchange between the ambient air and the condensate is modeled in steady state, neglecting the influence of its transient behavior. Again, the performance of this air-to-water heat exchanger is estimated according to the mean temperature difference method (see Equation 6.1) assuming a certain overall heat transfer coefficient as well as a certain area of heat transfer. The flow arrangement is assumed to be of ideal counter flow type, which, however, definitely is an abstraction and simplification of the real layout. Since this model is intended for performance simulations only, and not at all for component design, this simplification should be acceptable. The true mean temperature difference is again approximated via Equation 10.11. The overall heat transfer coefficient is approximated by only modeling the dominant thermal resistance, hence the forced convective heat transfer to the ambient air. Due to the rather low convective heat transfer coefficient on

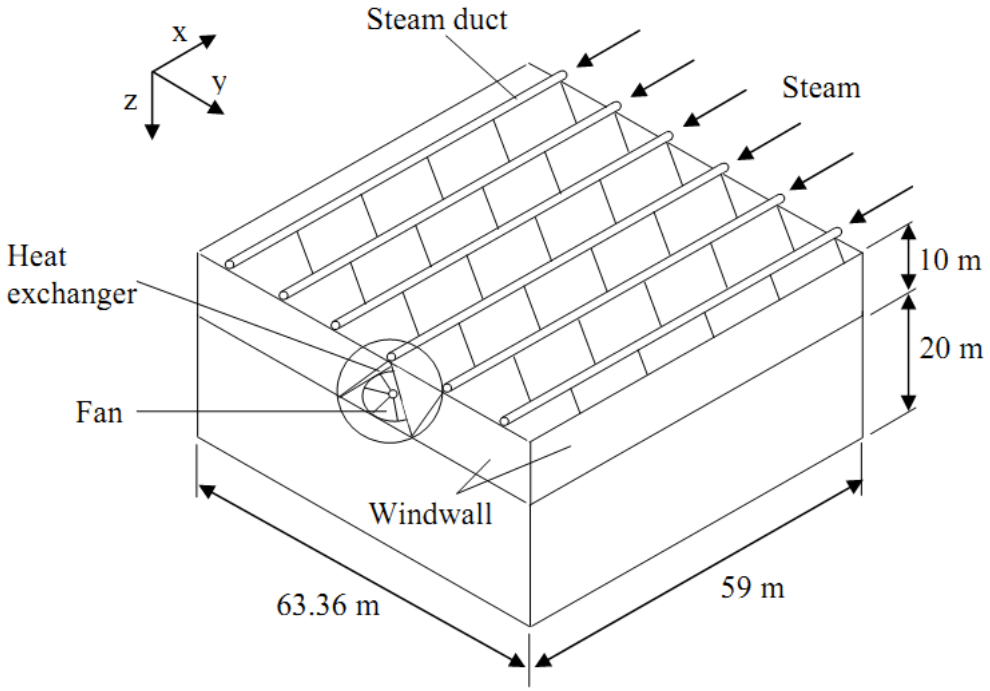

Figure 10.26: Forced-draft direct air-cooled A-frame condenser unit array [211]

the air side, a finned tube surface is typically used. Thus, in this model, the conductive resistance of the condenser's tubes, the conductive resistance of the fins as well as the convective resistance due to condensation is neglected. This simplification should yield acceptable results since the heat transfer via condensation and conduction is very efficient. In order to estimate the mean convective heat transfer coefficient between the fins' surfaces and the ambient air, the following Nusselt number correlation is applied, which is valid for bundles of radially finned tubes having an equilateral, triangular tube arrangement [210]:

$$Nu = \frac{h \cdot d_r}{k_{air}} = 0.134 \cdot Re_{air}^{0.681} \cdot Pr_{air}^{0.333} \cdot \left(2 \cdot \frac{P_f - t_f}{d_f - d_r}\right)^{0.2} \cdot \left(\frac{P_f - t_f}{t_f}\right)^{0.1134} \tag{10.17}$$

The ambient air is modeled as ideal gas using a polynomial based specific heat relationship as published by McBride et al. [173] as well as dynamic viscosity and thermal conductivity data according to Kadoya et al. [174].

The parasitic power consumption of the fan drive is estimated using numerical simulation results published by Zhao et al. [212]. They provided the fan speed in rotations per minute as a function of the volumetric flow rate for a typical A-frame condenser subunit. Additionally, they provided the fan shaft power as a function of the rotational speed. In particular, they provided this data at different operating points. A curve has been fitted to that data and implemented in the model. Thus, by calculating the required air flow rate via the steady-state energy balance, the fan shaft power is obtained via evaluating the following two Modelica functions:

```
function FanSpeed_FanVolumetricFlowRate
 "returns rotational speed as function
   of volumetric flow rate (Zhao et al. 2013)"
  input SI.VolumeFlowRate flowRate;
  output NonSI.AngularVelocity_rpm fanSpeed;
 algorithm
   fanSpeed := max(0,(flowRate + 192.695)/9.01224);
end FanSpeed_FanVolumetricFlowRate;

function FanShaftPower_FanSpeed
 "returns shaft power as function
   of rotational speed (Zhao et al. 2013)"
  input NonSI.AngularVelocity_rpm fanSpeed;
```

```
  output SI.Power shaftPower;
 algorithm
   shaftPower := if fanSpeed < 67 then 72103 * (fanSpeed/67)^3
                 else -199146 + 4048.5*fanSpeed;
end FanShaftPower_FanSpeed;
```

10.4.1.6 The feed water pump model

The feed water pump power is estimated by evaluating a pump efficiency correlation as published by Lippke [37]:

$$\eta_{pump} = \eta_{pump\,nom} \cdot \left(2 \cdot \frac{\dot{m}}{\dot{m}_{nom}} - \left(\frac{\dot{m}}{\dot{m}_{nom}} \right)^2 \right) \tag{10.18}$$

and the following relationship which is based on evaluating $\int v\, dp$ by neglecting work due to friction and assuming the specific volume v to be constant. This yields:

$$\dot{W}_{pump} = \frac{v \cdot \Delta p \cdot \dot{m}}{\eta_{pump}} \tag{10.19}$$

10.4.1.7 The steady-state deaerator model

The deaerator is assumed to be of tray-type, where a vertical domed deaerator section is mounted on top of a horizontal feed water vessel. The relatively cold feed water and the steam coming from the extraction turbine enters the deaerator at the vertical dome. Through mixing, the feed water is heated close to saturation temperature and dissolved gases such as oxygen and carbon dioxide leave through a vent at the top of the dome. Aggressive gases have to be removed from the feed water in order to avoid corrosion [16].

In this work, the deaerator model (see Figure 10.27) is based on a simple global energy and mass balance (see Equations 10.20 and 10.21). Furthermore, the enthalpy of the feed water leaving the deaerator is always that of saturated water (bubble point) at the current deaerator pressure level. Thus, the governing equations can be written as follows:

$$0 = \dot{m}_{extraction} + \dot{m}_{feed\,water\,entering} - \dot{m}_{feed\,water\,leaving} \tag{10.20}$$

$$\begin{aligned} 0 = {} & \dot{m}_{extraction} \cdot h_{extraction} + \dot{m}_{feed\,water\,entering} \cdot h_{feed\,water\,entering} \\ & - \dot{m}_{feed\,water\,leaving} \cdot h_{feed\,water\,leaving} \end{aligned} \tag{10.21}$$

10.4.1.8 The final Rankine cycle model

The final Rankine cycle model used in this work (power block model type A) (see Figure 10.27), is a combination of a transient one-dimensional distributed parameter steam generator model (see Section 10.4.1.1) and a quasi-steady zero-dimensional fluid circuit model including the turbine-generator set, the condenser, the feed water preheater, the deaerator as well as the feed water pumps.

This quasi-steady zero-dimensional fluid circuit model is defined in the following way: As already mentioned in Section 10.4.1.4, the condenser pressure level can be specifically set, i.e. the corresponding saturation temperature has to sufficiently exceed the current ambient air temperature in order to provide the needed temperature difference for rejecting the Rankine cycle's low temperature waste heat. Thus, considering that, the condenser's pressure level is an input to the quasi-steady zero-dimensional fluid circuit model and all remaining turbine stage pressure levels are calculated backwards applying Aurel Stodola's Cone Low (Equation 10.16). As can be seen in Figure 10.27, the turbine is assumed to consist of four stages having one reheat after the first stage and steam extractions for the feed water preheating after the second and the third stage. These extraction mass flows are determined by the energy balances of the feed water preheater and the deaerator. The turbine's live steam mass flow is an input variable as well, and is in this case determined by the connected steam generator model. The remaining free variable of the quasi-steady fluid circuit model is the pressure level of the deaerator, which is determined in such a way that there is always a certain offset to the second turbine stage's exit pressure (the first extraction pressure level).

Finally, the transient steam generator model, described in Section 10.4.1.1, is linked with the quasi-steady turbine-condenser-preheater model at the economiser inlet, i.e. the feed water mass flow source (see Section 10.4.1.2.1) and the superheater outlet, i.e. the live steam sink (see Section 10.4.1.2.1). Additionally, the heat transfer fluid mas flow that is required for the quasi-steady reheater model is extracted before the steam generator entry and again added after the steam generator exit using a T-junction model (as described in Section 10.5.1) in each case. In order to avoid convergence problems during model initialization, these fluid circuit couplings are implemented applying a smooth homotopy transformation as described in Section 10.6.1.

10.4.1.8.1 The steady-state fluid loop closer Modeling a closed fluid circuit in steady-state results in an overdetermined system of equations when

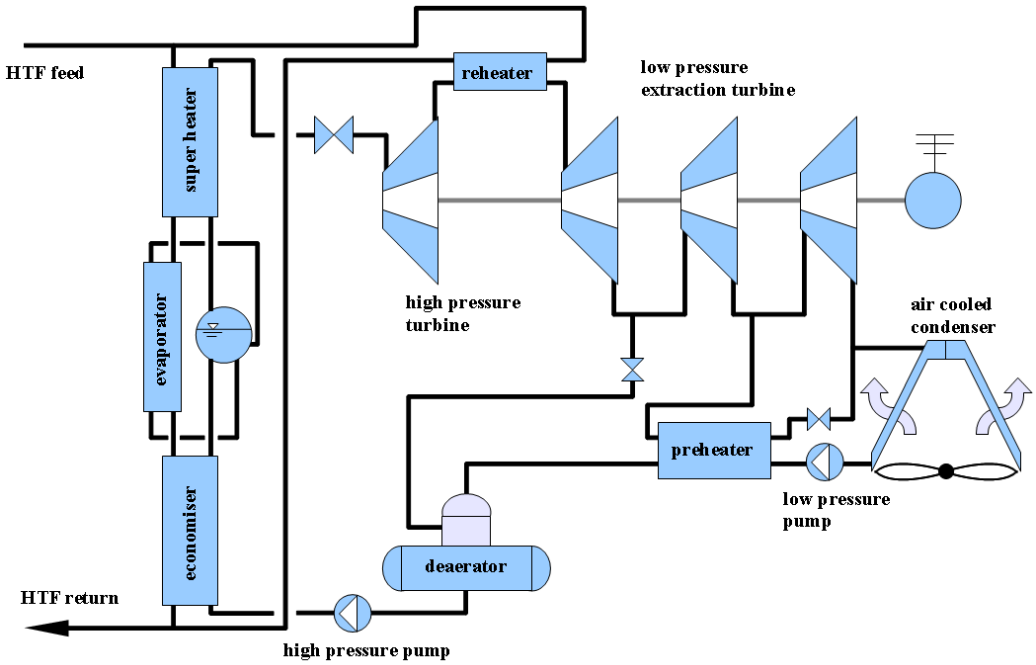

Figure 10.27: Rankine steam cycle model scheme

connecting models where each of them considers the conservation of mass, i.e. features the following equation[11]:

```
fluidConnector_a.massFlow = fluidConnector_b.massFlow;
```

Just imagine you were connecting two models that featured the above equation in the form of a closed loop. Then, by setting the mass flow rate at the "beginning" of this closed loop, i.e. at fluid connector a of model one, the mass flow rate at fluid connector b would be defined as well according to the equation above. As the second model's fluid connector a would be connected to the first model's fluid connector b, the mass flow rate at fluid connector b of model number two would be defined as well. Thus by closing the fluid circuit, i.e. connecting the second model's fluid connector b to the first model's fluid connector a, the equation system becomes overdetermined. However, this issue can be solved in a rather easy way by creating a fluid loop closer model that provides a free mass flow variable, hence, there will be no equation inside this fluid loop closer model that provides the relationship between the mass flow of fluid connector a and the mass flow of fluid connector b. It will

[11]The mass flow variable of the static fluid connector is not defined as flow variable.

only define an isenthalpic as well as an isobaric component according to the following example:

```
model StaticFluidLoopCloser
 "This model is necessary to close a steady-state fluid loop model
   - it gives a free mass flow variable"

 extends StaticTwoFluidConnectorsPartialModel;

equation

  //enthalpy
  fluidConnector_a.enthalpy = fluidConnector_b.enthalpy;

  //pressure
  fluidConnector_a.pressure = fluidConnector_b.pressure;

end StaticFluidLoopCloser;
```

If the mass balances are correctly evaluated in the closed fluid circuit, this component should have the same mass flow at fluid connector a and fluid connector b, of course within the numerical accuracy range. Note: The same would apply for the pressure variables in the closed fluid circuit. In this case, however, the pump models introduce the needed free pressure variables at their ports.

10.4.2 The power block model type B (quasi-steady only)

Power block model type B consists of a complete quasi-steady flow arrangement, applying the steady-state heat exchanger models as described in Section 10.4.1.3 for the economiser, the evaporator and the superheater as well, including a simple steady-state drum model that acts as phase separator.

In order to be able to capture basic transient effects for the plant's start-up or cool-down, this quasi-steady power block sub-model is now combined with a simple model of a thermal inertia that has to be heated up in the morning to a chosen temperature threshold before the power block can start its operation. Correspondingly, in the evening during plant shut-down, the return temperature to the solar field does not feature any unwanted discontinuities. Figure 10.28 displays the model scheme.

The thermal inertia (see Figure 10.28) is modeled using a tube bundle flow model as described in Section 8.2.3. Thus, by adjusting the number

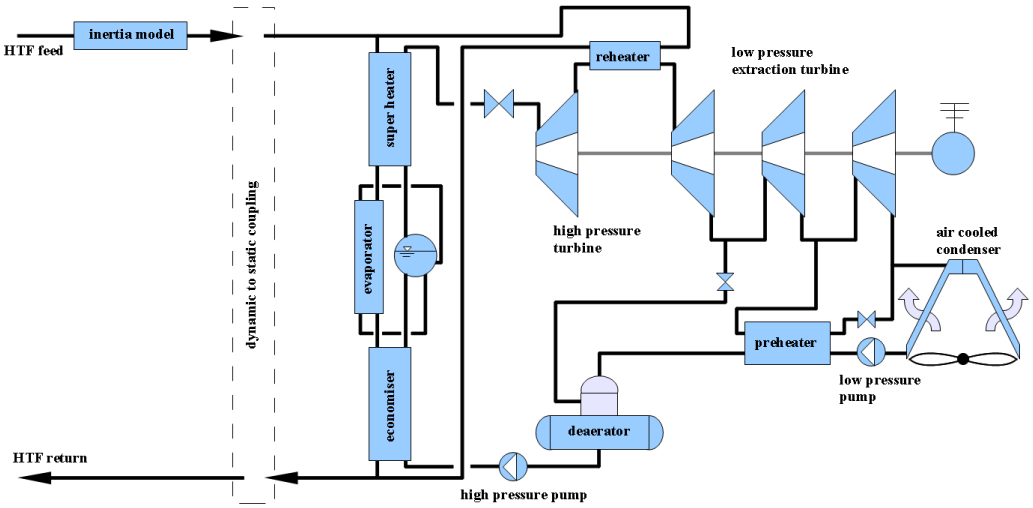

Figure 10.28: Quasi-steady zero-dimensional power block model scheme coupled with a simple thermal inertia model

of tubes as well as the number of volumes, the transient response can be fitted to simulation results of detailed models or measurements at real plants. The cool-down behavior over night or longer outage periods is taken into account by a simple heat loss model, which defines a certain overall heat loss coefficient for the heat flow between the tubes' outer surfaces and the ambient.

However, when combining non-causal models defined according to Modelica's principles with causal quasi-steady fluid circuit models that additionally only converge over a certain operating range and are not at all defined for zero-flow conditions or flow reversal, special care must be taken regarding all connecting equations. In Figure 10.28, this connecting problem is addressed by using a special model class ("dynamic-to-static coupling") that defines all the mass flow, pressure and enthalpy relationships according to defined criteria. For example, since the quasi-steady power block model is not defined for zero-flow conditions (e.g. during off-line hours at night), there is always a certain minimum HTF mass flow maintained within the model to keep it "running". Of course, all the output variables do not make sense during this "model-outage periods" and this must be taken care of in the model code.

10.5 The transport system sub-model

The transport system model has the task to correctly distribute the mass and energy flows between the solar thermal power plant's components. Further-

more, the pumping power for the HTF circuit has to be estimated. Figure 10.29 shows the top-level layout of the solar thermal power plant model.

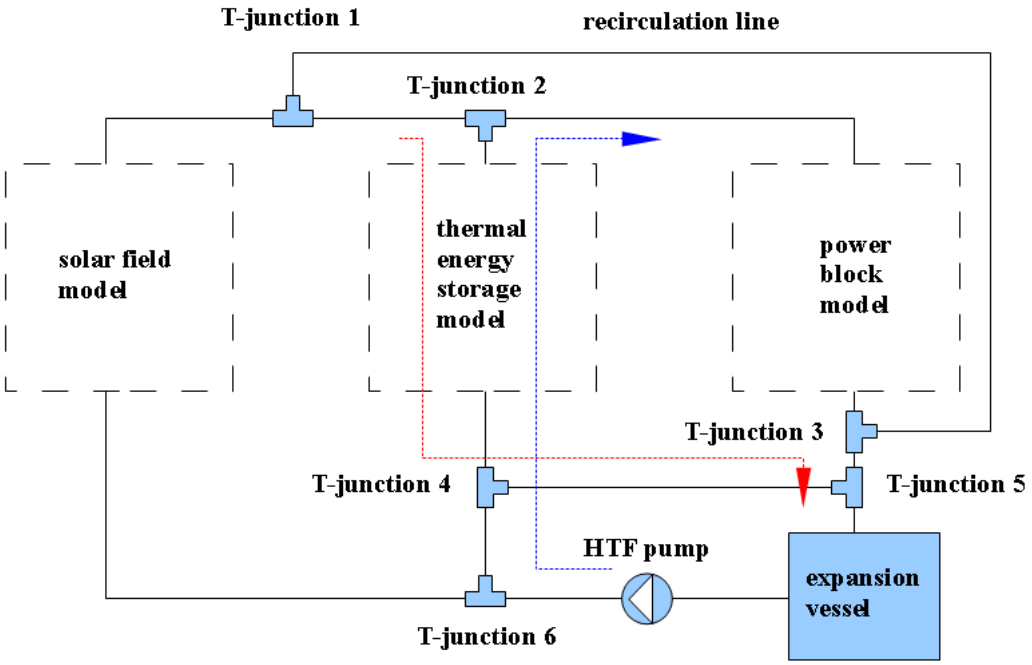

Figure 10.29: The top-level model scheme of a solar thermal power plant

Basically, the transport system model consists of a steady-state pump model (see Section 10.4.1.6), an expansion vessel model (which solves an ideally mixed energy balance; it thus features only one single control volume, extending from the "partial lumped volume" [163]), 6 instances of a T-junction model (which is explained in Section 10.5.1) and the corresponding connecting equations between the power plant components. Since this model setup features closed fluid loops, which, in principle, results in an overdetermined system of equations for the pressure[12], the corresponding T-junction models have to provide a free pressure variable. That is implemented by simply replacing the pressure drop model (see Figure 10.31).

T-junction models 1 and 3 (see Figure 10.29) define the HTF recirculation loop, a bypass for recirculating the HTF in the solar field, without feeding the steam generator of the power block or the thermal energy storage system.

T-junction models 2, 4, 5 and 6 are required for the correct coupling of the thermal energy storage system, in order to always route the HTF mass

[12]The whole HTF circuit is modeled as incompressible, i.e. all pressure drops are function of mass flows.

flow over the expansion vessel and the pump[13]; in charging mode (red) as well as in discharging mode (blue). Of course, the mass flows have to be correspondingly defined by the plant control.

10.5.1 The transient T-junction model

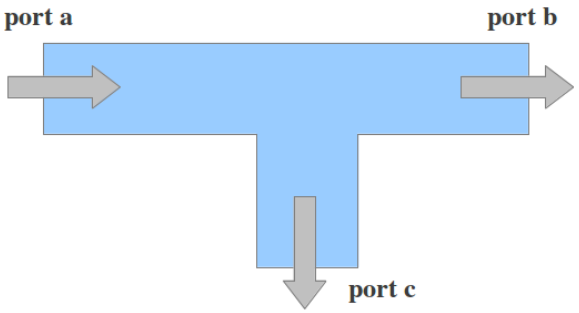

Figure 10.30: Generic T-junction scheme

A T-junction model for CSP performance simulations must fulfill three basic tasks, namely (i) the formulation of the mass balance, (ii) the formulation of the energy balance, and (iii) the consideration of pressure drop, which is needed to correctly estimate the required pumping power. Furthermore, the implementation of the corresponding equations has to be done in a numerically proper way that also works for flow reversal and zero flow. However, empirical pressure drop correlations for generic T-junctions (see Figure 10.30) are usually not designed for that task and they have to be considerably modified when implementing them into the model code. Hence, in order to obtain a numerically stable model, a certain abstraction from reality has to be made.

In this work, a T-junction model concept as proposed by Tummescheit [183] is used. In particular, this model concept reduces the T-junction to a fluid control volume and adds two flow models (in this work, only steady-state pressure drop models) between the control volume and the fluid ports b and c (see Figure 10.31). Hence, considering the abstract T-junction model, it is a quite reasonable approach to use a 90° tube bend pressure drop model for the flow model between the control volume and fluid port c (Figure 10.31), and a straight pipe pressure drop model for the flow model between the control volume and fluid port b.

[13]The HTF pump is considered in the model according to Equation 10.19.

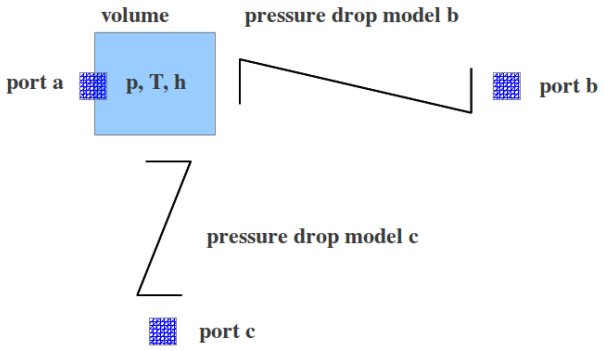

Figure 10.31: T-junction model scheme

The energy as well as the mass balance is solved within the control volume model. Thus, the T-junction model extends from the Modelica base class "partial lumped volume" that formulates the general energy and mass balance in terms of net mass flow, net enthalpy flow, net heat flow $\dot{Q}_{net}$ and net work flow $\dot{W}_{net}$. Obviously, in this case, the net work flow is set to zero. Furthermore, since the T-junction model is assumed to be ideally insulated, also the net heat flow is set to zero. This can be written as follows:

$$m = V \cdot \rho \tag{10.22}$$

$$\frac{dm}{dt} = \dot{m}_{port\,a} + \dot{m}_{port\,b} + \dot{m}_{port\,c} \tag{10.23}$$

$$U = m \cdot u \tag{10.24}$$

$$\frac{dU}{dt} = \dot{m}_{port\,a} \cdot h_a + \dot{m}_{port\,b} \cdot h_b + \dot{m}_{port\,c} \cdot h_c \tag{10.25}$$

It has to be noted that the mass flow rate variables ($\dot{m}_{port\,a}$, $\dot{m}_{port\,b}$ and $\dot{m}_{port\,c}$) are defined positive when entering the control volume and are defined negative when leaving the control volume. Furthermore, the specific enthalpy variables (h_a, h_b and h_c) are defined according to the Modelica "stream" concept (see the Modelica Language Specification [176]). Thus, as long as the mass flow rate at e.g. port a is negative (i.e. is leaving the control volume), the specific enthalpy variable h_a is the ideally mixing enthalpy of the control volume. On the other hand, when the mass flow rate switches

the sign, i.e. enters the control volume, the specific enthalpy variable h_a corresponds to the inflow enthalpy (i.e. the specific enthalpy of the adjacent control volume upstream).

Finally, in order to keep to the correct flow model structure (see Section 10.4.1.2.1), fluid port a of the T-junction model has to be connected to a component model that finishes with a flow model, i.e. is of type "...v_b". Correspondingly, ports b and c of the T-junction model have to be connected to component models that begin with a control volume at their ports (i.e. they are of type "av_...").

10.6 The final PTC power plant model and its control

This chapter will treat the final model layout and the control of the solar plant model on system level.

Figure 10.29 shows the final model setup on the top-level. Of course, the dashed rectangles have to be associated with the actual component models as the solar field model (see Figure 10.1), the thermal energy storage model (see Figure 10.20) and the power block model (see Figure 10.28). Thus, all plant sub-models are connected by the transport system model (see Section 10.5), resulting in a comprehensive Modelica class featuring 15770 variables (in the case of power block model type B).

Transient Modelica models of thermal processes where certain process variables need to be controlled, typically feature continuous[14] feedback proportional-integral (PI) or in some cases proportional-integral-derivative (PID) control loops (see Equation 10.26 for a "textbook's" PID controller). In general, the application of derivative control action (PID) is uncommon in process control, because the performance improvement is usually too small to justify the added complexity and the increased sensitivity to measurement noise [213].

$$u(t) = K_p \cdot \left(e(t) + \frac{1}{\tau_i} \cdot \int_0^t e(\tau) d\tau + \tau_d \cdot \frac{de(t)}{dt} \right) \tag{10.26}$$

The solar field model's mass flow control additionally features a feedforward term that uses a simple steady-state model of one representative loop,

[14]When the simulation time of a model is important, i.e. when it should be kept as low as possible, it is crucial to use continuous time controller blocks instead of their discrete time counterparts, since modern variable step size integrators can significantly contribute to fast simulation times.

in order to predict a reasonable mass flow signal depending on the current direct normal irradiance, i.e. the plant's disturbance. The additional feedback control loop with integral action removes the remaining error in outlet temperature.

Besides the fine tuning of the 2 basic parameters of a "textbook's" PI controller, as the proportional gain (K_p) and the integral time (τ_i), according to correlations available in literature[15], a first important step when simulating a model for the first time, is to choose good start parameters for each variable in order to avoid initialization problems. This issue will be dealt with in the following section.

10.6.1 Avoiding initialization problems when building a large model

The coupling of large sub-models in order to obtain one comprehensive Modelica model class, typically results in a huge system of equations having thousands of variables. Before starting a new simulation after successfully translating the Modelica code, the Modelica tool has to find the initial solution of the resulting differential-algebraic equation system. It is compulsory to provide consistent initial values for the state variables, their time derivatives, and good guess values for the algebraic unknowns. The default option in Modelica tools is the steady-state initialization, thus the time derivatives of the state variables are set to zero at simulation start ($t = 0$). If not all initial conditions have been specified by the user, the Modelica tool usually adds the missing initial equations, setting the corresponding state variables equal to their given start attribute[16].

The resulting system of equations is typically non-linear and has to be solved numerically, which, however, does not work right away for common industrial problems, even when using state-of-the-art non-linear solvers [214, 215]. Commonly applied are Newton or, historically better, Newton-Raphson-

[15]It is recommended to derive an appropriate starting value via an estimation, rather than just trying an arbitrary number that comes into mind. Typically, controller settings can be obtained via performing open-loop step response simulations close to the operating conditions considered. Thus, after estimating the process parameters as process gain or time constant through simulation, reasonable controller settings can be obtained using corresponding controller tuning rules as available in literature.

[16]Each variable defined in Modelica has a so-called start attribute (see the Modelica Language Specification [176]) that should basically provide a good solver seed value. By default, when not explicitly specified by the user, the start attribute is set to zero, which can lead to considerable convergence problems in cases where the variable has a completely different order of magnitude (e.g. Reynolds numbers in turbulent flow). Thus, providing good solver start values is a must for large models.

Simpson [216] methods. The large non-linear system of equations especially introduces severe problems during the initialization phase of the model at simulation start if poor solver guess values are provided for critical variables. Thus, it is crucial to appropriately set the "start" attribute (see the Modelica Language Specification [176]) of each variable before starting the simulation. This should be done via providing a start parameter for each variable when developing the model, and additionally providing a reasonable and user-friendly number of "master" parameters that accordingly set all dependent sub-level parameters during model compilation. In this way, all variables have good solver seed values and a Modelica tool will, in most cases, converge to an initial solution of the non-linear equation system.

However, providing good initial values for each simulation can be a tedious job, since many variable values are not known in advance by the user. Even using the same Modelica code with different Modelica tools may require a different start attribute set, resulting in useless models since they are impossible to simulate due to badly conditioned initialization problems [215].

A good working remedy for this problem has been presented by Sielemann et al. [214] and Casella et al. [215]. They introduced the so-called "homotopy" transformation in Modelica, which is now available in Modelica as a built-in function since version 3.2. The basic idea is to provide a simple version of the problem at simulation start and to transform it in a smooth way into the actual difficult problem. This is done via introducing a homotopy operator λ which varies within the interval $[0, 1]$ in a smooth way defining the problem as follows [215]:

$$f_{homotopy}(x, \lambda) = \lambda \cdot f_{actual}(x) + (1 - \lambda) \cdot f_{simplified}(x) \tag{10.27}$$

Thus, the Modelica tool should be able to solve the simplified initial problem with the given set of start attributes, enabling the continuous transformation into the actual complex problem, before starting the simulation. According to Casella et al. [215], for thermo-fluid networks, the built-in homotopy function should be applied in the following code sections, in order to avoid too complex non-linear equation systems:

- The homotopy function should be applied to the momentum balance equations where the relationships between pressure difference and flow rate are typically quadratic and depend on the upstream fluid properties, which in turn depend on the state variables as specific enthalpy and pressure, as well as flow direction. Therefore, complex relationships should be removed by providing simplified linear constant-coefficient correlations between pressure differences and flow rates [215].

- Furthermore, the energy balances of control volumes are non-linear because of the products between mass flow rates and specific enthalpies (see Equation 8.4). A possibility to avoid this problem is to use the nominal flow rate in the energy balance equations in the simplified equation system [215].

- Considering again the energy balance of control volumes, the current "instream"[17] (upstream) specific enthalpy value depends on the flow direction (flow reversal), further complicating the problem. Thus, the simplified equation system should assume design flow direction in the components [215].

- Additional problem-causing model formulations are flow-dependent heat transfer coefficient relationships. Typically, convective heat transfer coefficients are approximated via the use of empirical Nusselt number correlations that depend on the Reynolds number and the Prandtl number in a non-linear way (e.g. see Equation 8.19). A good remedy for model initialization is to set the heat transfer coefficient during model initialization to a constant value that is reasonable for the operating conditions to be simulated [215].

- Another important point to be considered are algebraic loops introduced by controllers. For example, in solar field models, the mass flow rate is controlled in order to keep the heat transfer fluid's outlet temperature at the given setpoint. Thus, the controller introduces a coupling between the outlet temperature and the entering mass flow rate. A viable solution to the problem is to hold the controller's output at a fixed value during initialization [215].

In this work, all developed models feature a start parameter for each variable having the same name with the extension "_start". Each parameter is defined by a small set of "master" parameters (as initial mass flow rate, pressure as well as temperature levels). Additionally, during initialization phase, the built-in homotopy function is applied in such a way that the points above are fulfilled. For instance, the parameter "massFlow_start" is used in the energy balance equations instead of the actual mass flow rates, furthermore assuming design flow direction. In addition, all heat transfer coefficients and controller outputs are set to their corresponding start attribute during initialization. For example, considering the initialization of heat transfer coefficients, the following code would apply:

[17] See the definition of the Modelica "stream" variable [176].

```
heatTransferCoefficient =
homotopy(actual=(nusseltNumber * conductivity) / diameter,
         simplified=heatTransferCoefficient_start);
```

A proper initialization is especially crucial for large quasi-steady fluid circuit models where many steady-state heat exchanger models are present, commonly defined according to the logarithmic mean temperature difference method (see chapter 10.4.1.3).

In this work, considering the special case of connecting a transient steam generator model with a quasi-steady turbine-condenser fluid circuit model, an additional "homotopy" transformation is applied in order to finally couple the two sub-models during simulation and not during the initialization phase, which can be quite useful when a model should be run using boundary conditions different from the default initialization parameter setting (e.g. at partial loads). Therefore, consider a quasi-steady fluid circuit model that is initialized via a set of start parameters that lead to convergence for a certain defined operating point. For example, taking a quasi-steady Rankine steam cycle model into account, a certain operating point would be defined by the heat transfer fluid's mass flow rate and temperature entering the steam generator (solar field outlet conditions). Now, if the same model wanted to be used for different boundary conditions (e.g. at partial loads), a different set of initialization parameters would be required. In relevant software packages (e.g. [29]) for solving non-linear systems of equations, there usually exists the possibility of loading the current solution of the model as estimates or solver seed values for the next solution process. Thus, if the model needs to be evaluated under boundary conditions different from the default initialization, the boundary settings have to be varied in small steps, importing the current solution vector as variable estimate vector for the next model evaluation. A Modelica tool does that automatically during simulation and even predicts the estimate vectors via extrapolation, using previous solutions of the system.

Hence, instead of providing the appropriate parameter setting for the model's initialization at simulation start, each sub-model can be initialized with its default parameters and the model coupling can be performed later during simulation similar to the above discussed built-in homotopy transformation, using a transition variable φ that smoothly varies between zero and 1 during a predefined simulation time interval:

$$x_{input\ model\ A} = x_{default\ model\ A} \cdot (1 - \varphi) + y_{output\ model\ B} \cdot \varphi \tag{10.28}$$

In this work, all outputs of the transient steam generator model are linked to the corresponding inputs of the quasi-steady turbine-condenser model (and vice-versa) by applying Equation 10.28.

10.6.2 The control of the solar field's outlet temperature

The basic task of a solar thermal power plant is to capture thermal power delivered by the sun and to convert this thermal power subsequently into mechanical power and finally electric power. The thermal power $\dot{Q}_{useful}$ is collected via the use of a heat transfer fluid having a certain mass flow rate $\dot{m}_{HTF}$ and undergoing a certain change in enthalpy Δh_{HTF}:

$$\dot{Q}_{useful} = \dot{m}_{HTF} \cdot \Delta h_{HTF} \tag{10.29}$$

According to its principle, a solar power plant is exposed to arbitrarily changing direct normal irradiance, which is the plant's major disturbance variable. Thus, when it comes to the control of a solar thermal power plant, one of the most challenging control tasks is to keep the outlet temperature of the solar field as close as possible to the assigned set point. Since the solar field's inlet temperature is a given boundary condition (steam generator or thermal energy storage system return temperature), the solar field's mass flow rate is the variable that needs to be adjusted in order to reach the outlet temperature target, which must be achieved satisfactorily well, as the HTF may degrade at high temperatures and connected plant components (e.g. the steam generator, or the thermal energy storage system) are rather sensitive to changes in HTF temperatures.

For example at the SEGS (Solar Electric Generating Systems) plants in California, USA, the solar field mass flow control was originally performed by a skilled operator that adjusted the HTF mass flow rate within upper and lower bounds [58]. Thus, the HTF mass flow adjustment was based on the knowledge of the sun's daily path, cloud observations and many years of experience and training [58].

The major aggravating fact regarding the solar field's outlet temperature control is the significant variation of the dynamic characteristics of the distributed solar collector field. For instance, the solar field's response rate and its time delay change drastically with varying mass flow rates, which makes it difficult to achieve good performance over the whole operating range when using a fixed parameter controller [53]. The application of advanced con-

trol methodologies is therefore usually a must as they exceed purely human control action in performance [58]. Regarding the topic of advanced solar field control methodologies, the interested reader is referred to the works published by Camacho et al. [53, 54, 55].

An additional issue regarding the solar field's mass flow control is the fact that the HTF flow rate can typically only be adjusted on sub-field[18] level. Hence, depending on the loops' mass flow adjustments during plant commissioning (hydraulic balancing), the actual mass flow through each loop is rarely the actually intended one.

In this work's model, a rather basic control methodology, a parallel feedforward-feedback combination is applied. Feedforward controllers are typically used where external disturbances of a plant can be measured. The feedforward term directly calculates the value of the manipulated variable (solar field mass flow rate) as a function of the external disturbances of the plant (solar irradiance or solar field inlet temperature) in order to reach the desired setpoint. Thus, feedforward control provides corrective action before the disturbance is detected as error in the controlled variable [53], i.e. the solar field's outlet temperature. However, since feedforward models do not exactly represent the actual behavior of the plant, the feedforward signal must be corrected by an additional feedback control loop that should feature integral behavior [53]. Nevertheless, since the feedforward model usually gives mass flow guess values close to the actually needed one, the corrective action of the feedback control loop is typically small.

The applied control scheme of this work is displayed in Figure 10.32. As can be seen in this figure, a proportional-integral (PI) block is applied as corrective feedback controller. The final mass flow signal ($\dot{m}_{HTF\,signal}$) is obtained by summation of the feedforward model's output and the feedback control loop's corrective output. An additional first order block is assumed to model the behavior of the actuator circuit (including the HTF pump).

Furthermore, besides the control loop for the nominal solar field outlet temperature, a defocussing control loop is implemented as well, in order to avoid an overheating of the heat transfer fluid. In this work, this defocussing control is implemented using a simple PI feedback structure. Thus, whenever the HTF temperature exceeds a maximum value of, e.g. 398 °C, the loop is defocussed in the model.

[18] A solar field usually consists of several sub-fields that in turn consist of one cold header, a certain number of parallel and identical solar collector loops and the hot return header.

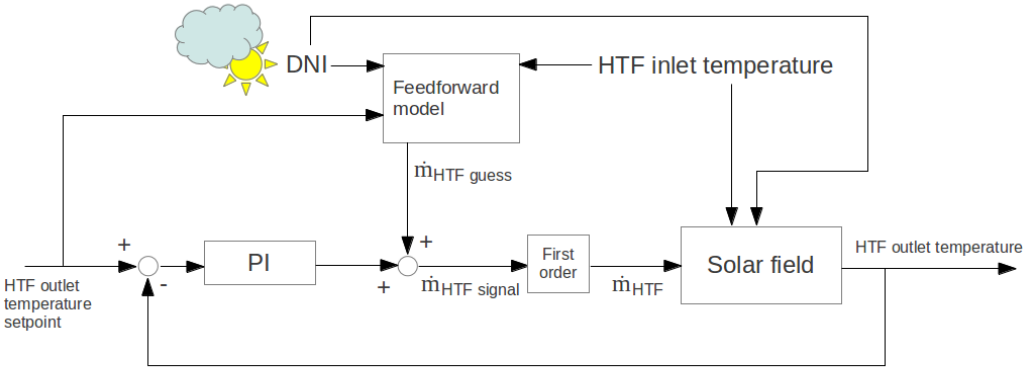

Figure 10.32: Parallel feedforward-feedback control scheme for a solar field

10.6.2.1 The solar field's feedforward controller

There exist many possibilities of implementing a feedforward model of a solar field. Approaches range from rather complex transient mathematical models (in the extreme case, an inverse model of the plant), over empirically known operating characteristics, to simplest steady-state energy balances [53].

This work applies the latter approach, assuming a linear temperature profile along the solar collector loop and estimating the thermal performance of the solar collectors via an empirical relationship available in the literature. In particular, the following correlation as published by Burkholder & Kutscher [199] is applied in order to estimate the heat loss of the linear absorber (Note: Additionally to the linear temperature profile, the absorber tube temperature is assumed to be equal the HTF bulk temperature, both drastic simplifications of the real problem):

$$\begin{aligned}\dot{Q}_{loss} = L_{loop} \cdot [&0.141 \cdot (T_{HTF\,mean} - 273.15) \\ &+ 6.48 \cdot 10^{-9} \cdot (T_{HTF\,mean} - 273.15)^4]\end{aligned} \tag{10.30}$$

The absorbed solar power for one representative solar collector loop of length L_{loop} can be expressed as follows:

$$\dot{Q}_{absorbed} = L_{loop} \cdot w_{coll} \cdot DNI \cdot \eta_{opt} \cdot \zeta_{shading} \tag{10.31}$$

The difference between the absorbed solar power and the thermal losses gives the useful thermal power under steady-state conditions:

$$\dot{Q}_{useful\,loop} = \dot{Q}_{absorbed} - \dot{Q}_{loss} \tag{10.32}$$

Finally, applying equation 10.29 for one loop, gives a rough theoretical HTF steady-state mass flow rate per loop:

$$\dot{m}_{HTF\,guess} = \frac{\dot{Q}_{useful\,loop}}{c_p \cdot (T_{HTF\,setpoint} - T_{HTF\,inlet})} \tag{10.33}$$

10.6.3 The control of the power block's thermal input

Given that the solar field's mass flow rate is adjusted by the outlet temperature control, the thermal input to the power block is determined too, of course, assuming zero-recirculation mass flow (power block bypass) and a power plant layout without thermal energy storage (see Figure 10.29).

Thus, for pure solar driven power plant operation, the current thermal load of the power block is determined by the solar field's performance and the power block is typically run in turbine-following control mode (see Section 10.6.4.2). However, depending on the applied solar multiple, the solar field will have to be defocussed during certain days in summer, when the maximum allowed solar field mass flow rate is not enough to guarantee the outlet temperature control target, especially without overheating the heat transfer fluid.

On the other hand, when applying thermal energy storage, the current solar field mass flow rate does not automatically define the thermal load of the power block, since a fraction of the solar field mass flow can either be used for storage system charging, or, in storage system discharging mode, a certain mass flow top-up can be supplied to the power block by the thermal energy storage system. Thus, for a solar thermal power plant with storage, the desired thermal load of the power block (usually the nominal one) is controlled via charging or discharging of the thermal energy storage system, of course, if the current state-of-charge of the storage system allows the desired operation. It is obvious that the solar field will have to be defocussed if the storage system is fully charged and the solar field provides more power than the power block is able to handle.

This work applies for both the defocussing control and the power block's thermal load control, via charging or discharging of the thermal energy storage system, standard PI feedback control loops. In the case of the HTF mass flow control for storage system charging or discharging, again, a parallel feedforward-feedback structure is used (see Section 10.6.2) applying a simple steady-state energy balance model assuming nominal temperature levels.

Having discussed the control of the thermal load delivered to the power block's steam generator, the drum-boiler and the closely related turbine load control modes will be treated in the following in a general way, giving examples for their application in conventional as well as solar thermal power generation.

10.6.4 Drum-boiler and turbine load control

The load of a power plant is typically determined by the current grid demand and the availability and the management of other power plants connected. Power stations are linked together in networks and have to meet the current grid demand in a kind of teamwork [217]. The current balance between the energy demand (electricity end-user) and the supply (power plants) is represented by the frequency of the power grid. For example, a sudden increase in demand will lead to a decrease in frequency and thus, the supplying power plants will have to increase their load in order to keep the frequency control target. This power grid frequency control loop, i.e. the balance between electricity demand and supply, is called electricity primary control [16]. The grid demand depends on the season and the current time of day. It is typically much higher during winter than in summer, due to electric heating (a real abuse of electric energy that is unfortunately still common in many places in the world, mainly because of low installation costs) and an increased demand for room lighting. However, depending on the country, air conditioning (let me call it the curse of "modern" buildings, since: *"Jedem Menschen Recht getan, ist eine Kunst, die niemand kann."*) in summer may constitute a considerable amount of the total energy demand as well. Furthermore, there are daily peaks in demand at noon and in the evening, i.e. times that are typically used for cooking and for running electric devices at home. Therefore, the grid demand can be subdivided in base load and peaking load. Which power plant is assigned what part of the current demand (either base load or peaking load) does mainly depend on the load following capability. The assignment of specific production plans and their compliance is referred to as electricity secondary control [16]. Typical peaking plants are gas-fired since modern gas turbines are very flexible regarding fast changes in load. On the other hand, steam driven plants are much slower in their response, mainly due to the thermal inertia of the steam and water circuits and limitations of the rate-of-change in temperature of thick component walls (e.g. steam drums). Furthermore, the applied fuel system of a thermal power plant plays an important role. For instance, a coal-burning boiler with a rather complex fuel-handling plant attached, will be much more limited regarding its load following capability than its oil-fired counterpart [217]. The same holds for

solar thermal power plants. Here, the fuel system is replaced by the solar field that harvests solar energy, which however, cannot be controlled by mankind. Thus, a solar thermal power plant in pure solar driven operating mode has a very limited load following capability. Besides the possibility of defocussing the solar field (i.e. reducing the load), a sudden increase in turbine load is only possible up to a certain and small extent and is very limited in time, depending on the steam generators thermal energy buffer (i.e. a sudden opening of the turbine valve, without increasing the "firing rate", the heat transfer fluid's mass flow rate, will inevitably lead to a considerable decrease in steam pressure). In contrast, solar thermal power plants using thermal energy storage, do of course have load following capabilities, that are, however, also limited due to the rather large thermal inertia of the heat transfer fluid circuit. Generally speaking, it can be said that an increased usage of renewable energy, which is for the most part intermittent in nature (e.g. the usage of pure solar driven power plants and wind turbines), will require an increased number of fossil-fired peaking plants for backup in order to always match the current electricity demand.

Apart from the applied thermal power supply (fuel system or solar energy capturing technology), also the turbo-generator's load control concept influences the plant's load following capability. When thinking about possible turbine load control options, one has to consider Equation 10.15, which states that the current turbine power is the product of the steam mass flow rate and the enthalpy difference across the turbine. Thus, if the turbine power had to be modified, this would either be possible via varying the steam mass flow rate, or via varying the inlet or outlet enthalpy. However, considering the fact that the turbine inlet enthalpy and the turbine outlet enthalpy are usually kept rather constant during operation in the upper load range, the turbine power is almost only controlled via modifying the steam mass flow rate [204]. The process variable that determines the steam mass flow rate across the turbine is the imposed pressure difference, i.e. the difference between the turbine inlet pressure and the turbine outlet pressure. Furthermore, considering that the turbine outlet pressure is determined by the current condenser pressure that depends on the ambient temperature (low temperature waste heat rejection to the ambient), the turbine inlet pressure is obviously the process variable of choice in order to control the turbine power. Consequently, there exist two options for varying the turbine inlet pressure:

- either keeping the steam generator (boiler) pressure constant and throttling the live steam mass flow via the turbine valve (constant pressure mode),
- or varying the steam generator (boiler) pressure level without throt-

tling, having the turbine valve fully open (sliding pressure mode).

Turbine load control methods where the boiler pressure is kept rather constant (constant pressure modes), i.e. it only varies within a narrow range due to control margins, can be subdivided into boiler-following control, turbine-following control and coordinated control [217, 218].

On the other hand, turbine load control methods where the boiler pressure considerably varies (sliding pressure modes) can be subdivided into natural sliding pressure mode and modified sliding pressure mode [204, 16].

A short summary of each control mode will be given in the following. Furthermore, their relevance in solar thermal power applications will be discussed.

10.6.4.1 Boiler-following control mode

As the name already implies, in this mode, the boiler, or better, the firing rate is "following" (or adapting to) the currently adjusted (via the turbine valve) turbine load in order to keep the steam generator pressure at the desired constant value. The load following control loop of the plant directly acts on the turbine valve, which opens, to rapidly increase the steam mass flow (increase the turbine power), or closes, to rapidly decrease the steam mass flow (decrease the turbine power). In this operating mode, load changes can be performed very fast, using the stored energy within the boiler. The boiler firing rate, or in solar applications, the solar heat input control loop responses (it follows) to this fast changes in steam discharging rate in order to keep the steam generator pressure constant (constant pressure mode).

A drawback of this control approach is that the turbine valve is throughout the operation always partially closed, reducing the steam cycle's overall efficiency. This especially applies for the operation at partial loads. For this reason, turbines that are operated in constant pressure mode are usually equipped with a partial arc admission control stage, rather than having one main turbine valve for throttling [16]. A partial arc admission control stage is an impulse stage that is equipped with a set of independently adjusted control valves in combination with single admission nozzles, allowing the steam to be admitted in full arc mode (nominal load) or partial arc mode (partial load) [218]. Partial arc admission provides better efficiencies at partial loads [16, 218].

At solar thermal power plants, the boiler-following control mode would only be feasible in combination with thermal energy storage or auxiliary fossil fuel burners, since the solar energy available cannot be controlled and a sudden power increase of the turbine (steam mass flow increase) could

mean a considerable decrease in steam generator pressure due to a current lack in solar irradiation. Consequently, a strong decrease in boiler pressure could mean an approach of the maximum allowed rate-of-change in temperature. This is especially an issue for the thick walled steam drums in natural or forced circulation boilers, since fast changes in temperature may cause harmful thermal stress.

10.6.4.2 Turbine-following control mode

The turbine-following control mode is another option of constant pressure control. In this mode, the load following control loop of the plant directly acts on the firing rate instead of controlling the turbine valve position. Thus, if the power plant has to increase its output because of an increased electricity demand, the firing rate is increased. This leads to an increase in steam generator pressure and the turbine valve control loop has to adjust the valve position accordingly, in order to keep the steam generator pressure constant (constant pressure mode). Hence, the turbine load follows the boiler load (turbine-following control mode). A disadvantage of this operating mode is that the load following capability is much slower (when compared to the rather fast boiler-following mode) since the turbine mass flow is not influenced until the boiler has reacted to the change in firing rate. This is particularly the case for coal-fired power plants having a relatively complicated and slowly reacting firing system [217]. Deviations from the ideal steam mass flow (as requested by the specific power plant load schedule) are at the expense of the electrical grid [204]. An advantage of the turbine-following control mode is that the steam generator's pressure variations are much smaller when compared to the boiler-following mode. As a consequence, the variations in saturation temperature in the steam drum are much smaller, considerably reducing thermal fatigue [204].

The turbine-following control mode is the typical option for solar thermal power plants that operate in solar-only mode, i.e. neither thermal energy storage, nor auxiliary fossil fuel burners are applied. There, the heat transfer fluid mass flow rate, which enters the plants steam generator, corresponds to the firing rate of conventional plants. Since the current heat transfer fluid mass flow rate is a function of the current solar irradiance (which cannot be controlled by mankind), the turbine valve opening has to be adjusted in order to maintain the steam generator pressure constant.

10.6.4.3 Coordinated control mode

Coordinated control is a combination of both the boiler-following and the turbine-following control mode. In this case, a sophisticated combined control strategy is applied by avoiding the disadvantages of each basic control mode.

10.6.4.4 Natural sliding pressure control mode

In natural sliding pressure mode, the turbine valve is always kept fully opened and the turbine load is only controlled via modifying the firing rate. Thus, the steam generator pressure varies accordingly (sliding pressure mode). Due to the thermal inertia of the boiler, also this control mode has limitations regarding the load following capability [16]. It is however a very efficient alternative, especially at low partial loads, since there is no throttling of the steam which is admitted to the turbine (the turbine valve is always fully opened) [204]. According to Strauß[16], sliding pressure operation has the following advantages:

- Due to the lower steam generator pressures at partial loads, there is lower fatigue of highly stressed components.
- Since a partial arc admission control stage is not needed, the plant is usually cheaper.
- Due to the lower steam generator pressure at partial loads, the power consumption of the feed water pump is considerably lower, reducing the parasitic power consumption.

However, it has to be mentioned that not all steam generator types are suitable for large and relatively fast changes in pressure that occur in sliding pressure operating mode. Especially, thick walled steam drums in natural or forced recirculation boilers are very sensitive to large rates-of-change in temperature that occur during changes in drum pressure due to changes in saturation temperature. Typically, once-through boilers are the preferred option for sliding pressure modes [204].

10.6.4.5 Modified sliding pressure control mode

The modified sliding pressure control mode is a combination of the constant pressure mode (boiler-following mode) and the natural sliding pressure mode in order to avoid the disadvantages of both concepts. Thus, the rather poor load following capability of the sliding pressure mode, and the rather poor

part load efficiency of the constant pressure mode may be improved. In principle, the load control works according to the boiler-following mode, i.e. the turbine valve is opened or closed in order to adjust the turbine power to the current demand. However, only small changes in turbine load are performed via throttling. Larger variations in power output are performed via increasing or decreasing the steam pressure set point, i.e. applying the sliding pressure control concept. This leads to a considerably improved part load efficiency due to less throttling. However, unlike the natural sliding pressure control mode, here, the turbine valve is slightly closed (5-10% [16]) during steady-state conditions. In this way, the live steam mass flow can be temporarily increased to rapidly meet the power demand, using the storage capability of the steam generator [204].

10.6.4.6 The process variables in drum-boiler control

The process variables in drum-boiler control are the live steam pressure, the live steam temperature, and the water level within the steam drum. The water level of the drum is controlled via the feed water mass flow rate (feed water pump). The live steam pressure is controlled via the firing rate (boiler-following mode), or, via the turbine valve opening (turbine-following mode). Since one of the two previously mentioned manipulated variables for the live steam pressure, either the turbine valve opening, or, the firing rate is used for adjusting the turbine load, an additionally manipulated variable has to be introduced in order to control the live steam temperature. This is typically done by adding a spray-water attemperator that mixes cool water and superheated steam [217]. Without steam temperature control, the live steam temperature is typically a function of load, following the "natural characteristic" of the boiler which additionally varies due to fouling of heat exchanger surfaces [217]. However, steam turbines are usually sensitive to changes in live steam temperature what requires the steam temperature to be controlled to a specified setpoint. This is commonly done via continuous spraying, which enables to adjust the live steam temperature both upwards (decreased spraying) and downwards (increased spraying) [217].

10.6.4.7 The control of this work's steam generator model

In this work, the constant pressure load control mode has been chosen. In particular, the turbine-following control mode has been implemented (see Section 10.6.4.2).

Furthermore, standard PI feedback control loops are applied for the drum pressure control as well as for the drum level control.

However, since this work's steam generator model does not capture drum level dynamics as shrink-and-swell effects, a realistic consideration of the drum level control is out of scope. Thus, the controller parameters (as gain K_p and integral time τ_i) have been adjusted to reasonable values giving good performance during the accomplished simulations. They have actually a negligible influence on the simulation result since the corresponding dynamics are relatively slow.

On the other hand, the drum pressure dynamics are relatively fast and the controller settings have to be well adjusted in order to obtain good simulation results. In reality, the drum pressure controller acts on the turbine valve, i.e. opens it or closes it depending on the current drum pressure. Since in this work the turbine valve is not explicitly modeled (see Section 10.4.1.2), the drum pressure controller's output signal is a direct steam mass flow signal, being able to implement the turbine valve as a simple mass flow sink. Despite the fact that this configuration does not correctly represent the real setup, it does however correctly indicate the required steam mass flow for the given thermal input ("firing rate") in order to keep the drum pressure at the chosen setpoint.

In principle, the steam generator shows first-order-plus-time-delay behavior when subjected changes in steam mass flow rate. After a positive step in extracted steam mass flow, the drum pressure decreases and converges to its new steady-state value after a certain period of time. Correspondingly, after a negative step in extracted steam mass flow, the drum pressure converges at its new steady-state value that is higher than the previous one.

In this work, the drum pressure controller's settings have been obtained via open-loop step response simulations at nominal load conditions applying controller tuning correlations according to Chien, Hrones and Reswick [193].

The resulting process parameters are approximately -344125 $Pa\ s\ kg^{-1}$ for the process gain K_s, 0.9 s for the dead time Θ and 325.4 s for the time constant τ. This gives a controller gain K_p of -0.000382 $kg\ s^{-1}\ Pa^{-1}$ and an integral time τ_i of 390.5 s.

10.6.5 The top-level control of the power plant - The operating strategy

The top-level control block implements the operating strategy of the power plant model, i.e. it acts as a virtual operator of the plant that defines allowed minimum and maximum mass flow rates, the solar field recirculation mass flow, the thermal load setpoint of the power block as well as the thermal energy storage system's operation.

An important point of the operation strategy control block is that it features discrete time variables that change their values at certain events during simulation[19].

For instance, the minimum HTF solar field mass flow is a discrete signal that changes its values at certain events during simulation. On the one hand, the solar field mass flow may range between zero and the maximum flow that can be handled by the pumps, during normal operation during the day. On the other hand, during certain times at night, the solar field's HTF mass flow may have a minimum mass flow rate of, e.g. 1 $\frac{kg}{s}$ per loop, in order to avoid freezing. Furthermore, during plant start-up in the morning (after the DNI level has reached a certain threshold) the minimum solar field mass flow can be automatically forced to a minimum of, e.g. 6 $\frac{kg}{s}$ per loop, in order to avoid overheating of the heat transfer fluid during solar field start-up if standard feedback control loops with constant tuning parameters (that have been adjusted for nominal operation of the plant) are applied in the model. For example, in this work, a "semi-automatic" solar field start-up strategy is applied. In particular, a virtual operator manually adjusts the HTF recirculation mass flow in the field during the start-up until the hot header's outlet temperature reaches the threshold temperature of 376 °C (the nominal discharge temperature of thermal energy storage system; see Section 10.3). After reaching this solar field outlet temperature threshold, the automatic feedforward-feedback control loop is activated (see Section 10.6.2). Furthermore, the solar field's HTF recirculation (see the so-called "recirculation line" in Figure 10.29) is deactivated.

In summary, any arbitrary operating strategy can be implemented that defines certain variable setpoints (e.g. the current thermal load of the power block) according to specific operating directives.

10.7 Discussion of simulation results

In order to show the application of the presented models, this section will treat two specific plant simulations.

Section 10.7.1 presents simulation results using the transient steam generator model as presented in Section 10.4.1.1. In particular, the power plant's response to a sudden cloud pass will be shown in pure solar driven operating mode.

Section 10.7.2 treats the power plant's behavior over two typical summer days, including the storage system's charging and discharging operation

[19]For detailed information about continuous and discrete-event system modeling and simulation, the interested reader is referred to the corresponding literature, e.g. [219].

and applying the fully quasi-steady power block model according to Section 10.4.2.

10.7.1 A short simulation under pure solar driven conditions - The impact of a cloud pass

Typical transients that occur during daily power plant operation are due to fluctuating direct normal irradiance, i.e. due to passing cloud fields that temporarily block the solar direct irradiance. If the plant features thermal energy storage, this temporal lack in solar radiation can be compensated via discharging the thermal energy storage system. However, without thermal energy storage, a cloud field will have direct impact on the power plant's electric output.

It is the aim of this section to show the impact of a temporal and sudden reduction in direct normal irradiance on the electric output of a solar thermal power plant using PTCs and operating under pure solar driven conditions.

Figure 10.33 shows the chosen direct normal irradiance data. It can be observed that the direct normal irradiance shows a strong, but short intermittence around simulation time 4000 s. Besides that, the used irradiance data shows minor variations which is typical for days where the sky is not perfectly clear.

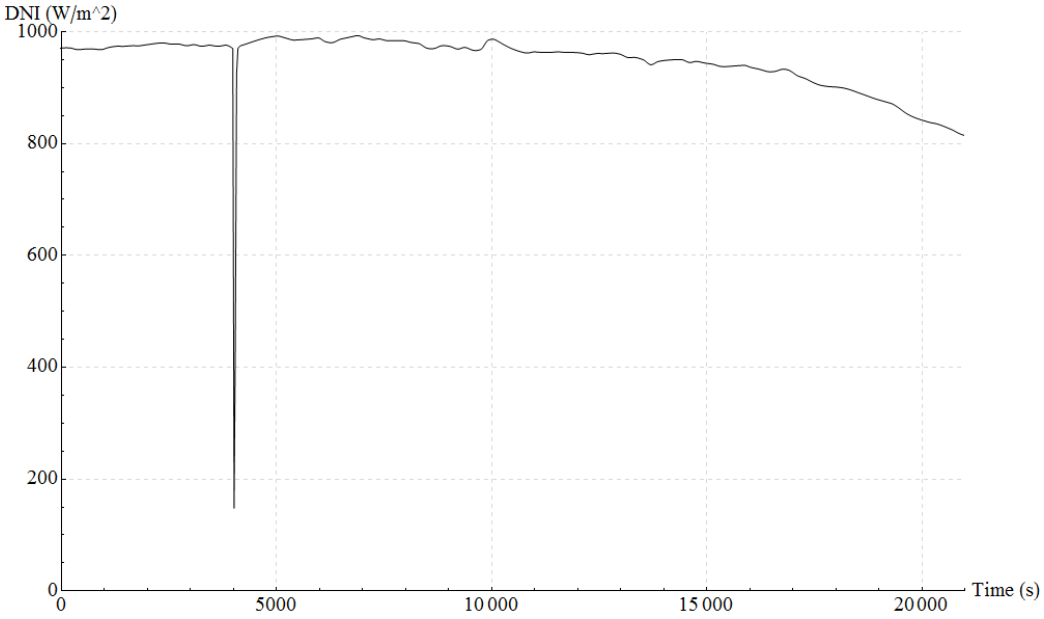

Figure 10.33: Solar direct normal irradiance incident on the solar field

For the chosen solar field parameters (see Section 10.2), the resulting HTF mass flow per loop is around 7 $\frac{kg}{s}$ (see Figure 10.34). Given the chosen total number of loops ($n_{loops} = 110$), the corresponding total solar field HTF mass flow results in values around 770 $\frac{kg}{s}$ (see Figure 10.35).

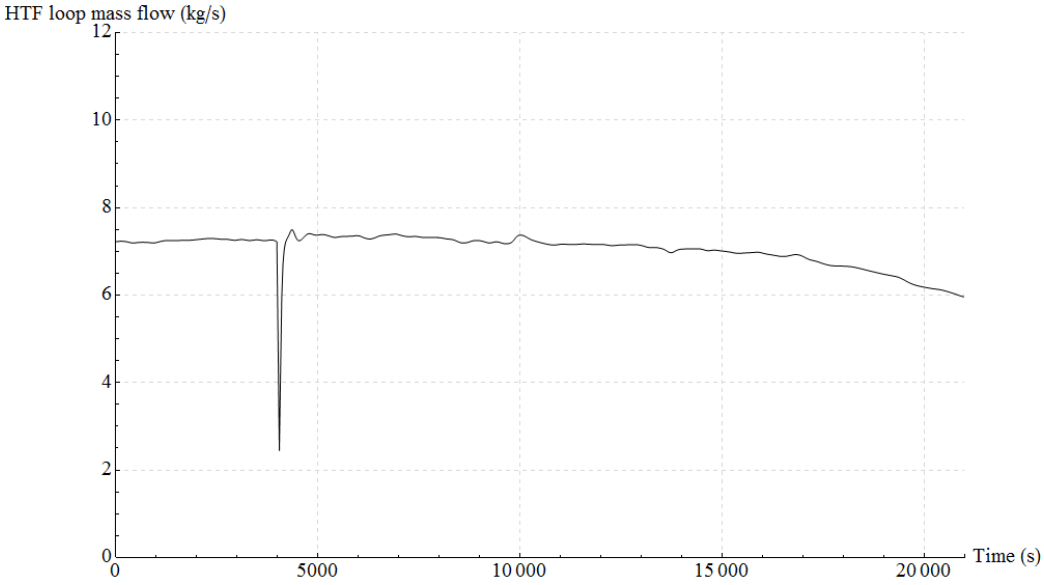

Figure 10.34: Heat transfer fluid mass flow per collector loop

Figure 10.36 displays the resulting HTF outlet temperature of the representative collector loop (black solid line) and the outlet temperature of the solar field's hot header (red solid line). It can be well observed that the solar field's control loop counteracts the disturbance in direct normal irradiance, however, not perfectly, since there appear oscillations around the outlet temperature setpoint of 391 °C. Due to the inertia of the hot header pipe, these oscillations appear considerably damped (red solid line) at the solar field's outlet (the steam generator's inlet).

The corresponding performance of the steam generator's drum pressure control is displayed in Figure 10.37. The strong reduction in HTF mass flow due to the sudden cloud pass leads to a decrease in drum pressure, since the live steam mass flow is not immediately reduced by the drum pressure control loop. Since a standard feedback control loop is applied, the controller does not act until an error in steam pressure is detected. The performed corrective action of the controller leads to a small overshoot in drum pressure, which again settles at the chosen setpoint of 99 *bar* after about 17 minutes.

The directly correlated change in saturation temperature within the drum is shown in Figure 10.38 by the solid blue line. The behavior of the drum's

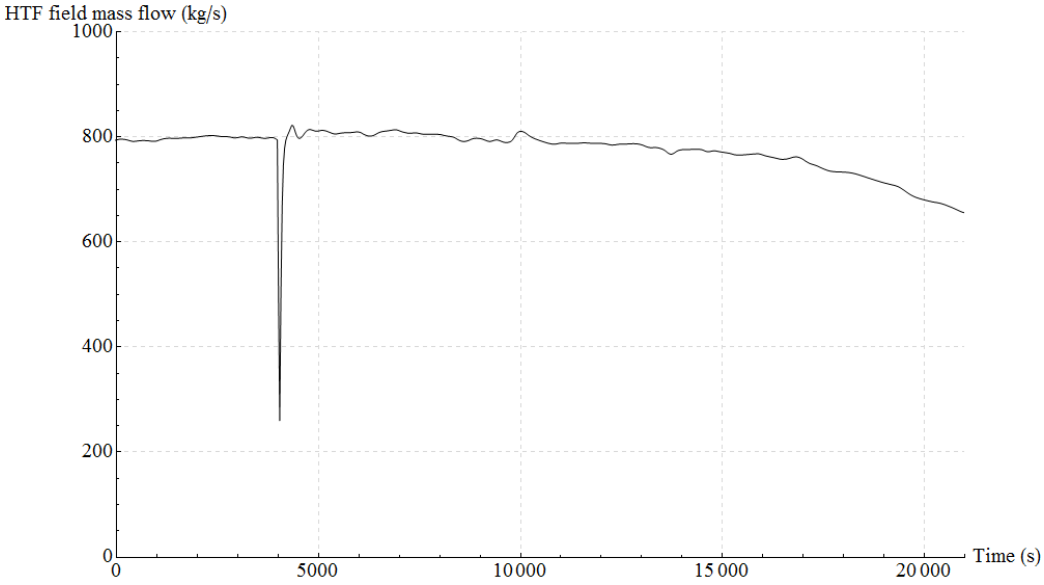

Figure 10.35: Heat transfer fluid mass flow leaving the solar field

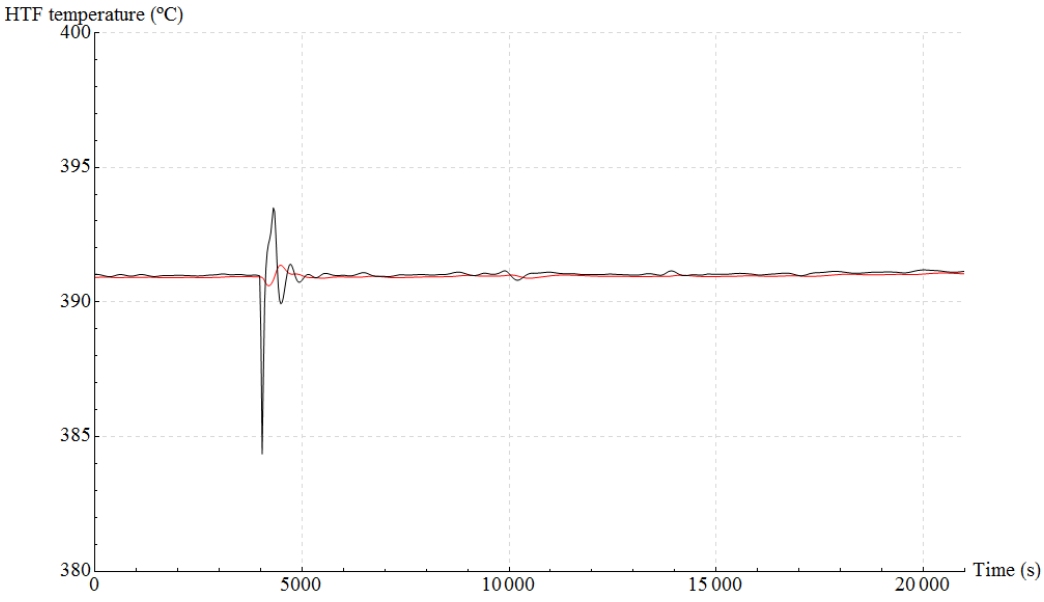

Figure 10.36: Outlet temperature of the representative collector loop (black) and the solar field's hot header (red)

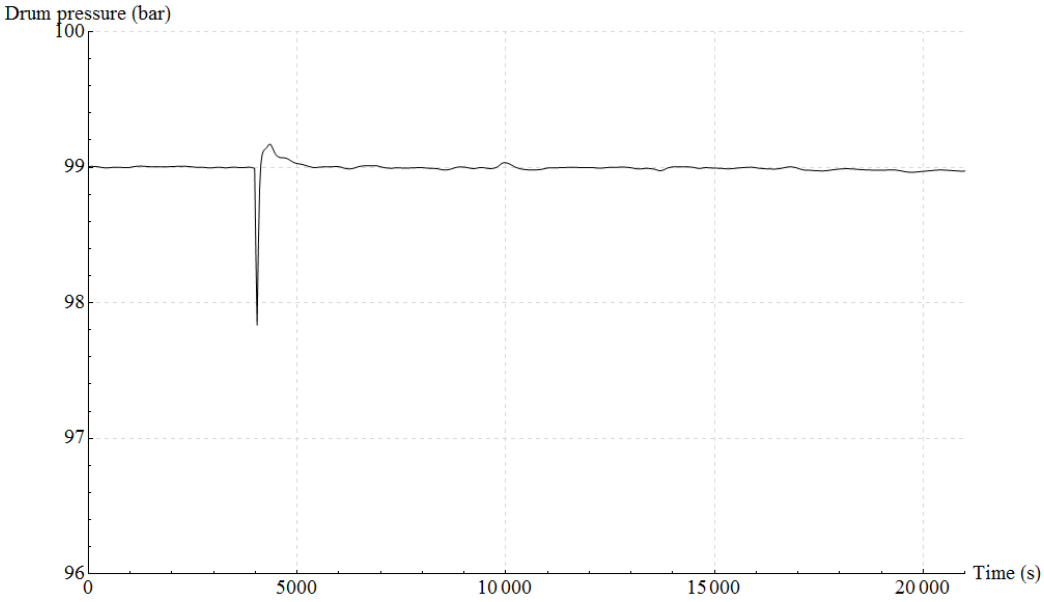

Figure 10.37: Behavior of the drum pressure of the natural circulation boiler

central wall temperature is represented by the solid black line in Figure 10.38. Here, the maximum rate of change in wall temperature stays considerably below the critical value of 2-3 °C per minute.

Figure 10.39 shows the corresponding live steam mass flow rate admitted to the turbine model. While constituting about 77 $\frac{kg}{s}$ under normal operation, it drops down to a minimum of about 31 $\frac{kg}{s}$ during the disturbance in direct normal irradiance.

The power block's corresponding electric gross power output is displayed in Figure 10.40.

10.7.2 Diurnal simulations using thermal energy storage

This section presents simulation results for two specific days of power plant operation applying power block model type B (see Section 10.4.2) and the thermal energy storage model according to Section 10.3. The environmental boundary conditions correspond to the data already presented in Section 7.3. In particular, the data for reference day set I (summer) is used. The two simulations have been performed for the first two days of this data set (see Figures 7.3, 7.6 and 7.7).

The power plant's specifications have been assumed as indicated in Table 10.3.

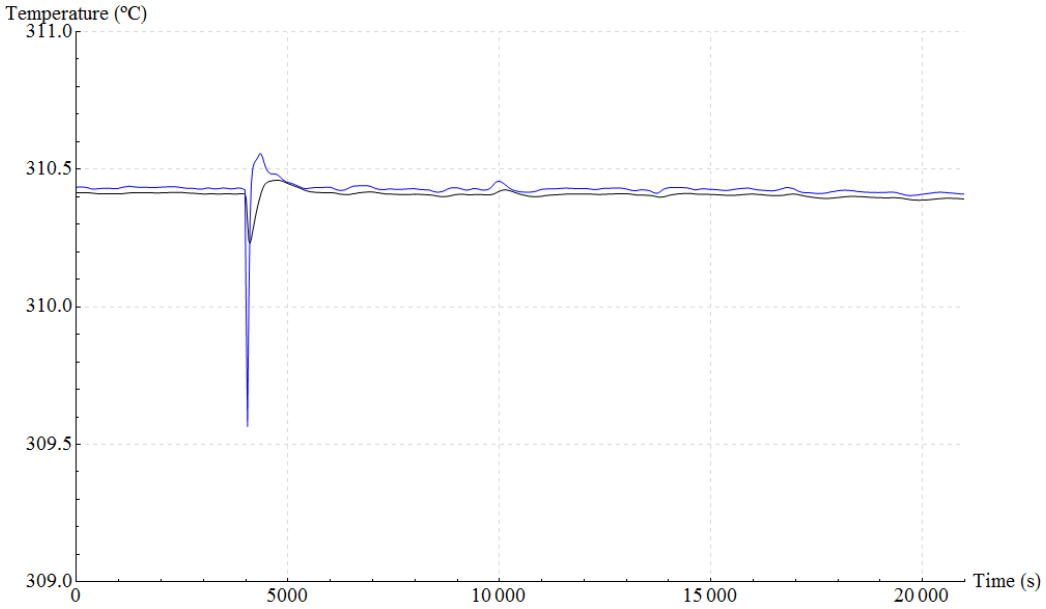

Figure 10.38: Drum saturation temperature (blue) and the drum wall node temperature (black)

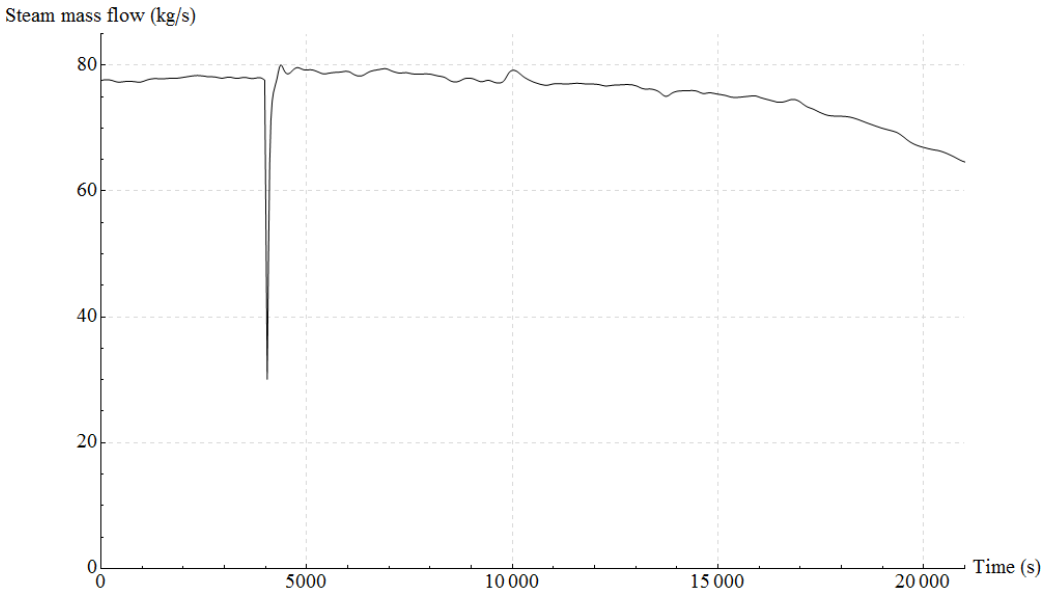

Figure 10.39: Live steam mass flow leaving the steam generator and admitted to the turbine

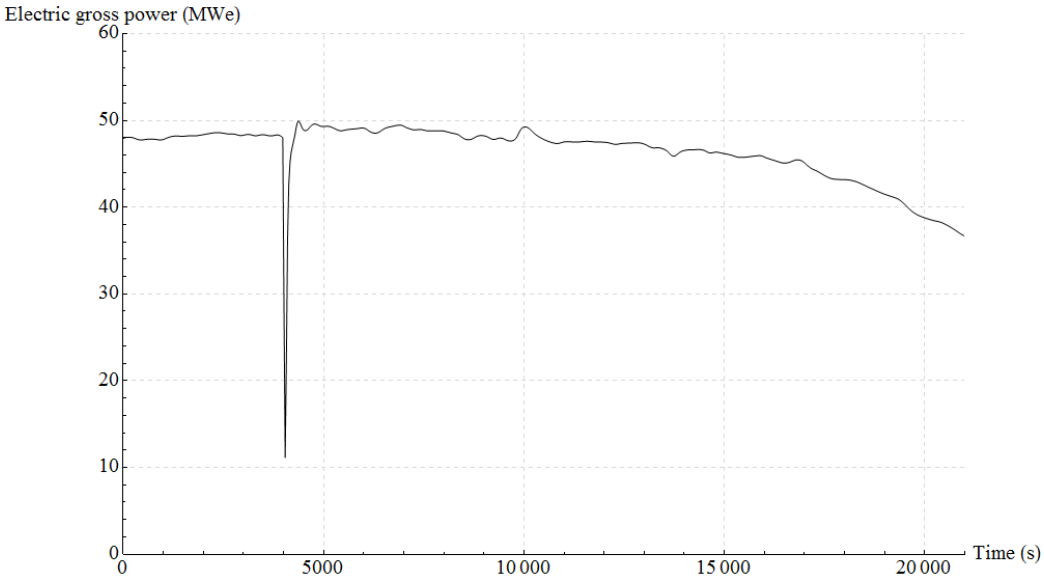

Figure 10.40: Electric gross power of the plant's power block

The environmental boundary conditions for day one (21st of June) feature a rather continuous direct normal irradiance trend. On the other hand, the second data set for day two (22nd of June) exhibits sudden cloud passes in the afternoon. For both simulations, the storage system's state of charge[20] has been set to 0.9 at simulation start (initial condition). Furthermore, a simple solar driven operation strategy with storage is applied. This means that the virtual plant operator always tries to meet the power block's thermal load target if possible. Hence, if solar energy is available in excess, the thermal energy storage system is charged. If the current incident solar irradiance is not sufficient to reach the thermal load setpoint of the power block, the thermal energy storage system is discharged.

In the following two simulations, the power block's thermal load setpoint has been set to 85% nominal load.

10.7.2.1 A diurnal simulation with continuous direct normal irradiance

The simulation starts on the 21st of June at midnight assuming an almost fully charged thermal energy storage system (the state of charge equals 0.9). Furthermore, the initial temperature in the solar field and the heat transfer

[20]Note: A state of charge of 1 indicates a fully charged storage system; a state of charge of zero indicates a completely discharged storage system.

Table 10.3: Power plant specifications

Parameter (unit)	Numerical value
Solar field	
Solar collector width (m)	5.76
Collector loop length (m)	600
Peak optical efficiency (-)	0.781
Number of loops (-)	122
Spacing between loops (m)	17
Tracking axis orientation (-)	North-south
Thermal energy storage system	
Inner diameter of storage tanks (m)	38.5
Inner height of storage tanks (m)	14
Maximum molten salt level height (m)	13
Height distribution header (m)	0.6
Height suction pump inlet (m)	0.4
Design temperature of the hot tank (^oC)	386
Design temperature of the cold tank (^oC)	292
State of charge at simulation start (-)	0.9
Oil-salt heat exchanger dimensions per subunit according to Table 8.1 (TEMA-F oil-salt)	
Discharge setpoint temperature of the HTF (^oC)	376
Maximum HTF charge and discharge mass flow rate (kg/s)	600
Power block	
Nominal gross electric power (MWe)	50
Nominal HTF mass flow rate (kg/s)	825
Live steam pressure (bar)	99
Live steam temperature (^oC)	366
Reheat temperature (^oC)	371
Nominal live steam mass flow rate (kg/s)	80
Nominal inlet pressure second turbine stage (bar)	80
Nominal inlet pressure third turbine stage (bar)	50
Nominal inlet pressure fourth turbine stage (bar)	3
Condenser pressure level (bar)	0.17
Area of heat transfer economiser (m^2)	1200
Nominal overall heat transfer coefficient economiser ($W/(m^2\,K)$)	1500
Area of heat transfer evaporator (m^2)	2500
Nominal overall heat transfer coefficient evaporator ($W/(m^2\,K)$)	2000
Area of heat transfer superheater (m^2)	750
Nominal overall heat transfer coefficient superheater ($W/(m^2\,K)$)	600
Area of heat transfer reheater (m^2)	800
Nominal overall heat transfer coefficient reheater ($W/(m^2\,K)$)	600
Area of heat transfer feed water preheater (m^2)	600
Nominal overall heat transfer coefficient feed water preheater ($W/(m^2\,K)$)	1000
Area of heat transfer per air-cooled condenser subunit (1 fan) (m^2)	4000
Number of air-cooled condenser subunits (-)	30

fluid circuit has been set to 325 °C, arbitrarily. The inventory temperatures of the storage tanks have been set to their design values.

Since the simulation starts at night and the thermal energy storage system is completely charged, the virtual plant operator starts to discharge the storage system at maximum load. Since the maximum HTF discharge mass flow rate of 600 $\frac{kg}{s}$ is not enough to run the power block at the desired setpoint of 85% thermal load, a considerably lower plant output is achieved (about 33 MWe gross, according to Figure 10.47).

During the nightly plant operation, the HTF mass flow rate per loop is set to a constant value of about 0.1 $\frac{kg}{s}$ (see Figure 10.43). It can be well observed that the collector loop's outlet temperature considerable decreases during the early morning hours due to the heat loss to the ambient. On the other hand, the well insulated header pipes show a much slower temperature decrease. For this reason, it is a common practice to increase the solar field's recirculation rate if the HTF temperature falls below a certain threshold during the night in order to avoid freezing.

Right before 5 am at sunrise, the solar collectors start tracking the sun and the heat transfer fluid's temperature (red solid line in Figures 10.41 and 10.42) within the absorber tubes starts to increase. According to the assumed semi-automatic operation strategy of the solar field, the virtual operator adjusts the mass flow rate of the solar field according to empirically known steady-state values for the given DNI level and the sun's current position. In particular, in the model, the steady-state mass flow values are determined using the feedforward model as explained in Section 10.6.2.1. It is important to note that during the solar field's start-up, the HTF mass flow is fully recirculated, thus not interfering te current operation of the power block, which is still entirely fed by the thermal energy storage system. The solar field's HTF recirculation must continue until the hot header's outlet temperature reaches a certain threshold temperature, in this work 376 °C, the discharge temperature setpoint of the thermal energy storage system. Due to the HTF's recirculation, the loop's inlet temperature considerable increases (blue solid line in Figures 10.41 and 10.42) resulting in a smaller possible temperature increase and thus causing relatively high mass flow rates (see Figure 10.43) when applying this simple solar field start-up methodology. Since high solar field mass flow rates cause a considerably increased pumping power (see Figure 10.47), the start-up procedure presented has room for improvements (e.g. additionally applying defocussing).

Right before 6 am the solar field's outlet temperature reaches the required minimum for operation and the solar field's mass flow control is switched to automatic mode (parallel feedforward-feedback combination according to Section 10.6.2). Thus the feedback control loop corrects the HTF mass flow

rate in order to reach the design outlet temperature of 391 °C. At the same time, the solar field's HTF recirculation is deactivated and the HTF coming from the solar field is pumped to the power block.

Now, there is more than enough thermal power available in order to reach the chosen thermal load setpoint of the power block. Correspondingly, the virtual plant operator starts to charge the thermal energy storage system. The storage system's mass flow rates are indicated in Figure 10.45. The light-gray shaded areas indicate discharging mode, the gray shaded ares indicate charging mode. Furthermore, molten salt and HTF mass flow rates are defined positive for charging mode and negative for discharging mode. In summery, it can be seen well, how the HTF mass flow entering the storage system is adjusted in order to reach the desired thermal load setpoint of the power block. The molten salt mass flow controller adjusts subsequently the molten salt flow in order to reach the hot tank's design temperature (see 10.46).

Figure 10.46 displays the fluid temperatures at the oil-to-molten-salt heat exchanger's ends. In particular, the fluid temperatures of the outermost control volumes of both fluid ducts are displayed. The blue lines are those for the molten salt, the red lines are those for the thermal oil (HTF). The dashed lines indicate the heat exchanger's outlet temperatures in discharging mode. The solid lines indicate the heat exchanger's outlet temperatures in charging mode.

Until right after 5 pm, there is enough solar energy available in order to charge the thermal energy storage system. Thereafter, the thermal energy storage system switches into discharging mode, since the incident solar irradiation considerably decreases in the late afternoon (see Figure 10.41). The solar field goes off-line at about half past 6 pm. Consequently, the power block is only fed by the thermal energy storage system from then on. Since the storage system's HTF mass flow is limited to 600 $\frac{kg}{s}$, the thermal load setpoint of the power block cannot be reached any more and the electricity gross output goes correspondingly down (see Figure 10.47).

Figure 10.47 displays the plant's gross electric output (black solid line), the total fan power (red solid line) of the air-cooled A-frame condenser units, the power block's feed water pumping power (red dashed line), and the solar field's HTF pumping power (black dotted line). It can be well observed that the condensers' fan power considerably increases during the day due to relatively high ambient air temperatures (up to about 38 °C, see Figure 7.6), which increases the required air mass flow rate for the waste heat rejection to the ambient. Note: The condenser pressure is kept constant at 0.17 *bar*, thus yielding a saturation temperature of about 56.5 °C.

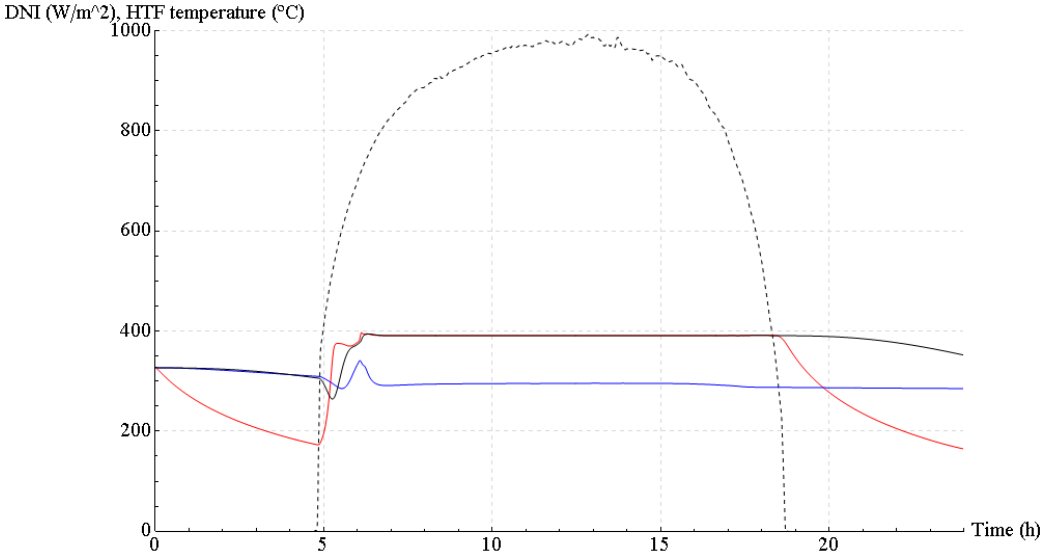

Figure 10.41: Direct normal irradiance (black dashed) on the 21st of June (Desert Rock, Nevada, USA) and the simulated solar field HTF temperatures; Loop outlet temperature: Red, Loop inlet temperature: Blue, Solar field outlet temperature: Black solid

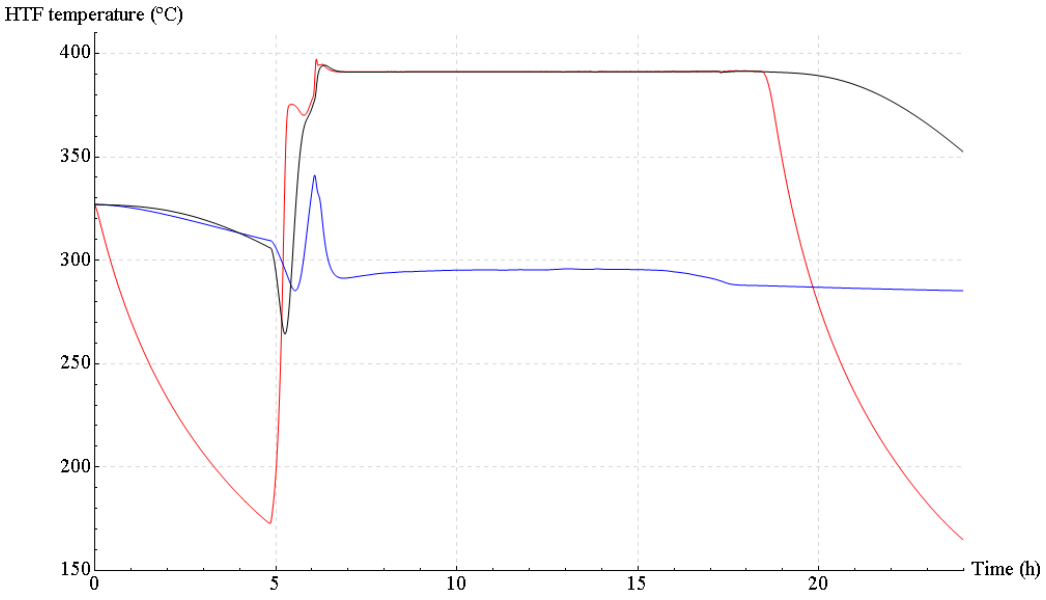

Figure 10.42: Simulated solar field HTF temperatures; Loop outlet temperature: Red, Loop inlet temperature: Blue, Solar field outlet temperature: Black

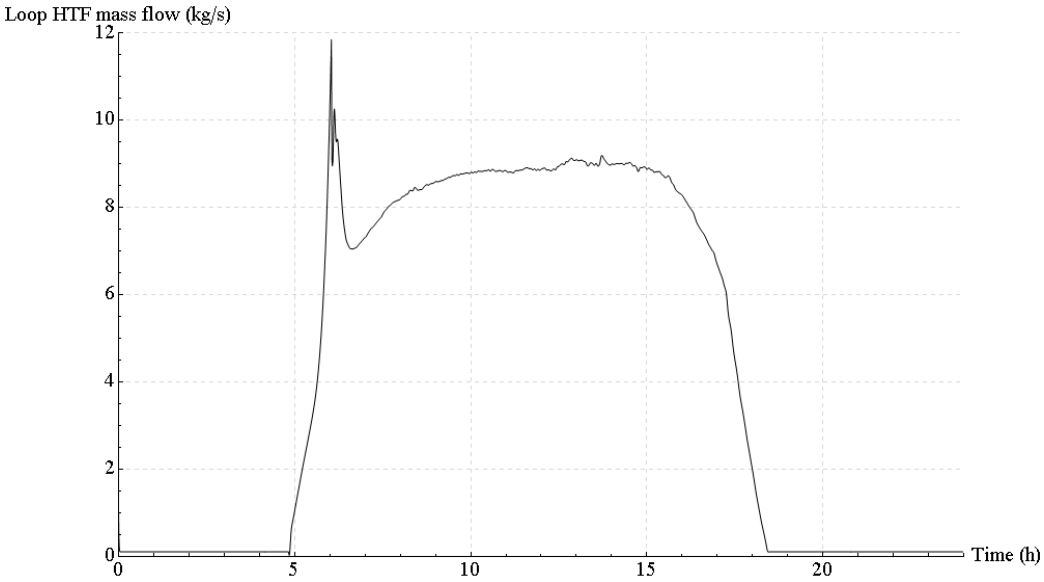

Figure 10.43: Simulated HTF mass flow rate per collector loop

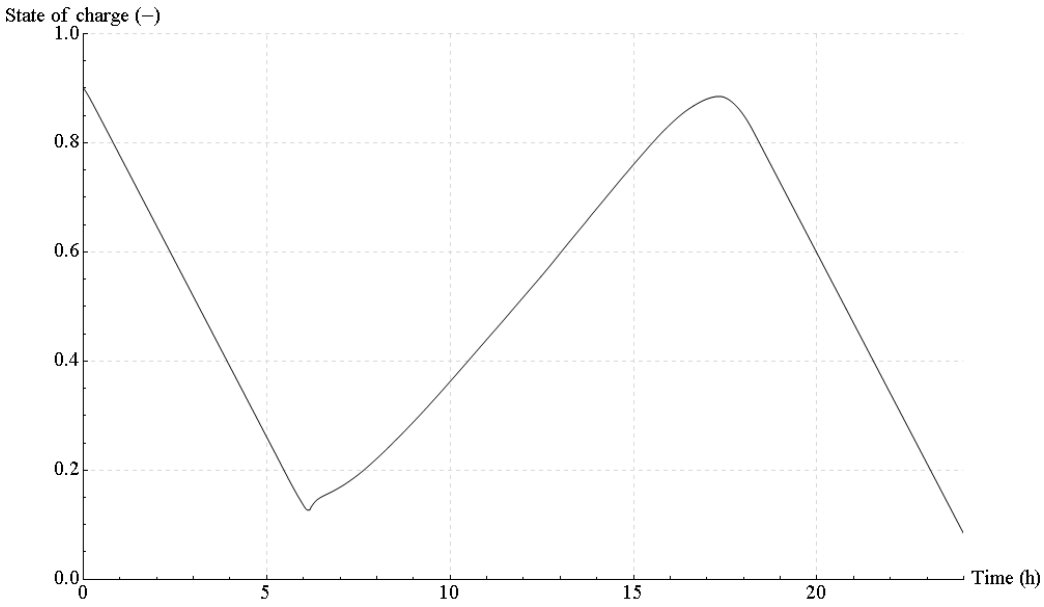

Figure 10.44: State of charge of the thermal energy storage system (1 = fully charged, zero = fully discharged)

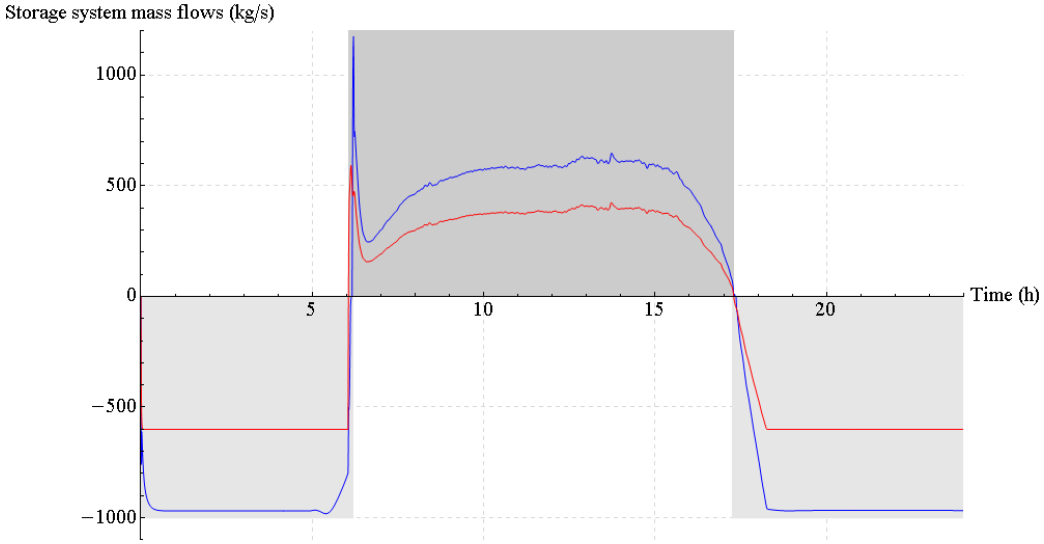

Figure 10.45: Mass flow rates of the thermal energy storage system; Thermal oil (HTF): Red, Molten salt: Blue, Charging: Positive, Discharging: Negative

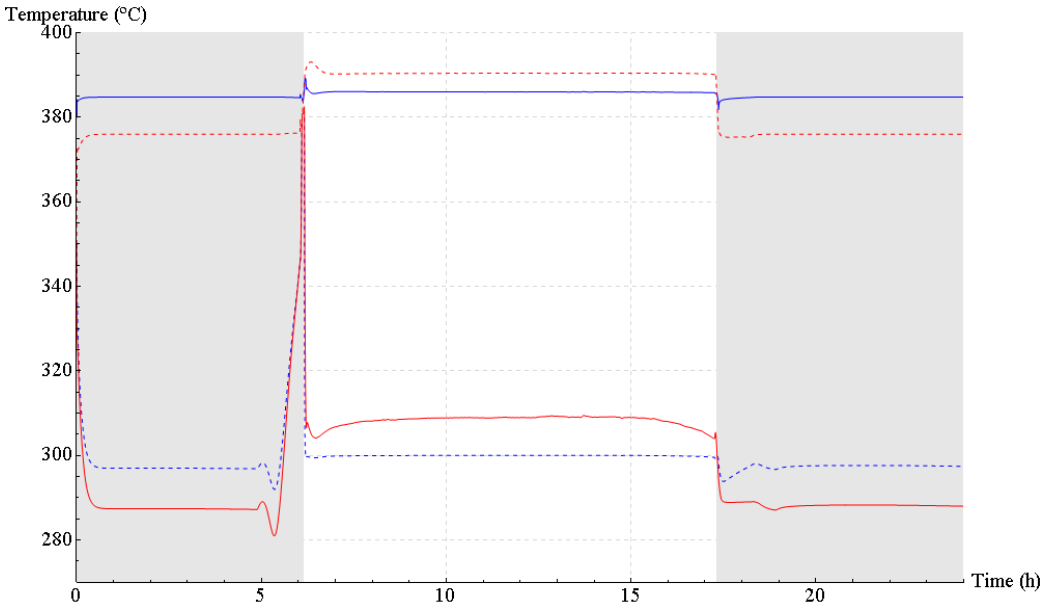

Figure 10.46: Temperatures at the oil-to-molten-salt heat exchanger's ends (outermost control volumes of both fluid ducts); Thermal oil (HTF): Red, Molten salt: Blue, Outlet temperatures during charging mode: Solid lines, Outlet temperatures during discharging mode: Dashed lines

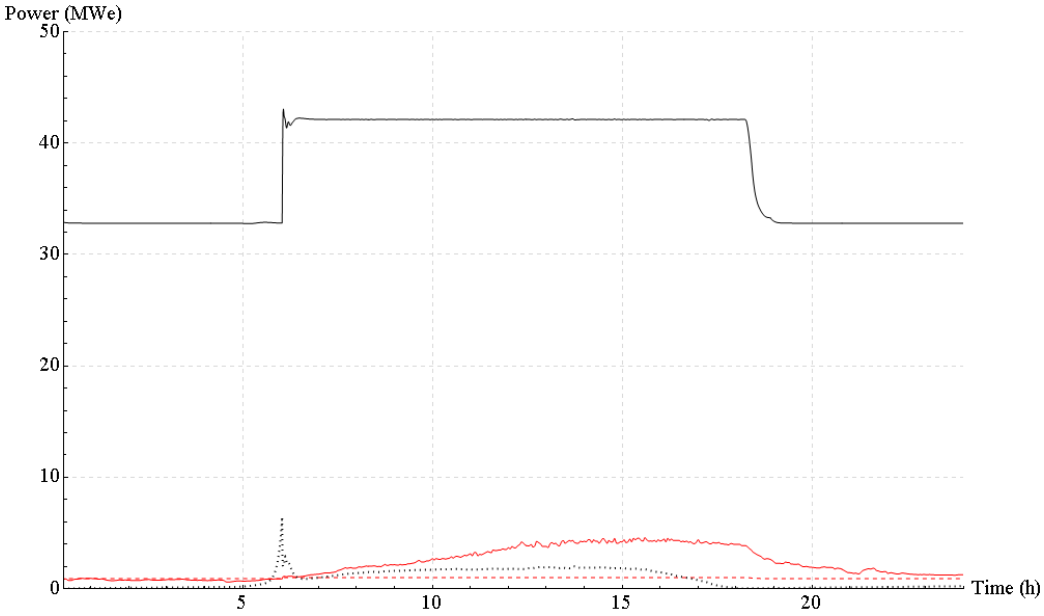

Figure 10.47: Gross electric power output (black) and parasitics (condenser fan power: Red solid, Feed water pump power: Red dashed, HTF pump power: Black dotted)

10.7.2.2 A diurnal simulation with discontinuous direct normal irradiance

This section presents simulations results providing almost identical environmental boundary conditions as model input as in Section 10.7.2.1, except that the direct normal irradiance is temporally blocked by passing clouds in the afternoon. This should give an example of the transients observed in the solar field and in the thermal energy storage system due to passing clouds.

The simulation results are very similar to those of the previous section until about 1:40 pm. From then on, 4 cloud passes occur (see 10.48). In Figure 10.50, it can be well seen how the solar field's outlet temperature control tries to keep the loop's outlet temperature at the given setpoint of 391 °C via adjusting the HTF mass flow rate accordingly.

The disturbance caused by the first cloud is quite well compensated, only causing a small deviation from the outlet temperature setpoint (see also Figure 10.49). Also the thermal load of the power block only features small deviations from the setpoint since the control of the thermal energy storage reduces the HTF charging mass flow rate (see Figure 10.52 and Figure 10.53 for a larger plot).

The second cloud, however, completely blocks the solar irradiance for

about 12 minutes, which causes a complete reduction in HTF mass flow rate in the solar field (see Figure 10.50). Consequently, the virtual plant operator starts to discharge the thermal energy storage system in order to keep the thermal load of the power block at the given setpoint. Figure 10.53 represents a larger view of the storage system's mass flow rates already presented in Figure 10.52. The HTF mass flow rate goes immediately up to its maximum value of 600 $\frac{kg}{s}$. However, within this short time frame of discharge operation, the thermal energy storage system is not able to achieve steady-state operation (full load discharge). As can be seen in Figure 10.55, which represents a larger view of the simulation results already given in Figure 10.54, the storage system's HTF outlet temperature fails to reach its design value of 376 °C, since the virtual plant operator switches from discharging to charging mode again as the cloud moves away. At the end of this second cloud pass, the direct normal irradiance dramatically increases from almost zero to slightly more than 900 $\frac{W}{m^2}$ again. This is the cause of a large change in HTF mass flow rate in the solar field, from zero to almost nominal load, which in turn causes a considerable overshoot of the collector loop's outlet temperature[21], clearly above the maximum allowed temperature of 400 °C (see Figure 10.49). Thus, there is room for improving the applied control methodology, by e.g. replacing the standard PI feedback control loop, having constant tuning parameters, with its adaptive counterpart. As already mentioned by Camacho et al. [53], the dynamic characteristics of the solar field vary significantly over the operating range, making it difficult to obtain acceptable overall performance with a fixed parameter PI controller. An adaptive control scheme copes much better with changes in plant dynamics than a standard fixed parameter controller [53].

Basically, a similar behavior can be observed for the third and the fourth cloud pass, causing major transients in the storage system's fluid circuit, far away from steady-state operation and nominal outlet temperatures. With the implemented control methodology it is impossible to keep the thermal load of the power block at its setpoint. Figure 10.56 shows remarkable setpoint deviations of the electric gross output due to the intermittent direct normal irradiance in the afternoon.

10.8 Conclusions

Chapter 10 of this work treats the implementation of a solar thermal power plant model on system level. In particular, an object-oriented and well struc-

[21] Note that the defocussing control has been deactivated for this simulation run, since the simulation results are difficult to interpret if many control loops are acting in parallel.

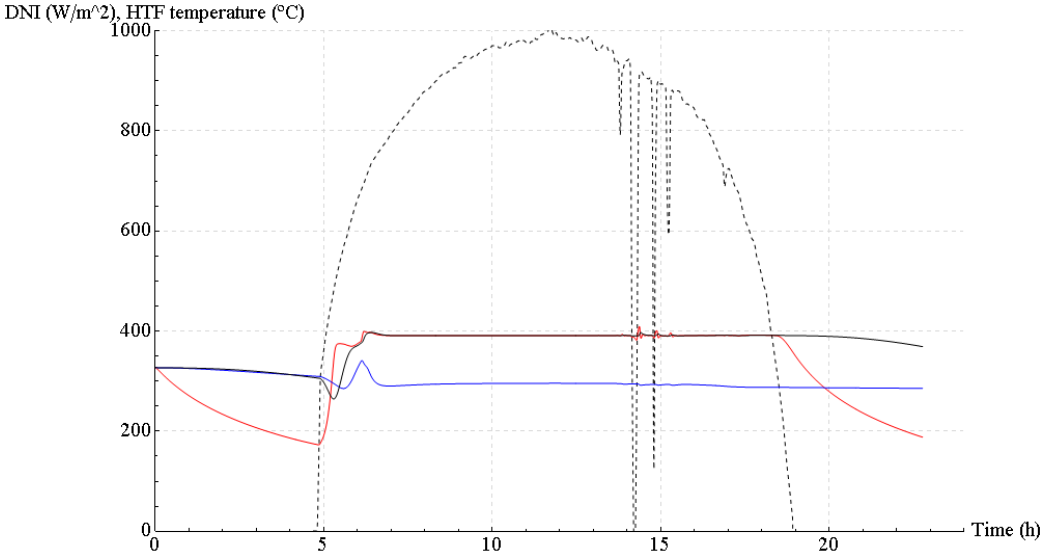

Figure 10.48: Direct normal irradiance (black dashed) on the 22nd of June (Desert Rock, Nevada, USA) and the simulated solar field HTF temperatures; Loop outlet temperature: Red, Loop inlet temperature: Blue, Solar field outlet temperature: Black solid

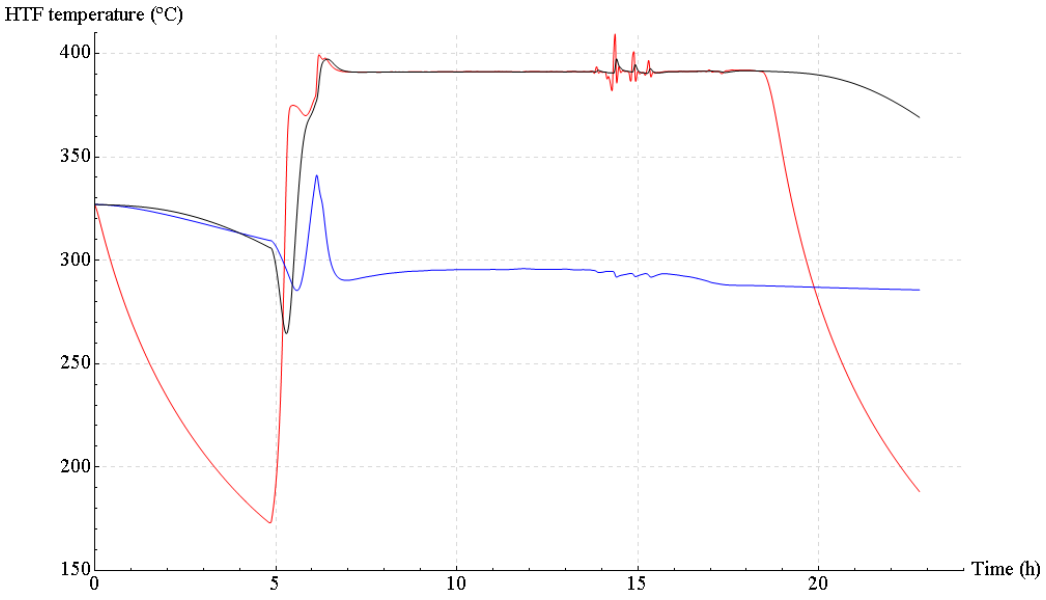

Figure 10.49: Simulated solar field HTF temperatures; Loop outlet temperature: Red, Loop inlet temperature: Blue, Solar field outlet temperature: Black

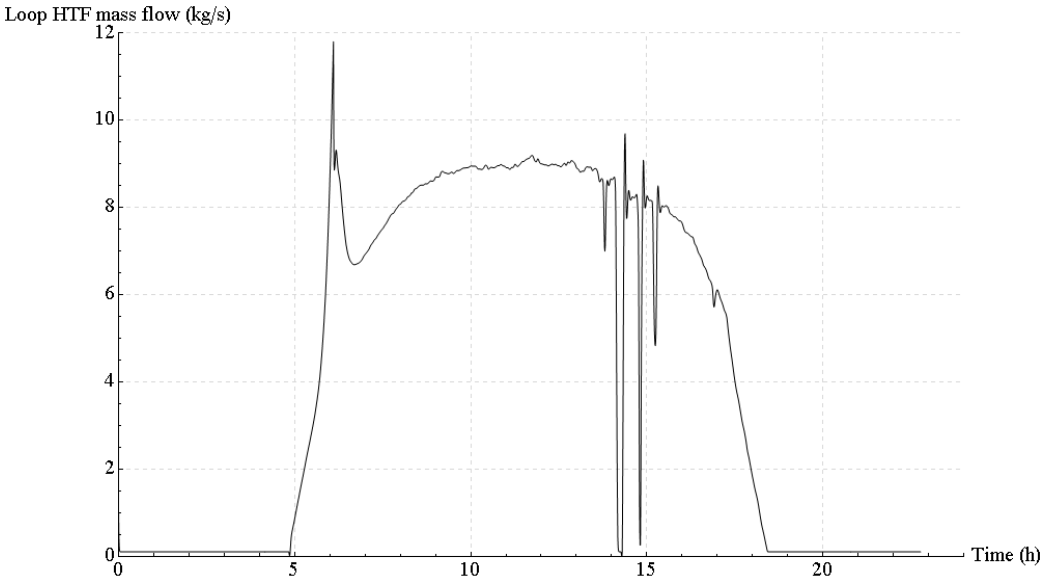

Figure 10.50: Simulated HTF mass flow rate per collector loop

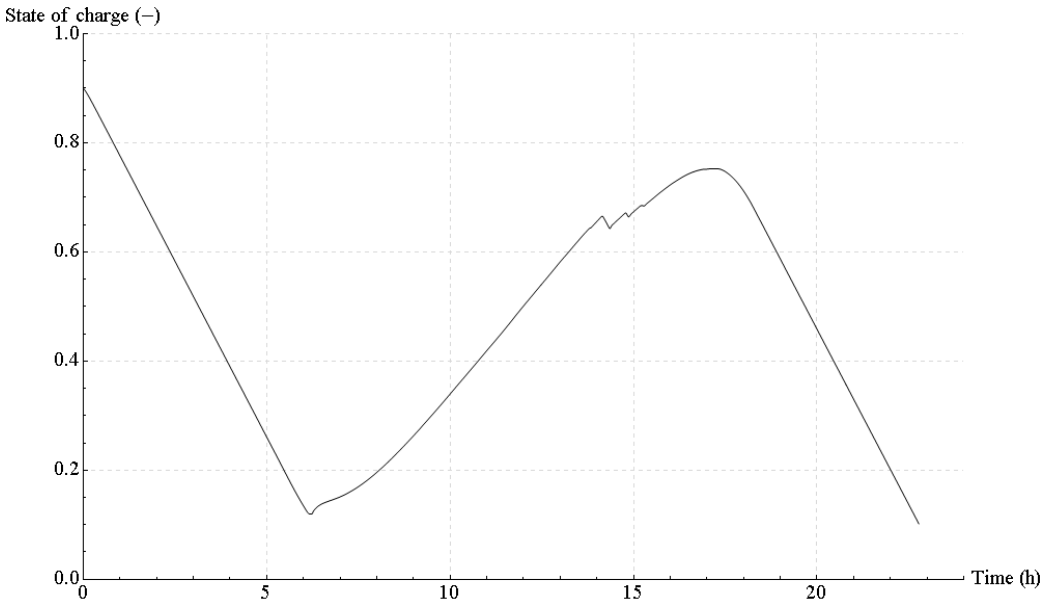

Figure 10.51: State of charge of the thermal energy storage system (1 = fully charged, zero = fully discharged)

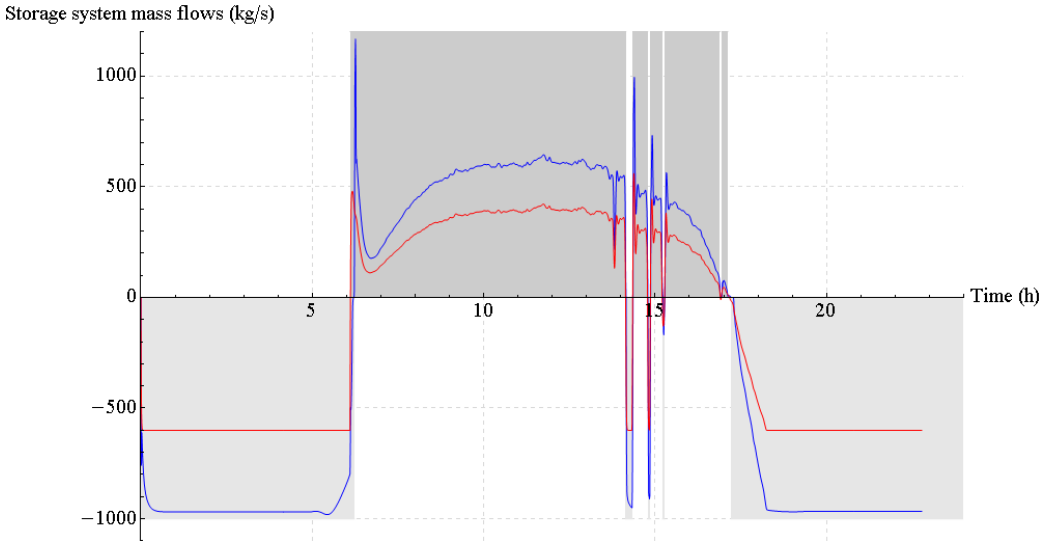

Figure 10.52: Mass flow rates of the thermal energy storage system; Thermal oil (HTF): Red, Molten salt: Blue, Charging: Positive, Discharging: Negative

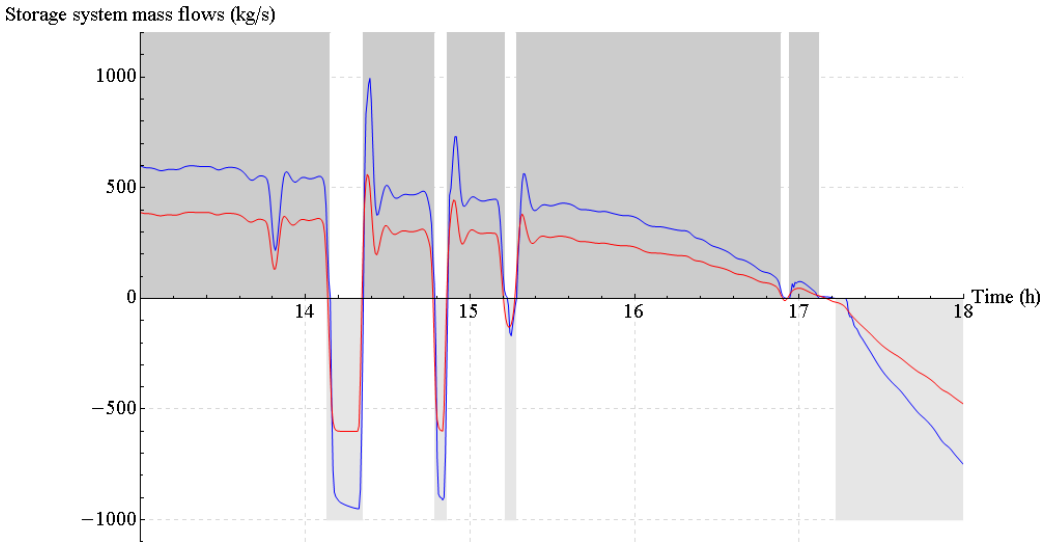

Figure 10.53: Mass flow rates of the thermal energy storage system; Thermal oil (HTF): Red, Molten salt: Blue, Charging: Positive, Discharging: Negative

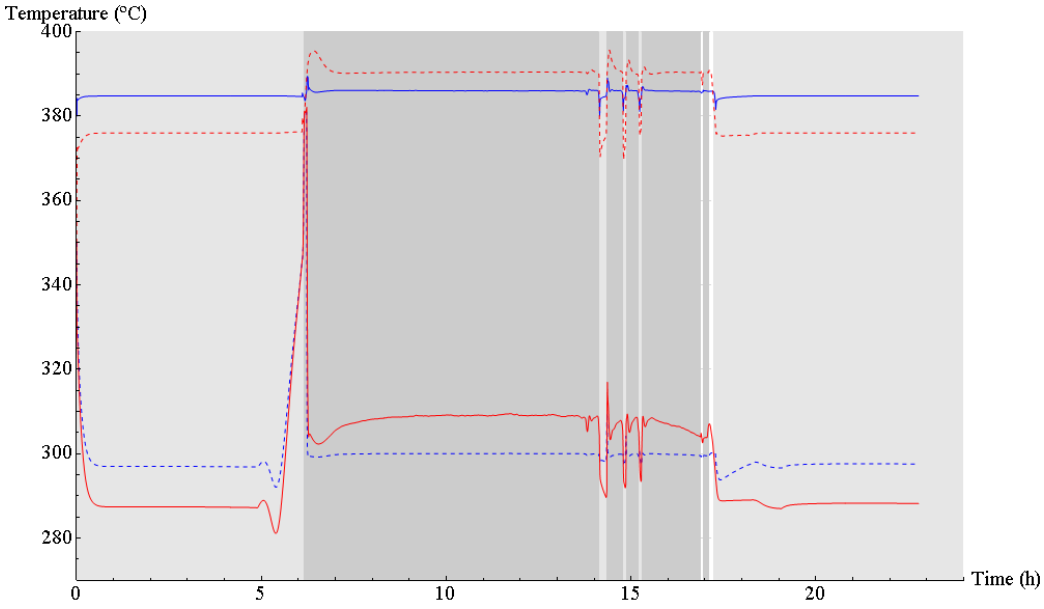

Figure 10.54: Temperatures at the oil-to-molten-salt heat exchanger's ends (outermost control volumes of both fluid ducts); Thermal oil (HTF): Red, Molten salt: Blue, Outlet temperatures during charging mode: Solid lines, Outlet temperatures during discharging mode: Dashed lines

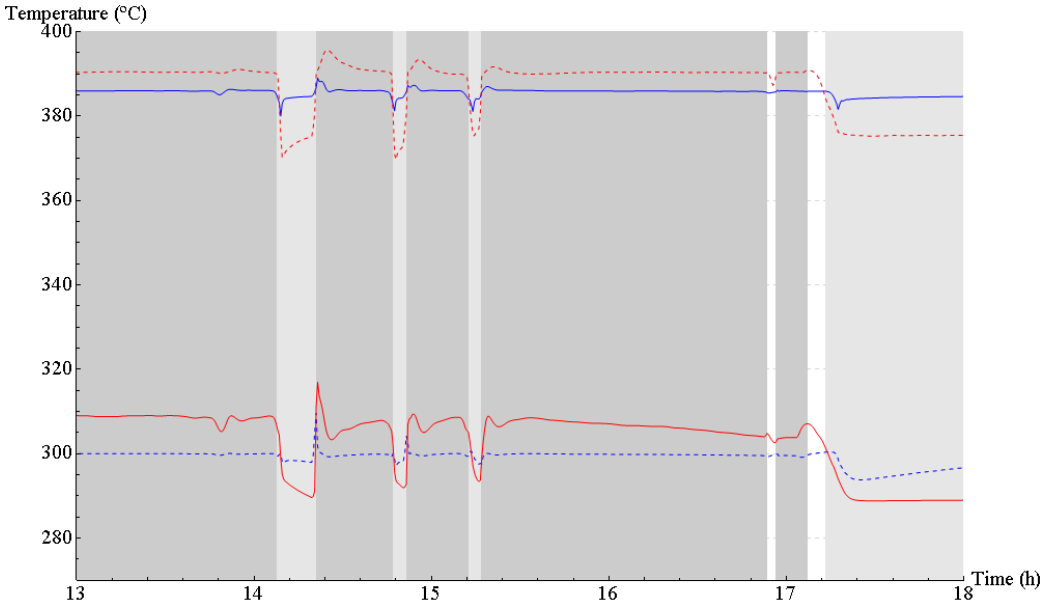

Figure 10.55: Temperatures at the oil-to-molten-salt heat exchanger's ends (outermost control volumes of both fluid ducts); Thermal oil (HTF): Red, Molten salt: Blue, Outlet temperatures during charging mode: Solid lines, Outlet temperatures during discharging mode: Dashed lines

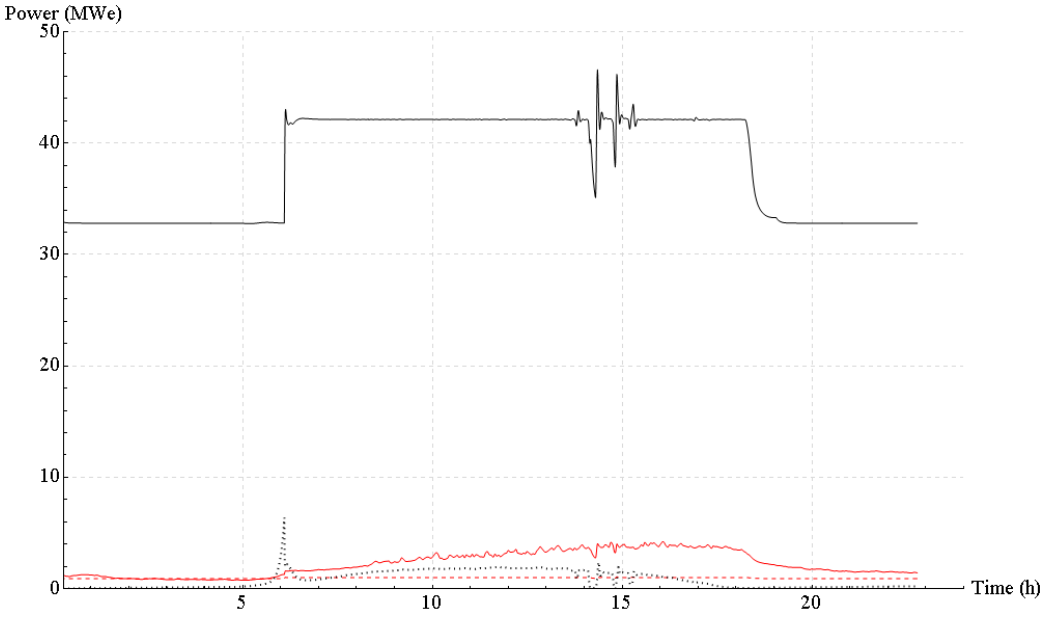

Figure 10.56: Gross electric power output (black) and parasitics (condenser fan power: Red solid, Feed water pump power: Red dashed, HTF pump power: Black dotted)

tured modeling concept is described, which is, in large part, based on non-causal models featuring true ordinary differential and algebraic equations, i.e. differential-algebraic equation (DAE) systems. Furthermore, the implementation in Modelica enables an incredible model flexibility and an efficient code structure, due to the re-declaration feature and the possibility of multiple inheritance.

As shown by the performed simulations in the previous sections, the operation of a solar thermal power plant is not a trivial task, since it is exposed to changing environmental boundary conditions, which is inherent to its principle. The establishment of reliable, efficient, and at the same time, safe operation strategies that maximize the power plants output on the one hand, but minimize fatigue (caused by, e.g., too large temperature gradients in critical components) on the other hand, is a must. Since the testing of alternative operation strategies at real power plants is expensive, and in risky cases, impossible, the development of transient performance models is essential.

The previous sections give an example for such a numerical model that is able to perform detailed transient performance simulations of a solar thermal power plant using PTCs. The model forms a valuable basis for improving

start-up and shut-down procedures. Additionally, it is useful for developing best practices regarding power plant operation strategies. In particular, it is important to establish operating directives and guidelines for normal operation as well as for emergency handling.

Finally, it has to be noted that despite the "initialization-friendly" implementation according to Section 10.6.1, the initialization of the power plant model that uses the transient steam generator model is still not at all an easy task. Even with very good variable initialization parameter settings, a Modelica tool may iterate for several minutes until finding the initial solution. This is definitely an issue that has to be solved in the future. There is the need for making the model more user-friendly.

Part IV

Conclusions and outlook

Part four of this work presents the main conclusions and gives recommendations for future work in that area.

Chapter 11

General conclusions

In the following, this work's main conclusions will be stated for each of the 3 parts, summarizing the most important facts and results obtained via the use of the described numerical models.

11.1 Conclusions of Part I - The state-of-the-art

Part I of this work has given a short introduction to concentrated solar power in general, and has then focused on the topic of thermal energy storage.

Thermal energy storage can be considered as the key advantage of solar thermal power plants over other renewable technologies (such as wind or photovoltaic power, which inherently depend on feasible electricity storage options)[1] as it represents an effective solution for harnessing solar energy, despite its highly fluctuating and inconstant nature. With the help of thermal energy storage, solar thermal power plants can provide dispatchable[2]

[1] In this context, it should be referred to possible options for storing electric energy, i.e. pumped hydro storage, compressed air energy storage, batteries, fly wheels, renewable fuels (hydrogen, natural gas) as well as supercapacitors [220, 221, 222, 223, 224, 225]. It has to be noted that recent advances in the conversion of electricity into natural gas [222] have made long-term storage and seasonal balancing of renewable energy sources technically feasible, in particular, providing a relatively large storage capacity. The conversion of electricity into natural gas offers the great possibility of feeding any type of renewable electricity (e.g. solar or wind power) into the existing natural gas infrastructure during times of high availability of renewable energy but low electricity demand, making it available for later use (which also implies the use of renewable natural gas for the transportation technology, i.e. natural gas powered vehicles) [222].

[2] Dispatchable power generation is referred to as operation according to the request of power grid operators. Thus, when sources of electricity are dispatched for frequency

power, which puts them on the same level as biomass and hydropower with reservoir. In principle, solar thermal power plants are also able to generate base load, provided that the solar multiple and the dimensions of the thermal energy storage system are adapted accordingly. In combination with the unquestionable abundant amount of solar energy incident on planet earth, solar thermal power plants represent a highly promising technology for providing a considerable fraction of tomorrow's electricity demand.

However, there is still a lot of research work left in order to do make solar thermal power plants more cost effective than conventional fossil fuel or nuclear power based technology. Obviously, down to the present day, this "cost effectiveness" does not consider irreversible long-term damages of both latter technologies.

There is, especially, much research work left in the area of thermal energy storage. Many of the proposed technologies are in their first stage of development and not yet ready for their application at commercial level. Nevertheless, the molten-salt-based active direct and active indirect two-tank thermal energy storage technology has successfully been introduced at commercial level in the recent years.

Considering the notable advances in computer technology within the last decades, the numerical modeling and simulation has become an indispensable tool when it comes to power plant design and preliminary assessment studies. Many established modeling methodologies can, of course, be directly applied to the evaluation of solar thermal power plants. However, in many areas completely new approaches are required and are not yet standardized. This especially holds for the evaluation of high-temperature thermal energy storage systems.

In particular, a new field of modeling has emerged from the fact that the performance evaluation of solar thermal power plants is strongly related to the environmental boundary conditions that significantly change over time (not only over one day, but also throughout the year). Thus, in order to evaluate the final yearly performance (e.g. in terms of net electricity production) of a specific plant, long-term simulations, with typical environmental boundary conditions as model input, are important. Creating a robust performance model of a solar power plant that runs stable, no matter what weather input data or operational strategy constraints are provided by the user, is not a trivial task. This especially holds for detailed transient performance models where the number of variables easily goes up to several thousands. It is thus important to optimize long-term performance models regarding their complexity and hence computational intensity.

regulation or load matching.

This work's objective has therefore been the modeling of the molten-salt-based two-tank thermal energy storage technology and the implementation of the proposed modeling approaches into a solar thermal power plant performance model on system level. There is a need for reliable performance models that enable the detailed consideration of operation and control strategies for solar thermal power plants.

11.2 Conclusions of Part II - Detailed examples and proposals of modeling approaches for the active direct and the active indirect two-tank TES concept

Part II, the main part of this work, considers the performance evaluation of the molten-salt-based two-tank thermal energy storage technology, considering the oil-to-molten-salt heat exchange process as well as the modeling of the molten salt storage tanks in detail.

Chapter 6 evaluates the performance of two different shell-and-tube[3] heat exchanger configurations. In particular, the behavior of a parallel-train setup is compared with the behavior of a single-train setup, having the same total area of heat transfer. In summary, the essential result obtained by this specific case study is, that the performance of the thermal energy storage system can be considerable improved by applying several heat exchanger trains in parallel instead of just one single correspondingly larger unit. The application of multiple heat exchanger trains in parallel reduces not only the nominal-load pressure drop, but also improves the thermal performance at low partial loads. It has to be emphasized that this is due to the fact that when having several heat exchanger trains in parallel, some can be put off-line at partial loads, enhancing the convective heat transfer coefficients, which clearly outweighs the reduction in total effective heat transfer area. This could especially be relevant for proposed high capacity solar thermal power plants, e.g., exceeding 100 MWe, where the two-tank concept is scaled up to a multiple of two-tank subunits.

Chapter 7 discusses the modeling of molten salt tanks for the two-tank heat storage concept. Emphasis is given on the analysis of the dominant sources of heat loss from the molten salt inventory to the environment. By

[3]Due to the required heat exchanger dimensions, typically, shell-and-tube heat exchanger trains, composed of several single subunits, are applied at the active indirect two-tank heat storage concept.

evaluating simulation results of the numerical model, it has been found that the dominant modes of heat transfer between the molten salt inventory and the tank's inner steel jacket are, on the one hand, the convective heat transfer at the wetted inner steel surfaces, and on the other hand, the radiative heat transfer between the molten salt surface and the non-wetted inner steel surfaces. The convective heat loss via the gas atmosphere above the molten salt surface does not have to be modeled in particular, since it has a negligible impact on the achieved accuracy of the model. Furthermore, the convective heat transfer coefficients between the molten salt and the wetted inner steel surfaces do not vary considerably. They may be set to the constant values. The storage tank's outer surface temperature, and therefore the absorbed solar irradiation, the wind speed, as well as the ambient air temperature, influence the heat loss significantly. For example, by neglecting the incident solar irradiation in the model, errors in temperature drop estimates of up to 5.6% may be introduced. Thus, a good approximation of the heat transfer at the tank's exterior surface is strongly recommended in order to correctly estimate the exterior surface temperature and consequently define a reasonable temperature difference for the heat flow through the walls. Assuming constant convective heat transfer coefficients at the tank's inner steel jacket and neglecting the heat exchange with the tank's gas atmosphere, reduces the complexity of the model considerable, making it ideal for CSP performance simulations on system level.

Chapter 8 focuses on the transient numerical modeling of multi-pass shell-and-tube heat exchangers that apply single-phase fluids. A one-dimensional modeling approach is used for the heat exchanger ducts. The governing partial differential equations are solved numerically by applying the finite volume method. In particular, the commonly applied cell-method is used, which is presented in a flexible, intuitive and simulation-platform-independent way. Applying the presented methodology subsequently to a typical shell-and-tube heat exchanger train as currently applied at CSP active indirect two-tank heat storage systems, yielded characteristic process parameters such as process gain, dead time and time constant at nominal as well as at partial loads. As expected, typical first-order-plus-time-delay behavior was observed. By comparing the detailed shell-and-tube heat exchanger model (that considers the real, rather complex flow setup of a TEMA-F type heat exchanger) with a simplified model only considering an equivalent axial double-pipe heat exchanger setup in counter-flow arrangement, has shown that the difference in simulation results is relatively small when using a sufficiently large number of discrete sections in the direction of flow. In particular, a spatial resolution of about 0.75 m in axial direction represents a good trade-off between computational effort and accuracy, introducing errors in outlet temperature estimates

of about 1.1 °C, which is about 1.2% based on a typical temperature difference of 94 °C along the heat exchanger's fluid duct length (shell side). Thus, it can be concluded that it is sufficiently accurate to only consider an ideal pure counter-flow model setup for CSP performance simulations on system level where the reduction in model complexity is important since fast models are desired.

Finally, Chapter 9 combines the models developed in Chapters 7 and 8, and focuses on the transient response simulation of an entire active indirect two-tank thermal energy storage system during changes in operating mode. Applying standard PI feedback control loops with tuning parameters according to Chien-Hrones-Reswick [193] showed that there are certain limitations regarding the storage system's charging and discharging performance during abrupt changes in operating mode, due to the thermal inertia of the storage system's fluid circuit. Hence, in order to store as much solar energy as possible, and to provide the power block with a continuous thermal power input regardless of fluctuations in current solar irradiance, control methodologies should be optimized and small HTF buffer storage is crucial.

11.3 Conclusions of Part III - A parabolic trough collector power plant model on system level

Part III of this work (Chapter 10) describes a transient parabolic trough collector power plant model on system level and presents its numerical simulation. In particular, it applies the simplified thermal energy storage model components as discussed in Chapter 7 and Chapter 8 of this work. An object-oriented and well structured modeling concept is used, which is, in large part, based on non-causal models featuring true ordinary differential and algebraic equations, i.e. differential-algebraic equation (DAE) systems. The specific implementation in Modelica enables an incredible model flexibility and an efficient code structure due to the re-declaration feature and the possibility of multiple inheritance.

The discussed model forms a valuable basis for detailed transient performance simulations of a solar thermal power plant. It is thus possible to evaluate start-up and shut-down procedures. Additionally, it is useful for developing best practices regarding power plant operation strategies. In particular, it is important to establish operating directives and guidelines for normal operation as well as for emergency handling.

In general, the operation of a solar thermal power plant is not a trivial

task since it is exposed to highly variable environmental boundary conditions, which is, however, inherent to its physical principle. Given that the testing of alternative operation strategies at real power plants is expensive, and in risky cases, impossible, the development of transient performance models is essential.

Chapter 12

Scientific contributions evolved from this thesis

Part II of this work is for the most part based on 2 scientific articles published at the SolarPACES conferences in 2012 (Marrakesh, Morocco) and 2013 (Las Vegas, USA), as well as 2 journal articles originally published in "Solar Energy" and "Energy":

- F. Zaversky, R. Medina, J. García-Barberena, M. Sánchez, and D. Astrain, 2012: Part load behavior of oil-to-molten-salt heat exchanger configurations for active indirect heat storage systems in CSP applications, SolarPACES, Marrakech, Morocco
- F. Zaversky, J. García-Barberena, M. Sánchez, and D. Astrain, 2013: Transient molten salt two-tank thermal storage modeling for CSP performance simulations, in: Solar Energy, volume 93:pp. 294–311
- F. Zaversky, M. M. Rodríguez-García, J. García-Barberena, M. Sánchez, and D. Astrain, 2014: Transient behavior of an active indirect two-tank thermal energy storage system during changes in operating mode – An application of an experimentally validated numerical model, in: Energy Procedia
- F. Zaversky, M. Sánchez, and D. Astrain, 2014: Object-oriented modeling for the transient response simulation of multi-pass shell-and-tube heat exchangers as applied in active indirect thermal energy storage systems for concentrated solar power, in: Energy, volume 65:pp. 647-664

Furthermore, Chapter 10.2.1 (in Part III) of this work is a corrected republication of the following article originally published in Elsevier's journal "Solar Energy":

- F. Zaversky, R. Medina, J. García-Barberena, M. Sánchez, and D. Astrain, 2013: Object-oriented modeling for the transient performance simulation of parabolic trough collectors using molten salt as heat transfer fluid, in: Solar Energy, volume 95:pp. 192–215

Chapter 13

Outlook and recommendations for future work

This work has mainly been focused on the development of transient models for the performance simulation of the active indirect two-tank heat storage concept. Additionally to this, Part III has given an example for the integration and usage of the developed models describing a comprehensive model of a parabolic trough collector power plant on system level. Thus, the task of future work is clearly the detailed application in order to, e.g., elaborate operating guidelines and control strategies that improve the performance of real plants.

Hence, recommendations for future work are, for instance, related to the implementation of advanced control methodologies, not only for the solar field control[1], but also for the control of the thermal energy storage system or the thermal load control of the power block. A detailed consideration of related control methodologies and their optimization has been beyond the scope of the present thesis. For example, one of the outcomes of the presented simulations has been that the applied start-up procedure of the solar field has clearly room for improvement regarding the necessary HTF pumping power. Thus, Chapter 10 only presents demonstrative simulation examples, applying basic operation strategies. Clearly, future works may build upon these settings and propose more efficient operating methods, which could lead to considerable improvements at real power plants.

Additionally, partial shading of the solar field or scattering of performance parameters of solar collectors could be considered in future works. Here, an extension of the presented solar field model would be necessary. Instead

[1] In this context, it has to be emphasized that the advanced control of distributed solar collector fields has already been treated in detail in previous works [53, 54, 55].

of the single representative collector loop, the solar field model would have to be composed of several representative loops, depending on the needed resolution.

Furthermore, different thermal energy storage concepts could be considered in the model, comparing them in terms of transient performance, especially regarding rapid changes in load that are crucial for efficient and safe power plant operation throughout days with highly fluctuating solar direct irradiance.

In many areas, the technology of solar thermal power plants is still in its early stage of development, leaving plenty of room for future research work.

As a closing remark, I strongly encourage engineers and especially politics to take concentrated solar power to its deserved level of competitiveness on the power market as soon as possible. It is clear that mankind has only one choice in order to guarantee an acceptable quality of life for everybody in the long run - *It is the large-scale capture, conversion and usage of solar energy!*

List of Figures

List of Tables

Bibliography

[1] D. Abbott, 2010: *Keeping the energy debate clean: How do we supply the world's energy needs?*, in: Proceedings of the IEEE, volume 98(1):pp. 42–66

[2] A. Fernández-García, E. Zarza, L. Valenzuela, and M. Pérez, 2010: *Parabolic-trough solar collectors and their applications*, in: Renewable and Sustainable Energy Reviews, volume 14:pp. 1695–1721

[3] A. Gil, M. Medrano, I. Martorell, A. Lázaro, P. Dolado, B. Zalba, and L. Cabeza, 2010: *State of the art on high temperature thermal energy storage for power generation. Part 1—Concepts, materials and modellization*, in: Renewable and Sustainable Energy Reviews, volume 14:pp. 31–55

[4] H. Michels and R. Pitz-Paal, 2007: *Cascaded latent heat storage for parabolic trough solar power plants*, in: Solar Energy, volume 81:pp. 829–837

[5] K. Williges, J. Lilliestam, and A. Patt, 2010: *Making concentrated solar power competitive with coal: The costs of a European feed-in tariff*, in: Energy Policy, volume 38:pp. 3089–3097

[6] M. Romero-Alvarez, E. Zarza, F. Kreith, and D. Goswami, 2007: *Handbook of Energy Efficiency and Renewable Energy*, CRC Press Taylor and Francis Group, Boca Raton, USA

[7] J. A. Duffie and W. A. Beckman, 2006: *Solar engineering of thermal processes*, John Wiley and Sons, Inc., Hoboken, New Jersey, USA, 3rd edition

[8] R. Winston, J. C. Miñano, and P. Benítez, 2005: *Nonimaging optics*, Elsevier Academic Press Inc., Burlington, MA 01803, USA

[9] M. Bolinger and S. Weaver, 2013: *Utility-scale solar 2012 - An empirical analysis of project cost, performance, and pricing trends in the united states*, Environmental Energy Technologies Division, Lawrence Berkeley National Laboratory, USA

[10] roka34, 2012: *A broad view of parabolic trough solar collectors at Kramer Junction in the Mojave desert in California*, http://www.flickr.com (accessed 20.11.2013)

[11] The-Dow-Chemical-Company, 2001: *Dowtherm A - synthetic organic heat transfer fluid — liquid and vapor phase data*, The-Dow-Chemical-Company, http://www.dow.com (accessed 27.7.2012)

[12] Solutia-Inc., 2008: *Therminol VP-1 Heat Transfer Fluid by Solutia - Vapor Phase, Liquid Phase Heat Transfer Fluid (Technical Bulletin 7239115C)*, Solutia Inc., St. Louis, Missouri, USA

[13] D. Kearney, U. Herrmann, P. Nava, B. Kelly, R. Mahoney, J. E. Pacheco, R. Cable, N. Potrovitza, D. Blake, and H. Price, 2003: *Assessment of a molten salt heat transfer fluid in a parabolic trough solar field*, in: Journal of Solar Energy Engineering, volume 125:pp. 170–176

[14] G. Cau, D. Cocco, and V. Tola, 2012: *Performance and cost assessment of Integrated Solar Combined Cycle Systems (ISCCSs) using CO2 as heat transfer fluid*, in: Solar Energy, volume 86:pp. 2975–2985

[15] C. Richter, S. Teske, and R. Short, 2009: *Concentrating Solar Power – Global Outlook 09 – Why Renewable Energy is Hot*, Greenpeace International, Amsterdam, The Netherlands

[16] K. Strauss, 2006: *Kraftwerkstechnik zur Nutzung fossiler, nuklearer und regenerativer Energiequellen*, Springer-Verlag, Berlin (Germany), 5th edition

[17] M. Eck and T. Hirsch, 2007: *Dynamics and control of parabolic trough collector loops with direct steam generation*, in: Solar Energy, volume 81:pp. 268–279

[18] T. Johansson, H. Kelly, A. Reddy, and R. Williams, 1992: *Renewable Energy, Sources for Fuels and Electricity*, Islandpress, Washington DC, USA

[19] M. J. Montes, A. Abánades, and J. M. Martínez-Val, 2009: *Performance of a direct steam generation solar thermal power plant for electricity production as a function of the solar multiple*, in: Solar Energy, volume 83:pp. 679–689

[20] S. Odeh, G. Morrison, and M. Behnia, 1998: *Performance of Horizontal and Inclined Direct Steam Generation Trough Solar Collectors*, pp. 588–595, ANZSES 36th Annual Conference, Christchurch, New Zealand

[21] T. Hirsch, F. Feldhoff, K. Hennecke, and R. Pitz-Paal, 2014: *Advancements in the field of direct steam generation in linear solar concentrators - A review*, in: Heat Transfer Engineering, volume 35(3):pp. 258–271

[22] D. Mills and G. Morrison, 2000: *Compact Linear Fresnel Reflector Solar Thermal Power Plants*, in: Solar Energy, volume 68:pp. 263–283

[23] D. J. Reynolds, M. Behnia, and G. L. Morrison, 2002: *A Hydrodynamic Model for a Line-Focus Direct Steam Generation Solar Collector*, Solar 2002 - Australian New Zealand Solar Energy Society, Newcastle

[24] M. Mertins, 2009: *Technische und wirtschaftliche Analyse von horizontalen Fresnel-Kollektoren, PhD Thesis*, Universität Karlsruhe, http://digbib.ubka.uni-karlsruhe.de/volltexte/documents/1067166 (accessed: 31.10.2013)

[25] S. Bockamp, T. Griestop, M. Fruth, M. Ewert, H. Lerchenmüller, M. Mertins, G. Morin, A. Häberle, and D. J., 2003: *Solar Thermal Power Generation*, PowerGen Europe, Düsseldorf, Germany

[26] C. K. Ho and B. D. Iverson, 2014: *Review of high-temperature central receiver designs for concentrating solar power*, in: Renewable and Sustainable Energy Reviews, volume 29:pp. 835–846

[27] Wikipedia, 2013: *Stirling engine*, http://en.wikipedia.org (accessed 12.11.2013)

[28] D. Laing, W. Schiel, and P. Heller, 2002: *Dish-Stirling-Systeme - Eine Technologie zur dezentralen solaren Stromerzeugung*, FVS Themen 2002, Jahrestagung des Forschungs-Verbunds Sonnenenergie, Stuttgart, Germany

[29] SimTech-Simulation-Technology, 2011: *IPSEpro - Integrated Process Simulation Environment*, http://www.simtechnology.com (accessed 30.4.2013)

[30] J. D. Pye, 2008: *System modelling of the compact linear Fresnel reflector - PhD Thesis*, University of New South Wales, Australia

[31] S. S. Sahoo, S. Singh, and R. Banerjee, 2012: *Analysis of heat loss from a trapezoidal cavity used for Linear Fresnel Reflector system*, in: Solar Energy, volume 86:pp. 1313–1322

[32] F. Zaversky, J. García-Barberena, M. Sánchez, and D. Astrain, 2012: *Probabilistic modeling of a parabolic trough collector power plant - An uncertainty and sensitivity analysis*, in: Solar Energy, volume 86:pp. 2128–2139

[33] M. J. Blanco, A. Mutuberria, A. Monreal, and R. Albert, 2011: *Results of the empirical validation of Tonatiuh at Mini-Pegase CNRS-PROMES facility*, SolarPACES, Granada, Spain

[34] F. Zaversky, R. Medina, J. García-Barberena, M. Sánchez, and D. Astrain, 2013: *Object-oriented modeling for the transient performance simulation of parabolic trough collectors using molten salt as heat transfer fluid*, in: Solar Energy, volume 95:pp. 192–215

[35] M. W. Edenburn, 1976: *Performance analysis of a cylindrical parabolic focusing collector and comparison with experimental results*, in: Solar Energy, volume 18:pp. 437–444

[36] J. A. Clark, 1982: *An analysis of the technical and economic performance of a parabolic trough concentrator for solar industrial process heat application*, in: International Journal of Heat and Mass Transfer, volume 25(9):pp. 1427–1438

[37] F. Lippke, 1995: *Simulation of the part-load behavior of a 30 MWe SEGS plant*, Sandia National Laboratories, Solar Thermal Technology Department, Albuquerque, New Mexico 87185

[38] N. Fraidenraich, J. M. Gordon, and R. d. C. Fernandes de Lima, 1997: *Improved solutions for temperature and thermal power delivery profiles in linear solar collectors*, in: Solar Energy, volume 61(3):pp. 141–145

[39] S. Odeh, G. Morrison, and M. Behnia, 1998: *Modelling of parabolic trough direct steam generation solar collectors*, in: Solar Energy, volume 62(6):pp. 395–406

[40] S. A. Jones, R. Pitz-Paal, N. Blair, and R. Cable, 2001: *TRNSYS modeling of the SEGS VI parabolic trough solar electric generating system*, Solar Forum 2001: Solar Energy: The Power to Choose, Washington, DC, USA

[41] R. Forristall, 2003: *Heat transfer analysis and modeling of a parabolic trough solar receiver implemented in Engineering Equation Solver, NREL/TP-550-169*, NREL - National Renewable Energy Laboratory, Golden, Colorado, USA

[42] A. M. Patnode, 2006: *Simulation and performance evaluation of parabolic trough solar power plants - Master's Thesis*, University of Wisconsin-Madison, USA

[43] J. Rheinländer, S. Bergmann, and M. R. Erbes, 2008: *Technical and economic performance of parabolic trough solar power plants - A computational tool for plant feasibility studies*, SolarPACES, Las Vegas, USA

[44] M. M. Rolim, N. Fraidenraich, and C. Tiba, 2009: *Analytic modeling of a solar power plant with parabolic linear collectors*, in: Solar Energy, volume 83:pp. 126–133

[45] T. Larraín, R. Escobar, and J. Vergara, 2010: *Performance model to assist solar thermal power plant siting in northern Chile based on backup fuel consumption*, in: Renewable Energy, volume 35:pp. 1632–1643

[46] G. Manzolini, A. Giostri, C. Saccilotto, P. Silva, and E. Macchi, 2011: *Development of an innovative code for the design of thermodynamic solar power plants part A: Code description and test case*, in: Renewable Energy, volume 36:pp. 1993–2003

[47] G. Manzolini, A. Giostri, C. Saccilotto, P. Silva, and E. Macchi, 2012: *A numerical model for off-design performance prediction of parabolic trough based solar power plants*, in: Journal of Solar Energy Engineering, volume 134:pp. 011003–1 – 011003–10

[48] V. E. Dudley, G. J. Kolb, R. Mahoney, T. Mancini, C. Matthews, M. Sloan, and D. Kearney, 1994: *Test results: SEGS LS-2 solar collector SAND94-1884*, Sandia National Laboratories, Albuquerque, New Mexico, USA

[49] I. L. García, J. L. Álvarez, and D. Blanco, 2011: *Performance model for parabolic trough solar thermal power plants with thermal storage:*

Comparison to operating plant data, in: Solar Energy, volume 85:pp. 2443–2460

[50] S. Bergmann, J. Rheinländer, and M. R. Erbes, 2011: *Transient performance modeling of a CSP plant with cascaded sensible and latent TES subsystems*, SolarPACES, Granada, Spain

[51] A. G. Rossi, A. Maggi, and M. Falchetta, 2011: *Modeling of a typical molten salt based ISCC plant*, SolarPACES, Granada, Spain

[52] J. Spelling, M. Jöcker, and A. Martin, 2012: *Annual performance improvement for solar steam turbines through the use of temperature-maintaining modifications*, in: Solar Energy, volume 86:pp. 496–504

[53] E. F. Camacho, M. Berenguel, and F. R. Rubio, 1997: *Advanced control of solar plants*, Springer-Verlag, Berlin-Heidelberg

[54] E. F. Camacho, F. R. Rubio, M. Berenguel, and L. Valenzuela, 2007: *A survey on control schemes for distributed solar collector fields. Part I: Modeling and basic control approaches*, in: Solar Energy, volume 81:pp. 1240–1251

[55] E. F. Camacho, F. R. Rubio, M. Berenguel, and L. Valenzuela, 2007: *A survey on control schemes for distributed solar collector fields. Part II: Advanced control approaches*, in: Solar Energy, volume 81:pp. 1252–1272

[56] A. Meaburn and F. M. Hughes, 1993: *Resonance characteristics of distributed solar collector fields*, in: Solar Energy, volume 51:pp. 215–221

[57] S. Zunft, 1995: *Temperature control of a distributed collector field*, in: Solar Energy, volume 55(4):pp. 321–325

[58] T. Stuetzle, N. Blair, J. W. Mitchell, and W. A. Beckman, 2004: *Automatic control of a 30 MWe SEGS VI parabolic trough plant*, in: Solar Energy, volume 76:pp. 187–193

[59] L. Valenzuela, E. Zarza, M. Berenguel, and E. F. Camacho, 2006: *Control scheme for direct steam generation in parabolic troughs under recirculation operation mode*, in: Solar Energy, volume 80:pp. 1–17

[60] T. Hirsch, W. D. Steinmann, and M. Eck, 2005: *Simulation of transient two-phase flow in parabolic trough collectors using Modelica*, pp.

403–412, Proceedings of the 4th International Modelica Conference, Hamburg, Germany

[61] M. Gálvez-Carrillo, R. De Keyser, and C. Ionescu, 2009: *Nonlinear predictive control with dead-time compensator: Application to a solar power plant*, in: Solar Energy, volume 83:pp. 743–752

[62] L. J. Yebra, M. Berenguel, S. Dormido, and E. Zarza, 2008: *Object oriented modelling and simulation of parabolic trough collectors with Modelica*, in: Mathematical and Computer Modelling of Dynamical Systems: Methods, Tools and Applications in Engineering and Related Sciences, (14:4):pp. 361–375

[63] L. J. Yebra, M. Berenguel, J. Bonilla, L. Roca, S. Dormido, and E. Zarza, 2010: *Object-oriented modelling and simulation of ACUREX solar thermal power plant*, in: Mathematical and Computer Modelling of Dynamical Systems: Methods, Tools and Applications in Engineering and Related Sciences, pp. 211–224

[64] K. M. Powell and T. F. Edgar, 2012: *Modeling and control of a solar thermal power plant with thermal energy storage*, in: Chemical Engineering Science, volume 71:pp. 138–145

[65] Z.-D. Cheng, Y.-L. He, J. Xiao, Y. B. Tao, and R. J. Xu, 2010: *Three-dimensional numerical study of heat transfer characteristics in the receiver tube of parabolic trough solar collector*, in: International Communications in Heat and Mass Transfer, volume 37:pp. 782–787

[66] Y.-L. He, J. Xiao, Z.-D. Cheng, and Y.-B. Tao, 2011: *A MCRT and FVM coupled simulation method for energy conversion process in parabolic trough solar collector*, in: Renewable Energy, volume 36:pp. 976–985

[67] M. Wirz, M. Roesle, and A. Steinfeld, 2012: *Three-dimensional optical and thermal numerical model of solar tubular receivers in parabolic trough concentrators*, in: Journal of Solar Energy Engineering, volume 134:pp. 041012–1 – 041012–9

[68] R. V. Padilla, G. Demirkaya, D. Goswami, E. Stefanakos, and M. M. Rahman, 2011: *Heat transfer analysis of parabolic trough solar receiver*, in: Applied Energy, volume 88:pp. 5097–5110

[69] D. Laing, W. D. Steinmann, R. Tamme, and C. Richter, 2006: *Solid media thermal storage for parabolic trough power plants*, in: Solar Energy, volume 80:pp. 1283–1289

[70] S. Relloso and Y. Gutiérrez, 2008: *Real Application of Molten Salt Thermal Storage to Obtain High Capacity Factors in Parabolic Trough Plants*, SolarPACES, Las Vegas, USA

[71] M. J. Hale, 2000: *Subcontractor Report - Survey of Thermal Storage for Parabolic Trough Power Plants*, NREL, National Renewable Energy Laboratory, Golden, Colorado 80401-3393, USA

[72] L. Martín, L. F. Zarzalejo, J. Polo, R. Navarro, Ana Marchante, and M. Cony, 2010: *Prediction of global solar irradiance based on time series analysis: Application to solar thermal power plants energy production planning*, in: Solar Energy, volume 84:pp. 1772–1781

[73] L. Chang, L. Feng, M. Lai-Peng, and C. Hui-Ming, 2010: *Advanced Materials for Energy Storage*, in: Advanced Materials, volume 22:pp. E28–E62

[74] Z. Yang and S. V. Garimella, 2010: *Thermal analysis of solar thermal energy storage in a molten-salt thermocline*, in: Solar Energy, volume 84:pp. 974–985

[75] J. E. Pacheco, S. K. Showalter, and W. J. Kolb, 2002: *Development of a molten-salt thermocline thermal storage system for parabolic trough plants*, in: Journal of Solar Energy Engineering, volume 124:pp. 153–159

[76] A. Kofler, 1955: *Mikrothermoanalyse des Systems NaNO3-KNO3*, in: Monatshefte für Chemie - Chemical Monthly, volume 86:pp. 643–652

[77] R. W. Bradshaw and R. W. Carling, 1987: *A review of the chemical and physical properties of molten alkali nitrate salts and their effect on materials used for solar central receivers - SAND87-8005*, Sandia National Laboratories, Albuquerque, New Mexico, USA

[78] J. E. Pacheco, S. K. Showalter, and W. J. Kolb, 2001: *Development of a molten-salt thermocline thermal storage system for parabolic trough plants*, Solar Forum 2001 Solar Energy: The Power to Choose, Washington, DC

[79] M. Medrano, A. Gil, I. Martorell, X. Potau, and L. F. Cabeza, 2010: *State of the art on high-temperature thermal energy storage for power generation. Part 2 - Case studies*, in: Renewable and Sustainable Energy Reviews, volume 14:pp. 56–72

[80] U. Herrmann, B. Kelly, and H. Price, 2004: *Two-tank molten salt storage for parabolic trough solar power plants*, in: Energy, volume 29:pp. 883–893

[81] J. E. Pacheco, R. W. Bradshaw, D. B. Dawson, W. De la Rosa, R. Gilbert, S. H. Goods, M. J. Hale, P. Jacobs, S. A. Jones, G. J. Kolb, M. R. Prairie, H. E. Reilly, S. K. Showalter, and L. L. Vant-Hull, 2002: *Final Test and Evaluation Results from the Solar Two Project*, Sandia National Laboratories, Albuquerque, USA

[82] Abengoa-Solar, 2011: *Solúcar Platform - PS10: The first commercial tower of the world*, Abengoa Solar, Sevilla, Spain, http://www.abengoasolar.com (accessed 24.05.2011)

[83] A. F. Baker, S. E. Faas, L. G. Radosevich, A. C. Skinrood, J. Peire, M. Castro, and J. L. Presa, 1989: *U.S. - SPAIN Joint Evaluation of the Solar One and CESA-I Receiver and Storage Systems*, National Technical Information Service, Springfield, VA 22161, USA

[84] S. Flueckiger, Z. Yang, and S. V. Garimella, 2013: *Review of molten-salt thermocline tank modeling for solar thermal energy storage*, in: Heat Transfer Engineering, volume 34(10):pp. 787–800

[85] U. Herrmann, M. Geyer, and D. Kearney, 2002: *Overview on Thermal Storage Systems*, FLABEG Solar International GmbH, Workshop on Thermal Storage for Trough Power Systems

[86] D. Laing, C. Bahl, T. Bauer, D. Lehmann, and W. D. Steinmann, 2011: *Thermal energy storage for direct steam generation*, in: Solar Energy, volume 85:pp. 627–633

[87] K. Hennecke, P. Schwarzbözl, S. Alexopoulos, J. Göttsche, B. Hoffschmidt, M. Beuter, G. Koll, and T. Hartz, 2008: *Solar power tower Jülich - The first test and demonstration plant for open volumetric receiver technology in Germany*, SolarPACES, Las Vegas, USA

[88] M. Hänchen, S. Brückner, and A. Steinfeld, 2011: *High-temperature thermal storage using a packed bed of rocks - Heat transfer analysis*

and experimental validation, in: Applied Thermal Engineering, volume 31:pp. 1798–1806

[89] H. W. Fricker, 2004: *Regenerative thermal storage in atmospheric air system solar power plants*, in: Energy, volume 29:pp. 871–881

[90] D. Laing, W. D. Steinmann, P. Viebahn, F. Gräter, and C. Bahl, 2008: *Economic analysis of modular storage operation concepts and life cycle assessment of concrete thermal energy storage for parabolic trough power plants*, SolarPACES, Las Vegas, USA

[91] D. Laing and C. Bahl, 2008: *Concrete storage for solar thermal power plants and industrial process heat*, IRES III, 3rd International Renewable Energy Storage Conference, Berlin, Germany

[92] I. Fernández, C. J. Renedo, S. Pérez, J. Carcedo, and M. Mañana, 2010: *Advances in phase change materials for thermal solar power plants Quality*, International Conference on Renewable Energies and Power Quality (ICREPQ'11), Las Palmas de Gran Canaria, Spain

[93] A. Hoshi, D. Mills, A. Bittar, and T. S. Saitoh, 2005: *Screening of high melting point phase change materials (PCM) in solar thermal concentrating technology based on CLFR*, in: Solar Energy, volume 79:pp. 332–339

[94] D. Laing, 2007: *Storage Development for Direct Steam Generation Power Plants*, DLR Deutsches Zentrum fuer Luft und Raumfahrt, Parabolic Trough Technology Workshop, Golden CO, USA

[95] K. E. N'Tsoukpoe, H. Liu, N. Le Pierrès, and L. Luo, 2009: *A review on long-term sorption solar energy storage*, in: Renewable and Sustainable Energy Reviews, volume 13:pp. 2385–2396

[96] Q. Ma, L. Luo, R. Z. Wang, and G. Sauce, 2009: *A review on transportation of heat energy over long distance: Exploratory development*, in: Renewable and Sustainable Energy Reviews, volume 13:pp. 1532–1540

[97] M. Keunecke, 2004: *Die solarthermische Dissoziation von Zinkoxid: Experimentelle Untersuchung und Modellierung der Rückreaktion - Doctoral Thesis*, Mathematisch - Naturwissenschaftliche Fakultaet der Universitaet Augsburg, Augsburg, Germany

[98] A. Luzzi, K. Lovegrove, E. Filippi, H. Fricker, M. Schmitz-Goeb, M. Chandapillai, and S. Kaneff, 1999: *Techno-economic analysis of a 10 MWe solar thermal power plant using ammonia-based thermochemical energy storage*, in: Solar Energy, volume 66:pp. 91–101

[99] K. Lovegrove, A. Luzzi, I. Soldiani, and H. Kreetz, 2004: *Developing ammonia based thermochemical energy storage for dish power plants*, in: Solar Energy, volume 76:pp. 331–337

[100] K. Lovegrove, A. Luzzi, and H. Kreetz, 1999: *A solar-driven ammonia-based thermochemical energy storage system*, in: Solar Energy, volume 67:pp. 309–316

[101] H. Kreetz and K. Lovegrove, 1999: *Theoretical analysis and experimental results of a 1 kWchem ammonia synthesis reactor for a solar thermochemical energy storage system*, in: Solar Energy, volume 67:pp. 287–296

[102] K. Lovegrove and A. Luzzi, 1996: *Endothermic reactors for an ammonia based thermo-chemical solar energy storage and transport system*, in: Solar Energy, volume 56:pp. 361–371

[103] M. Levy, R. Levitan, H. Rosin, and R. Rubin, 1993: *Solar energy storage via a closed-loop chemical heat pipe*, in: Solar Energy, volume 50:pp. 179–189

[104] J. H. Edwards, K. T. Do, and A. M. Maitra, 1996: *The use of solar-based CO2/CH4 reforming for reducing greenhouse gas emissions during the generation of electricity and process heat*, in: Energy Conversion and Management, volume 37:pp. 1339–1344

[105] J. F. Muir, R. E. Hogan, R. D. Skocypec, and R. Buck, 1994: *Solar reforming of methane in a direct absorption catalytic reactor on a parabolic dish: I - test and analysis*, in: Solar Energy, volume 52:pp. 467–477

[106] M. Forster, 2004: *Theoretical investigation of the system SnOx/Sn for the thermochemical storage of solar energy*, in: Energy, volume 29:pp. 789–799

[107] S. Relloso and E. Delgado, 2009: *Experience with Molten Salt Thermal Storage in a Commercial Parabolic Trough Plant. Andasol-1 Commissioning and Operation*, SolarPACES, Berlin, Germany

[108] S. Relloso and J. Lata, 2011: *Molten Salt Thermal Storage: A Proven Solution to Increase Plant Dispatchability. Experience in Gemasolar Tower Plant*, SolarPACES, Granada, Spain

[109] B. Kelly, 2008: *Two Tank Indirect Thermal Storage Systems*, Ausra Inc., Nexant Inc., Palo Alto, California, USA

[110] R. K. Shah and D. P. Sekulic, 2003: *Fundamentals of Heat Exchanger Design*, John Wiley and Sons, Inc., Hoboken, New Jersey, USA

[111] F. Zaversky, M. Sánchez, and D. Astrain, 2014: *Object-oriented modeling for the transient response simulation of multi-pass shell-and-tube heat exchangers as applied in active indirect thermal energy storage systems for concentrated solar power*, in: Energy, volume 65:pp. 647–664

[112] M. Prithiviraj and M. J. Andrews, 1998: *Three dimensional numerical simulation of shell-and-tube heat exchangers. Part I: Foundation and fluid dynamics*, in: Numerical Heat Transfer, Part A: Applications: An International Journal of Computation and Methodology, volume 33(8):pp. 799–816

[113] J.-F. Zhang, Y.-L. He, and W.-Q. Tao, 2009: *3D numerical simulation on shell-and-tube heat exchangers with middle-overlapped helical baffles and continuous baffles – Part I: umerical model and results of whole heat exchanger with middle-overlapped helical baffles*, in: International Journal of Heat and Mass Transfer, volume 52:pp. 5371–5380

[114] E. Ozden and I. Tari, 2010: *Shell side CFD analysis of a small shell-and-tube heat exchanger*, in: Energy Conversion and Management, volume 51:pp. 1004–1014

[115] Y. You, A. Fan, S. Huang, and W. Liu, 2012: *Numerical modeling and experimental validation of heat transfer and flow resistance on the shell side of a shell-and-tube heat exchanger with flower baffles*, in: International Journal of Heat and Mass Transfer, volume 55:pp. 7561–7569

[116] H. J. Morris, 1960: *Dynamic response of shell and tube heat exchangers to temperature disturbances*, pp. 354–359, Automatic and Remote Control - Proceedings of the First International Congress of the International Federation of Automatic Control, Moscow

[117] M. Masubuchi, 1959: *Dynamic response and control of multipass heat exchangers*, Instruments and Regulators Conference of the ASME, Cleveland, Ohio, USA

[118] E. S. Gaddis and E. U. Schlünder, 1975: *Temperaturverlauf und übertragbare Wärmemenge in Röhrenkesselapparaten mit Umlenkblechen*, in: Verfahrenstechnik, volume 9(12):pp. 617–621

[119] M. N. Roppo and E. N. Ganic, 1981: *Time-dependent heat exchanger modeling*, in: Heat Transfer Engineering, volume 4(2):pp. 42–46

[120] E. S. Gaddis and E. U. Schlünder, 1979: *Temperature distribution and heat exchange in multipass shell-and-tube exchangers with baffles*, in: Heat Transfer Engineering, volume 1(1):pp. 43–52

[121] D. J. Correa and J. L. Marchetti, 1987: *Dynamic simulation of shell-and-tube heat exchangers*, in: Heat Transfer Engineering, volume 8(1):pp. 50–59

[122] W. Roetzel and Y. Xuan, 1992: *Transient behaviour of multipass shell-and-tube heat exchangers*, in: International Journal of Heat and Mass Transfer, volume 35(3):pp. 703–710

[123] T. W. Botsch, K. Stephan, J. L. Alcock, and D. R. Webb, 1997: *Modelling and simulation of the dynamic behaviour of a shell-and-tube condenser*, in: International Journal of Heat and Mass Transfer, volume 40(17):pp. 4137–4149

[124] F. Manenti and Z. Ravaghi-Ardebili, 2013: *Dynamic simulation of concentrating solar power plant and two-tanks direct thermal energy storage*, in: Energy, volume 55:pp. 89–97

[125] V. Milián, J. Navarro-Esbrí, D. Ginestar, F. Molés, and B. Peris, 2013: *Dynamic model of a shell-and-tube condenser. Analysis of the mean void fraction correlation influence on the model performance*, in: Energy, volume 59:pp. 521–533

[126] S. E. Mattsson, 1997: *On modeling of heat exchangers in Modelica*, 9th European Simulation Symposium, Passau, Germany

[127] H. Elmqvist and S. E. Mattsson, 1997: *Modelica - The next generation modeling language - An international design effort*, Proceedings of the 1st World Congress on System Simulation, Singapore

[128] S. E. Mattsson, M. Ericson, and P. Östberg, 1994: *An object-oriented model of a heat-exchanger unit*, European Simulation Multiconference, Barcelona, Spain

[129] F. Casella and F. Schiavo, 2003: *Modelling and Simulation of Heat Exchangers in Modelica with Finite Element Methods*, Proceedings of the 3rd International Modelica Conference, Linköping, Sweden

[130] T. Skoglund, K.-E. Arzén, and P. Dejmek, 2006: *Dynamic object-oriented heat exchanger models for simulation of fluid property transitions*, in: International Journal of Heat and Mass Transfer, volume 49:pp. 2291–2303

[131] K. Assaf, A. Zoughaib, and D. Clodic, 2011: *Modelica-based modelling and simulation of dry-expansion shell-and-tube evaporators working with alternative refrigerant mixtures*, in: International Journal of Refrigeration, volume 34:pp. 1471–1482

[132] F. Zaversky, J. García-Barberena, M. Sánchez, and D. Astrain, 2013: *Transient molten salt two-tank thermal storage modeling for CSP performance simulations*, in: Solar Energy, volume 93:pp. 294–311

[133] L. G. Radosevich and C. E. Wyman, 1983: *Thermal energy storage development for solar electrical power and process heat applications*, in: Journal of Solar Energy Engineering, volume 105:pp. 111–118

[134] M. Castro, J. L. Presa, J. Díaz, J. Peire, A. F. Baker, S. E. Faas, L. G. Radosevich, and A. C. Skinrood, 1991: *C.R.S. receiver and storage systems evaluation*, in: Solar Energy, volume 47(3):pp. 197–207

[135] J. M. Andújar, F. Rosa, and M. Geyer, 1991: *CESA-I thermal storage system evaluation*, in: Solar Energy, volume 46(5):pp. 305–312

[136] M. Castro, J. Peire, and P. Martinez, 1987: *Five-year CESA-I simulation program review*, in: Solar Energy, volume 38(6):pp. 415–424

[137] F. A. Al-Sulaiman, I. Dincer, and F. Hamdullahpur, 2011: *Exergy modeling of a new solar driven trigeneration system*, in: Solar Energy, volume 85:pp. 2228–2243

[138] A. Rovira, M. J. Montes, M. Valdes, and J. M. Martinez-Val, 2011: *Energy management in solar thermal power plants with double thermal storage system and subdivided solar field*, in: Applied Energy, volume 88:pp. 4055–4066

[139] J. Schulte-Fischedick, R. Tamme, and U. Herrmann, 2008: *CFD Analysis of the Cool Down Behaviour of Molten Salt Thermal Storage Systems*, ES2008 Energy Sustainability, Jacksonville, Florida, USA

[140] A. C. McMahan, 2006: *Design and Optimization of Organic Rankine Cycle Solar-Thermal Powerplants, Master's Thesis*, University of Wisconsin-Madison, USA

[141] F. R. Villatoro, J. Pérez, F. Domínguez-Muñoz, and J. M. Cejudo-López, 2009: *Approximate analytic solution for the heat transfer in packed beds for solar thermal storage in building simulators*, International IBPSA Conference, Glasgow, Scotland

[142] T. E. W. Schumann, 1929: *Heat transfer: A liquid flowing through a porous prism*, in: Journal of the Franklin Institute, volume 208:pp. 405–416

[143] A. Mawire and M. McPherson, 2009: *Experimental and simulated temperature distribution of an oil-pebble bed thermal energy storage system with a variable heat source*, in: Applied Thermal Engineering, volume 29:pp. 1086–1095

[144] J. T. Van Lew, P. Li, and C. L. Chan, 2009: *Transient heat delivery and storage process in a thermocline heat storage system*, ASME 2009 International Mechanical Congress and Exposition IMECE 2009, Lake Buena Vista, Florida, USA

[145] W. D. Steinmann and J. Buschle, 2005: *Analysis of thermal storage systems using Modelica*, pp. 331–337, International Modelica Conference, Hamburg , Germany

[146] R. Tamme, D. Laing, and W. D. Steinmann, 2003: *Advanced thermal energy storage technology for parabolic trough*, ISEC 2003: International Solar Energy Conference, Hawaii, USA

[147] A. Meier, C. Winkler, and D. Wuillemin, 1991: *Experiment for modeling high temperature rock bed storage*, in: Solar Energy Materials, volume 24:pp. 255–264

[148] A. Stückle, 2009: *Modelling of high temperature storage systems for latent heat*, International Modelica Conference, Como, Italy

[149] V. Morisson, M. Rady, E. Palomo, and E. Arquis, 2008: *Thermal energy storage systems for electricity production using solar energy direct*

steam generation technology, in: Chemical Engineering and Processing, volume 47:pp. 499–507

[150] R. D. Skocypec, R. E. Hogan, and J. F. Muir, 1994: *Solar reforming of methan in a direct absorption catalytic reactor on a parabolic dish: II - modeling and analysis*, in: Solar Energy, volume 52:pp. 479–490

[151] F. Zaversky, R. Medina, J. García-Barberena, M. Sánchez, and D. Astrain, 2012: *Part load behavior of oil-to-molten-salt heat exchanger configurations for active indirect storage systems in CSP applications*, SolarPACES, Marrakech, Morocco

[152] F. Kreith, R. M. Manglik, and M. S. Bohn, 2011: *Principles of Heat Transfer*, Cengage Learning, Stamford, USA

[153] Y. A. Cengel, 2006: *Heat and Mass Transfer - A Practical Approach*, McGraw-Hill, New York, USA, 3rd edition

[154] V. Gnielinski, 1979: *Equations for calculating heat transfer in single tube rows and banks of tubes in transverse flow*, in: International Chemical Engineering, volume 19:pp. 380–391

[155] VDI-Gesellschaft-Verfahrenstechnik-Chemieingenieurwesen, 2006: *VDI-Wärmeatlas*, Springer-Verlag, Berlin, Germany, 10th edition

[156] E. S. Gaddis and V. Gnielinski, 1997: *Pressure drop on the shell side of shell-and-tube heat exchangers with segmental baffles*, in: Chemical Engineering and Processing, volume 36:pp. 149–159

[157] I. E. Idelchik, 2001: *Handbook of Hydraulic Resistance*, Begell House, 3rd edition

[158] A. B. Zavoico, 2001: *Solar Power Tower Design Basis Document - Revision 0*, Sandia National Laboratories, Albuquerque, New Mexico 87185 and Livermore, California 94550

[159] M. Peet, H. Hasan, and H. K. D. H. Bhadeshia, 2011: *Prediction of thermal conductivity of steel*, in: International Journal of Heat and Mass Transfer, volume 54:pp. 2602–2608

[160] F. Ochs and H. Müller-Steinhagen, 2005: *Temperature and Moisture Dependence of the Thermal Conductivity of Insulation Materials*, NATO Advanced Study Institute on Thermal Energy Storage for Sustainable Energy Consumption (TESSEC), Izmir, Cesme

[161] B. Kelly, D. Kearney, and H. Price, 2006: *Thermal Storage Commercial Plant Design Study for a 2-Tank Indirect Molten Salt System, NREL/SR-550-40166*, NREL National Renewable Energy Laboratory, Golden, Colorado, USA

[162] H. P. Ebert and F. Hemberger, 2011: *Intercomparison of thermal conductivity measurements on a calcium silicate insulation material*, in: International Journal of Thermal Sciences, volume 50:pp. 1838–1844

[163] Modelica-Association, 2010: *Modelica Standard Library 3.2 - Free library from the Modelica Association to model mechanical (1D/3D), electrical (analog, digital, machines), thermal, fluid, control systems and hierarchical state machines*, Modelica-Association, http://www.modelica.org (accessed 14.11.2012)

[164] C. Richter, 2008: *Proposal of New Object-Oriented Equation-Based Model Libraries for Thermodynamic Systems - Dissertation*, Technische Universität Carolo-Wilhelmina zu Braunschweig, Germany

[165] G. Cao, S. J. Weber, S. O. Martin, M. H. Anderson, K. Sridharan, and T. R. Allen, 2012: *Spectral emissivity measurements of candidate materials for very high temperature reactors*, in: Nuclear Engineering and Design, volume 251:pp. 78–83

[166] P. Sabharwall, M. Ebner, M. Sohal, P. Sharpe, M. H. Anderson, K. Sridharan, J. Ambrosek, L. Olson, and P. Brooks, 2010: *Molten Salts for High Temperature Reactors: University of Wisconsin Molten Salt Corrosion and Flow Loop Experiments – Issues dentified and Path Forward*, Idaho National Laboratory, Idaho Falls, Idaho 83415, USA

[167] B. Y. H. Liu and R. C. Jordan, 1963: *A rational procedure for predicting the long-term average performance of flat-plate solar-energy collectors*, in: Solar Energy, volume 7(2):pp. 53–74

[168] P. Berdahl and R. Fromberg, 1982: *The thermal radiance of clear skies*, in: Solar Energy, volume 29(4):pp. 299–314

[169] A. L. Buck, 1981: *New equations for computing vapor pressure and enhancement factor*, in: Journal of Applied Meteorology, volume 20:pp. 1527–1532

[170] H. Suehrcke, E. L. Peterson, and N. Selby, 2008: *Effect of Roof Solar Reflectance on the Building Heat Gain in a hot Climate*, in: Energy and Buildings, volume 40:pp. 2224–2235

[171] D. J. Naus, 2005: *The effect of elevated temperatures on concrete materials and structures - A literature review*, Oak Ridge National Laboratory, Tennessee, USA

[172] R. Ferri, A. Cammi, and D. Mazzei, 2008: *Molten salt mixture properties in RELAP5 code for thermodynamic solar applications*, in: International Journal of Thermal Sciences, volume 47:pp. 1676–1687

[173] B. J. McBride, M. J. Zehe, and S. Gordon, 2002: *NASA Glenn Coefficients for Calculating Thermodynamic Properties of Individual Species*, Glenn Research Center, Cleveland, Ohio, USA

[174] K. Kadoya, N. Matsunaga, and A. Nagashima, 1985: *Viscosity and Thermal Conductivity of Dry Air in the Gaseous Phase*, in: Journal of Physical and Chemical Reference Data, volume 14(4):pp. 947–970

[175] K. Stephan and R. Krauss, 1987: *Viscosity and thermal conductivity of nitrogen for a wide range of fluid states*, in: Journal of Physical and Chemical Reference Data, volume 16(4):pp. 993–1023

[176] Modelica-Association, 2012: *Modelica® - A Unified Object-Oriented Language for Systems Modeling - Language Specification - Version 3.3*, Modelica-Association, https://www.modelica.org (accessed 14.11.2012)

[177] H.-J. Bartsch, 2001: *Taschenbuch mathematischer Formeln*, Fachbuchverlag Leipzig im Carl Hanser Verlag, München (Germany), Wien (Austria), 19th edition

[178] L. R. Petzold, 1982: *A description of DASSL: A differential/algebraic system solver*, Sandia National Laboratories, Albuquerque, New Mexico, USA

[179] K. E. Brenan, S. L. Campbell, and L. R. Petzold, 1996: *Numerical Solution of Initial-Value Problems in Differential-Algebraic Equations*, SIAM - Society for Industrial and Applied Mathematics, Philadelphia, USA

[180] Dassault-Systèmes, 2012: *Dymola - Multi-Engineering Modeling and Simulation*, Dassault-Systèmes, http://www.3ds.com (accessed 14.11.2012)

[181] Open-Source-Modelica-Consortium, 2013: *OpenModelica - An open-source Modelica-based modeling and simulation environment*, Open

Source Modelica Consortium (OSMC), http://www.openmodelica.org (accessed 8.1.2013)

[182] R. Franke, F. Casella, M. Sielemann, K. Proelss, M. Otter, and M. Wetter, 2009: *Standardization of Thermo-Fluid Modeling in Modelica.Fluid*, Proceedings 7th Modelica Conference, Como, Italy

[183] H. Tummescheit, 2002: *Design and Implementation of Object-Oriented Model Libraries using Modelica - PhD Thesis*, Department of Automatic Control - Lund Institute of Technology, Lund, Sweden

[184] H. E. Siekmann, 2000: *Strömungslehre - Grundlagen*, Springer-Verlag, Berlin, Heidelberg, Germany

[185] TEMA, 1999: *Standards of the Tubular Exchanger Manufacturers Association*, TEMA-Tubular Exchanger Manufacturers Association, Inc., New York, USA

[186] M. Wetter, 2013: *Modelica Buildings Library - A free open-source library for building energy and control systems*, Lawrence Berkeley National Laboratory, http://simulationresearch.lbl.gov/modelica (accessed: 11.02.2013)

[187] V. Gnielinski, 1975: *Neue Gleichungen für den Wärme- und den Stoffübergang in turbulent durchströmten Rohren und Kanälen*, in: Forschung im Ingenieurwesen A, volume 41(1):pp. 8–16

[188] J. P. Abraham, E. M. Sparrow, and J. C. K. Tong, 2009: *Heat transfer in all pipe flow regimes: laminar, transitional/intermittent, and turbulent*, in: International Journal of Heat and Mass Transfer, volume 52:pp. 557–563

[189] L. F. Moody, 1944: *Friction factors for pipe flow*, in: Transactions of the ASME, volume 66(8):pp. 671–684

[190] W. Wagner and A. Kruse, 1998: *Properties of water and steam: the industrial standard IAPWS-IF97 for the thermodynamic properties and supplementary equations for other properties: tables based on these equations*, Springer-Verlag

[191] D. E. Seborg, T. F. Edgar, D. A. Mellichamp, and F. J. Doyle, 2011: *Process Dynamics and Control*, John Wiley and Sons, Inc., Hoboken, New Jersey, USA, 3rd edition

[192] F. Zaversky, M. M. Rodríguez-García, J. García-Barberena, M. Sánchez, and D. Astrain, 2014: *Transient behavior of an active indirect two-tank thermal energy storage system during changes in operating mode – An application of an experimentally validated numerical model*, in: Energy Procedia

[193] H. Lutz and W. Wendt, 2010: *Taschenbuch der Regelungstechnik - mit MATLAB und Simulink*, Wissenschaftlicher Verlag Harri Deutsch, Frankfurt am Main, Germany, 8th edition

[194] K. Krüger, R. Franke, and M. Rode, 2004: *Optimization of boiler start-up using a nonlinear boiler model and hard constraints*, in: Energy, volume 29:pp. 2239–2251

[195] T. Hirsch and H. Schenk, 2010: *Dynamics of oil-based parabolic trough plants - A detailed transient simulation model*, SolarPACES, Perpignan

[196] T. D. Bui and T. R. Bui, 1979: *Numerical methods for extremely stiff systems of ordinary differential equations*, in: Applied Mathematical Modelling, volume 3:pp. 355–358

[197] M. N. Spijker, 1996: *Stiffness in numerical initial-value problems*, in: Journal of Computational and Applied Mathematics, volume 72:pp. 393–406

[198] Archimede-Solar-Energy, 2012: *HEMS11 - ASE receiver tube datasheet*, Archimede-Solar-Energy (ASE), http://www.archimedesolarenergy.com (accessed: 17.12.2012)

[199] F. Burkholder and C. Kutscher, 2009: *Heat Loss Testing of Schott's 2008 PTR70 Parabolic Trough Receiver - Technical Report NREL/TP-550-45633*, National Renewable Energy Laboratory, Golden, Colorado, USA

[200] M. J. Blanco, D. C. Alarcón-Padilla, T. López-Moratalla, and L.-C. Martín, 2001: *Computing the solar vector*, in: Solar Energy, volume 70(5):pp. 431–441

[201] M. T. Cicero, 43 B.C.: *12th Philippic Senatorial Speech*

[202] S. E. Hieronymus, 395: *Letter LVII - To Pammachius on the Best Method of Translating*

[203] F. Zaversky, S. Bergmann, and W. Sanz, 2012: *Detailed modeling of parabolic trough collectors for the part load simulation of solar thermal power plants - GT2012-68032*, pp. 235–247, Proceedings of the ASME Turbo Expo, Copenhagen, Denmark

[204] B. Epple, R. Leithner, W. Linzer, and H. Walter, 2009: *Simulation von Kraftwerken und wärmetechnischen Anlagen*, Springer-Verlag, Wien (Austria)

[205] Aalborg-CSP, 2013: *Aalborg CSP - Steam generators for concentrated solar power plants*, http://www.aalborgcsp.com/ (accessed 2.5.2013)

[206] K. J. Aström and R. D. Bell, 2000: *Drum-boiler dynamics*, in: Automatica, volume 36:pp. 363–378

[207] Aalborg-CSP, 2011: *Aalborg CSP steam generators - Technical information*, www.aalborgCSP.com (accessed 16.09.2012)

[208] W. R. Paterson, 1984: *A replacement for the logarithmic mean*, in: Chemical Engineering Science, volume 39(11):pp. 1635–1636

[209] H. Jericha, 1985: *Thermal Turbomachinery*, Institute for Thermal Turbomachinery and Machine Dynamics, Graz University of Technology, Austria

[210] A. E. Conradie and D. G. Kröger, 1996: *Performance evaluation of dry-cooling systems for power plant applications*, in: Applied Thermal Engineering, volume 16(3):pp. 219–232

[211] J. A. Van Rooyen and D. G. Kröger, 2007: *Performance trends of an air-cooled steam condenser under windy conditions*, California Energy Commission - PIER Energy-Related Environmental Research Program, California, USA

[212] W. Zhao, Q. Qu, and Q. Li, 2013: *Numerical investigation on the flow field of an axial flow fan in a direct air-cooled condenser for a large power plant*, in: Heat Transfer - Asian Research, volume 42(1):pp. 60–72

[213] S. Skogestad and I. Postlethwaite, 2005: *Multivariable feedback control - Analysis and design*, John Wiley and Sons, Ltd., West Sussex, England, 2nd edition

[214] M. Sielemann, F. Casella, M. Otter, C. Clauss, J. Eborn, S. E. Mattsson, and H. Olsson, 2011: *Robust initialization of differential-algebraic equations using homotopy*, 8th International Modelica Conference, Dresden, Germany

[215] F. Casella, M. Sielemann, and L. Savoldelli, 2011: *Steady-state initialization of object-oriented thermo-fluid models by homotopy methods*, 8th International Modelica Conference, Dresden, Germany

[216] P. Deuflhard, 2004: *Newton Methods for Nonlinear Problems - Affine Invariance and adaptive Algorithms*, Springer-Verlag, Berlin, Heidelberg, Germany

[217] D. Lindsley, 2000: *Power Plant Control and Instrumentation - The Control of boilers and HRSG systems*, IET Control Engineering Series, London, United Kingdom

[218] D. Flynn, 2003: *Thermal Power Plant Simulation and Control*, IEE Power and Energy Series, London, United Kingdom

[219] P. Fritzson, 2004: *Principles of Object-Oriented Modeling and Simulation with Modelica 2.1*, IEEE Press - Wiley-Interscience

[220] H. Ibrahim, A. Llinca, and J. Perron, 2008: *Energy storage systems - Characteristics and comparisons*, in: Renewable and Sustainable Energy Reviews, volume 12:pp. 1221–1250

[221] W. Li and G. Joós, 2008: *A power electronic interface for a battery supercapacitor hybrid energy storage system for wind applications*, pp. 1762–1768, Power Electronics Specialists Conference - IEEE, Rhodes, Greece

[222] M. Specht, F. Baumgart, B. Feigl, V. Frick, B. Stürmer, U. Zuberbühler, M. Sterner, and G. Waldstein, 2009: *Storing bioenergy and renewable electricity in the natural gas grid*, in: Forschungsverbund Erneuerbare Energien - AEE Topics, pp. 69–78

[223] V. M. Fthenakis and T. Nikolakakis, 2012: *Storage options for photovoltaics*, in: Comprehensive Renewable Energy, volume 1:pp. 199–212

[224] D. D. Banham-Hall, G. A. Taylor, C. A. Smith, and M. R. Irving, 2012: *Flow batteries for enhancing wind power integration*, in: IEEE Transactions on Power Systems, volume 27(3):pp. 1690–1697

[225] R. Madlener and J. Latz, 2013: *Economics of centralized and decentralized compressed air energy storage for enhanced grid integration of wind power*, in: Applied Energy, volume 101:pp. 299–209